



**HAL**  
open science

# Photo-electrochemical cells for green H<sub>2</sub> production : a contribution to scaling up studies

Angela Maragno

## ► To cite this version:

Angela Maragno. Photo-electrochemical cells for green H<sub>2</sub> production : a contribution to scaling up studies. Chemical and Process Engineering. Université Claude Bernard - Lyon I, 2024. English. NNT : 2024LYO10038 . tel-04719166

**HAL Id: tel-04719166**

**<https://theses.hal.science/tel-04719166v1>**

Submitted on 3 Oct 2024

**HAL** is a multi-disciplinary open access archive for the deposit and dissemination of scientific research documents, whether they are published or not. The documents may come from teaching and research institutions in France or abroad, or from public or private research centers.

L'archive ouverte pluridisciplinaire **HAL**, est destinée au dépôt et à la diffusion de documents scientifiques de niveau recherche, publiés ou non, émanant des établissements d'enseignement et de recherche français ou étrangers, des laboratoires publics ou privés.

# THESE de DOCTORAT DE L'UNIVERSITE CLAUDE BERNARD LYON 1

**Ecole Doctorale N° 206**  
**Chimie (Chimie, Procédés, Environnement)**

**Discipline** : Génie des Procédés

Soutenue publiquement le 12/03/2024, par :  
**Angela Rosa Angelica MARAGNO**

---

## **Photo-electrochemical cells for green H<sub>2</sub> production: a contribution to scaling up studies**

---

Devant le jury composé de :

HAUSSENER Sophia	Professeure Associée École Polytechnique Fédérale de Lausanne (Suisse)	Rapporteure
SPECCHIA Stefania	Professeure des Universités Ecole polytechnique de Turin (Italie)	Rapporteure
ARTERO Vincent	Directeur de Recherche CEA Grenoble	Examineur
GROS Fabrice	Professeur des Universités SIGMA Clermont, UMR 6602 - Institut Pascal	Examineur
TAYAKOUT-FAYOLLE Melaz	Professeure des Universités Université Lyon 1, UMR 5007 - LAGEPP	Présidente
CHARTON Sophie	Directrice de Recherche CEA Marcoule	Directrice de thèse
MATHERON Muriel	Directrice de Recherche CEA Grenoble	Invitée

## Acknowledgements

*My years of research in France have been a journey full of discoveries, both scientific and personal, rich friendships, new passions, love and creativity. I enjoyed croissants aux amandes, raclettes and pastis but also artificial photosynthesis, sustainability and renewable energy.*

*I collected memories thanks to the many people I met along the way, to many visited places and all the emotions that science aroused in me. The enthusiasm and the desire to discover more and more have been the cornerstones of my project in order to be an example for the new scientists of the future, always contributing to the exploration of advanced ecological solutions.*

*After carrying out this research project in the best possible way, I would like to express my gratitude to my PhD director, Sophie CHARTON, the first person who wanted this adventure to begin. From our first call during the Covid pandemic, I knew I could count on you. You have been a caring and supportive guide through all the thesis, helping me to face every obstacle and enjoying with me the positive results. Thank you, Sophie, for always caring about my well-being, both professionally and personally. You made sure I felt comfortable in my work and daily life. Thank you for teaching me that determination and integrity are the foundations of true scientific research.*

*My sincere thanks go to Vincent ARTERO, first of all for welcoming me in the LCBM laboratory and in the Solhycat group in Grenoble, always including me in all initiatives. Vincent, your prompt decision-making, your preparation and your good humor, even in difficult moments, were a constant example for me. The trust you placed in me from the beginning has encouraged and motivated me to deal with every challenge during the 3 years.*

*To Muriel MATHERON, thank you so much for introducing me to and teaching me some of the most interesting points in my research. Your clarity, passion, and patience in explaining new concepts about solar cells, optics, photons and electricity have been very remarkable for me. You made our experiments and assembly work more pleasant and efficient.*

*Thank you, Sophie, Vincent, and Muriel, for being not only my supervisors but also wonderful people I will always carry in my heart.*

*I would also like to give a special thank to Matthieu KOEPF for showing me the joy of working in reaserch, enjoying every single experiment. Your willingness to help me both in my thesis projects and in my daily life, along with your thoughtful advice, have made me a better scientist.*

*Many thanks to my colleagues, friends and advisors, Adina MOROZAN and Jennifer FIZE, I miss you both already. I miss the complicity we had, I even miss the thousand connection problems, short circuits and stuck screws that drove us crazy. I never doubted our success because I knew we could always count on each other. The journey was beautiful, long but it passed fast, full of "current" swings. I also warmly thank Gregory, Romain, and the rest of the EASI Fuel team for being essential pieces of a wonderful puzzle that allowed us to complete a major project.*

*An infinite thank you goes to Jonathan, Matthieu, Yao and Nabil, to our evenings, our breaks and all those moments that served as recharge after full weeks. You have been my batteries and*

*I am infinitely grateful to you. In reality, a special thank you is for Nabil, not only for always believing in me and always supporting me but for being the most beautiful gift of my French trip.*

*Thanks to all my colleagues in Solhycat group: Claire, Léo, Bertrand, Murielle, Caitilín, Nina, Laura, Mariam etc. You all made me miss home much less and gave me the security of knowing I could count on you.*

*I deeply thank Duc and Afridi for his guidance from the beginning, his altruism, and his full desire to learn and teach new scientific discoveries. Thanks for guiding me on how to take the first steps in the lab and how to make the first electrochemical measurements, for welcoming me on my first day, making me feel at ease, and showing me friendship even from far.*

*I want to express my sincere thanks to the Claude Bernard University Lyon 1 and to the Chemistry Doctoral School of Lyon for the opportunity to pursue my doctoral degree, to the CEA for the funding and the chance to work on ECC FOCUS thesis.*

*Additionally, I am grateful to Prof. Sophia HAUSSENER, Prof. Stefania SPECCHIA, Prof. Fabrice GROS and Prof. Melaz TAYAKOUT-FAYOLLE for agreeing to be members of the jury and evaluate this work. I deeply appreciate the engaging discussions during the defense, and the valuable suggestions provided.*

*Special thanks to Manuel MIGUIRDITCHIAN, the director of my laboratory LRVE in Marcoule, and to Fabrice LAMADIE. You have been valuable reference points that made my last year much easier and stimulating.*

*I would also like to express my gratitude to my LRVE colleagues. Kassem, Clément, Chloé, Thomas, Tamar and all the others for bringing sunshine into a new place, a bit of alternative research, and nice evenings in company. A special thanks for my laughing and wine partner Tamar for being full of energy and optimism, always present, in happy and difficult moments.*

*I also extend my infinite gratitude to all the people I met along my years in France (Ahmad, Hadi, Lucas, Bea, Steven, Salah, Colette, Osmonde, Ambre, Helena, Kavya etc.), to my dear friend Francesca for her constant inspiration and encouragement in my PhD research, to all my other Italian friends who always have supported me from far.*

*Finally, a special thanks to Mum, Dad, and my siblings, my heart is always with you. Thank you so much to Nonna, Angela, and all the rest of our big family. You all have always believed in me and stood by my side, providing the energy needed to embrace all that life will offers me.*

*Today, I proudly acknowledge the courage it took to leave for a new country four years ago. This journey has enriched me immeasurably, continually improving and strengthening who I am.*

*Working with and for a beautiful and correct science is the message I wish to convey and the path I will continue to follow. Grazie Francia, merci ma chère France. I will carry you with me always, with a touch of melancholy and sadness, but above all, with a secret happiness.*



## English abstract

This PhD project focuses on the study of two types of solar fuel generators: a PEC cell based on a bismuth vanadate ( $\text{BiVO}_4$ ) photoanode, and an integrated photoelectrochemical (IPEC) cell combining a solar cell with an electrolyser. Both devices achieve the artificial photosynthesis process of capturing solar energy and storing it in chemical bonds. The goal of the work is to identify the limiting parameters that hinder the large-scale deployment of these photoelectrochemical devices and to propose solutions in order to facilitate research in this field. Two specific scientific questions are at the heart of this research:

1. What is the impact of heterogeneities, inherent to large-scale preparation processes, on the performance of photoactive materials?
2. What role can integration play in transferring performance from the laboratory to the pilot scale?

To answer the first question, an experimental parametric study was undertaken on  $\text{BiVO}_4$  photoanodes, considered as photoactive semiconductors representative for artificial photosynthesis.

In parallel, in order to answer to the second question, an IPEC cell, the combination of a PK/Si tandem solar cell with a proton exchange membrane (PEM) electrolyser, was realized, tested and optimized. Scale-up was then considered, via the design of a monolithic module, integrating 9 IPEC cells. The realization of 5 of these modules enabled the assembly of the EASI Fuel device (European Autonomous Solar Integrated fuel station) for the continuous conversion of  $\text{H}_2$  (produced under sunlight by the IPEC cells) and  $\text{CO}_2$  into  $\text{CH}_4$  within a methanogenesis Archaea-based bioreactor. Thanks to this innovative coupling, the EASI Fuel device was selected and successfully tested for 72 hours of continuous operation in total autonomy, during the final of the *Horizon Prize - Fuel from the Sun: Artificial Photosynthesis* competition, which took place at the end of the 2<sup>nd</sup> year of the thesis.

**Keywords:** energy, environment, solar processes, artificial photosynthesis, photo-electrochemical cells, scale-up, integration, photoanodes, optical simulations, hydrogen production.



# French title

Cellules photo-électrochimiques pour la production d'H<sub>2</sub> vert : une contribution aux études de mise à l'échelle

## French abstract

Ce projet de thèse porte sur l'étude de deux concepts de générateurs de carburant solaire : une cellule PEC basée sur une photoanode de vanadate de bismuth (BiVO<sub>4</sub>) et une cellule intégrée (IPEC) combinant une cellule solaire à une cellule d'électrolyse. Les deux dispositifs réalisent le processus de photosynthèse artificielle consistant à capturer l'énergie solaire et à la stocker dans les liaisons chimiques. L'objectif de ces travaux est d'identifier les verrous au déploiement à grande échelle de ces dispositifs photo-électrochimiques et de proposer des solutions pour les lever. Deux questions scientifiques sont en particulier au cœur de mes travaux de recherche :

1. Quel est l'impact des hétérogénéités, inhérentes aux procédés d'élaboration à grande échelle des matériaux photo-actifs, sur leurs performances ?
2. Quel rôle peut jouer l'intégration dans la transposition, à l'échelle pilote, des performances obtenues en laboratoire ?

Pour répondre à la première question une étude paramétrique expérimentale a été proposée et menée. Elle porte sur des photo-anodes à base de BiVO<sub>4</sub>, un matériau modèle pour la photosynthèse artificielle.

En parallèle, afin de répondre à la seconde question, nous avons réalisé, testé et optimisé une cellule IPEC consistant en la combinaison d'une cellule solaire tandem PK/Si et d'un électrolyseur à membrane échangeuse de protons (PEM).

Le changement d'échelle a ensuite été considéré, avec la conception d'un module monolithique original, intégrant 9 cellules IPEC. La réalisation de 5 de ces modules a permis l'assemblage du démonstrateur **EASI Fuel** (*European Autonomous Solar Integrated fuel station*) pour la conversion continue d'hydrogène (produit sous ensoleillement par les IPEC) et de CO<sub>2</sub> en CH<sub>4</sub> par des Archées, au sein d'un bioréacteur de méthanation. Grâce à ce couplage innovant, le prototype EASI Fuel a été sélectionné et testé avec succès pendant 72h en continu et en totale autonomie, lors de la finale du concours *Horizon Prize - Fuel from the Sun: Artificial Photosynthesis*, qui s'est déroulée à la fin de la 2<sup>ème</sup> année de thèse.

**Mots-clés** : énergie, environnement, procédés solaires, photosynthèse artificielle, cellules photo-électrochimiques, changement d'échelle, intégration, photoanodes, simulations optiques, production d'hydrogène.



# Extended French abstract

## Introduction

Une approche couplant recherche fondamentale et génie des procédés est essentielle pour mettre au point de nouvelles technologies à zéro impact environnemental, en alternative aux combustibles fossiles. L'électrolyse de l'eau dans des cellules photo-électrochimiques (PEC) est une stratégie prometteuse pour convertir l'énergie solaire en carburant propre et durable, tel que l'hydrogène.

Ce projet de thèse porte sur l'étude de deux concepts de générateurs de carburant solaire : une cellule PEC basée sur une photoanode de vanadate de bismuth ( $\text{BiVO}_4$ ) et une cellule intégrée (IPEC) combinant une cellule solaire à une cellule d'électrolyse. Les deux dispositifs, de maturités technologiques et de surfaces actives différentes, réalisent le processus de photosynthèse artificielle consistant à capturer l'énergie solaire et à la stocker dans les liaisons chimiques. L'objectif de ces travaux est d'identifier les verrous au déploiement à grande échelle de ces dispositifs photo-électrochimiques et de proposer des solutions pour les lever. Deux questions scientifiques sont en particulier au cœur de mes travaux de recherche :

1. Quel est l'impact des hétérogénéités, inhérentes aux procédés d'élaboration à grande échelle des matériaux photo-actifs, sur leurs performances ?
2. Quel rôle peut jouer l'intégration dans la transposition, à l'échelle pilote, des performances obtenues en laboratoire ?

## Matériels et méthodologies

Pour répondre à la 1<sup>ère</sup> question une étude paramétrique expérimentale a été proposée et menée. Elle est basée sur des photo-anodes à base de  $\text{BiVO}_4$ , un matériau modèle pour la photosynthèse artificielle. Cette étude a consisté en :

- la fabrication d'une quarantaine de photo-anodes de  $\text{BiVO}_4$ , dopé et non dopé, avec et sans catalyseur. Seules des techniques potentiellement transposables à grande échelle ont été choisies, revêtement par centrifugation (spin coating) où par électrodéposition, sur des supports en FTO et ITO de résistivités électriques et d'épaisseurs différentes.
- l'analyse de la structure cristallographique des dépôts de  $\text{BiVO}_4$  par diffraction des rayons X, de leur microstructure par microscopie électronique à balayage (MEB) et de l'homogénéité macroscopique de cette couche active par profilométrie, réalisée en salle blanche ;
- La détermination des propriétés optiques, à l'aide d'un *spectrophotomètre UV/Vis/NIR* ;
- Enfin, la mesure des performances recherchées, c'est à dire du photo-courant et du courant d'électrolyse de l'eau, pour chaque photo-électrode, sous irradiation contrôlée à l'aide d'un simulateur solaire et d'un potentiostat de laboratoire.

En parallèle, afin de répondre à la 2<sup>ème</sup> question, l'efficacité de l'intégration d'une cellule solaire tandem pérovskite/silicium de dernière génération (surface illuminée de l'ordre de  $10 \text{ cm}^2$ ) à un électrolyseur à membrane échangeuse de protons (PEM) a été étudiée, en fonction de la géométrie de ce dernier, adaptée grâce aux potentialités offertes par l'impression 3D.

Pour évaluer l'efficacité et la stabilité de ces IPEC, le courant produit a été mesuré sur des périodes longues, à potentiel imposé (chrono-ampérométrie), sous illumination constante ou variable, contrôlée par un simulateur solaire. Des balayages de potentiel (entre 0 et 1.6 V) ont été réalisés au préalable sur les cellules d'électrolyse seules, afin de vérifier la répétabilité des réactions d'oxydo-réduction. Le volume d'hydrogène produit a été quantifié et analysé par chromatographie en phase gaz. Tous ces tests ont été effectués à différentes températures.

## Résultats

Dans les photo-anodes réalisées le  $\text{BiVO}_4$  a une structure cristalline principalement monoclinique (clinobisvanite), caractérisée par une largeur de bande interdite de 2.4 – 2.5 eV, compatible avec le faible potentiel de polarisation recherché dans la photoélectrolyse, et une plage d'absorption de la lumière située entre 250 et 500 nm. Les caractérisations électrochimiques et photoélectrochimiques confirment l'intérêt des dopants pour améliorer la mobilité des électrons, et des catalyseurs pour améliorer la cinétique de la réaction. Une très bonne reproductibilité des résultats a également été mise en évidence.

Enfin, les photo-anodes de  $\text{BiVO}_4$  fabriquées par électrodéposition sur les supports en FTO, les plus conducteurs, semblent les plus adaptées à une future mise à l'échelle. En effet, avec ce procédé, la rugosité du dépôt est faible (de l'ordre de 0,05  $\mu\text{m}$ ) et les couches photo-catalytiques, ayant des épaisseurs de l'ordre de 1,7  $\mu\text{m}$ , sont plus homogènes que dans le cas des échantillons fabriqués sur des supports moins conducteur et/ou par spin coating.

Dans la deuxième partie de l'étude, nous avons pu confirmer le rôle clé de l'intégration dans le maintien des performances à travers les échelles.

La cellule IPEC a une surface active (à la fois optique et catalytique) de l'ordre de 8  $\text{cm}^2$ . Le contact électrique direct entre la face arrière de la cellule solaire et la structure conductrice de l'électrolyseur permet le transport des charges électriques sans fil, sans pénalisation au niveau de la résistance électrique. Du point de vue thermique, l'intégration d'un échangeur de chaleur à la structure de l'IPEC permet de pré-chauffer la solution électrolytique (ce qui réduit la tension d'électrolyse), tout en refroidissant les cellules solaires (ce qui permet de maintenir leur efficacité). Enfin, le circuit fluide a été conçu afin minimiser la perte de charge, permettant ainsi de travailler à pression quasi atmosphérique. L'impression 3D permet en outre de réduire les volumes morts et le risque de fuite.

Les résultats obtenus démontrent l'efficacité du système ainsi intégré, avec un rendement de conversion de l'énergie solaire en hydrogène (STH) d'environ 9%, ce qui est remarquable par rapport à l'état de l'art, en particulier compte tenu de la taille et de la durée des essais.

Dans une deuxième étape, cette démarche a été poursuivie par la conception d'un module monolithique original, intégrant 9 IPEC de 21  $\times$  22  $\text{cm}^2$  pour une surface totale illuminée de l'ordre de 70  $\text{cm}^2$ . La réalisation de 5 de ces modules a au final permis de répondre aux besoins en hydrogène du démonstrateur **EASI Fuel** (*European Autonomous Solar Integrated fuel station*) pour la conversion continue de cet  $\text{H}_2$  (produit sous ensoleillement par les IPEC) et de  $\text{CO}_2$ , en méthane ( $\text{CH}_4$ ) au sein d'un bioréacteur de méthanation à base d'archées mésophiles opérant à pression et température modérées. Grâce à ce couplage innovant, le prototype EASI Fuel a été sélectionné et testé avec succès pendant 72h en continu et en totale autonomie, lors de la finale du concours *Horizon Prize - Fuel from the Sun: Artificial Photosynthesis*.

## Conclusion et perspectives

Aujourd'hui les photo-anodes de  $\text{BiVO}_4$  qui présentent des bonnes performances ont des surfaces de dépôt de l'ordre de 2.5  $\text{cm}^2$ . L'étude paramétrique, réalisée ici sur des photo-anodes de taille similaire (environ 3  $\text{cm}^2$ ), met en évidence les effets des hétérogénéités macroscopiques liées au procédé de fabrication et à la nature du support dès cette échelle. Des simulations optiques, basées sur la combinaison des équations de l'optique ondulatoire et du transfert radiatif, et considérant des géométries modèles (sillons sinusoidaux) et/ou les textures réelles des échantillons réalisés, ont permis de mieux comprendre l'impact de ces hétérogénéités sur les propriétés optiques et photo-électrochimiques apparentes des photo-anodes. De tels modèles peuvent notamment permettre de remonter aux propriétés « apparentes » du matériaux photoactifs, tels qu'utilisés pour réaliser des simulations à l'échelle d'une cellule complète et optimiser la géométrie et les conditions opératoires.

Corolairement à cette approche *bottom-up*, la combinaison de composants de l'état de l'art pour la réalisation de modules IPEC extrapolés, et leur mise en œuvre dans le démonstrateur EASI Fuel, ont permis d'appréhender les problématiques de la photo-électrolyse de l'eau, à une échelle significative (350 cm<sup>2</sup> de surface éclairée), plus représentative d'une application commerciale et en conditions réelles d'ensoleillement (TRL 5), et d'atteindre un rendement « sun to fuel » de l'ordre de 7% grâce à l'optimisation fluidique et thermique apportés. L'état de l'art récent rapporte des rendements STH proches de 21%, mais ces valeurs élevées concernent des dispositifs de taille significativement plus faible (surface solaire active ~ 1 cm<sup>2</sup>), généralement sous irradiation artificielle et contrôlée.

La démarche d'investigation menée dans cette thèse, dédiés à la recherche des phénomènes limitants les performances de PEC, de concept différent, a ainsi permis d'identifier de proposer et de tester des pistes d'optimisation pour le changement d'échelle. Les connaissances acquises pourront être utiles à la mise à l'échelle d'autres types de dispositifs PEC.

La dernière étape étudiée (passage à TRL 5) a également permis de démontrer la pertinence et la performance du couplage direct d'un réacteur continu mettant en œuvre du matériel biologique, avec une source alternative d'H<sub>2</sub>, ce qui à notre connaissance constitue une première mondiale.





# Table of Contents

<b>Abbreviations and symbols</b> .....	17
<b>Chapter 1:</b> .....	22
<b>Introduction: Context and Objectives</b> .....	22
<b>1 Global context: from CO<sub>2</sub> emissions to solar energy</b> .....	22
1.1 <i>Carbon Circular Economy in CEA</i> .....	23
<b>2 PEC for water electrolysis: why and how</b> .....	26
2.1 <i>Water electrolysis</i> .....	28
2.2 <i>About semiconductors</i> .....	29
2.3 <i>Photoelectrolyser for water splitting: state of art</i> .....	31
<b>3 Key aspects for technology screening and increasing TRL</b> .....	34
3.1 <i>Limiting phenomena</i> .....	36
3.2 <i>Deployment of PEC: the major role of simulation</i> .....	39
<b>4 Summary and objectives of the thesis</b> .....	40
<b>Chapter 2:</b> .....	44
<b>PEC scale-up: case of a BiVO<sub>4</sub> photoanode</b> .....	44
<b>1 BiVO<sub>4</sub> photoanodes: literature review</b> .....	44
1.1 <i>The transition metal oxides</i> .....	44
1.2 <i>BiVO<sub>4</sub>: chemical and physical properties</i> .....	45
1.3 <i>BiVO<sub>4</sub>: photoelectrochemical performances</i> .....	47
<b>2 Experimental parametric study</b> .....	49
2.1 <i>Methodology</i> .....	49
2.2 <i>Fabrication Methods</i> .....	50
2.2.1 <i>Sol-gel spin coating</i> .....	52
2.2.2 <i>Electrodeposition (and drop casting)</i> .....	56
2.3 <i>Macroscopic and Microscopic Characterization</i> .....	59
2.3.1 <i>Scanning Electron Microscopy</i> .....	59
2.3.2 <i>X-ray diffraction</i> .....	60
2.3.3 <i>Profilometry</i> .....	61
2.4 <i>Optical Characterizations</i> .....	63
2.5 <i>Photoelectrochemical Characterizations</i> .....	66
2.6 <i>Results and discussion</i> .....	67
<b>3 Role of optical processes: numerical sensitivity approach</b> .....	72
3.1 <i>Optical codes</i> .....	73
3.1.1 <i>Transfer Matrix</i> .....	73

3.1.2	CROWM .....	76
3.2	<i>Simulation of the synthesized BiVO<sub>4</sub> photoanodes</i> .....	79
3.2.1	Identification of BiVO <sub>4</sub> properties .....	79
3.2.2	Estimation of the photocurrent .....	81
3.3	<i>Numerical Sensitivity Study</i> .....	83
3.3.1	Definition of the “model” textures .....	84
3.3.2	Results .....	84
<b>4</b>	<b>Conclusions and perspectives</b> .....	<b>87</b>
<b>5</b>	<b>Appendix</b> .....	<b>89</b>
5.1	<i>Chemicals</i> .....	89
5.2	<i>Table of manufactured photoanodes</i> .....	89
5.3	<i>Ag/AgCl reference electrode</i> .....	90
5.4	<i>KPi electrolytic solution</i> .....	91
5.5	<i>Electrochemical active surface area</i> .....	91
5.6	<i>Photoelectrochemical tests using H<sub>2</sub>O<sub>2</sub> as hole scavenger</i> .....	92
5.7	<i>Scanning Electron Microscopy</i> .....	93
5.8	<i>X ray diffraction: theoretical aspects</i> .....	94
5.9	<i>Numerical Sensitivity Study: supplementary information</i> .....	96
<b>Chapter 3:</b>	.....	<b>100</b>
<b>Thermally integrated, scalable, 3D-printed photoelectrochemical cells and modules based on perovskite / silicon tandem solar cells for high-efficiency hydrogen production</b> .....		<b>100</b>
<b>1</b>	<b>Introduction</b> .....	<b>100</b>
<b>2</b>	<b>Materials and methods</b> .....	<b>102</b>
2.1	<i>Component description</i> .....	102
2.1.1	Tandem solar cell fabrication and encapsulation .....	102
2.1.2	PEM electrolyser .....	103
2.1.3	IPEC cell and module.....	104
2.2	<i>Characterization and performance measurement</i> .....	105
2.2.1	Photovoltaic efficiency measurement .....	105
2.2.2	Active area measurement .....	105
2.2.3	(Photo)Electrochemical measurements .....	105
2.2.4	Gas flow measurements .....	106
2.2.5	Outdoor stability tests.....	106
2.3	<i>Data analysis and calculation of solar to hydrogen efficiency</i> .....	106
<b>3</b>	<b>Results and discussions</b> .....	<b>107</b>
3.1	<i>IPEC cell description and motivation for thermal integration</i> .....	107
3.2	<i>Influence of heat exchanger on IPEC cell efficiency</i> .....	108

3.3	<i>IPEC cell stability and efficiency under light (1 sun)-dark cyclic illumination</i> .....	110
3.4	<i>IPEC module efficiency</i> .....	112
3.5	<i>IPEC module stability outdoors and origin of degradation</i> .....	113
<b>4</b>	<b>Comparison with State-of-the-Art</b> .....	<b>116</b>
<b>5</b>	<b>Conclusions and perspectives</b> .....	<b>117</b>
<b>6</b>	<b>Appendix</b> .....	<b>119</b>
6.1	<i>Determination of solar cells active area</i> .....	119
6.2	<i>Determination of the correction factor for the horizontal irradiance</i> .....	120
6.3	<i>Typical maximum power point voltages of perovskite / silicon solar cells under 1 sun</i> .....	120
6.4	<i>Structure of the 3D-printed cathode with the heat exchanger</i> .....	121
6.5	<i>Faradaic efficiency during various IPEC cell performance tests</i> .....	121
6.6	<i>Influence of heat exchanger on IPEC cell performance</i> .....	122
6.7	<i>Estimation of STH efficiency from I(V) curves of perovskite / silicon tandem solar cells</i> .....	122
6.8	<i>IPEC cell stability under light/dark cycles (repeated)</i> .....	123
6.9	<i>Operating current of the nine IPEC cells from the IPEC module</i> .....	123
6.10	<i>Impact of variations in perovskite and p-layer thicknesses on performance</i> .....	124
6.11	<i>Details of reports from literature used to build the graphs from Figure 54</i> .....	125
<b>Chapter 4:</b>	<b>.....</b>	<b>128</b>
<b>A scalable integrated solar device for the autonomous production of green methane.....</b>		<b>128</b>
<b>1</b>	<b>Introduction</b> .....	<b>128</b>
<b>2</b>	<b>Results and discussion</b> .....	<b>130</b>
2.1	<i>A compact and integrated design for intensification and scalability</i> .....	130
2.1.1	<i>Integrated Photoelectrochemical Cells</i> .....	130
2.1.2	<i>Strain selection and bioreactor</i> .....	132
2.1.3	<i>System Integration : from light capture to fuel production</i> .....	133
2.2	<i>Real-life tests to assess the device versatility and resilience</i> .....	135
2.3	<i>Discussion on device performance</i> .....	138
2.3.1	<i>Solar-to-Hydrogen and Solar-to-Fuel yield</i> .....	138
2.3.2	<i>Solar cells degradation: a major bottleneck that limits green CH<sub>4</sub> production</i>	138
2.4	<i>Market potential</i> .....	139
<b>3</b>	<b>Conclusion and perspectives</b> .....	<b>140</b>
<b>4</b>	<b>Experimental procedures</b> .....	<b>141</b>
4.1	<i>Monitoring of gas production and Safety limits</i> .....	141
4.1.1	<i>O<sub>2</sub> monitoring and safety</i> .....	141
4.1.2	<i>Produced gas control and supply</i> .....	142
4.2	<i>Irradiance monitoring</i> .....	143

4.3	<i>Data analysis and performance calculation</i> .....	143
<b>5</b>	<b>Appendix</b> .....	<b>145</b>
<b>Chapter 5:</b>	.....	<b>154</b>
<b>Conclusions and perspectives</b>	.....	<b>154</b>
<b>References</b>	.....	<b>157</b>

## Abbreviations and symbols

A	Absorbance (%) and Active surface (cm <sup>2</sup> )
a	Amplitude (μm)
α	Absorption coefficient (cm <sup>-1</sup> )
AM	Additive manufacturing
AM1.5G	Air mass 1.5 global
AFG	Association France Gaz
APAVE	Association des Propriétaires d'Appareils à Vapeur et Electriques
APCE	Absorbed photon-to-current efficiency
BCR	Bubble column reactor
BI	Back illumination
CA	Chronoamperometry
CB	Conduction band
CCE or ECC	Carbon circular economy
CCS	Carbon capture and storage
C <sub>DL</sub>	Double layer capacitance (F)
CFD	Computational Fluid Dynamics
CIGS	CuInGaSe <sub>2</sub>
CoPi	Cobalt oxide catalyst
C <sub>s</sub>	Specific capacitance (mF.cm <sup>-1</sup> )
CSTR	Continous Stirred-Tank Reactor
DI	Deionized
DLH	Layered double hydroxides
DNI	Direct normal irradiance (W.m <sup>-2</sup> )
D <sub>oE</sub>	Department of Energy
d_RT	Ray tracing step (μm)
DSSC	Dye-sensitized solar cell
E	Electric field (V.m <sup>-1</sup> )
E <sub>0</sub>	Standard potential (V)
EASI	European autonomous solar integrated
EBPVD	Electron-beam physical vapour deposition
ECSA	Electrochemical active surface area (cm <sup>2</sup> )
E <sub>g</sub>	Band gap energy (eV)
EIC	European Innovation Council
El	Electrodeposition (it includes a drop casting step)
EPA	Environmental Protection Agency
EQE	External quantum efficiency (%)
E <sub>sun</sub>	Incident solar energy (Wh.m <sup>-2</sup> )
ESTI	European solar test installation

ETA	Extremely thin absorber
ETL	Electron transport layer
FDM	Fused Deposition Modeling
FE	Faradaic efficiency (%)
FI	Front illumination
$\phi_{sep}$	Electron-hole separation efficiency (%)
FTO	Fluorine-doped tin oxide (SnO <sub>2</sub> :F)
GHG	Greenhouse gases
GHI	Global horizontal irradiance (W.m <sup>-2</sup> )
GNI	Global normal irradiance (W.m <sup>-2</sup> )
H	Thickness measured via SEM (nm)
HER	Hydrogen evolution reaction
HHV	Higher heating value (J.mol <sup>-1</sup> )
h <sub>p</sub>	Thickness measured via profilometry (nm)
HTE	High temperature electrolysis
HTL	Hole transport layer
hν	Photon energy (eV)
I <sub>0</sub>	Incident AM 1.5 photon flux (cm <sup>-2</sup> .s <sup>-1</sup> )
I <sub>c</sub>	Capacitive current (mA)
I <sub>op</sub>	Operating current (mA)
IEA	International energy agency
IPCC	Intergovernmental Panel on Climate Change
IPCE	Incident-Photon-to-electron Conversion Efficiency (%)
IPEC	Integrated photoelectrochemical
IQE	Internal quantum efficiency (%)
IR	Infrared
IRIG	Interdisciplinary Research Institute of Grenoble
ISEC	Science and Technology Institute for Circular Economy of Low Carbon Energies
ISAS	Institute of Applied sciences and Simulation for low-carbon energy
ITO	Indium Tin Oxide (In <sub>2</sub> O <sub>3</sub> :Sn)
J <sub>ph</sub>	Photocurrent density (mA.cm <sup>-2</sup> )
J <sub>ph, flat</sub>	Photocurrent density for flat textures (mA.cm <sup>-2</sup> )
JRC	Joint Research Center
J <sub>sc</sub>	Short-circuit current density (mA.cm <sup>-2</sup> )
k	Extinction coefficient (-)
KPi	Potassium phosphate buffer
λ	Wavelength (nm)
LB	Langmuir-Blodgett
LbL	Layer-by-layer
LCA	Life Cycle Assessment

$L_d$	Diffusion length (nm)
$L_d^h$	Hole diffusion length (nm)
LEL	Lower explosive limit (% by volume)
LITEN	Laboratory for Innovation in New Energy Technologies and Nanomaterials
L-PBF	Laser Powder Bed Fusion
LSV	Linear sweep voltammetry
LTE	Low-temperature electrolysis
LVDT	Linear Variable Differential Transformer
MEA	Membrane electrode assembly
MOD	Metal-organic decomposition
m – s	Monoclinic scheelite
n	Refractive index (-)
$\tilde{n}$	Complex refractive index (-)
$\eta_e$	Electrical efficiency (%)
$n_o$	Initial refractive index value (-)
NDIR	Non-dispersive infrared
NHE	Normal hydrogen electrode
NPLC	Number of power line cycles
$\nu$	Scan rate ( $V.s^{-1}$ ) and frequency (Hz)
OER	Oxygen evolution reaction
PC	Photocatalytic
PEC	Photoelectrochemical
PECVD	Plasma enhanced chemical vapour deposition
PEG-PPG-PEG	Pluronic <sup>®</sup> F-108
P2G	Power-to-gas
PEM	Proton exchange membrane
PGMs	Platinum-group metals
PID	Process and instrumentation diagram
PPR	Photocatalyst panel reactors
PTAA	Poly (triaryl amine)
PTLs	Porous transport layer
PVD	Physical vapor deposition
PVE	Photovoltaic-Electrolyser
PV	Photovoltaic module (including tandem solar cell)
PV + EC	Photovoltaic + electrochemical
R	Reflectance (%)
Ra	Roughness ( $\mu m$ )
Rp	Maximum profile peak height ( $\mu m$ )
$I_{product}$	Product rate ( $mol.m^{-2}.h^{-1}$ )
Rv	Maximum profile valley depth ( $\mu m$ )

SATP	Standard Ambient Temperature (°C) and Pressure (bar)
Sc	Spin coating
SCE	Saturated calomel electrode
SEM	Scanning electron microscopy
SG	Sol-gel
Si/PK	Silicon / perovskite
SLM	Selective Laser Melting
SMR	Steam methane reforming
SOPs	Standard operating procedures
STH	Solar-to-hydrogen <sup>1</sup> (%)
STH*	Solar-to-hydrogen <sup>2</sup> (%)
STF	Solar-to-fuel (%)
QE	Quantum efficiency (%)
T	Transmittance (%) and Period (s)
TCO	Transparent conductive oxide
TM	Transfer matrix
TMO	Transition metal oxides
TRL	Technology Readiness Level (-)
t – s	Tetragonal scheelite
t – z	Tetragonal zircon
UV/Vis/NIR	Ultraviolet / visible / near-infrared
VB	Valence band
V <sub>op</sub>	Operating voltage (V)
WPVS	World Photovoltaic Scale
XRD	X-ray diffraction



# Chapter 1:

## Introduction: Context and Objectives



# Chapter 1:

## Introduction: Context and Objectives

### 1 Global context: from CO<sub>2</sub> emissions to solar energy

Climate change is now a key issue that captures the attention of the world, a consequence of the long-term shifts in temperatures and weather patterns, caused by the industrial revolution. More in detail, the human activities, above all the burning of fossil fuels such as oil gas and coal have increased the carbon dioxide concentration by more than 40% from 1970 to 2020.<sup>3</sup>

The rising of CO<sub>2</sub> and other greenhouse gases (GHG) influenced the global average surface temperature that increased by ~ 1°C since 1900. Many other climatic effects such as the ice melting, ocean warming, rising of the sea level are associated with the problem of the global warming. Actually, the magnitude and frequency of these changes are influenced by numerous factors, and warming slowdowns and accelerations lasting a decade or more will continue to persist. The evolution of global GHG emissions over the period 1970-2022 (for the principal activity sectors) is shown in Figure 1<sup>4</sup>.

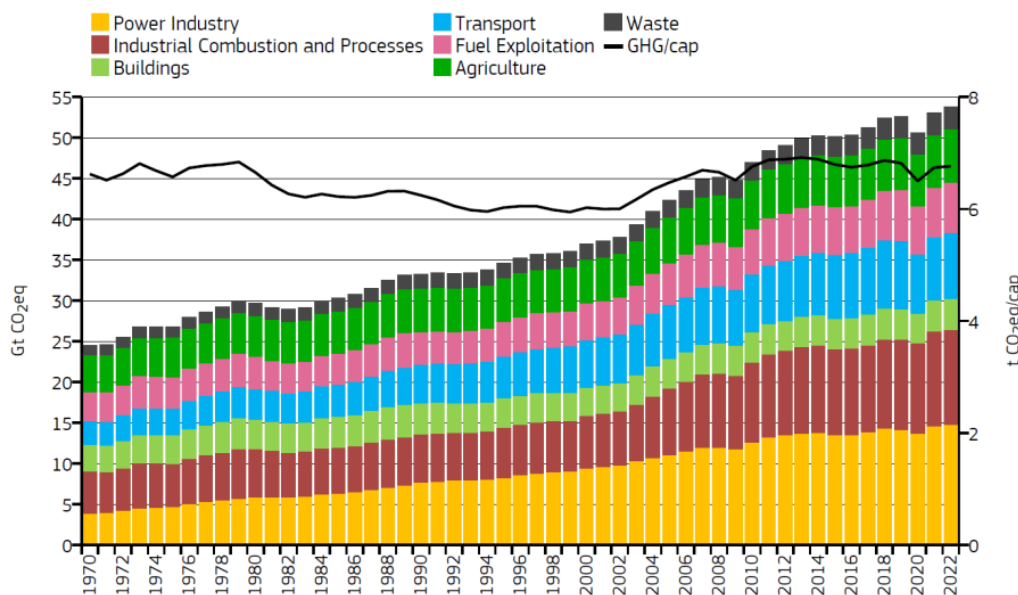


Figure 1. Global GHG emissions by sector (left axis, bars) and per capita (right axis, black line), from 1970 to 2022. Source: JRC, 2023. The Land-Use Change and Forestry (LULUCF) sector is not taken into account in the calculation of global GHG emissions.

In 2022, the majority of total emissions was fossil CO<sub>2</sub> (71.6%), CH<sub>4</sub> contributes by 21%, China, the United States, India, Russia, Brazil and the EU27 being the six world largest GHG emitters.<sup>4</sup>

To face the climate change, in December 2015 the Paris National Agreement was adopted by 196 nations. The agreement includes the commitment of all parties to reduce CO<sub>2</sub> and greenhouse gas emissions, working together on alternative solutions and trying to adapt to

current climate impacts in order to significantly slow down the negative consequences of this industrial revolution.

To fulfill the Paris Agreement and to support climate mitigation, a method based on circular economy (CE) has been introduced. The transition to a circular economy focuses on maximizing the use of resources and minimizing waste, recycling the materials. This closed-loop system (reduce, reuse and recycle) can be further extended by including *remove*<sup>5</sup> and focusing on the reduction of carbon emissions and energy saving (Carbon circular economy – CCE). This concept is essential to achieve net-zero greenhouse gas emissions by 2050 and offer a pathway towards a more green and sustainable world. Several projects concerning renewable energy devices, electric vehicles, energy storage systems, carbon and air capture demonstrators, biogas digesters, nuclear power plant, smart grid technologies and energy-efficient appliances have been launched. Further gain is expected from the effective combination of this different sustainable ways to reduce carbon emissions.

These objectives are highly supported by European Union.

An example is the SUNER-C project an initiative shared by 30 different EU partners, to introduce and drive actions on the new generations of energy carriers, in order to replace fossil fuels. More in detail, SUNER-C, co-chaired by the French CEA, is a Coordination and Support Action (CSA) based on the foundations of the SUNERGY “Community and eco-system for accelerating the development of solar fuels and chemicals”, aims to analyze the current energy needs from all perspectives and to promote the acceleration of the transition of solar fuels and chemical technologies, from the laboratory to large-scale. The objective of the SUNER-C CSA is indeed to develop a strategic and innovative roadmap, to be implemented in the actual society in order to encourage the creation of new ecosystems based on solar and clean fuels and chemicals, thanks to large-scale research. The initiative propose also activity for dissemination and education of the next student generation to the actual ecological transition or a climate-neutral Europe in 2050.

In 2016, the European Innovation Council (EIC) started to promote various Horizon Prizes for studying and development of the most innovative solutions for solving the major societal challenges such as ‘Low-Cost Space Launch’, ‘Innovative Batteries for eVehicle’, ‘Fuel from the Sun: Artificial Photosynthesis’ or ‘Early Warning for Epidemics’, etc. Among the EIC Horizon Prizes, “Fuel from the Sun: Artificial Photosynthesis” aims to build a fully functional, scaled-up prototype, using artificial photosynthesis that can produce useable synthetic fuel. Several laboratories of the CEA, mainly LITEN (Laboratory for Innovation in New Energy Technologies and Nanomaterials), IRIG (Interdisciplinary Research Institute of Grenoble) , ISAS (Institute of Applied sciences and Simulation for low-carbon energy) and ISEC (Science and Technology Institute for Circular Economy of Low Carbon Energies ) decided to apply jointly in the name of CEA, through the development of a demonstrator coupling an photo-electrolyser, for the production of solar hydrogen, to a bioreactor, for the conversion of CO<sub>2</sub> into CH<sub>4</sub>, a valuable fuel. I had the opportunity to take an active part of this collaborative research project, as will be detailed in chapters 3 and 4 of the manuscript.

## **1.1 Carbon Circular Economy in CEA**

The CEA is strongly committed to achieving the goal of carbon neutrality by 2050. This was in particular materialized by the creation a dedicated CCE program within the Energy Division. The funding of the CCE program was increased in 2022, after the Intergovernmental Panel on Climate Change's (IPCC) Sixth Assessment Report<sup>6</sup> and the Fit for 55 Package<sup>7</sup>.

The concept of a "circular carbon economy" refers to technological advancements facilitating the production of carbon-based molecules and synthesized materials useful for the energy,

chemical, and transportation industries, with positive sustainable outcomes. The CEA's research within this domain contributes to realizing the objective of reducing CO<sub>2</sub> emissions (Figure 2) in France to 80 Mt CO<sub>2,eq</sub> by 2050, compared with 445 Mt CO<sub>2,eq</sub> emitted in 2018.

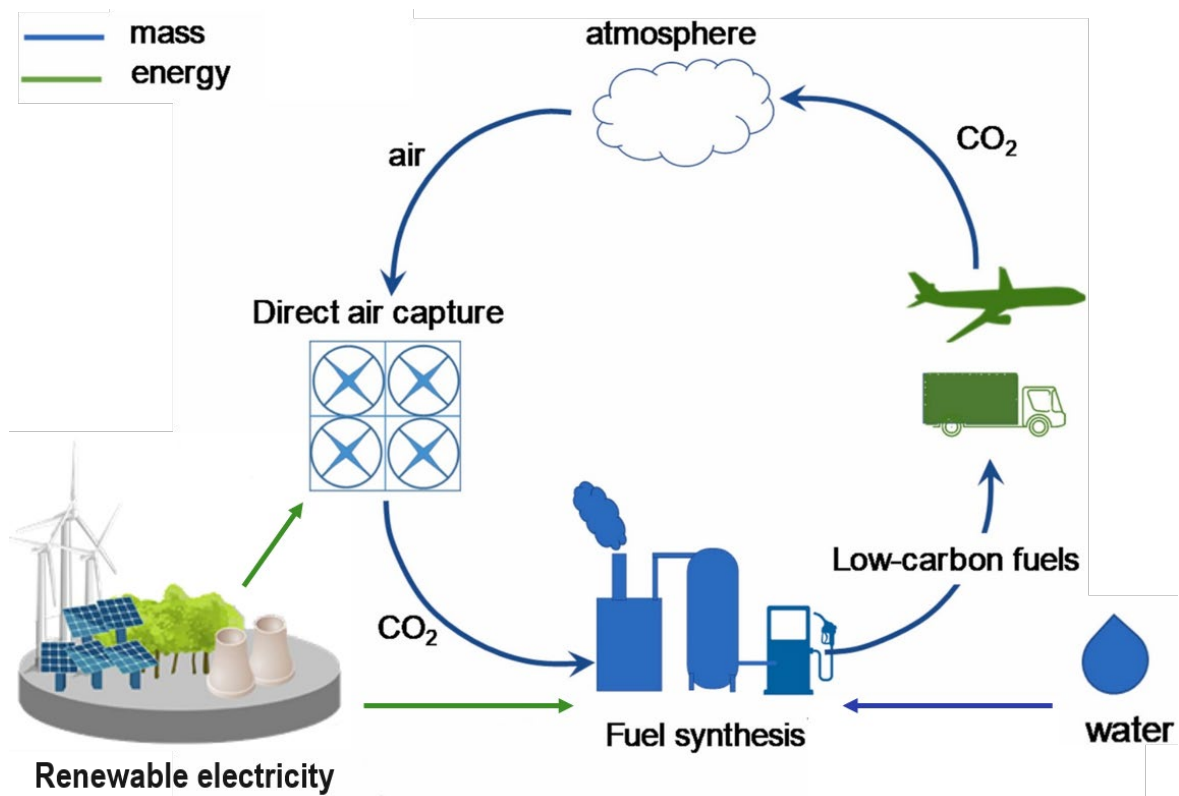


Figure 2. Closing of the carbon cycle capturing CO<sub>2</sub> from the atmosphere and using it to synthesize fuel, resulting in zero net CO<sub>2</sub> emissions.

In this context CEA is exploring three main areas of research :

- The valorization and recycling of atmospheric and industrial carbon dioxide to generate liquid or gaseous synthetic fuels, along with carbon precursors for chemistry or plastic materials. For instance, captured CO<sub>2</sub>, sourced from industrial processes or directly from the atmosphere, undergoes reactions with low-carbon hydrogen. This hydrogen, produced via water electrolysis using nuclear and/or renewable electricity sources, serves as an essential precursor for converting carbon into targeted molecules of interest. Simultaneously, the CEA is advancing various processes such as torrefaction, gasification, and hydrothermal processes to valorize biomass and waste, whether in dry or wet forms.
- the exploitation of solar energy for the production of hydrogen or carbon-based molecules, by artificial photosynthesis. Ongoing efforts aim to continuously enhance the efficiency of converting solar energy into chemical energy, primarily achieved through the development of new materials and innovative catalysts. The objective here is to minimize reliance on rare or critical elements, progressively transitioning to more abundant and less costly metals, ensuring the scalability of these technologies on an industrial level.
- the development of third-generation biofuels utilizing biological microorganisms such as microalgae, archaea, and bacteria capable of producing energy-rich molecules. The

production of biofuels aims to achieve up to 70% reduction in CO<sub>2</sub> emissions compared to the production of fossil fuels.

In 2020, a specific CEA FOCUS program on Carbon Circular Economy was set up to fund projects by young researchers and to promote the exploration of diverse technologies dedicated to converting carbon dioxide and its by-products into synthetic products through the utilization of low-carbon energy sources.

The FOCUS program encompasses several challenges; a primary objective is the promotion of a resilient energy system to foster the production of sustainable, carbon-based fuel. This point necessitates the development of innovative devices, integrating nuclear and renewable energy sources, capable of rapidly progressing through the Technology Readiness Level (TRL) spectrum, to meet industrial needs aligned with contemporary climate change imperatives. Central to this program is the integration of CEA's diverse interdisciplinary capabilities, strengthening an innovative framework that consolidates progress within the scientific community. This collaborative project aims to promote technological and sustainable progress. Furthermore, the program is dedicated to accelerating fundamental scientific knowledge aimed at enhancing the energy efficiency of processes, as well as at facilitating the conversion of electrical and solar energy into chemical energy, producing charge carriers (H<sub>2</sub>, NH<sub>3</sub>, etc.), carbon-based molecules useful in the energy, chemistry and transport sectors, with favorable environmental and societal impacts.

The ECC FOCUS program comprises four main pillars:

- Designing and constructing solar fuel production systems
- Exploring innovative biological and biohybrid methodologies
- Researching and developing high-performance photo and electro-catalytic materials
- Addressing integration and value chain challenges in the thermochemical conversion of renewable carbon resources

My thesis aligns with the first pillar of the program, focus of designing solar fuel production systems. Nowadays the use of green energy in our electricity mix raised significantly.

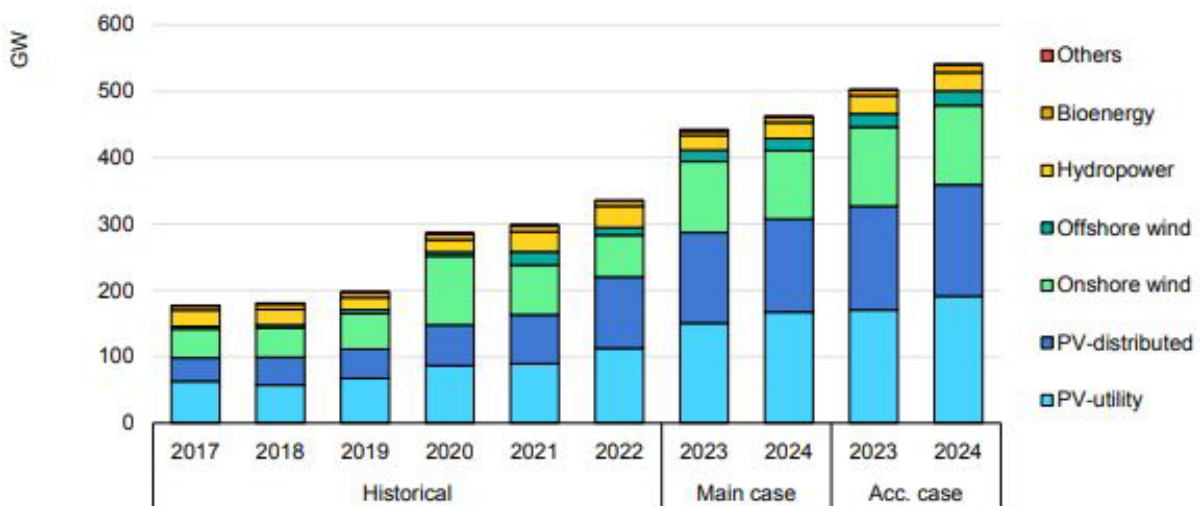


Figure 3. Net renewable electricity capacity additions by technology, historical, main and accelerated cases. From IEA. Licence: CC BY 4.0.

The coupling of clean and renewable energy sources (solar energy, wind energy, hydro energy, tidal energy, geothermal energy and biomass energy) with fuel generators such as electrolysers and photoelectrolysers, bioreactors and photobioreactors, fuel cells etc., is a major challenge

for the carbon circular economy. Many systems that differ in terms of concept, architecture and degree of integration are continuously optimized. From Figure 3 it is possible to observe that the total renewable energy capacity increases by almost 13% to nearly 340 GW in 2022.<sup>8</sup> In 2023, photovoltaic (PV) is the main source of global renewable capacity expansion, accounting for 65% of the growth; solar energy is not just growing in large-scale utility projects but also in smaller, decentralized installations such as individual home. The storage of solar energy as primary energy source is essential, for example in the form of chemical bonds<sup>9</sup> as provided by natural photosynthesis, to facilitate energy distribution and enable end-users to have access to it according to their needs.

Therefore, one of the challenge of the valorization of solar energy and CO<sub>2</sub> is to construct an ‘artificial leaf’<sup>10</sup> that captures and converts solar energy, and then stores it in the form of a fuel such as H<sub>2</sub>, at the same time producing O<sub>2</sub> through the water splitting reaction. Even with the current advancements in artificial photosynthesis, reliable and efficient components such as electrocatalysts and semiconductors with appropriate electronic properties to capture solar photons by charge separation, and store them in chemical bonds on a large scale, are still lacking.

## 2 PEC for water electrolysis: why and how

Hydrogen is of major importance in the energy-climat transition. It can be exploited as a charge carrier that can directly or indirectly react with oxygen to release energy.<sup>11</sup> It can also be used in fuel cells, semiconductor manufacturing, aerospace applications, glass purification etc.

Nowadays, the most part of the world’s hydrogen is produced by *steam methane reforming*<sup>12,13</sup> (SMR). In this process high-temperature steam (1300°F to 1800°F) under 3 bar – 25 bar pressure reacts with methane in the presence of a catalyst to produce a gas mixture of hydrogen, carbon monoxide, and a small amount of carbon dioxide (CO<sub>2</sub>), known as syngas. Nevertheless, depending on the quality of the feedstock (natural gas, rich gases, naphtha, etc.), one ton of hydrogen produced will also produce 9 to 12 tons of CO<sub>2</sub>.<sup>14</sup>

Other fossil fuel methods are *partial oxidation* where a fuel-air or fuel-oxygen mixture is partially burnt, resulting in a syngas rich in hydrogen and carbon monoxide; *plasma reforming* where hydrogen and carbon black are produced from various feedstocks, such as methane, natural gas and liquid hydrocarbons; *coal gasification* that converts coal into syngas, here, coal reacts with oxygen, steam, or a mixture of the two at high temperatures (> 700°C) and controlled pressure.

To obtain further quantities of H<sub>2</sub> from all the thermochemical processes<sup>15</sup> listed, the produced carbon monoxide is reacted with steam in a water-gas shift reaction.

Hydrogen produced by these technologies is referred as “grey hydrogen” when CO<sub>2</sub> emissions are released to the atmosphere, and as “blue hydrogen” when emissions are captured through a carbon capture and storage (CCS) process.

All the various processes for hydrogen production can be characterized by assigning a colour label to the hydrogen (Figure 4).



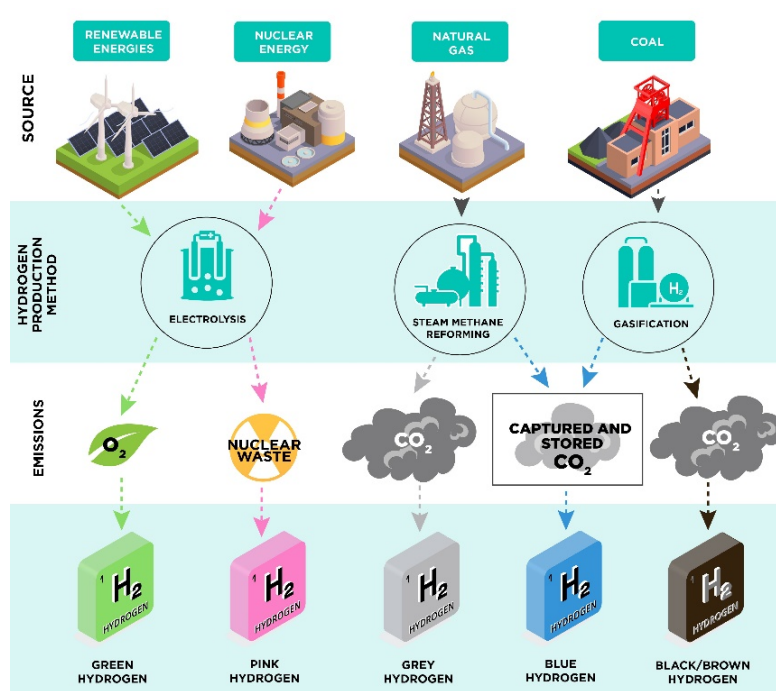


Figure 4. Main H<sub>2</sub> colors. Source: CIC energiGUNE.

The alternative path that is being actively encouraged is the production of hydrogen by the electrolysis of water (water splitting, Sec. 2.1), especially if renewable electricity can be used. As stated in 2021<sup>16</sup>, ~ 47% of the global hydrogen production comes from natural gas, 27% from coal, 22% from oil (as a by-product) and only around 4% derives from electrolysis.

Nowadays, the efficiency of industrial water electrolysis ranges from 70% to 80%, with conversion losses between 20% and 30%. This process operates at lower temperatures, up to 80°C, in contrast to steam methane reforming (SMR). SMR exhibits a thermal efficiency ranging from 70% to 85%.<sup>17</sup>

In 2030, an increase in the electrical efficiency of water electrolysis up to 86%<sup>18</sup> is expected, this process will become the key entity for an effective hydrogen supply.

The scientific community focuses on reducing hydrogen production costs through water-splitting techniques that utilize electricity as primary energy source. A growing interest is shown in carbon-free energy sources (such as solar, wind, hydroelectric and nuclear power) to drive electrolysis processes.

In addition, coupling water splitting reactions, via the hydrogen production, with methanation plants (or others alternative applications for hydrocarbons and ammonia) promotes the production of solar/biofuels recycling carbon dioxide.<sup>19</sup>

The electrolysis of water can be divided in two categories: low-temperature electrolysis (LTE) and high temperature electrolysis (HTE). Actually, the most studied way to produce green H<sub>2</sub> is the LTE (T < 100°C), based on solid polymer or liquid electrolyte.

Precisely, the most common sustainable and direct technologies studied in this field are the photoelectrochemical (PEC) cells.

PEC cells are electrochemical devices that exploit solar energy to drive the production of chemical fuels, as well as to produce electricity. A variety of PEC cells are considered nowadays, which, according to their basic principle, are presented at different TRL in the state of the art. PEC cells are differentiated by their physical, geometrical and mechanical features but they always use light to drive chemical reactions at the interface between a photoactive component and an electrolyte.

Photoelectrochemical cells are impacting and advantageous devices in the world of energy challenges. They differ from photovoltaic cells in a few aspects. In current research and optimization, PEC cells can be assembled in three different ways, based on either:

- a “dark” counter electrode linked with a semiconducting photoelectrode that has a semiconductor/electrolyte junction,
- two semiconducting photoelectrodes having both a semiconductor/electrolyte junction,
- two semiconducting photoelectrodes in a monolithic integrated structure where the cathodic and the anodic half-chemical reactions are carried out simultaneously.<sup>20</sup>

In all cases, one or more semiconductor electrodes absorb the light by generating, through charges separation and transport, a difference in potential,  $\Delta V$ , and subsequently an electric current.

## 2.1 Water electrolysis

The water splitting process produces hydrogen with a very low environment impact. It is the result of two half-reactions showed in Figure 5, involving ions (protons in an acidic medium, hydroxyl ions in a basic medium) and electrons.

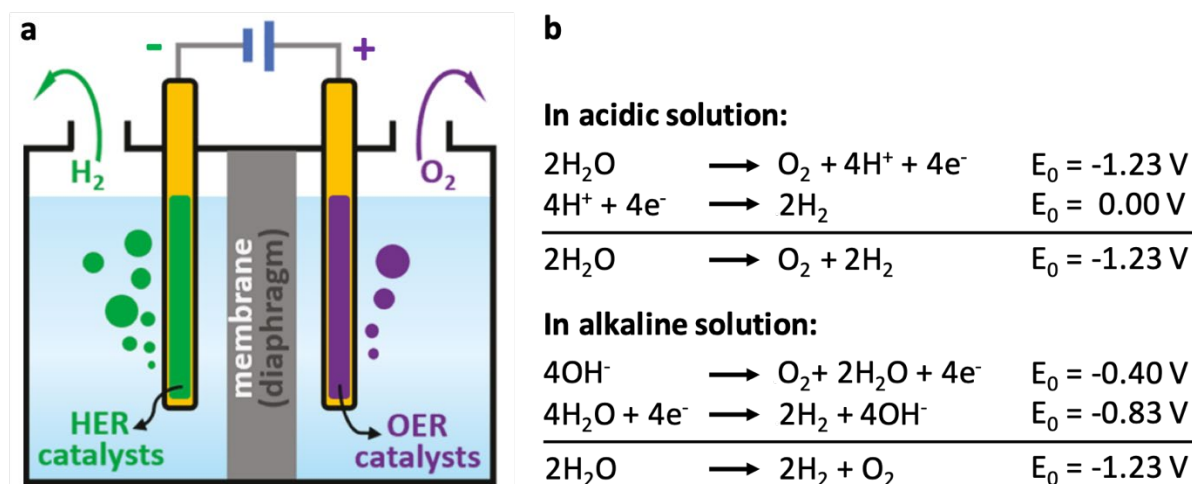


Figure 5. Electrochemical water decomposition. a) Scheme of conventional water electrolyser. b) Electrochemical reactions of water decomposition under acidic and alkaline conditions.

The 2 half-compartments are physically separated, while the 2 electrodes are electrically connected. This can be achieved *e.g.* by an impermeable membrane or a diaphragm, allowing only the passage of the charged species. The electrolyte solutions are normally the same, usually an aqueous solution between 20 and 40 %wt of sodium hydroxide (NaOH) or potassium hydroxide (KOH), sulfuric acid ( $\text{H}_2\text{SO}_4$ ), phosphoric acid ( $\text{H}_3\text{PO}_4$ ), etc., depending on whether the electrolysis is considered in alkaline or acidic conditions.

The kinetics of these reactions are generally slow and expressed by overvoltages, which represent the difference between the thermodynamic potential of the half-reaction considered and the potential at which the redox reaction is observed experimentally.<sup>21</sup> Catalysts play a major role in improving  $\text{H}_2$  and  $\text{O}_2$  production, reducing charge recombination. Their choice depends mainly on the operating conditions of the cell mainly the pH of the electrolyte and the cell temperature.

Under these usual conditions, non-noble catalysts such as nickel, cobalt, molybdenum, manganese, iron, and copper are generally stable. They play an important role in reducing costs and increasing the efficiency of the system. In alkaline conditions, the catalytic activity results



in a reaction rate 2-3 orders of magnitude lower than that observed in acidic solution, due to the slower water dissociation step.<sup>22</sup>

An active part of research is dedicated to the development of catalysts to lower the kinetic barriers and to reduce the voltage necessary for (photo)electrolysis.

An ideal catalyst must have active sites capable of tackling multiple elementary reaction steps. The oxygen evolution reaction (OER) is more complex than the hydrogen evolution reaction (HER) due to the four-electron transfer steps; in alkaline media, it is further complicated by the adsorption and transformation of numerous oxygen-containing intermediates.<sup>23</sup>

At the same current, the OER overpotential is higher than the HER overpotential.

In alkaline electrolysis, oxygen gas is formed at the (photo)anode by the oxidation of hydroxide ions (OH<sup>-</sup>) to oxygen molecules and water, then hydrogen gas is produced by the reduction of water molecules in the cathodic compartment. HER catalysts in alkaline media are based on Ni, Mo and Fe; an attractive option is MoS<sub>2</sub>/Mo<sub>2</sub>C fabricated by Luo et al.<sup>24</sup>, MoS<sub>2</sub> microspheres decorated by Mo<sub>2</sub>C nanoparticles.

At the same time, it is possible to improve OER activity coupling Ni and Fe catalysts, e. g., with the synthesis of NiFe layered double hydroxide (LDH).<sup>25</sup> In this case, the high catalytic activity depends from the Ni-Fe electronic interaction and the presence of fine crystalline grains.

Correlatively, under acidic conditions, water is oxidized to oxygen molecules at the (photo)anode, while H<sub>2</sub> gas results from the reduction at the (photo)cathode of the H<sup>+</sup> ions released into solution. The HER is generally fast, using expensive Platinum-group metals (PGMs) catalysts. However, new high-performance HER catalysts such as MoS<sub>2</sub><sup>23</sup> (which offers favorable edge planes for hydrogen adsorption) or cobalt phosphide catalysts<sup>26</sup> have emerged. Conversely, OER catalysts options remain limited to noble metals and their oxides, notably platinoids, further increasing cell cost.

The reaction pathway and the study of the structure and composition of the catalytic active sites are essential for further improve the catalyst's intrinsic activity.

The standard dissociation potential of water is equal to  $E_0 = -1.23\text{V}$  vs normal hydrogen electrode (NHE). The negative sign indicates that the reaction is not spontaneous, but requires energy input. The voltage required to achieve water dissociation is higher (in absolute value) due to the above-mentioned HER and OER overpotentials and electrical losses in the cell (in the electrolyte, depending on the pH, across the separator, etc.). In the case of a PEC cell, this energy is provided by the absorption and photovoltaic conversion of solar radiation thanks to semiconductor materials.

The energy requirements of a photoelectrochemical device for water electrolysis is written according to Eq. 1 (derived from a Schottky-type photochemical diode).

$$E_g - V_B - (E_C - E_F) = \left(\frac{\Delta G}{nF}\right) + \eta_a + \eta_c + iR \quad \text{Eq. 1}$$

where  $E_g$  is the band gap of the semiconductor,  $V_B$  is the band bending at the semiconductor-electrolyte junction,  $E_C$  is the conduction band energy,  $E_F$  is the Fermi level,  $\frac{\Delta G}{nF}$  is the free energy per electron for the overall cell reaction (1.23 eV for H<sub>2</sub>O decomposition),  $\eta_a$  and  $\eta_c$  are the respective overpotentials at the anode and cathode,  $iR$  is the Ohmic loss in the cell.<sup>27</sup>

## 2.2 About semiconductors

The reaction in a PEC cell requires an irradiation with an energy equivalent or higher than the bandgap of the semiconductor. It is hence of prime importance for the semiconductor to have a

**small band gap** to absorb light in a wide spectrum range, enabling high solar-to-hydrogen (STH) values to be achieved.<sup>28</sup>

The band gap or energy gap is the energy difference between the valence band and the conduction band in the electronic band structure of insulators, conductors or semiconductors. It represents the minimum energy value to move an electron from the valence band to the conduction band (located just above the valence band). The electrons in the valence band have relatively low energy and they are strongly associated with the individual atoms or ions. Instead, in the conduction band the electrons have sufficient energy to move freely through the material and contribute to electrical conduction. It is fundamental for the photocatalytic reaction to ensure an energy gap (Figure 6) in the semiconductor that is higher or at least equal to the difference between the redox and the oxidation potentials in the PEC cell.

For example, to carry out the water splitting reaction, the bottom of the conduction band must exhibit a more negative value than the reduction potential of  $H^+$  to  $H_2$  (0 V vs. NHE at pH 0), while the top of the valence band must have a more positive value than the oxidation potential of  $H_2O$  to  $O_2$  (1.23 V vs. NHE).<sup>29</sup>

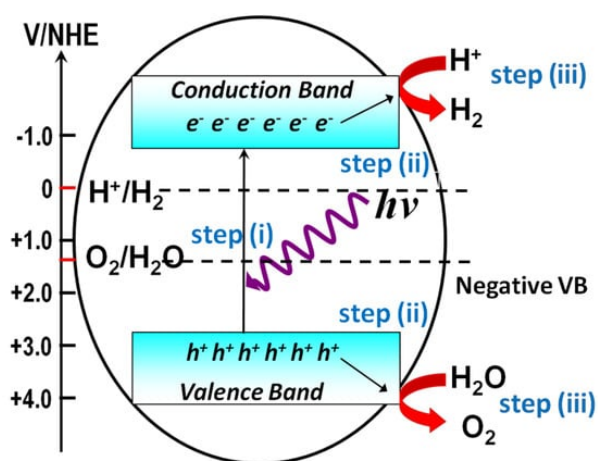


Figure 6. Band Gap of semiconductor materials  $\leq 2.1$  eV for Solar Water Splitting.

In this case, a minimum photon energy of 1.23 eV (at 298 K) is thermodynamically required to drive the reaction, which means that the minimum band gap of the semiconductor must be 1.23 V, plus the required overpotentials and energy losses. The optical band gap of a semi-conductor can be determined by the Tauc method<sup>30</sup>, preferred for amorphous (or glassy) materials, or by means of the Boltzmann function<sup>31</sup>, an efficient approach for semiconductor materials.

The 2<sup>nd</sup> fundamental characteristic for a high-performance photoelectrode is to **ensure a good charge carrier mobility and a long charge carrier diffusion<sup>28</sup> length**. Maximizing charge carrier diffusion length ( $L_d$ ), as well as improving the charge mobility, minimizes the rate of charge recombination rate, thus increasing the efficiency (or STH) of the system. The mobility of charge carriers can be influenced by various factors including the material's structure, temperature, and the presence of impurities or defects.

1. In conductors, semiconductors, and insulators materials, the arrangement of atoms affects how easily charge carriers can move. In crystalline semiconductors charge carriers move through periodic lattices. Amorphous semiconductors, where disorder induces the absence of periodicity,<sup>32</sup> are usually characterized by a low mobility of the charge carriers. Materials with wide bandgaps generally have lower carrier mobility than those with narrower bandgaps.

2. Temperature plays a significant role in charge carrier mobility. At higher temperatures, carriers have more thermal energy, allowing them to overcome energy barriers and move more freely through the material. Additionally, the scattering mechanisms that limit the mobility of monolayer semiconductors are temperature dependent. In general ionized impurity scattering dominates at low temperatures, while phonon scattering dominates at higher temperatures.<sup>33</sup>

Polymorphism, defects, impurities, high flexibility of the molecules and electrostatic effects (local dipoles) reduce the mobility by slowing down the charge carriers which then tend to occupy spatially the trapping sites. Furthermore, in polycrystalline films, the grain boundaries limit the current transmission between crystallites by limiting the number of conduction channels or by trapping charges at the interface between the crystalline grains.<sup>34</sup> Finally, a strong catalytic activity of the semiconductor (that reduces the overpotential and improves the kinetics of the reactions), as well as electrochemical and photoelectrochemical stability, is necessary to have a performing PEC cell.

### 2.3 Photoelectrolyser for water splitting: state of art

Three main types of PEC cells can be identified<sup>35</sup>: the regenerative cell<sup>36</sup>, which converts light into electric power (like dye-sensitized solar cell (DSSC)<sup>37,38</sup> with solar energy conversion efficiencies up to 30%), the photocatalytic cell<sup>39,40</sup> (one of the simplest methods to generate solar hydrogen) and the photoelectrosynthetic cells<sup>20</sup>.

Photoelectrosynthetic cells are a type of advanced PEC cells that combines principles of photosynthesis and electrochemistry to convert solar energy into chemical energy. The holes at the surface of the semiconductor electrode react to oxidize the molecules, while the electrons collected at the counter electrode react to reduce the molecules. Photoelectrosynthetic cells have various possible applications beyond water oxidation, such as electrocatalytic or photoredox reactions for the degradation of pollutants, biomass valorization, organic chemical synthesis, and carbon-neutral fuel production.<sup>41</sup> In the case of the water splitting triggered by sunlight, the RedOx processes are similar than in “dark” electrolyzers: water is oxidized to oxygen (O<sub>2</sub>) at the anode/photoanode and reduced to hydrogen (H<sub>2</sub>) at the cathode/photocathode.

The photoelectrosynthetic cells have been developed in 1972 by Fujishima and Honda<sup>42</sup>, followed by works of Turner<sup>43</sup> and Nocera<sup>44</sup>. This kind of devices are currently a typical implementation for artificial photosynthesis<sup>9</sup>.

They are solar-driven water splitting devices that can be differentiated according to their projected manufacturing and technological maturity<sup>45</sup>, first of all identifying two limiting cases, namely integrated PEC cells and non-integrated PEC cells.

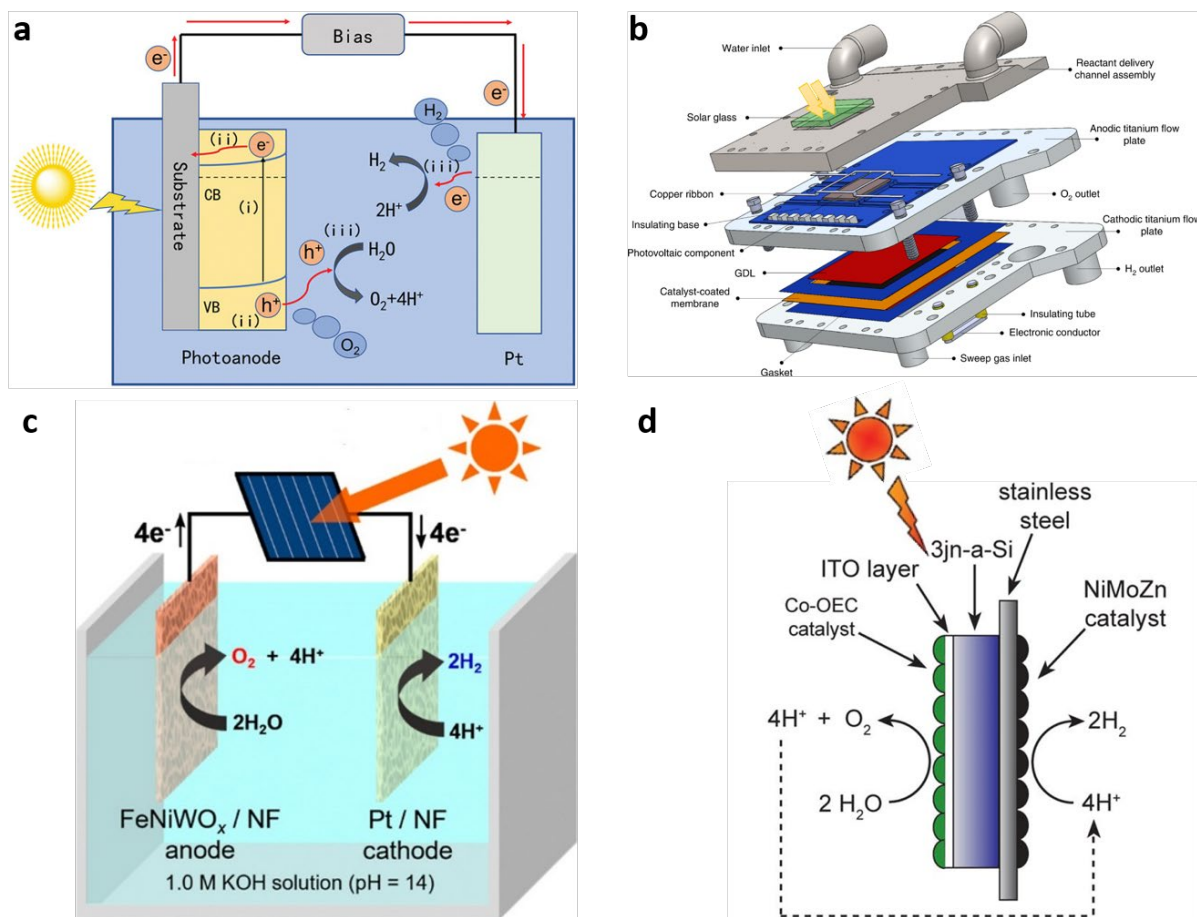


Figure 7. Photoelectrosynthetic cells. a) non integrated PEC cell based on n-type semi-conductor photoanode.<sup>46</sup> b) thermally integrated design of the IPEC device<sup>47</sup> c) non integrated PEC cell based on a Photovoltaic device connected with an electrolyser.<sup>48</sup> d) Integrated PEC cell: Si junction sandwiched by Co-OEC and NiMoZn, OER and HER catalysts, respectively.<sup>44</sup>

In integrated PEC cells (Figure 7b, Figure 7d) light absorption and water splitting are combined in a single module that can be an *Artificial leaf*<sup>49,50,51</sup>, (technology sandwiching a triple-junction amorphous silicon solar cell between H<sub>2</sub> and O<sub>2</sub> evolving catalysts, typically made from NiMoZn and a cobalt–phosphate cluster) or a combination of an integrated photovoltaic (PV) component and an integrated electrochemical component (IPEC<sup>52,53</sup> cell geometry discussed in the thesis, chapter 3 and 4).

In integrated PEC cell the anode and cathode are in physical contact and/or partially connected through external wiring, there is “zero gap”<sup>54</sup> between the (photo)electrode and separator. Current density and cell efficiencies are improved by removing the resistance of the electrolytic solution, hence not contributing to the ohmic losses anymore. An example of IPEC design shows porous gas-liquid transport layers (PTLs) and catalytic layers important for the mediation of the gas bubble formation and detachment. The electrolyte flow it is necessary to wet the electrodes/photoelectrodes and the separator (membrane, if present). These materials have a high level of hydrophilicity and in general, gases (in humid environments) tend to accumulate on hydrophobic surfaces.

In order to reduce degradation during PEC reactions, it is possible to reduce the water content in the device, particularly on the cathode side<sup>53</sup>, by ensuring sufficient humidity on both sides of the membrane.

In non integrated PEC cells (Figure 7a, Figure 7c) water splitting and light absorption are achieved by electrodes and photovoltaic cells, respectively.

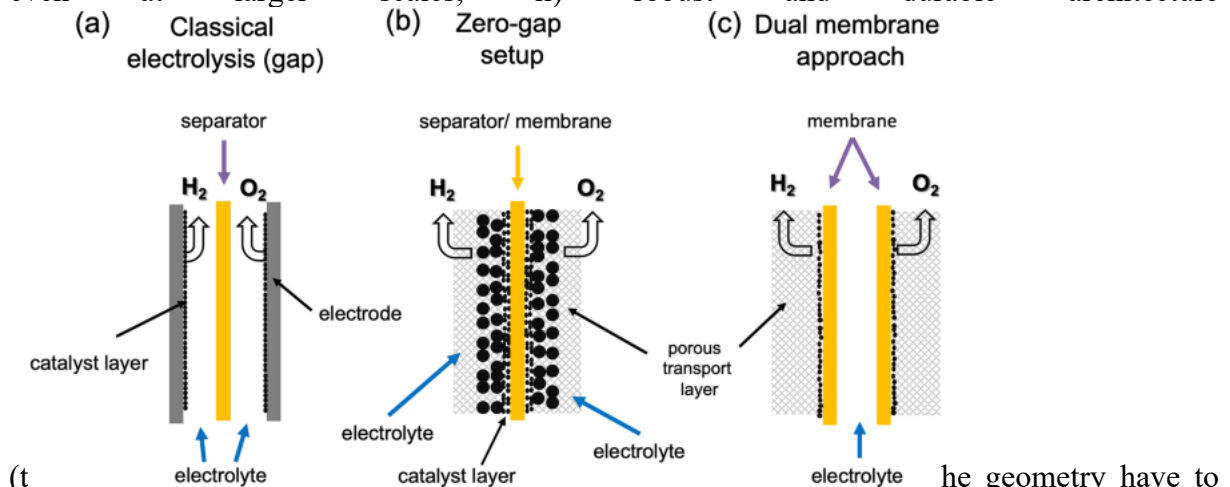
In this group are included also PEC cell based on n-type semiconductor (host/guest)<sup>46</sup> photoanodes such as SnO<sub>2</sub>, WO<sub>3</sub>, and ZnO (host materials), Fe<sub>2</sub>O<sub>3</sub> and BiVO<sub>4</sub> (guest materials).

In Chapter 2, the potential of the BiVO<sub>4</sub> photoanode (for a PEC cell based on it) are investigated. In a classical PEC cell based on n-type photoanode, 2 photoelectrodes or a couple of electrode/photoelectrode are separated by a finite distance. For instance, a photoactive UV absorbing semiconductor material can be employed as photoanode and an inert metal like Pt can be used as cathode; the electrodes, both dipped in an electrolytic solutions, can be separated by a semi-permeable membrane or by a salt-bridge (gap between the electrodes and the separator)<sup>41</sup>.

Incident photons are absorbed, generating electron-hole pairs, because they have an energy higher than the semiconductor bandgap. Subsequently, photogenerated electrons move towards the counter electrode through the closed external circuit, while holes diffuse and migrate to the semiconductor/electrolyte interface concurrently. Ultimately, electrons or holes that have reached the semiconductor/electrolyte or metal/electrolyte interface participate to the reactions.

The different types of PEC cells studied have different TRL levels, and current research aims to advance our understanding by systematically studying the inherent limitations associated with photon capture and hydrogen production in each component of the solar generators.

The transposition of PEC cells to the industrial scale therefore represents a major scientific and technological challenge, in order to guarantee i) integrated and safe devices, which are efficient even at larger scales, ii) robust and durable architecture



(t he geometry have to be well designed for the easy removal of the gases from the cathodic and anodic separated chamber).

Furthermore, it is essential to select low-cost, ideal active materials<sup>55</sup> for a large-scale manufacturing, without degrading their optical/electronic and catalytic properties. To achieve optimal yield and small energy footprint, the electrochemical surface area of the semiconductors needs to be expanded. The best solution is to increase the porosity and the roughness of the photoactive layers, by investigating, for example, nanoparticles<sup>56</sup>, metallic nanofibers and nanoporous foam<sup>57</sup>.

The (photo)electrochemical cells are also studied for applications in reduced gravitational environments (space missions), in this case, a suggested design corresponds to a dual-membrane cell<sup>58</sup>, where the electrolytic solution passes between the two membrane foils.

### 3 Key aspects for technology screening and increasing TRL

For scientific research, the processing and characterization of photoactive materials, such as molecular-modified photoelectrodes<sup>59</sup> with metallic and bioinspired catalysts, and/or semiconductor electrodes, such as carbon nanotubes and bioanodes<sup>60</sup>/cathodes, is attracting growing interest.

The investigation of performance at small active surface ( $\sim 1 \text{ cm}^2$ ) and under short-period operations (minutes/hours) is not a critical point, however when the complexity of the material and device studied increases, the criticality of discerning the limiting phenomena that impede the scalability amplifies.

Chemical and process engineering can play a significant role for achieving this higher TRL:

- Understanding the couplings among matter, heat and charges transport phenomena in order to:
  - identify limiting phenomena for translating kinetics measured on a small scale into effective kinetics, considering material heterogeneities and chemical, thermal, fluidic conditions in which they evolve.
  - Select optimal operation methods (continuous vs. batch) and semiconductor configurations (planar or suspended) to guarantee efficiency, capacity, and safety, depending on the reaction.
  - Propose optimized cell/reactor designs with regard to optical, thermal, fluidic and electrical integration (for cells with thin film semiconductor), enhancing light access for dense suspensions in colloidal reactors.
  - Anticipate aging effects.
- Identifying the obstacles associated with industrial or commercial large-scale implementation of the most promising technologies, considering operational, technological, economic, and regulatory aspects. This includes:
  - Establishing standard operating procedures (SOPs) and protocols to ensure reliable, repeatable, continuous and stable operations at large scale.
  - Driving the validation and the optimization of systems, by analyzing variables, equipment performance, as well as the degree of systems integration to facilitate potential scale-up.
  - Mitigating potential risks inherent in scaling up processes.
  - Managing investments for scaling-up, minimizing operational costs and waste to align with circular economy principles.
  - Adopting strict control measurements to detect and correct performance drift (weak signals) thereby aiming to minimize their long-term impacts.
  - Dealing with regulatory compliance issues by designing processes that adhere to safety and environmental laws.

To sum-up, chemical engineering science is at the cornerstone between physical and chemical sciences and technology, to handle the complexities of scaling up, carefully considering the overall system dynamics and equipment limitations, analyzing technical and physical variables.

Table 1 shows the state of the art performance for devices similar to those studied in the thesis. The data are grouped by device type and ranked in ascending order based on the size of the illuminated surface.

Notably, PEC cells based on  $\text{BiVO}_4$  semiconductors exhibit good stability and record STH values up to 8.1% in a PEC - PV tandem device.

IPEC cell and modules exhibit higher STH values, reaching up to 21.5%. However, the reported results in these cases are limited by the active surface (no higher than 1 cm<sup>2</sup> for STH of 21%). In both cases, an increase in the active surface is observed to induce a decrease in STH values. In contrast, technologies like photocatalyst panel reactors (PPR) present the potential for more extensive scale-ups but are still limited by the STH values.

Table 1. State of art performance of various photoelectrochemical devices.

	Illuminated area (cm <sup>2</sup> )	Test conditions		STH (%)	Ref.
		Irradiance (W.m <sup>-2</sup> )	Tested lifetime (h)		
Artificial leaves (Grätzel cells) <sup>†</sup>	0.318	1000 (chopped light)	2	12.3	Luo <i>et al.</i> <sup>61</sup>
Perovskite-BiVO <sub>4</sub> artificial leaves <sup>††</sup>	0.25	1000 (1 sun simulated)	72	0.06 (H <sub>2</sub> ) 0.2 (CO)	Andrei <i>et al.</i> <sup>62</sup>
PEC based on BiVO <sub>4</sub>	unspecified	1000 (1 sun simulated)	unspecified	9.1 – 9.2	Li and Wu. <sup>28</sup>
PEC based on CoPi- BiVO <sub>4</sub> / WO <sub>3</sub> NRs biased by PV	0.16	1000 (1 sun simulated)	1	8.1	Pihosh <i>et al.</i> <sup>63</sup>
PEC based on Fe(Ni)OOH-Mo:BiVO <sub>4</sub>	0.25	1000 (1 sun simulated)	5	6.2	Qiu <i>et al.</i> <sup>64</sup>
HaP/Si PEC	0.44	1000 (1 sun simulated)	120 (lifetime)	20.8	Fehr <i>et al.</i> <sup>65</sup>
Monolithic PK/Si PEC	1	1000 / 0 (1 sun simulated)	72 (cyclic illumination)	21.5	Datta <i>et al.</i> <sup>66</sup>
Embedded triple-junction PV-PEC*	1	variable (outdoor)	100	11-14	Kistler <i>et al.</i> <sup>67</sup>
Integrated PEC-PV (2 CoPi- W:BiVO <sub>4</sub> and 2 Si SHJ)	50	1000 (1 sun simulated)	0.16	2.1	Ahmet <i>et al.</i> <sup>68</sup>
Integrated PV (Si) – PEM module	64	1000 (1 sun simulated)	1.33	5	Becker <i>et al.</i> <sup>69</sup>
Photocatalyst Panel Reactor	90,000	880 (outdoor)	0.5	0.76	<u>Nishiyama <i>et al.</i></u> <sup>70</sup>
Photocatalyst Panel Reactor	100,000	variable (outdoor)	~ 2200	0.45	<u>Nishiyama <i>et al.</i></u> <sup>70</sup>

<sup>†</sup> Combination of PK tandem cell with NiFe DLH/Ni foam electrodes.

<sup>††</sup> Combination of PK|CoMTPP@CNT photocathode and Co WOC-BiVO<sub>4</sub> photoanode



\*PEC cell fed with vapor (temperature 70-75°C)

### 3.1 Limiting phenomena

Actually, in a more general context, the strong and multi-scale couplings of numerous physical processes affect the development of materials and technologies for the achievement of large-scale devices. In this respect, the study of low-cost and non-noble materials organic and non-organic) is essential, both with regard to the life-cycle of the devices (LCA), and of their efficiency and long-term stability.

The composition and texture of semiconductor absorbing materials impact the physical phenomena responsible for the light attenuation and conversion (Figure 8) : the generation of electrons and holes, their separation, trapping and recombination, to which it is appropriate to add the charge transfer kinetics at the liquid junction in the case of a photo-electrode. In complex systems, the performances are linked not only to charge and mass transport, but also to momentum and heat transport (internal and external to the cells).

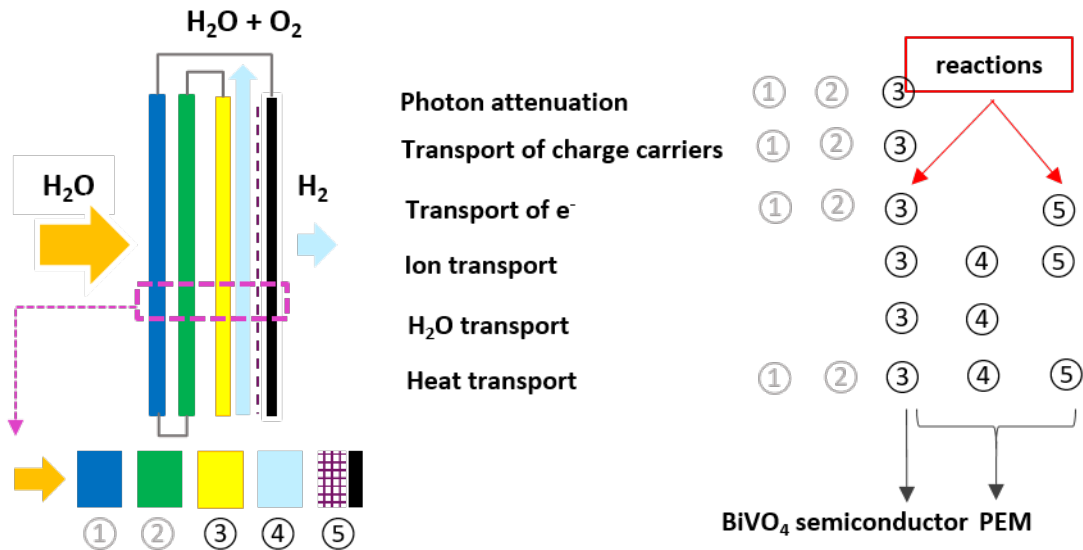


Figure 8. Schematic illustration of charge, mass and heat transport on a PEC cell based on a BiVO<sub>4</sub> photoanode. The illustrated cell consist on a photovoltaic module coupled with a proton exchange membrane (PEM) electrolyser (BiVO<sub>4</sub>/ H<sub>2</sub>-Cocat<sup>71</sup> on Carbon based materials).

In PEC models, the accurate representation of relevant transport phenomena. This may involve solving i) the Navier-Stokes equations for liquid electrolytes, or simplified momentum equations as Darcy law in porous media dynamics, ii) the Butler-Volmer equations for electrochemical reactions, or their simplified version the Tafel laws.

The transport of charge carriers in semiconductor is governed by the electrons and holes balance equation (Eq. 2).

$$\frac{\partial c_i}{\partial t} = -\nabla N_i + G + R \quad \text{Eq. 2}$$

where  $c_i$  is the intrinsic charge carrier concentration,  $G$  and  $R$  are the generation and the recombination rates, respectively.  $N_i$  is the flux of the carriers (electrons or holes) defined with the combined effects of diffusion and migration of charge carriers by the Nernst-Planck equation:



$$N_i = -D_i \nabla c_i - z_i \times \mu_i \times F(c_i \nabla \Phi) \quad \text{Eq. 3}$$

where  $D_i$  is the diffusion coefficient in the material,  $\Phi$  is the electrostatic potential and  $z_i$  is the charge of the species. Following,  $\mu_i$  is the mobility and  $F$  is the Faraday's constant.

The recombination is always a function of the reactant concentrations (electrons, holes) and of the rate constant of the recombination reaction. The recombination rate constants are determined experimentally. The formulation of the recombination term is expressed in Eq. 4.

$$R = k_{rec} \times (c_i^2 - c_e \times c_h) \quad \text{Eq. 4}$$

where  $k_{rec}$  is the recombination rate,  $c_h$  is the hole concentration, and  $c_e$  the electron concentration.

Finally, the generation term  $G$  is defined as the sum of the exponentially decaying generation profiles of all wavelengths that the material can absorb:

$$G = \int_{\lambda} \alpha(\lambda) \times I_0 \times e^{-\alpha(\lambda)x} d\lambda \quad \text{Eq. 5}$$

where  $\alpha(\lambda)$  is the wavelength dependent spectral absorption coefficient of the materials and  $I_0$  is the incident AM 1.5 photon flux and  $x$  is the propagation direction of the photon flux.

The generation term has the same value for both electrons and holes since one photon generates simultaneously the two of them.

Generation can be calculated using a simplified approach, derived by the Beer-Lambert law (Equation 7).

Additionally, the Poisson equation presented below (Eq. 6), relates the electric field vector  $\vec{E}$  (charge transport) to the electrostatic potential  $\Phi$ , more details are detailed by Selberherr<sup>72</sup>

$$\nabla^2 \Phi = -\frac{F}{\epsilon_0 \times \epsilon_r} \times (c_h - c_e + N_{bk}) \quad \text{Eq. 6}$$

where  $F$  is the Faraday constant and  $N_{bk}$  the concentration of dopant atoms in the material. The numerator of the right hand terms represent the space charge density  $\rho$ . Homogeneous scalar permittivity is assumed, with,  $\epsilon_0$  and  $\epsilon_r$  the permittivity of vacuum and the dielectric constant of the light absorber respectively.

This correlation is also applicable for semiconductor materials exhibiting very strong polarization effects, as well as for devices where piezoelectric or ferromagnetic phenomena and non linear optics are involved.

In (photo)electrochemical cells used for water splitting or for the direct conversion of  $\text{CO}_2$ <sup>1</sup>, the physical phenomena occurring in the absorbent and/or the semiconductor material must be considered together with those occurring locally at the liquid junction between the solution and the electrode, themselves connected to those relating to the complex system, more macroscopic.

Light transport is the major process affecting the performance. It can be coupled to macroscopic transport phenomena due to the possible light attenuation and bubble scattering in the liquid<sup>73</sup>.

Several approaches can be used to describe the transport of photons, depending on the desired level of refinement, ranging from simple optical models (Beer-Lambert law), to electromagnetic ones (Maxwell equations).

The Beer-Lambert law (Eq. 7) can be used to predict the number of photons absorbed in a medium of absorption coefficient  $\alpha$ :

$$I(\lambda, x) = I_0(\lambda) \times e^{-\alpha(\lambda)x} \quad \text{Eq. 7}$$

Where  $\lambda$  is the wavelength of the photons and  $x$  the thickness of the medium through which the light travels.

Alternatively, the electromagnetic approach is based on the Maxwell equations given by:

$$\vec{\nabla} \cdot \vec{D}(\vec{r}, t) = -\rho_F(\vec{r}) \quad \text{Eq. 8}$$

$$\vec{\nabla} \times \vec{E}(\vec{r}, t) = -\frac{\partial \vec{B}(\vec{r}, t)}{\partial t} \quad \text{Eq. 9}$$

$$\vec{\nabla} \cdot \vec{B}(\vec{r}, t) = 0 \quad \text{Eq. 10}$$

$$\vec{\nabla} \times \vec{H}(\vec{r}, t) = \frac{\partial \vec{D}(\vec{r}, t)}{\partial t} + \vec{J}_F(\vec{r}) \quad \text{Eq. 11}$$

where  $\mathbf{D}$  is the electric displacement,  $\mathbf{E}$  the electric field,  $\mathbf{B}$  the magnetic induction and  $\mathbf{H}$  the magnetic field;  $\mathbf{r}$  and  $\mathbf{t}$  denote location and time, respectively. Lastly,  $\rho_F$  is the free charge density and  $\mathbf{J}_F$  is the free current density.

The coupling between the phenomena occurring “up to” and “at” the junction of photo and chemically active materials, where strong multi-physics couplings prevail, requires special attention in order to transcribe the effects of the smallest scales on macroscopic performances (efficiency, aging). Indeed, radiative transfer, photo-catalysis, electrochemistry, and hydrodynamics (including heat and mass transfer), occur at very different scales of time and space, which generally requires out-of-equilibrium processing.

The challenge for modelling, is to predict the effect of operating conditions and of the micro and macrostructure of the materials, with their intrinsic properties, as well as the effect of the aging of materials, on the performance of PEC devices, regardless of their concept, design and scale.

PEC models have been reviewed recently by P. Scassellati.<sup>74</sup> The processes involved in the absorbent materials, on one hand, and water splitting reaction and technology, on the other hand, have been largely simulated individually, with either an electrokinetic<sup>75</sup> or an electrochemical approach<sup>76</sup>. Few studies have undertaken to model them in a coupled manner<sup>77,78</sup>; a significant effort is in progress for defining the boundary conditions at the liquid and buried junction in order to develop a simulation tool useful for the design and scaling of a complete operational devices.<sup>79</sup>

In addition to the research on physical phenomena, it is essential to highlight other important issues for the deployment of new solar device technologies.

On the manufacturing aspects, the realization of innovative designs is today made possible thanks to new manufacture approaches like 3D printing, but also thin film deposition on large surface (by dip coating, spin coating, chemical and physical vapor deposition etc.), offering possible, and optimal modulation of texture and/or chemical composition. This provides additional levers to improve the net energy performance of the system at scale, also linked to the cost and the lifetime of the innovative material/device considered. A cell life span shorter than 5 years faces energy constraints, while about 10 years are required for a positive net energy balance.<sup>1</sup>

Not less important is to consider the overall energy balance of solar fuel generators, from their fabrication to their operation costs, including up and downstream processes, in order to optimize them from both an energy and life cycle points of view. This includes the determination of the electrical, faradaic and solar to hydrogen energy conversion efficiencies ( $\eta_e$ ,  $FE$ ,  $STH$ ), that are key parameters for this kind of systems.

### **3.2 Deployment of PEC: the major role of simulation**

As previously mentioned, mathematical modelling and numerical simulation are powerful tools to facilitate the scale-up process, several physics aspect must be considered for comprehensive representation. These scientific tools aid in the interpretation of the optical and transport phenomena discussed in the Sec. 3.1.

Provided that the physical models are sufficiently reliable, their numerical transcription (e.g. on Python, Matlab, C++, etc.) constitutes an essential complement to operando experiments for optimization and scale-up purpose. The behavior and the design of a system can be reformulated in mathematical terms defining an objective function, in this way the formal relationship between the values of the designable parameters and the system performance can be established.<sup>80</sup> Depending on the numerical method (e.g. Monte-Carlo, Finite Elements, Finite Volumes, etc.) and on the decision criteria, thanks to the implementations of several algorithms it is possible to solve also non-linear and non-conventional problems.

Similarly, numerical simulators like Aspen Plus and CHEMCAD, Computational Fluid Dynamics (CFD) simulators such as Ansys Fluent and COMSOL Multiphysics, optical simulators such as CROWM and 3DOptix, and statistical formulation, as in the EDStar Platform, can help in unravelling macroscopic and microscopic interactions, predicting their effects, and optimizing the process accordingly.

Simulation reduces the need for extensive physical trials and assists in overcoming challenges, lowering risks, and avoiding costly mistakes. In addition, it plays a significant role in the optimization of operating parameters and design. It is suitable to evaluate multiple scenarios, key variables, and identify the most efficient configurations for higher TRL operations, to investigate numerous design variations in a relatively short time, accelerating the development of sustainable and ecological processes.

Eventually, simulations will generate massive data that will be invaluable in establishing the correlations and meta-models needed to compare technologies across the time and space scales. Numerous publications focus on atomistic and coarse-grained simulations and models able to represent, for instance, the local environment of a reactive interfaces<sup>81</sup> or the morphology of an active layer<sup>82</sup>.

On the other hand, a more comprehensive examination of the systems is undertaken, exploring aspects such as, the coupling between semiconductor and electrolyte and developing the numerical simulation settings.<sup>83</sup>

Simulation plays a pivotal role to accelerate the development of efficient photoelectrochemical systems. In this thesis, the potential of heterogeneous systems was explored (with a first approach focused on the photon-electron-active layer interactions) thanks to numerical optical simulations.

## 4 Summary and objectives of the thesis

The research project falls within the framework of solar-based carbon circular economy (Focus ECC program) that envisages the production of solar fuels and chemicals, via CO<sub>2</sub> recycling, starting from non-fossil resources and renewable energy. The study relies on the synergy between chemical science and process engineering. By combining experimental methods with theoretical analysis (modeling and simulation), the goal is to pinpoint and understand the bottlenecks associated with upscaling PEC materials and cells.

This involves the development of scalable semiconductors, photoelectrochemical cells (PEC) and integrated photoelectrochemical (IPEC<sup>47</sup>), which are seen as highly promising solutions for enhancing the production of green alternative fuels. The state of art in these different areas constitutes the main theoretical basis of this work that helped define the parameters of the study.

Actually, the project focuses on the transposition of the PEC cell to a scale representative of a commercial device, with a scientific and technological approach. The research work particularly investigated the issues associated with *i*) the large-scale fabrication of the conducting and semiconducting materials, without degrading their optical/electronic and catalytic properties, *ii*) the conception of integrated and durable devices performing in real weather conditions, *iii*) the potential commercial application of a sustainable autonomous device.

First, the manuscript focuses on the major role played by an n-type semiconductors in a PEC cell, highlighting the behavior of a photoanode as a function of the optical properties and of the morphological features of the photoactive layer at the interface with the electrolyte solution. The case study was BiVO<sub>4</sub>, a well-documented material<sup>84,85</sup> that offers different processing routes, some of which can be transposed on a large scale<sup>86</sup>.

Chapter 2 tackles the 1<sup>st</sup> fundamental scientific query driving my research:

### **What is the impact of heterogeneities, inherent to large-scale preparation processes, on the performance of photoactive materials?**

Initially, the experimental sensitivity study of the BiVO<sub>4</sub> photoanode<sup>87</sup> is detailed at small/medium scale (3 cm<sup>2</sup>), aimed at investigating the effect of the materials properties (ideally varied in a large range) on the achieved photocurrent. This is essential for understanding transport phenomena, studying the nanometric structure of the interface and the interaction between light transmission and the catalytic reaction. Then, once the relevant coupling(s) and limiting phenomena are identified, the implementation of optical models (Transfer Matrix, Crowm) is described. The latter are the key to acquire additional knowledge on the effects of non-uniform conditions on the performances that can limit the development of a large-scale PEC cell.

After the examination of the BiVO<sub>4</sub> photoanode (TRL 3) in Chapter 2, the manuscript follows a progression towards an increasing TRL, described in subsequent chapters. (Figure 9).

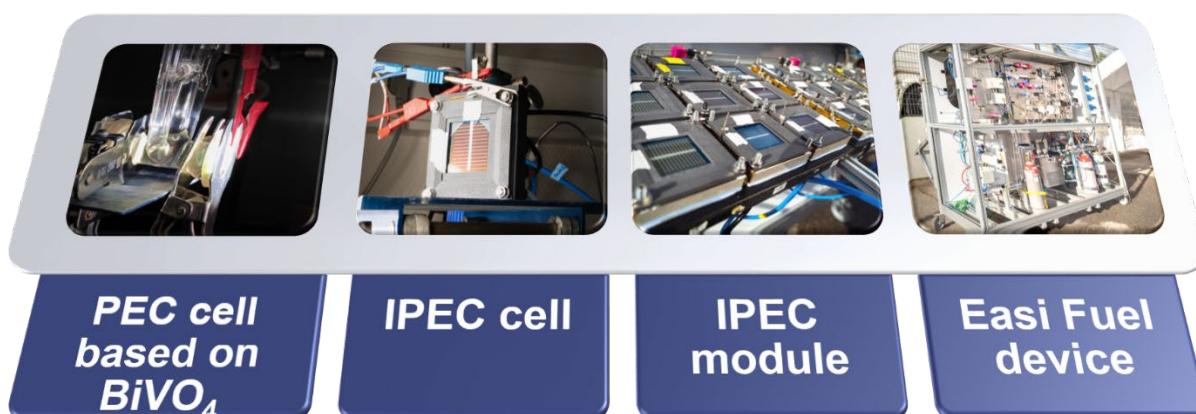


Figure 9. Overall view of the studied devices.

Chapters 3 and 4 answer the following scientific and technological question:

**What role can integration play in transferring performance from the laboratory to the pilot scale?**

Chapter 3 is organized as a manuscript ready for submission. It focuses on the integration of an IPEC cell<sup>88</sup> (TRL 3) for the water splitting reaction, and its transposition to an IPEC module with a factor of approximately 10, thanks to judicious fluidic, electrical and thermal integration (TRL 4). It discusses the design and the optimization of an IPEC cell, which consists in the effective combination of a PK/Si tandem solar cell<sup>89</sup> and a PEM type electrolyser. The PEM electrolyser consists of two fully printed plates i) a conductive polypropylene flow plate on the anode side and ii) a stainless steel AM plate with an internal cathode side heat exchanger. Thermal integration is considered to limit the heating of the solar cell and to improve the global performances of the process. The gain of such thermal integration was recently evidenced in the case of device coupling a 1 cm<sup>2</sup> photoactive (III-V) PV cell mounted in parallel with a 25 cm<sup>2</sup> active area PEM electrolyser, operating under concentrated solar irradiation for periods of 10 s to 20 min.<sup>47</sup>

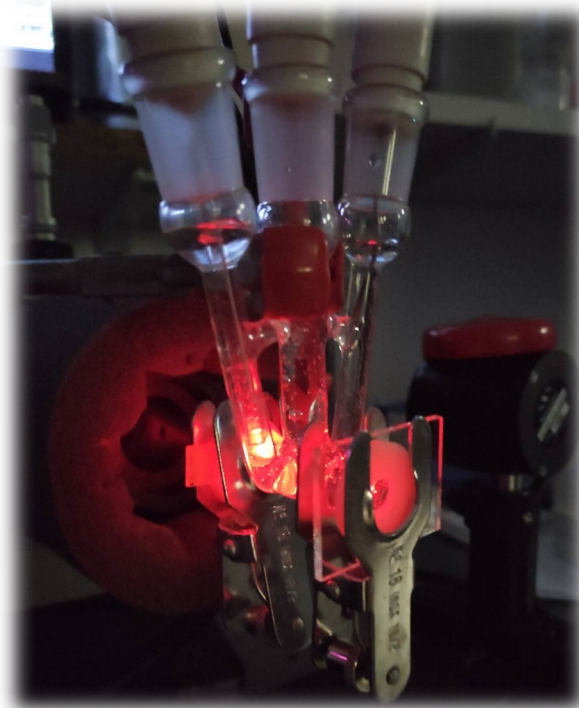
So far, the PEM cell geometry was improved, achieving a stable and quantitative H<sub>2</sub> production thanks to effective water management, efficient separation of the hydrogen and oxygen flows, robustness of the electrical contacts and deposition of a Cr/Au layer on the flow plates. The combination of the system with a PK/Si tandem solar cell allow achieving relevant photoelectrochemical results. After the realization and testing at small scale (i.e. single cell with approx. 8 cm<sup>2</sup> solar and catalytic active surfaces), the IPEC cell was scaled-up to approx. 70 cm<sup>2</sup> solar and catalytic active surface, by designing a 22 x 24 cm<sup>2</sup> monolithic IPEC module. This compact and light weight module, achieves the work of 9 single-cells electrically independent but connected in series as regards to the water circuit, and constitutes the basis brick for further extrapolation.

Chapter 4 addresses the integration of the IPEC modules into a functional demonstrator for the autonomous production of green methane. This autonomous solar integrated fuel (EASI Fuel) device, with which the CEA competed in the Horizon Prize challenge, represents the final transposition, up to a TRL of 5, thanks to the combination of the 5 IPEC modules (45 IPEC cells) with a flexible methanogenesis bioreactor. The developed demonstrator occupies about 2 m<sup>2</sup>. It is an original and stand-alone technological device which converts in real time and safely, solar light, water and carbon dioxide (CO<sub>2</sub>) into a stream of methane (CH<sub>4</sub>) fuel. The reactor operates near ambient temperature and at moderate pressure, and more importantly under real weather conditions.

Again, Chapter 4 is organized as a manuscript submitted to Joule.

## Chapter 2:

### PEC scale-up: case of a $\text{BiVO}_4$ photoanode



## Chapter 2:

### PEC scale-up: case of a BiVO<sub>4</sub> photoanode

Among the key points identified to achieve the scaling of a PEC device, the development of large active surface photoelectrodes, with performance similar to those of their (small-scale) laboratory counterparts resulting from fundamental research, is particularly considered. One aspect of scaling materials is the presence of heterogeneities in composition and texture, likely to modify their optical and catalytic performance.

In this chapter, the work focuses on studying how these heterogeneities are likely to affect the photocurrent generated by a photoelectrode. For this purpose, BiVO<sub>4</sub>, was selected due to its ease of elaboration, its promising in the actual State-of-Art, and well documented.

The study of this material is a 1<sup>st</sup> step toward the scalability of a photoelectrode that could be subsequently integrated in multiple types of PEC cells. The chapter is divided in three parts.

- In Sec. 1, the main properties of Bulk material and BiVO<sub>4</sub> photoanodes from literature are introduced.
- In Sec. 2, an experimental sensitivity study of the system at small-scale (1-3 cm<sup>2</sup>) is presented. This parametric study aims at investigating the effect of the materials properties (ideally varied in a large range) on the achieved photocurrent. This is essential for understanding transport phenomena, studying the microscopic and crystallographic structure of the interface and the interaction between light transmission and the catalytic reaction. A complete characterization of different BiVO<sub>4</sub> photoanodes is carried out, collecting a large quantity of data concerning both their photoelectrochemical and optical properties, as well as their microscopic and structural features.
- In Sec. 3, a numerical sensitivity study is implemented in order to further investigate the impact of possible modifications of the photoanode structure, likely to occur at large scale, on the photocurrent. The study is based on optical simulations with Transfer Matrix and CROWM.

## 1 BiVO<sub>4</sub> photoanodes: literature review

### 1.1 The transition metal oxides

Transition metal oxides (TMO) are an important class of materials that possess photophysical and chemical abilities to generate electron-hole pairs by absorbing sunlight as well as to promote oxygen and hydrogen evolution reaction (Figure 10).



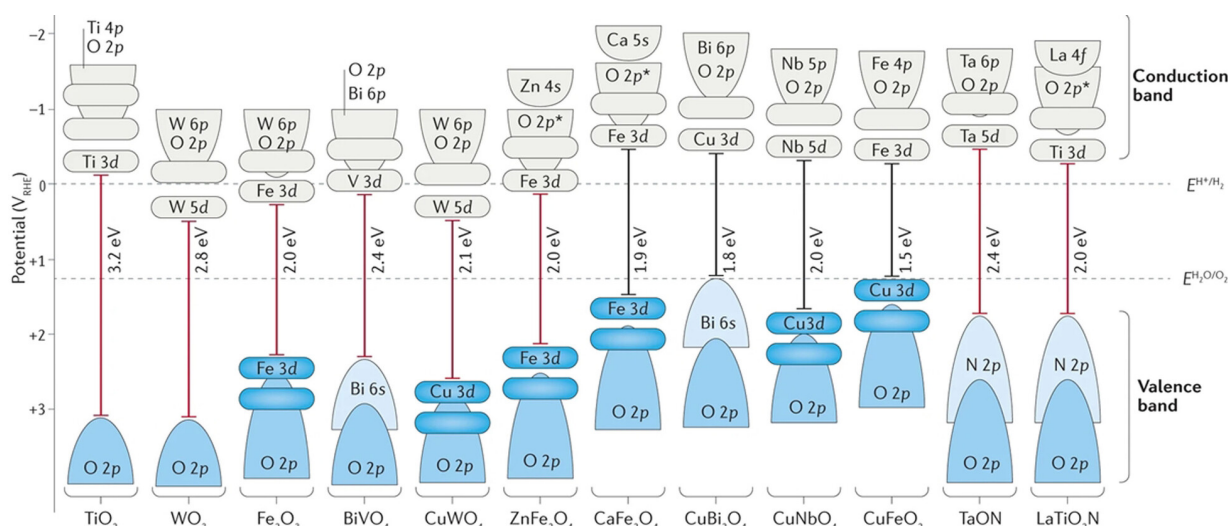


Figure 10. TMO photocatalysts' band gap energies (red for n-type, black for p-type) displayed in relation to the reversible hydrogen electrode and to the water redox energy levels at pH=0. From Rahman et al.<sup>90</sup>

Titanium dioxide ( $\text{TiO}_2$ ) was one of the first TMO, utilized from 1972<sup>42</sup> to produce  $\text{H}_2$  via water splitting applications such as photocatalysis and photoelectrocatalysis.  $\text{TiO}_2$  is simple to synthesize, cheap, and exhibits fast electron transfer. However due to its relatively inefficient quantum yield and its large band gap of 3.2 eV, it was not retained in this study dedicated to scale-up for industrial purpose.

The strategy nowadays is to study novel materials with band gap lower than 3 eV as well as to combine new catalysts and doping agents to reach higher efficiencies. Among possible candidates are the n-type oxide semiconductors, such as bismuth vanadate ( $\text{BiVO}_4$ ), tungsten trioxide ( $\text{WO}_3$ ), and hematite ( $\text{Fe}_2\text{O}_3$ ) that have been shown to be photocatalytically active as photoanodes under visible light.<sup>91</sup>

$\text{Fe}_2\text{O}_3$  revealed to have a suitable energy gap of 2.1 eV, a high chemical stability, and a very low prospective production cost, but it exhibits an extremely short hole diffusion length ( $L_d^h$ ), of the order of 10 nm<sup>1</sup>.  $L_d^h$  is higher for  $\text{TiO}_2$  (104 nm)<sup>92</sup>, but also for  $\text{WO}_3$  (150 nm)<sup>93</sup> and  $\text{BiVO}_4$  (70-100 nm)<sup>94,95</sup>. Finally, among these four materials,  $\text{BiVO}_4$  and  $\text{WO}_3$  are the most attractive ones.  $\text{WO}_3$  has the advantages of low price, good water stability (particularly in acidic conditions) and excellent electron transport property, but a larger bandgap (2.8 eV) and thus a lower sunlight absorption than that of  $\text{BiVO}_4$ , which considerably limits the performance of the PEC.<sup>96</sup>

## 1.2 $\text{BiVO}_4$ : chemical and physical properties

Bismuth vanadate ( $\text{BiVO}_4$ )<sup>84</sup> is a non-toxic, inexpensive, yellow n-type semiconductor material that has attracted considerable interest over the years.

More precisely, it is considered as the best performing transition metal oxide photoanode with very high photocatalytic activity, achieving practical STH efficiencies up to 6.7 %<sup>1,63,64</sup>, and theoretical STH efficiency approaching 9.2%.<sup>97</sup>

In its monoclinic crystal structure, the  $\text{BiVO}_4$  absorbs a substantial portion of the visible spectrum and has a moderate indirect bandgap energy of 2.4 -2.5 eV<sup>98</sup>. The edge position of the conduction band (CB) is very close to the thermodynamic evolution potential of  $\text{H}_2$ . Additionally, its valence band (VB) is closer to the oxidation potential of water than that of  $\text{WO}_3$ ; which is beneficial for the transfer and separation of photogenerated carriers.<sup>96</sup>

The band-gap of a  $\text{BiVO}_4$  photoanode is temperature-dependent and tends to decrease slightly with increasing temperature. This phenomenon aligns with the behavior observed in many

semiconductors, the thermal energy of which increases with temperature, causing electrons to move to higher energy states and therefore reducing the bandgap energy.

In addition, unlike other conductive materials, the bandgap of BiVO<sub>4</sub> does not result specifically from electronic correlation because its electronic structure does not contain partially occupied d-orbitals<sup>1</sup>. Indeed, the *monoclinic scheelite* bismuth vanadate (Figure 11c), which has the most efficient crystal structure for promoting water oxidation, is characterized by a layered structure containing cations with formal oxidation states of Bi<sup>3+</sup> (6s<sup>2</sup>) and V<sup>5+</sup> (3d<sup>0</sup>) in coordination with O<sup>2-</sup> (2p<sup>6</sup>).<sup>99</sup>

BiVO<sub>4</sub> has a poor electron-hole separation efficiency ( $\phi_{\text{sep}}$ ). Doping studies as well as investigations on catalytic agents have been attempted to improve the  $\phi_{\text{sep}}$  of the photoanode.<sup>100</sup> However, the photocurrent remains very limited because the diffusion length of the minority carrier is shorter than the thickness of the BiVO<sub>4</sub> film necessary to obtain sufficient light absorption. A large surface area nanoporous BiVO<sub>4</sub> electrode composed of particles smaller than its hole diffusion length can effectively increase  $\phi_{\text{sep}}$  also without additional doping.

An alternative approach to compensate for the short  $L_d$  is to use an extremely thin absorber (ETA) heterojunction structure, in which the layer of the BiVO<sub>4</sub> absorber is thinner than the  $L_d$  and the optical thickness depends on a structured interface with a high aspect ratio.<sup>101</sup> The ETA structure significantly improves the generation, separation and transfer of photogenerated carriers, as well as light scattering and photon absorption.

BiVO<sub>4</sub> has many other interesting properties. It is synthesized with low cost materials and Earth-abundant elements, it exhibits long-term durability in aqueous electrolytes (neutral conditions). Not to mention its ferroelasticity, photochromic effect, ionic conductivity and high crystal quality with minimal defects.

Depending on the starting compounds, light resistance can vary significantly. Small amounts of impurity phases do not appear to affect photochromism. In contrast, impurities like Fe and Pb are known to cause a more intense photochromism.<sup>102,103</sup>

BiVO<sub>4</sub> has three main polymorphs (Figure 11): *pucherite*, *dreyerite* and *clinobisvanite*.

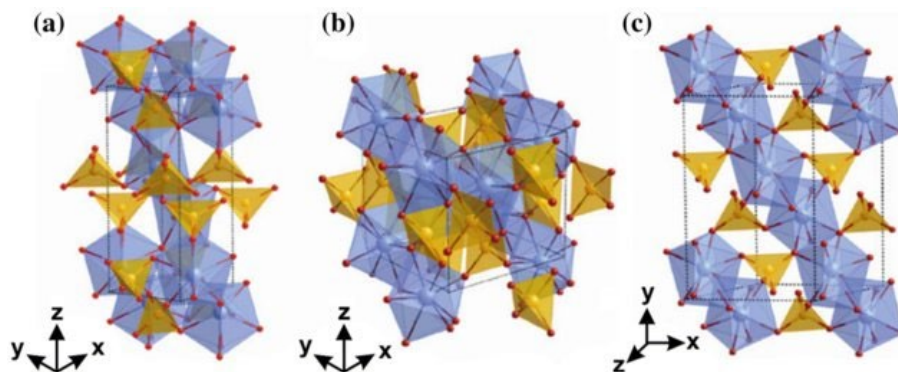


Figure 11. Crystal structure of BiVO<sub>4</sub>: a) *pucherite*, b) *dreyerite* and c) *clinobisvanite*.

*Pucherite* corresponds to the orthorhombic crystal structure, the *dreyerite* polymorph has a tetragonal zircon (t-z) structure, and *clinobisvanite* has a monoclinic scheelite (m-s) structure. Additionally, there is another tetragonal scheelite (t-s) structure with differences in terms of the atomic positions in the *clinobisvanite* polymorph.<sup>104</sup>

The orthorhombic crystal structure is the natural mineral form of BiVO<sub>4</sub>. However, it has never been reproduced in laboratory.

Low-temperature synthesis yields a tetragonal, zirconia-like BiVO<sub>4</sub>, while high temperature synthesis results in a monoclinic form of bismuth vanadate, a monoclinic distortion of the tetragonal scheelite structure (Figure 12).

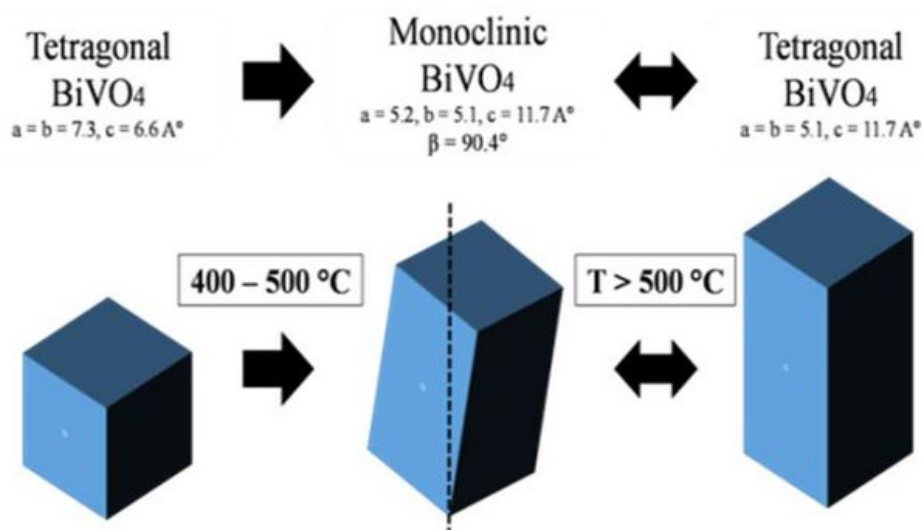


Figure 12. Example of phase transformations with temperature.

This tetragonal form is different from the Zirconia-form mentioned above, the main difference being the lattice parameter. Scheelite structures consist of vanadium ions coordinated by four oxygen atoms in tetrahedral sites, and bismuth ions coordinated by eight oxygen atoms from eight different  $\text{VO}_4$  tetrahedral units. More details regarding the orientation and specifications of  $\text{BiVO}_4$  structures are reported by Noor *et al.*<sup>105</sup>. In tetragonal structures, the lengths of identical bonds are equal while distortion occurs in monoclinic structure. At temperature around  $255^\circ\text{C} \pm 2^\circ\text{C}$ <sup>106</sup> the monoclinic scheelite structure of  $\text{BiVO}_4$  becomes tetragonal scheelite, due to a ferroelastic to paraelastic phase transition<sup>107</sup>. The ferroelasticity is a reversible deformation under specific conditions of mechanical and/or thermal stress, resulting in a change of crystal shape or structure. Below  $255^\circ\text{C}$  the material is optically biaxial, above  $225^\circ\text{C}$  the material is optically uniaxial. While, the irreversible conversion of the zircon-type tetragonal  $\text{BiVO}_4$  into its monoclinic isomorph begins between  $350^\circ\text{C}$  and  $400^\circ\text{C}$ <sup>108</sup> and continues up to  $940^\circ\text{C}$ <sup>109</sup>, temperature at which  $\text{BiVO}_4$  starts to melt congruently, without changing its chemical composition.

### 1.3 $\text{BiVO}_4$ : photoelectrochemical performances

The maximum theoretical photocurrent density of  $\text{BiVO}_4$  is  $7.5 \text{ mA/cm}^2$  assuming that all photons from solar irradiation with energy above 2.4-2.5 eV are absorbed by the semiconductor and contribute to the photocurrent so that the external quantum efficiency is equal to the absorbance ( $\text{EQE} = \text{A}$ ).<sup>110</sup>

The work of Pihosh *et al.*<sup>63</sup> shows that an optimized  $\text{BiVO}_4$  photoanode (Co-Pi/ $\text{BiVO}_4/\text{WO}_3$  nanowire), prepared by glancing angle deposition (GLAD) technique on ITO/Pt/ITO, produces a maximum water splitting photocurrent of  $6.72 \text{ mA}\cdot\text{cm}^{-2}$  under 1 sun illumination at 1.23  $\text{V}_{\text{RHE}}$ . This value is approximately 90% of the theoretically possible result for  $\text{BiVO}_4$  and stands as the highest photocurrent density ( $J_{ph}$ ) ever reported for a metal oxide-photoanode.

Kim and Lee<sup>111</sup> correlated the performance of the  $\text{BiVO}_4$  photoanode with the Incident-Photon-to-electron Conversion Efficiency (IPCE) results, demonstrating a synergistic effect in IPCE of the  $\text{BiVO}_4/\text{WO}_3$  heterojunction. The current *state-of-the-art* data will be useful to have a more precise comparison between the theoretical and experimental results obtained in this thesis (see Sec. 3.2).

In its monoclinic clinobisvanite structure (Figure 11c),  $\text{BiVO}_4$  presents a very high photocatalytic activity, it has the best photon harvesting property thanks to its moderate indirect

bandgap of  $\sim 2.4$  eV,<sup>112</sup> lower than in pure tetragonal BiVO<sub>4</sub> (2.9 eV)<sup>113</sup>. Today, high-performance efficiencies are typically reported for BiVO<sub>4</sub> photoanodes having an illuminated area of 2.5 cm<sup>2</sup>.<sup>114</sup> Most works related to the testing of semiconductor photocatalysts in PEC cells also uses small areas of around 1–2 cm<sup>2</sup>.

This research work focused on one of the first approaches aimed at testing a large-scale photoanode with an electrode surface of 3 cm<sup>2</sup> (illuminated area: 0.46 cm<sup>2</sup>) and to identify, when it was possible thanks to modeling and simulation, the effects of macroscopic heterogeneities linked to the fabrication process and to the nature of the substrate at this scale. Figure 13a shows a PEC cell (based on a BiVO<sub>4</sub> photoanode) for water photoelectrolysis; an example of application for the results of my study.

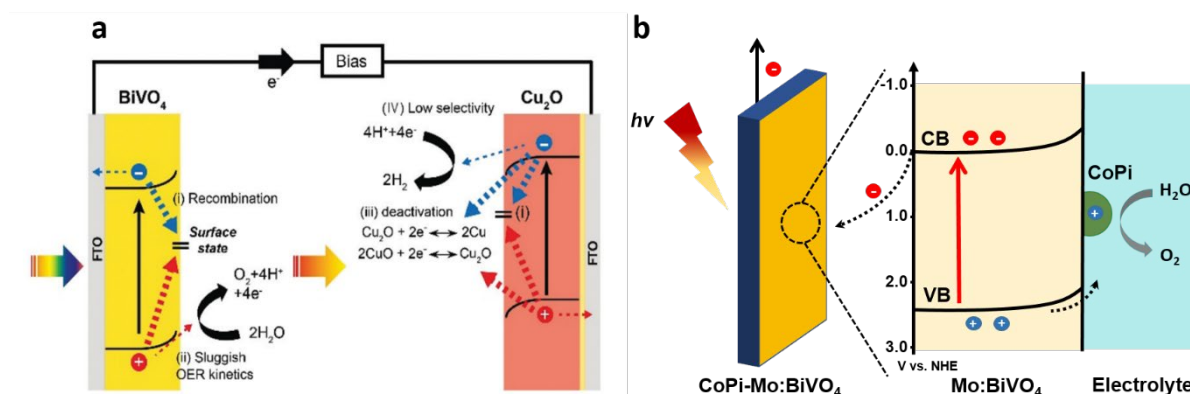


Figure 13. BiVO<sub>4</sub> photoanode in PEC cell, BI. a) Example of a PEC cell based on a BiVO<sub>4</sub> photoanode, b) Band diagram showing charge transfer in the bulk and at the interface with electrolyte.<sup>115</sup>

To increase the BiVO<sub>4</sub> efficiency, a cobalt oxide (CoPi) catalyst was photo-electrodeposited on several BiVO<sub>4</sub> electrodes, fabricated by an electrodeposition technique, on FTO and ITO conductive glass supports. At the same time, molybdenum ions were added, as dopant to improve the performance of BiVO<sub>4</sub> electrodes produced by spin coating. Figure 13b shows an example of Mo-doped BiVO<sub>4</sub> electrode, modified with the CoPi catalyst.

In the majority of the studies, the BiVO<sub>4</sub> photoanode exhibits a higher photocurrent when illuminated under back illumination (support side) than front illumination (semiconductor side) since the most part of the photogenerated electron-hole pairs originates in the thin layer of the incident surface.<sup>116</sup>

So, under back illumination, holes tend to traverse longer distances than electrons. Nevertheless, the holes diffusion length of BiVO<sub>4</sub> is considered to be longer than the electron diffusion length, with the latter being identified as one of the principal limiting factor for photocurrent generation by BiVO<sub>4</sub>

In the case of undoped BiVO<sub>4</sub>, the electron diffusion length at room temperature is only 10 nm<sup>117</sup>, conversely, the hole diffusion length in BiVO<sub>4</sub> ( $\sim 100$  nm)<sup>118</sup> is approximately an order of magnitude greater than that of electrons. In addition, the thickness of an undoped BiVO<sub>4</sub> layer is limited to less than 200 nm to obtain a high separation efficiency, but such a thin film is not sufficient for a consistent light absorption, and constrains the BiVO<sub>4</sub> qualities.<sup>119</sup> To achieve high absorption and separation efficiencies, many research have been performed, involving doping, heterojunctions and nanostructures (see Sec. 2.6).

This thesis work is inspired by the work of Hernández *et al.*<sup>120</sup> who compared the performance achieved by a CoPi-BiVO<sub>4</sub> photoanode with an illuminated area of 0.785 cm<sup>2</sup> and on a larger scale of 6 cm<sup>2</sup>. The results show good PEC stability in both cases, but photoanode enlargement resulted in a reduction in photocurrent density by a factor of two. In the 6 cm<sup>2</sup> BiVO<sub>4</sub>

photoanode, the spin-coating process exhibits minimal thickness variation compared to photoanodes with smaller active areas, but contributes to an elevated concentration of defective states, particularly at the edges of the large deposit area.

As the active area of the photoanode increases, there are more morphological and qualitative difference in the BiVO<sub>4</sub> layer, between the center and the edges of the photoanode.

This is the main cause of the lower photocatalytic efficiency of the film when the entire 6 cm<sup>2</sup> area is illuminated.

To address this issue, it becomes important to refine the spin-coating process, enhancing control over deposit homogeneity. Alternatively, one may explore different techniques such as sputtering or electrodeposition to achieve uniform coverage over larger surfaces. These kinds of approaches are described in Sec. 2.2.

## 2 Experimental parametric study

### 2.1 Methodology

The study of the BiVO<sub>4</sub> photoanode is based on a global characterization aimed at analyzing the properties of photoanodes having an electrode surface area of 3 cm<sup>2</sup>. Collecting a large amount of data from different samples, allows to analyze the impact of heterogeneities, indicative of the possible limitation encountered at large scale. In this aim, numerous BiVO<sub>4</sub> photoanodes (up to 100, Table 10 in Appendix 5.2) have been synthesized and characterized in terms of structural (at the crystal and layer scales) and optical properties, and up to the generation of a photocurrent.

The parametric study includes samples prepared with and without heteroatoms doping and catalyst addition, deposited on a transparent conductive oxide (TCO) coated glass among three candidates differing by their thickness and conductivity.

The TCO coated glass utilized consists in semiconductor wafer with Fluorine-doped tin oxide (SnO<sub>2</sub>:F) or Indium Tin Oxide (In<sub>2</sub>O<sub>3</sub>:Sn) as substrate.

The FTO 80 and ITO 12 substrates were purchased from SOLEMS:

- FTO AGC 80 (sheet resistance 80 Ω.sq<sup>-1</sup>, with an 80 nm FTO layer on a 1.1 mm thick glass slide)
- ITO SOL 12 (sheet resistance 12 Ω.sq<sup>-1</sup>, with a 370 nm ITO layer on 1.1 mm thick glass slide)

FTO 7 was purchased from SIGMA-ALDRICH:

- FTO TEC 7 (sheet resistance 7 Ω.sq<sup>-1</sup>, with a 550 nm FTO layer on 2.2 mm thick glass slide)

The photoanodes are prepared by two different synthesis methods: electrodeposition, which includes a drop casting step, (El) and sol-gel (SG) spin coating (Sc). Both processes, depending on their operating conditions, can influence the uniformity of the BiVO<sub>4</sub> film. This enables us to synthesize various samples in terms of thickness and texture and to assess the dispersion of these elaboration processes, analyzing their impact on the performance and stability (under 1 sun illumination, with and without hole scavenger) during photoelectrochemical tests.

These characterizations are preferably carried out on a sample-by-sample manner (Figure 14), in order to correlate as closely as possible the changes in light absorption and photocurrent generated (properties in use) with the microstructure, texture and thickness of the samples (intrinsic properties). To this end, an appropriate mapping sequence has been proposed for each series of measurements, starting from the most conservative tests to the most intrusive ones.



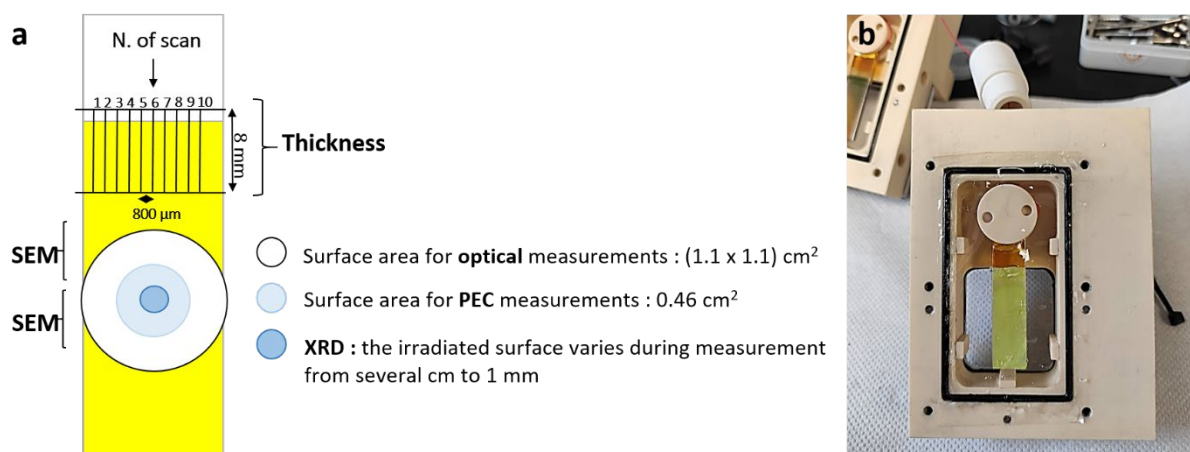


Figure 14. BiVO<sub>4</sub> sample. a) Mapping overview of a complete BiVO<sub>4</sub> characterization. b) Example of a BiVO<sub>4</sub> photoanode in a PEC cell.

## 2.2 Fabrication Methods

Low cost, inexpensive, scalable and reproducible techniques were adopted for the thin BiVO<sub>4</sub> film fabrication. These coating processes are actually available for the manufacturing of semiconductor photoanodes ready to be integrated in water splitting technologies, as well as in carbon dioxide reduction applications. **Sol-gel spin coating** is a metal-organic decomposition (MOD) technique<sup>121</sup>, generally used to deposit various efficient coatings, including photoresists, nanomaterials, micro and nanoparticles, and organic, inorganic or hybrid organic / inorganic semiconductors.<sup>122</sup> The deposition of thin layer of material on flat substrates is achieved in a spin coater with vacuum chucks designed to secure substrates during operation. This process is relevant to obtain coated layers with thickness higher than 1-10 nm<sup>123</sup> and both dense and porous structures under mild reaction conditions, thanks to the simplicity of synthesis, and the possibility of controlling particle size and distribution.<sup>124</sup>

Precisely, a small amount of liquid sol is dropped on a conductive coated glass, the latter can be static or spinning at low speed. The sample is then rotated at fixed speed, causing the spreading of the viscous liquid by centrifugal force and the solvent evaporation. The thickness of the BiVO<sub>4</sub> layer was modulated by repeating the spin coating deposition. A sequential deposition of more than one layer is generally suggested improving the performance of solution-processed BiVO<sub>4</sub> photoelectrodes. The thickness of the deposited layer depends on the process parameters, mainly on rotational speed  $s_r$  and rotational time  $t_r$ , but also on the acceleration (with less influence). It is additionally affected by the viscosity and the concentration of the dropped solution, and possible irregularities and wettability of the substrate. Other factors that influence the spin coating method are linked to the environmental conditions (temperature, solvent partial pressure in the surrounding atmosphere) where the process is conducted, as well as to the temperature of the solvent and substrate.

Organic additives and block co-polymers such as polyethylene glycol (PEG) 200 and Pluronic® F-108 (PEG-PPG-PEG: polyethylene glycol-block-polypropylene glycol-block-polyethylene glycol) can be added to the sol-gel solution as structure-directing agents to form and modulate a well-defined nanostructure within the solid material that emerges from the sol-gel process.

Precisely, in the presence of organic additives and block co-polymers, the carbon components are pyrolyzed during annealing, leading to the formation of a microporous or mesoporous microstructure with vacancy and/or defects. The sequential crystallization of the inorganic network must precede the carbon decomposition to maintain the integrity of the porous network; otherwise, its structural stability will be compromised.<sup>92</sup>

In conclusion, the benefits of combining polymers to an inorganic matrix in a sol-gel process are principally linked to the formation of the micro/mesoporous structure that influences the porosity, morphology, and properties of the final material. The addition of polymers can promote charge migration and enhance surface area, homogeneity and adhesion of the sol-gel solution to the substrate, thanks to the controlled porous network formation. However typically increases tortuosity, resulting in a more convoluted path for charge carriers. Modifying the polymer concentration or using distinct polymers with different molecular weights or structures can help to modulate the tortuosity of the path, as well as to tune the viscosity of the sol-gel solution, decrease surface tension (to improve substrate wetting) and to control the film thickness and uniformity.

**Electrodeposition** represents a more versatile electrochemical technique than spin coating due to its ability to offer precise thickness control, uniformity of the deposit, and adaptability across a diverse range of materials and substrate shapes.

In this process, upon the application of an electrical potential, ionic species within a solution are reduced and subsequently deposited on the electrode surface, to form a cohesive and conductive thin film.

It is used at industrial scale for a wide variety of two- and three-dimensional materials such as coatings and films.<sup>125</sup>

This electrochemical process takes place in aqueous solution under mild conditions. It can be used to provide a desired electrical resistance, improve the corrosion resistance or the heat tolerance of material. The main influencing parameters of the process are the electrolyte composition, the operating potential or current, and the deposition time. The thickness of the deposited layer is indeed related to the total electric charges used and is more precisely tuned than by sol-gel spin coating. Consequently, electrodeposition enables access to a larger range of thicknesses, allowing the production of thicker photoactive layers than those treated with spin coating.

**Remark:** The scaling of coating processes is in continuous development and more and more progress is being made in the field of electrodeposition. In the race of solar energy, electrodeposition is expected to be a game changer to increase the efficiency of (for example) large CuInGaSe<sub>2</sub> (CIGS)<sup>126</sup> solar module, and to reduce manufacturing costs to less than \$0.50/W.<sup>127</sup> The challenges for promising electrode in the industry of green energy conversion systems are related to a deepest investigation of the factors (cost and sustainability of chemicals, porosity, wettability, gas permeability, etc.) limiting electrochemical performance and the long-term stability.

In this context, the fabrication techniques just mentioned play a central role for the addition of catalysts or doping agents, also enhancing the efficiency of the devices. Catalysts ensure the acceleration of desired reactions, such as oxygen reduction or hydrogen evolution, while minimizing unwanted side reactions and slowing recombination of charges. At the same time, doping agents have an important influence on the stability and durability of the electrode. They modify the material's composition as well as its macroscopic and microscopic structure, strengthening the resistance to degradation and corrosion of the electrode, and extending the life of the semiconductors. Specifically, doping agents modify factors such as conductivity, electron transfer kinetics, and band structure, which have a substantial effect on the electrical properties of electrode materials.

To summarize, the incorporation of catalysts and doping agents into electrodes, by spin coating, electrodeposition (often combined with **drop casting**<sup>128,129</sup>) and photoelectrodeposition<sup>68</sup>, is a fundamental strategy for promoting the necessary improvements in terms of reaction kinetics, selectivity, stability and material properties.

To overcome the weaknesses of the electrodes, other modification strategies, such as controlling nanostructural morphology, heterostructures (particularly Z-scheme), plasmonic enhancement and surface passivation<sup>130</sup> can be investigated. Simultaneously, many alternatives<sup>131</sup> such as dip coating<sup>132</sup>, sputtering, photoassisted electrodeposition<sup>49</sup>, chemical vapor deposition, physical vapor deposition but also layer-by-layer (LbL) deposition and Langmuir-Blodgett (LB) technique, etc. have their own advantages and may be suitable for different applications.

### 2.2.1 Sol-gel spin coating

Sol-gel spin coating method for the fabrication of the BiVO<sub>4</sub> photoelectrodes was optimized (Figure 15).

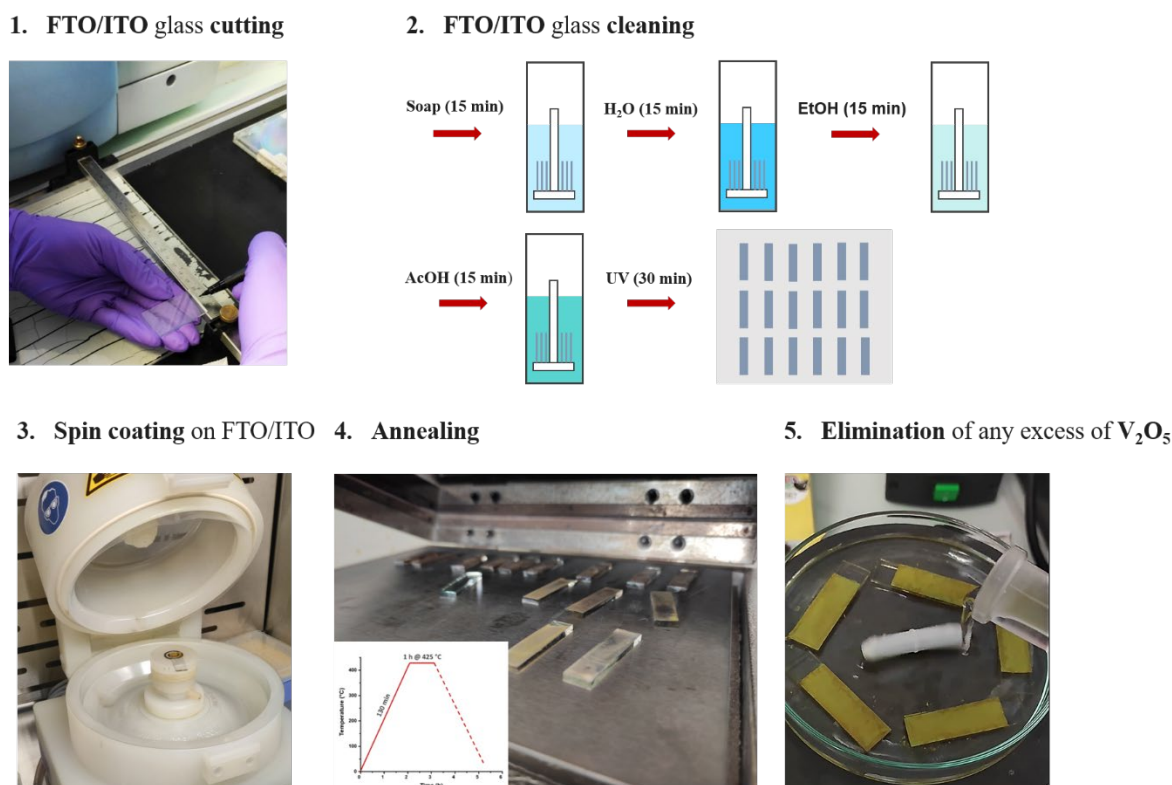


Figure 15. Fabrication of BiVO<sub>4</sub> photoanodes by sol-gel spin coating method.

ITO and FTO glass wafers of approximately 3 cm<sup>2</sup> were cut and washed before being positioned on a vacuum spin coater.

The conductive glass wafers were initially cleaned in an ultrasonic bath for 15 minutes each in soapy deionized (DI) water, DI water, ethyl alcohol, and acetone. Subsequently, they underwent a 30-minute UV-ozone treatment.

Then, a sol-gel solution was prepared and dropped with a pipette on the substrate which is fixed (under vacuum) on a stage of the spin coater. The amount of liquid dispensed is determined by the size of the item to be coated.

The electrode is then removed from the spin coater and dried to release the solvent and form a thin film. A heat treatment process (annealing) was essential to eliminate the remaining solvent by evaporation into gaseous products, as well as to drive crystallization of the BiVO<sub>4</sub>, finally to promote adhesion between the layers. The annealing temperature changes the structure of the material to achieve desired characteristics or to remove defects. The chosen annealed temperature in correlation with the various protocols used for the preparation of the SG solution, for all the synthesized photoanodes, are reported in Table 4. Finally, after the annealing process performed in a furnace open to ambient air, the obtained semiconductor was rinsed thoroughly



with an aqueous solution of 0.5 M KOH, for 5 min, to remove any residual impurities and excess of  $V_2O_5$ , then washed with deionized water and dried under nitrogen.

The 1<sup>st</sup> protocol for the preparation of the SG solution used to synthesize undoped and doped (with Mo)  $BiVO_4$  electrodes is described in Table 2, optimized from <sup>133</sup>.

Table 2. Protocol n1.

BiVO <sub>4</sub> on FTO/ITO substrates		3 at. %Mo:BiVO <sub>4</sub> on FTO/ITO substrates	
<i>Bi(NO<sub>3</sub>)<sub>3</sub>·5H<sub>2</sub>O</i> 0.20 M	Glacial acetic acid 0.97 mL	<i>Bi(NO<sub>3</sub>)<sub>3</sub>·5H<sub>2</sub>O</i> 0.20 M	Glacial acetic acid 0.90 mL
<i>C<sub>10</sub>H<sub>14</sub>O<sub>5</sub>V</i> 0.03 M	Acetylacetone 6.29 mL	<i>C<sub>10</sub>H<sub>14</sub>O<sub>5</sub>V</i> 0.03 M	Acetylacetone 5.82 mL
PEG 200 (50 vol%) or Pluronic <sup>®</sup> F-108 (1 mol if <i>C<sub>10</sub>H<sub>14</sub>O<sub>5</sub>V</i> = 1 mol)		<i>C<sub>10</sub>H<sub>16</sub>MoO<sub>6</sub></i> 0.01 M	Acetylacetone 0.54 mL

Bismuth(III) nitrate pentahydrate in glacial acetic acid and vanadyl acetylacetonate in acetylacetone were mixed with a 1 : 1 mol ratio of Bi : (V) to make the undoped  $BiVO_4$  photoanode. While, bismuth(III) nitrate pentahydrate in glacial acetic acid, vanadyl acetylacetonate and molybdenyl acetylacetonate in acetylacetone were mixed with a 1 : 1 mol ratio of Bi : (V + Mo) to make the Mo :  $BiVO_4$  photoanodes.

The solutions were obtained after 20 min of ultrasonication at room temperature.

Hydrolysis and condensation reactions occur to produce a sol-gel solution with precise pH and concentration, easily deposited by spin coating.

In order to define the rotational speed at which the substrate is efficiently spun during the coating process, and the time required to achieve the desired thickness or uniformity, numerous electrodes have been prepared by changing the parameters of the spin coater, namely rotational speed and time.

Multiple layers (from 4 to 6) of a colloidal solution were coated on FTO and ITO substrates (40  $\mu\text{l}\cdot\text{cm}^{-2}$  for each layer). Imposed rotation speeds varied between 250 and 1500 RPM, and rotational times were set at 120 s, 60 s and 10 s.

An annealing between layers was carried out at 400°C for 5 min, preceded by a first ramp up of 5 min, an intermediate step at 50°C (for 3 min), and a second ramp up of 10 min. Then followed by natural cooling. As reported in Table 4, a final annealing at 425°C for 1 h, using a ramp time of 130 min was performed.

In parallel, PEG 200 and Pluronic<sup>®</sup> F-108 were incorporated in two different sol-gel solutions of undoped  $BiVO_4$ . First, PEG 200 (50 vol%)<sup>134</sup> was added in a sol-gel solution, then the latter was concentrated by rotary evaporation of solvent for 25-35 min.

In order to further increase the viscosity of the solution and the efficiency of the semiconductor, the amount of polymer mixed in the undoped  $BiVO_4$  sol-gel solution was increased, using Pluronic<sup>®</sup> F-108 (1:1 molar ratio of precursor (V) : block co-polymers) and following the same procedure as for PEG 200.

After that, a visual examination of the photoelectrodes (made with and without polymers in the solution) complemented by electrochemical tests allowed us to identify and reduce the limiting factors of the chosen protocols, opening the basis for new investigations.

Finally, accordingly to this, a further protocol was highlighted (Table 3), from which more efficient photoelectrodes were fabricated, then selected for the detailed and comprehensive characterization discussed in the following paragraphs.

Table 3. Protocol n2.

BiVO <sub>4</sub> on FTO/ITO substrates		Mo:BiVO <sub>4</sub> on FTO/ITO substrates	
<i>Bi</i> <sub>2</sub> <i>O</i> <sub>3</sub> (99.8 %) 0.03 M	<i>HNO</i> <sub>3</sub> (68.8– 70.0%) 6.6 ml	<i>Bi</i> <sub>2</sub> <i>O</i> <sub>3</sub> (99.8 %) 0.03 M	<i>HNO</i> <sub>3</sub> (68.8– 70.0%) 6.6 ml
<i>NH</i> <sub>4</sub> <i>VO</i> <sub>3</sub> 0.14 M		<i>NH</i> <sub>4</sub> <i>VO</i> <sub>3</sub> 1.14 M	
BiVO <sub>4</sub> solution adjusted to 20 mL with deionized (DI) water		BiVO <sub>4</sub> solution adjusted to 20 mL with deionized (DI) water	
<i>C</i> <sub>14</sub> <i>H</i> <sub>22</sub> <i>O</i> ( <i>C</i> <sub>2</sub> <i>H</i> <sub>4</sub> <i>O</i> ) <sub><i>n</i>=9–10</sub> : 1 drop before spin coating for each 10 mL of BiVO <sub>4</sub> solution		<i>C</i> <sub>14</sub> <i>H</i> <sub>22</sub> <i>O</i> ( <i>C</i> <sub>2</sub> <i>H</i> <sub>4</sub> <i>O</i> ) <sub><i>n</i>=9–10</sub> : 1 drop before spin coating for each 10 mL of BiVO <sub>4</sub> solution	
-		<ul style="list-style-type: none"> <li>• 250 μL of Mo peroxo solution added to 20 mL of BiVO<sub>4</sub> solution (1.25% Mo : V)<sup>117</sup></li> <li>• 500 μL of Mo peroxo solution added to 20 mL of BiVO<sub>4</sub> solution (2.5% Mo : V)</li> </ul>	

The transparent yellow BiVO<sub>4</sub> solution contains ~4 mol.L<sup>-1</sup> HNO<sub>3</sub>, 0.2 M Bi(NO<sub>3</sub>)<sub>3</sub>, 0.45 M VO<sub>2</sub>(NO<sub>3</sub>), and 0.45 M NH<sub>4</sub>NO<sub>3</sub>.


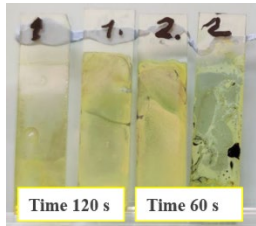

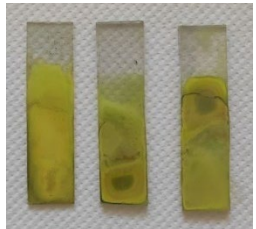
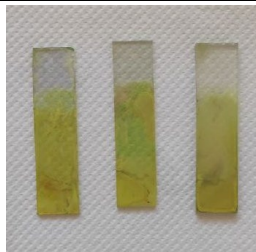
Here, the surfactant, *C*<sub>14</sub>*H*<sub>22</sub>*O*(*C*<sub>2</sub>*H*<sub>4</sub>*O*)<sub>*n*=9–10</sub> (Triton X-100) was used to improve the substrate's wettability and the final film uniformity. BiVO<sub>4</sub> solutions prepared without surfactant remained quite stable over several months of storage. Otherwise, the Triton X-100, will gradually reduces some yellow VO<sub>2</sub><sup>+</sup> species to the blue VO<sup>2+</sup> species, resulting in a green solution.<sup>117</sup>

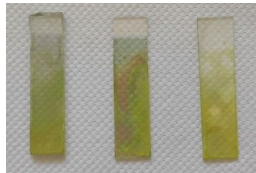
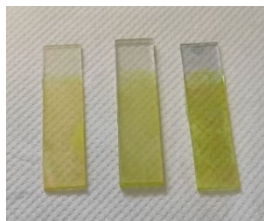
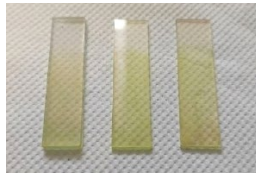
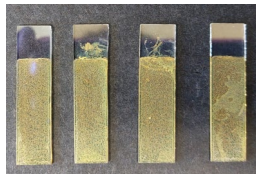
The preparation of the molybdenum peroxo solution consists in the dissolution of 0.86 g of Mo powder (APS 3–7 micron, 99.95%) in 10 mL H<sub>2</sub>O<sub>2</sub> (certified ACS, 30%) with slow addition of the powder to the H<sub>2</sub>O<sub>2</sub>, over a 5-minute interval.

As the process is exothermic, the temperature rise was controlled using a water bath. The transparent yellow solution obtained was diluted with DI water up to 20 mL to obtain a 0.45 M Mo solution. The Mo peroxo solution was added to the BiVO<sub>4</sub> solution to get the required percentage of doping relative to the V content (e.g., 1.25% Mo : V and 2.5% Mo : V).

Once the overall solution was ready, 200 μl per layer (4 layers in total) were deposited on a 3 cm<sup>2</sup> surface. The coating was performed with a 1 step spinning program (1500 RMP, 10 s for each step). The 1<sup>st</sup> three layers were subsequently dried using a stepwise annealing elevation ramp of 5 min, from room temperature to 50°C. After 3 min, a second ramp up of 10 min was carried out to achieve a temperature of 400°C for 5 min. This procedure, reported in Table 4, was repeated to increase the film thickness, concluding with a final annealing at 425°C for 1 h, using a ramp time of 130 min.

Table 4. Detailed protocol specifications.

Protocol	Porogen	Num. of Layers	$t_r$ (s)	$S_r$ (RPM)	Final calcination treatment*	$\text{BiVO}_4$ electrodes
1 <sup>133,134</sup>	-	4	10	500	<ul style="list-style-type: none"> <li>• 30 min ramp up</li> <li>• 150°C for 10 min</li> <li>• 180 min ramp up</li> <li>• 470°C for 30 min</li> <li>• natural cooling</li> </ul>	
1 <sup>133,134,135</sup>	PEG 200	4	60	250	<ul style="list-style-type: none"> <li>• 30 min ramp up</li> <li>• 150°C for 10 min</li> <li>• 180 min ramp up</li> <li>• 400°C for 5 min</li> <li>• natural cooling</li> </ul>	
1 <sup>133,134,135</sup>	PEG 200	4	120	250	<ul style="list-style-type: none"> <li>• 30 min ramp up</li> <li>• 150°C for 10 min</li> <li>• 180 min ramp up</li> <li>• 400°C for 5 min</li> <li>• natural cooling</li> </ul>	
1 <sup>133,134,135</sup>	PEG 200	4	10	500	<ul style="list-style-type: none"> <li>• 30 min ramp up</li> <li>• 150°C for 10 min</li> <li>• 180 min ramp up</li> <li>• 400°C for 5 min</li> <li>• natural cooling</li> </ul>	
1 <sup>133,134,135</sup>	PEG 200	4	60	500	<ul style="list-style-type: none"> <li>• 30 min ramp up</li> <li>• 150°C for 10 min</li> <li>• 180 min ramp up</li> </ul>	

					<ul style="list-style-type: none"> <li>• 400°C for 5 min</li> <li>• natural cooling</li> </ul>	
1 <sup>133,134,135</sup>	PEG 200	4	60	1000	<ul style="list-style-type: none"> <li>• 30 min ramp up</li> <li>• 150°C for 10 min</li> <li>• 180 min ramp up</li> <li>• 400°C for 5 min</li> <li>• natural cooling</li> </ul>	
1 <sup>133,134,135</sup>	PEG 200	6	60	1500	<ul style="list-style-type: none"> <li>• 30 min ramp up</li> <li>• 150°C for 10 min</li> <li>• 180 min ramp up</li> <li>• 400°C for 30 min</li> <li>• natural cooling</li> </ul>	
1 <sup>133,134</sup>	Pluronic <sup>®</sup> F-108	4	60	1500	<ul style="list-style-type: none"> <li>• 30 min ramp up</li> <li>• 150°C for 10 min</li> <li>• 180 min ramp up</li> <li>• 400°C for 30 min</li> <li>• natural cooling</li> </ul>	
2 <sup>117</sup>	-	4	10	1500	<ul style="list-style-type: none"> <li>• 130 min ramp up</li> <li>• 425°C for 60 min</li> <li>• natural cooling</li> </ul>	

\*Annealing between layers: ramp up of 5 min, intermediate step at 50°C (for 3 min), second ramp up of 10 min, final step at 400°C for 5 min, natural cooling.

### 2.2.2 Electrodeposition (and drop casting)

Several photoanodes (~40), made of crystalline BiVO<sub>4</sub> nanoplates, were synthesized by a multistep electrodeposition method, which involved a first electrodeposition step followed by drop casting and thermal evaporation. For simplicity, in the manuscript, the term “*electrodeposition*” is used to refer to one of the two methods employed for the synthesis of

$\text{BiVO}_4$  photoanodes, and therefore also encompasses the drop casting step necessary to add the vanadium-based precursor.

The fabrication of a  $\text{BiVO}_4$  photoanode is detailed in Figure 16.

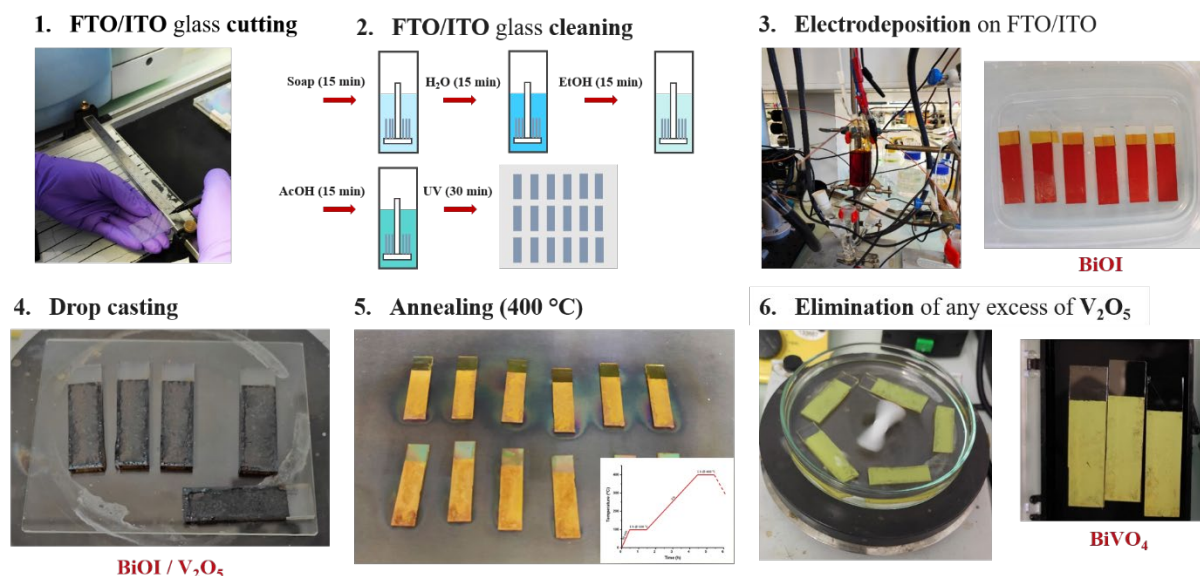


Figure 16. Fabrication of  $\text{BiVO}_4$  photoanodes by electrodeposition technique.

The initial stages, as in the sol-gel spin coating method, involve preparatory cutting and cleaning procedures.

The next step involves the electrodeposition of a variable amount of  $\text{BiOI}$  onto a  $4 \text{ cm}^2$  FTO or ITO glass substrate, with a working area restricted to  $3 \text{ cm}^2$  using thermal tape.

A conductive glass substrate (working electrode), a  $\text{Ag}/\text{AgCl}/3 \text{ M KCl}$  electrode (reference electrode), and a platinum wire (counter electrode) were immersed in the brown-red precursor solution<sup>136</sup> as detailed in Le *et al.*<sup>137</sup> and Kim *et al.*<sup>100</sup>.

A  $0.45 \text{ M}$  precursor solution was prepared by dissolving  $1.494 \text{ g}$  of  $\text{KI}$  in  $20 \text{ mL}$  deionized water. Then,  $0.388 \text{ g}$  of  $\text{Bi}(\text{NO}_3)_3 \cdot 5 \text{ H}_2\text{O}$  was added to the solution, creating an opaque red suspension with a concentration of  $0.04 \text{ M}$ . After  $5 \text{ min}$  in an ultrasonic bath,  $\text{HNO}_3 \text{ 1M}$  was added gradually to adjust the pH to  $1.7\text{-}1.8$ , leading to the transformation of the suspension into a clear red solution of  $\text{Bi}$  precursor.

Next, the electrolyte solution was completed with  $0.216 \text{ g}$  of  $p$ -benzoquinone (its (photo)electrochemical reduction favors the cross-linking of the film) dissolved in  $8 \text{ mL}$  of absolute ethanol, resulting in a reddish-brown electrolyte solution.

The conductive glass substrate was held at  $-0.1 \text{ V vs. Ag}/\text{AgCl}$  for  $10\text{-}15 \text{ minutes}$  in a standard three-electrode configuration, to achieve a total charge density of  $225 \text{ mC}\cdot\text{cm}^{-2}$ , to ensure a uniform film thickness and good performance for all samples. The process leads to the deposition of a bright red film of  $\text{BiOI}$  on the conductive substrate.

The electrodeposition time depends significantly on the sheet resistance of the chosen ITO or FTO glass substrate and on the desired charge density. The same electrodeposition process, in a standard three-electrode configuration cell, was adopted to synthesize 2D  $\text{BiOI}$  crystals via  $p$ -benzoquinone reduction, imposing a total charge density of  $150 \text{ mC}\cdot\text{cm}^{-2}$  and  $300 \text{ mC}\cdot\text{cm}^{-2}$  (Figure 17).

The notations  $\text{CoPi-BiVO}_4/\text{support}$  or  $\text{BiVO}_4/\text{substrate}$ , used in the manuscript, imply an imposed total charge density of  $225 \text{ mC}\cdot\text{cm}^{-2}$  (during the  $\text{BiOI}$  electrodeposition).



Before proceeding to the next step, the BiOI photoanode was rinsed with deionized water and dried with a stream of nitrogen.

Next, a dark green 0.5 M solution of 132.58 mg of VO(acac)<sub>2</sub> in 1 mL of dimethyl sulfoxide (DMSO) was dropped (120 μl for each electrode) on the surface of the electrodeposited BiOI film (drop casting technique).

The electrode was heated at ~ 60°C on a hot plate for 1-2 hours, until the solution has dried, to facilitate removal of most of the DMSO before annealing in a ceramic plate oven.

The thermal annealing process comprised four distinct steps: first, a 30-minute ramp from room temperature (RT) to 100°C to remove organics, followed by 60 minutes at 100°C; and a second 180-minute ramp from 100°C to 400°C to fully define the crystalline structure. Finally, a 60-minute heating run at 400°C was carried out to remove any excess VO(acac)<sub>2</sub>, in order to form a bright yellow film.

The BiVO<sub>4</sub> photoanode electrode was washed for 30 minutes in a NaOH solution, then rinsed with deionized water and dried under nitrogen.

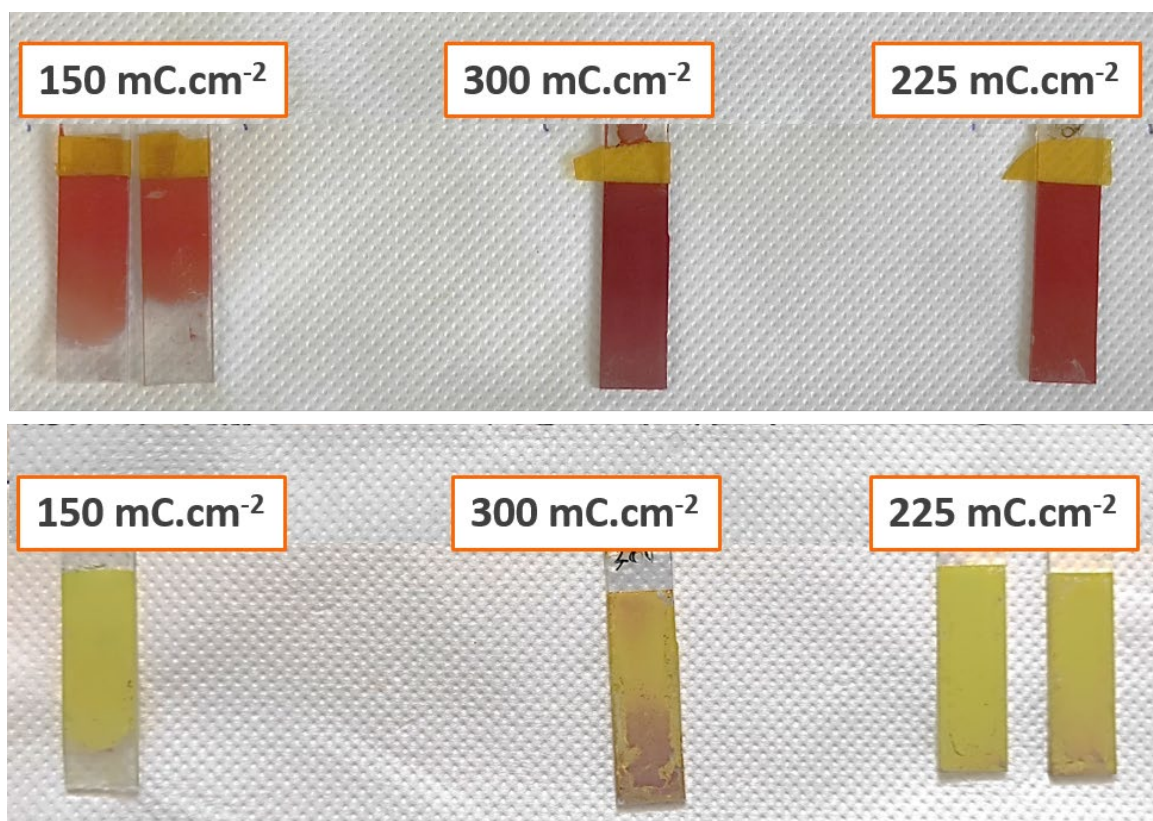


Figure 17. BiVO<sub>4</sub> and BiOI photoanodes made on FTO 80 by applying three distinct charge densities (150 mC.cm<sup>-2</sup>, 225 mC.cm<sup>-2</sup>, 300 mC.cm<sup>-2</sup>) across a 3 cm<sup>2</sup> electrode surface. Orange samples: BiOI photoanodes, yellow samples: BiVO<sub>4</sub> photoanodes.

**Remark:** In Figure 17, photoanodes having experienced an intermediate charge density (225 mC.cm<sup>-2</sup>) exhibit a visibly more uniform deposit both pre and post drop casting. Consequently, these (BiVO<sub>4</sub>) photoanodes were specifically chosen for the parametric experimental study.

To further improve photoelectrode performance, a CoPi cocatalyst<sup>71</sup> layer was introduced onto the BiVO<sub>4</sub> layer using a photo-assisted electrodeposition technique adapted from Hamd *et al.*<sup>138</sup> and Liu *et al.*<sup>139</sup>. This process took place in a three-electrode setup, where a Pt wire served as counter-electrode, a Ag/AgCl/3 M KCl electrode as reference electrode and a BiVO<sub>4</sub> photoanode as working electrode. Photoelectrodeposition took place at 0.4 V versus Ag/AgCl for a duration of at least 40 minutes, depending on the mC.cm<sup>-2</sup> passing through the electrode.

The electrolyte solution contains  $0.5 \text{ mmol.L}^{-1} \text{ Co(NO}_3)_2 \times 6\text{H}_2\text{O}$  in a sodium phosphate buffer (KPi 0.1 M) at pH 7. In order to refine the structural aspects and properties of the photoanodes, a series of photo-assisted electrodepositions of CoPi was undertaken (Figure 26a). Varying the imposed charge  $q$  between 0.7 C and 1.5 C, over a working area of  $3 \text{ cm}^2$ , several electrodes were prepared. With these, it was possible to increase the concentration of catalyst on the photoanode, performing various linear sweep voltammeteries (LSVs), shown in Figure 18, which allowed the definition of the optimum charge density ( $0.42 \text{ C.cm}^{-2}$ ) required to obtain an efficient electrode. The optimum charge density value was then imposed to synthesize all the CoPi-BiVO<sub>4</sub> electrodes used for the characterization study.

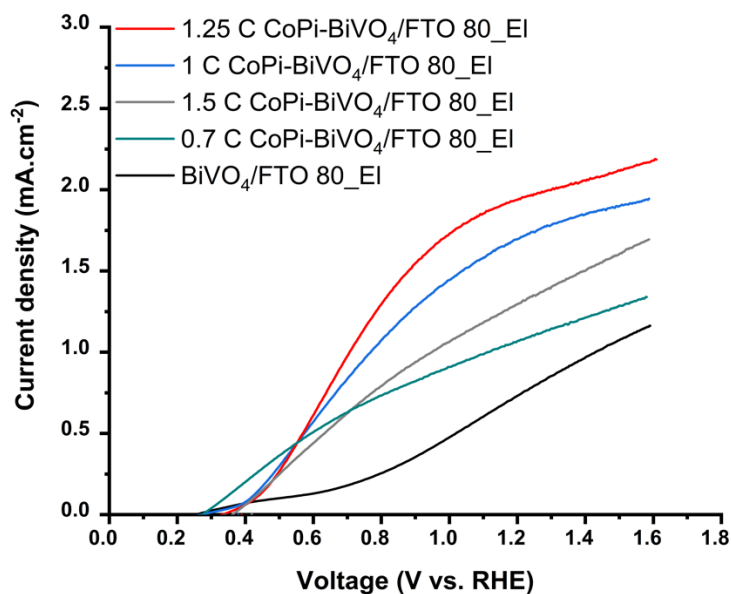


Figure 18. LSV scans to evaluate the optimal charge density in 1M KPi electrolyte (pH 7) under AM1.5G back illumination (BI). BiVO<sub>4</sub>/FTO 80 (black line), 0.7C CoPi-BiVO<sub>4</sub>/FTO 80 (bluegreen line), 1C CoPi-BiVO<sub>4</sub>/FTO 80 (blue line), 1.25 C CoPi-BiVO<sub>4</sub>/FTO 80 (red line, optimal charge), 1.5C CoPi-BiVO<sub>4</sub>/FTO 80 (grey line). Electrode surface:  $3 \text{ cm}^2$ , illuminated area:  $0.46 \text{ cm}^2$ .

## 2.3 Macroscopic and Microscopic Characterization

The characterization of photoanodes is based first on the measurement of their intrinsic properties. The following techniques were used: scanning electron microscopy (SEM), X-ray diffraction, and profilometry.

### 2.3.1 Scanning Electron Microscopy

A Scanning Electron Microscope (Zeiss Ultra 55) was used to characterize the BiVO<sub>4</sub> photoanodes made on various conductive glass supports, with or without catalysts and dopants. SEM analysis provided information on the surface morphology and thickness of layered samples. The SEM images were recorded at an accelerating voltage of 5 keV or 10 keV, and the working distance was set between 5 and 7 mm. Small pieces of samples were glued to an aluminium SEM holder using double-sided conductive carbon tape (Figure 19a). A holder SEM inclined at 90 degree was used to measure the cross-sectional thickness of the samples (Figure 19b). A comparative analysis was carried out between these SEM measurements and those obtained by profilometry detailed in Sec. 2.3.3.

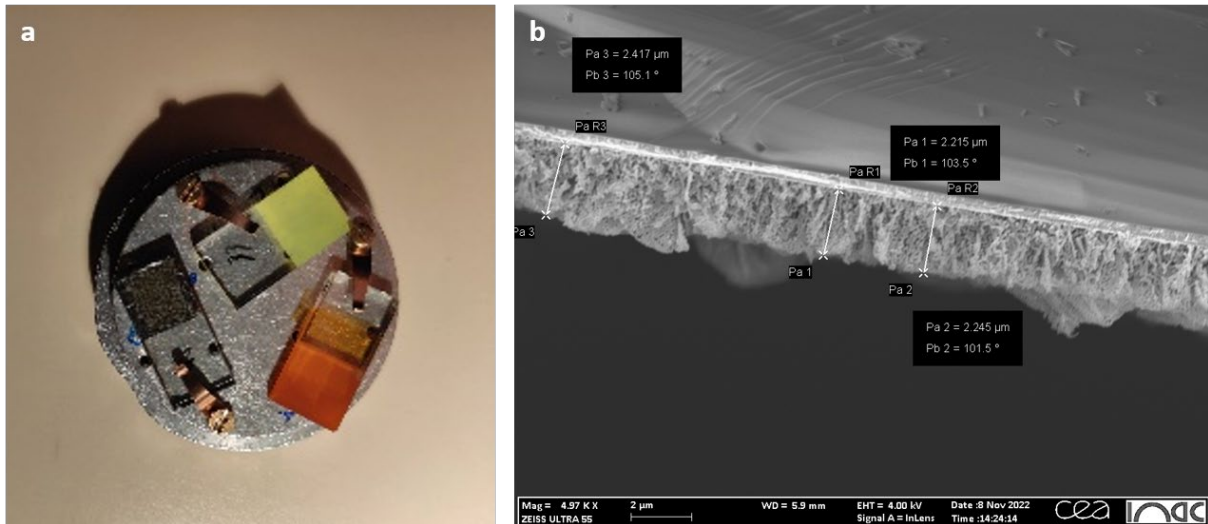


Figure 19. SEM measurements. a) small samples of BiOI, BiOI + V<sub>2</sub>O<sub>5</sub>, BiVO<sub>4</sub> electrodes. b) Example of thickness measurements on 3D images.

### 2.3.2 X-ray diffraction

X-ray diffraction (XRD) characterizations were performed using an Empyrean Panalytical diffractometer (Figure 20), equipped with an X-ray tube having a Cobalt anode ( $\lambda_{K\alpha_1} = 1.789 \text{ \AA}$ )<sup>140</sup> for which  $K_{\alpha}$  radiation prevents fluorescence for samples containing iron and cobalt. The equipment includes two detectors: a 2D Pixcel detector (255 x 255 pixels, 55 μm pixel size) and a proportional point detector. The Pixcel detector can operate in 0D, 1D, or 2D modes.

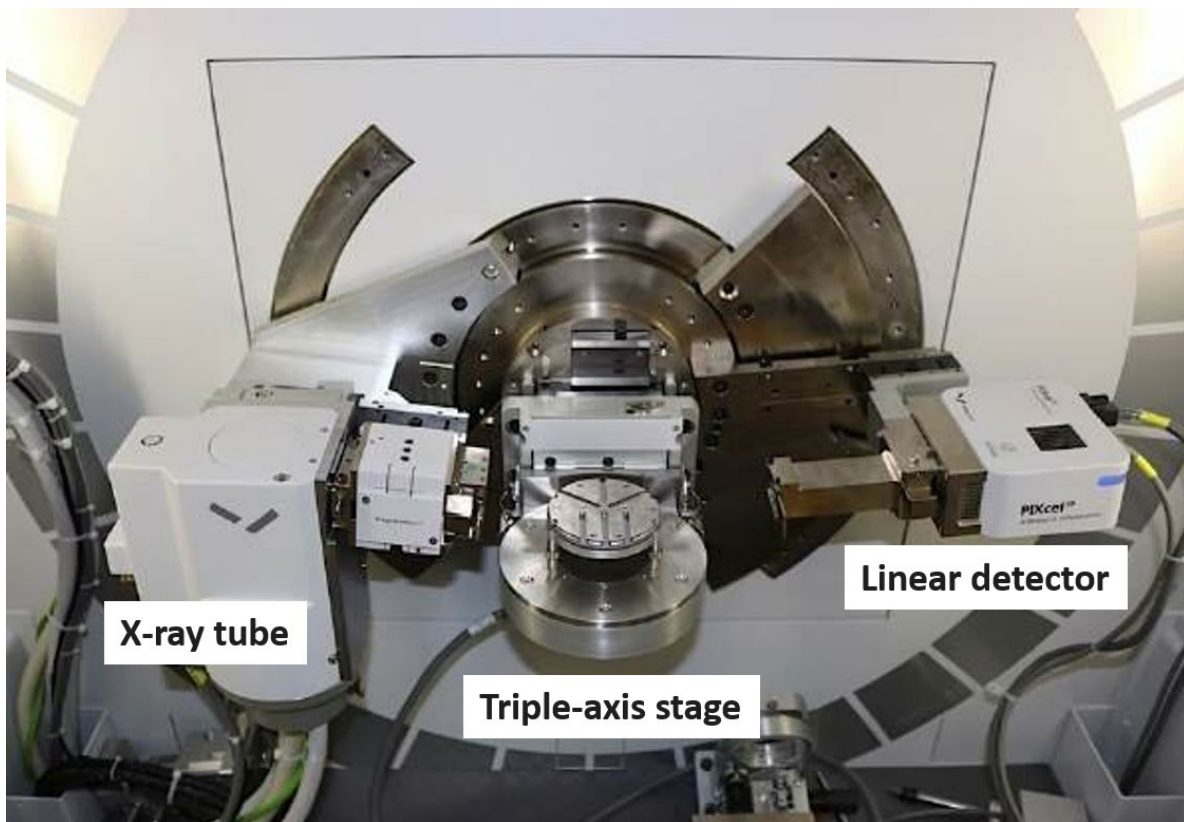


Figure 20. Thin Film Diffractometer (Panalytical Empyrean)



Several samples of BiVO<sub>4</sub> photoanodes were analyzed to confirm the crystallographic structure obtained.

Before starting XRD measurements, it is necessary to control the alignment of the detector. To do so, the Pixcel detector was set in a 0D mode configuration (Receiving Slid-3pixel).

The alignment sequence is the following:

1.  $2\theta$  (range 0.3 mm, step size 0.005 mm), scan without sample
2. Z: starting from 10.4 mm (range 0.4 mm, step size 0.01 mm, time per step 0.5 s)
3.  $\omega$  (range 1 mm – 1.5 mm, step size 0.04 mm)
4. Final Z

During the thin film alignment operation, the incident beam passes through a reception slit of  $1/32^\circ$ ; moreover, a beam attenuator ( $1/84^\circ$ ) is active.

Following this 1<sup>st</sup> step, the photoanode characterization study can be initiated and measurements can be carried out in diverging, parallel, or mixed configurations.

For this study, a parallel geometry configuration was chosen: the equipment integrates a *Goebel* parabolic *mirror* within the primary optics to ensure a parallel beam. The incident beam passes through a  $1/4^\circ$  divergent slit, then through 4 mm and 10 mm masks.

Then, the diffracted beam passes through a 8 mm anti-scattering slit. No attenuator was used after alignment, but a long plate collimator (0.04 rad Soller slit) and a large  $K\beta$  filter are essential at this stage. The Pixcel detector (255 Pixel) was used in 1D mode (line detector 1D).

XRD patterns (Figure 21) are valuable indicators of crystalline phase obtained, and also of particle size and defects, while relative peak intensities provide insights into the atomic distribution within the unit cell.

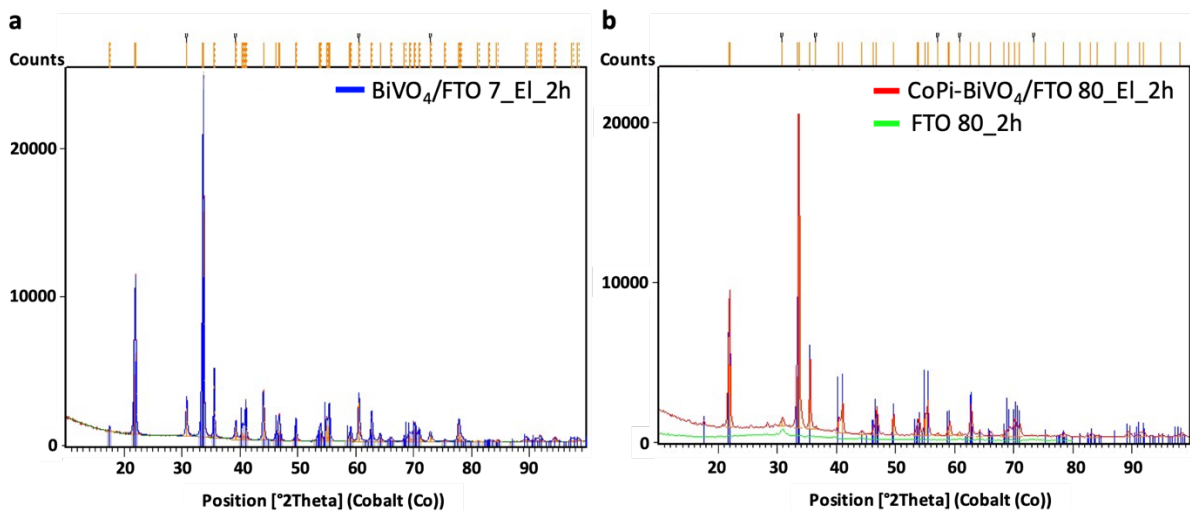


Figure 21. Crystal phase identification from the XRD patterns a) XRD pattern of BiVO<sub>4</sub>/FTO 7 photoanode. b) XRD patterns of BiVO<sub>4</sub>/FTO 7 photoanode (red line) and FTO 80 coated glass (green line). The continuous blue line marks the peak position expected for this kind of materials.

To analyze the obtained XRD patterns, qualitative evaluations were performed using HighScore Plus, a specialized crystallographic software for phase identification, semi-quantitative phase analysis, pattern treatment, and profile fitting, in conjunction with a reference Material File structure database.

More details concerning the XRD measurements are in Appendix 5.8.

### 2.3.3 Profilometry

A Dektak® 150 profilometer<sup>141</sup> was used to characterize the structure of the photoanodes.

This device (in the standard 2-D Dektak 150 configuration) controls the heights of both thin and thick films  $t$ , it is capable of measuring steps of less than  $100\text{\AA}$ , and measures samples up to  $15.24\text{ cm}$  in size and  $10.16\text{ cm}$  in thickness.

The Dektak 150 can profile surface topography and waviness.

Measurements can be carried out over a one or more scans (Figure 22) for more precise results and to study layer homogeneity.

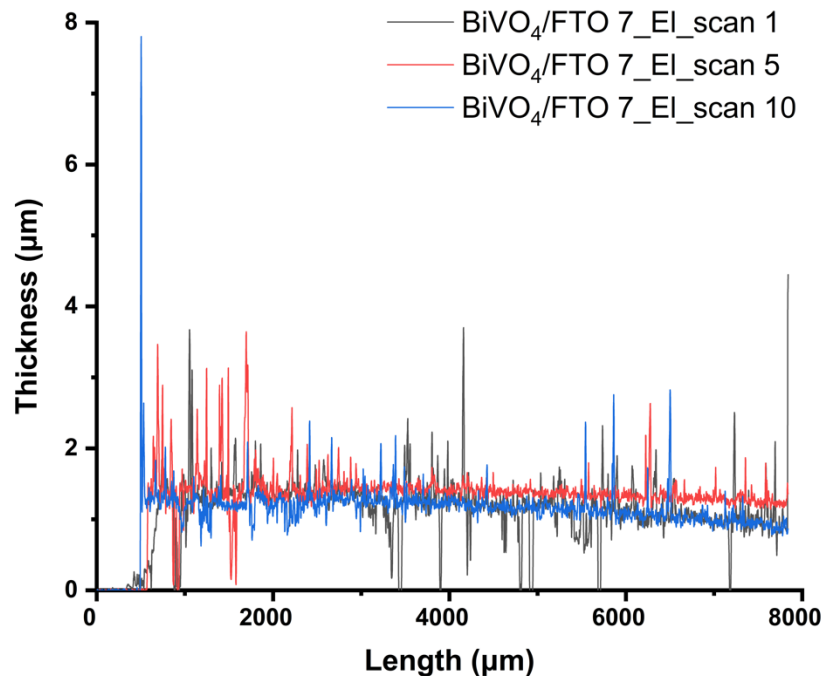


Figure 22. Profilometer measurements of a  $\text{BiVO}_4$  layer deposited on a FTO 7 coated glass. Scan 1 (black line), Scan 5 (red line), Scan 10 (blue line). Scan positions are shown in Figure 14a.

The sample is fixed (under vacuum) on the stage. An initial calibration is performed to identify the position (X/Y and theta) of the electrode. The scan routine begins next with the setting of individual scan parameters such as scan length (up to  $8000\text{ }\mu\text{m}$ ) and scan speed ( $100\text{ }\mu\text{m}\cdot\text{s}^{-1}$ ), sampling rate (100 Hz), leveling (an automatic method allows the system to quickly and automatically level the profile trace), stylus force (3 mg), contact speed (3), range/resolution ( $131\text{ }\mu\text{m}/0.357\text{ A}$ ), profile type (Hills&Valleys) etc.

In addition, it is important to set the X/Y and theta position for each scan (Figure 14a) in each program file.

The Dektak 150 profilometer follows an electromechanical process (Figure 23) in which the sample is moved beneath a diamond-tipped stylus. A high-precision stage controls the sample's movement according to user-defined parameters. The stylus is mechanically connected to a Linear Variable Differential Transformer (LVDT).

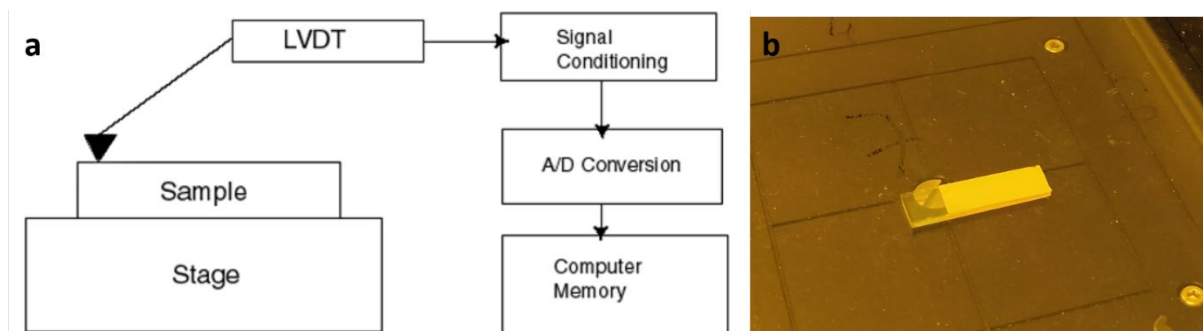


Figure 23. Dektak® 150 profilometer. a) Block Diagram of the Dektak 150 Architecture describing instrument operation. b) BiVO<sub>4</sub> sample positioned on the stage.

As the stage moves the sample, the stylus glides over its surface, generating electrical signals that reflect the movement of the stylus as the position of the LVDT core shifts. The LVDT produces an AC signal proportional to the change in position, which is then converted into a digital format displayed on the computer. Before recording thickness results, it necessary to automatically reposition the profile trace and establish the zero point (point of reference) moving the reference **R** cursor and the measurement **M** cursor that define the portion of the profile trace for leveling or performing analytical functions.

## 2.4 Optical Characterizations

Among the considered properties of use, a particular attention was paid to the optical properties of the photoanode and its components. Indeed, the absorption, scattering and reflection of incident light depend on the microstructure, and have a major influence on the efficiency of the photoanodes. The results of the optical characterizations also served as a basis and/or validation case for the numerical study carried out in Sec. 3.2 and 3.3.

*Reflectance* and *Transmittance* characterizations were carried out on all types of fabricated photoanodes, to determine their optical properties as a function of the wavelength, to quantify reflection and transmission losses, and to assess the effect of electrode heterogeneity.

Measurements were carried out using a *Perkin Elmer Lambda 950* spectrophotometer in the ultraviolet, visible, and near-infrared (UV/Vis/NIR), with an integrating sphere that provides accurate results for the optical properties of thin-film photoanodes.

This spectrophotometer consists of 2 lamps, a deuterium lamp (250-319.2 nm) and a tungsten lamp (319.2-2500 nm), which take turns to measure over a wide wavelength range. Depending on the wavelength produced, the optical filter is positioned before the radiation enters the 2 monochromators. Duex detector: a photomultiplier (250-860.8 nm) and an InGaAs detector (860.8-2500 nm) are placed in an integrating sphere (see SI). Detector changeover is automatic as the monochromators are rotated.

The function of the integrating sphere (Figure 24) is to spatially integrate the radiation flux. Several arrangements are possible for measuring diffuse reflection, specular reflection or light transmission. Specular reflection is the portion of light reflected by the surface, assumed to be perfectly flat, while diffuse reflection is the portion of light reflected by the surface's asperities.

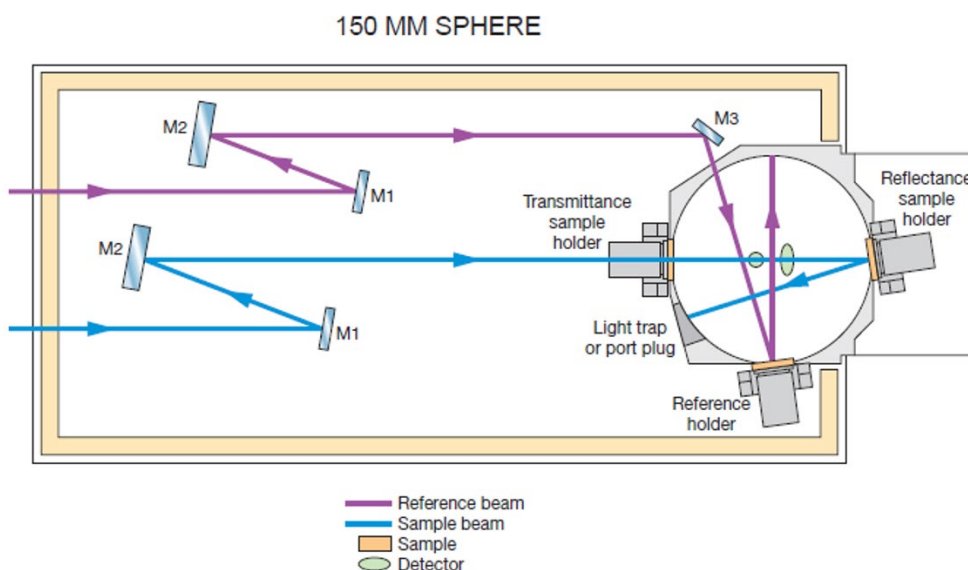


Figure 24: Optical design of 150 mm integrating sphere. The reference beam is used to correct temporal intensity fluctuations in the measurements. For reflectance

and transmittance measurements the BiVO<sub>4</sub> layer is the first layer to receive the light (FI).

To quantify the total reflected and transmitted light, absolute transmittance  $T\%$  and absolute reflectance  $R\%$  spectra are obtained from spectral measurements of the sample under study and a reference. The absorbance  $A\%$  is then deduced using the following relation:

$$A\% = 100 - R\% - T\% \quad \text{Eq. 12}$$

Reflectance and transmittance measurements were made between 300 and 800 nm.

For reflectance measurements, a monochromatic beam is directed onto the electrode to be measured. The sample is placed in an integrating sphere (angle of incidence of 90°), so that the radiation reflected by the electrode (with the BiVO<sub>4</sub> layer facing the internal part of the sphere) in all directions is reflected from the walls and ultimately received by the detectors.

For transmittance measurements, the sample (angle of incidence of 8°) receives the monochromatic beam directly, while the BiVO<sub>4</sub> layer is not positioned facing the internal part of the integrating sphere, but is the first layer to receive the light.

A reference measurement (spectralon white) is necessary for the calculation of  $R_{photoanode}$ , made immediately before the sample measurement.

The spectral hemispherical transmittance and global hemispherical reflectance of the KPi **electrolytic solution** (pH 7) were measured using a *Perkin Elmer Lambda 950 UV/Vis/NIR* spectrophotometer with a step of 5 nm ( $\lambda = 280 \text{ nm}-2500 \text{ nm}$ ), equipped with a 150 mm diameter Spectralon®-coated integrating sphere. Results are expressed in relation to the solar transmittance  $\tau_s$  and the solar reflectance  $\rho_s$ . (Eq. 13, Eq. 14, Eq. 15).

$$\tau_s = \frac{\int_{280}^{2500} t(\lambda) \cdot S_n(\lambda) \cdot d\lambda}{\int_{280}^{2500} S_n(\lambda) \cdot d\lambda} \quad \text{Eq. 13}$$

$$\rho_s = \frac{\int_{280}^{2500} \rho(\lambda) \cdot S_n(\lambda) \cdot d\lambda}{\int_{280}^{2500} S_n(\lambda) \cdot d\lambda} \quad \text{Eq. 14}$$

$$\alpha_s = 1 - \tau_s - \rho_s \quad \text{Eq. 15}$$

$t(\lambda)$  et  $\rho(\lambda)$  are the total transmittance and reflectance at the wavelength  $\lambda$ ,  $S_n(\lambda)$  is the solar irradiance at the wavelength  $\lambda$ .

The semiconductors optical properties are linked to the characteristics of the electronic bands and to the atomic structure of the materials, in particular the atoms and chemical bonding.

The band gaps of the BiVO<sub>4</sub> electrodes made on the three considered substrates (FTO 7, FTO 80, ITO 12), were calculated by Eq. 16 as follows:

$$(\alpha h\nu)^n = A \times (h\nu - E_g) \quad \text{Eq. 16}$$

where  $\alpha$  is the absorption coefficient,  $h$  the Planck constant,  $\nu$  the frequency of light,  $A$  is an energy-independent constant,  $E_g$  the band gap energy, and  $n$  indicates the nature of the transition.<sup>30</sup> For direct bandgap energy  $n = 2$ , for indirect bandgap energy  $n = 0.5$ .

These relations can be used to estimate direct and indirect bandgaps of BiVO<sub>4</sub> in the photoanodes, using the Tauc Plot<sup>142</sup> method (Figure 25).

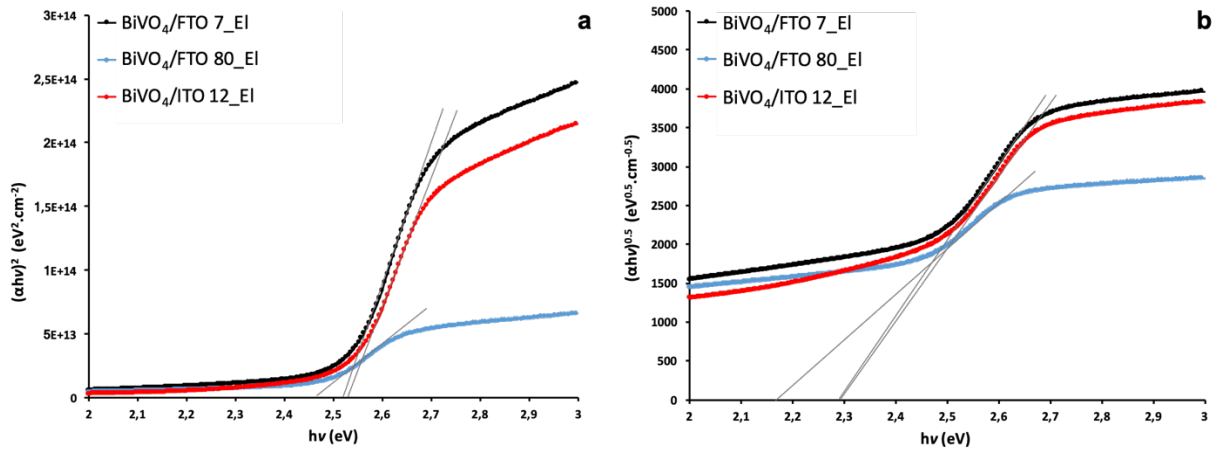


Figure 25. Tauc's plots of BiVO<sub>4</sub> photoanodes for a) direct and b) indirect bandgaps. BiVO<sub>4</sub>/FTO 7 (black line), BiVO<sub>4</sub>/FTO 80 (blue line), BiVO<sub>4</sub>/ITO 12 (red line).

In the Tauc plot, the photon energy  $h\nu$  in  $eV$  is plotted on the  $x$ -axis, and  $(\alpha h\nu)^n$  in  $eV^n.cm^n$  on the  $y$ -axis. By extrapolating the linear part of the curve into a line that intersects the  $x$ -axis at the material's optical band-gap energy value.

It can be assumed that the bandgap of BiVO<sub>4</sub> semiconductor is indirect because the graph  $(\alpha h\nu)^2$  vs  $h\nu$  shows a bandgap value higher than the one reported in the State of the Art (2.3 - 2.4 eV).

Additionally, the graph  $(\alpha h\nu)^{0.5}$  vs  $h\nu$  shows a slower increase in absorption at the bandgap energy, confirming an indirect bandgap of  $\sim 2.3$  eV.

## 2.5 Photoelectrochemical Characterizations

At last, the photocurrent achieved under 1 sun irradiation was measured for each specimen of BiVO<sub>4</sub>.

Several measurement campaigns were carried out to evaluate the performance of the BiVO<sub>4</sub> photoanodes, depending on the elaboration process (electrodeposition and spin coating) and the conductive substrate used (three substrates of different thicknesses and conductivities). The improvement provided by the addition of molybdenum and CoPi catalyst in/on the BiVO<sub>4</sub> layer was also studied (Figure 26).

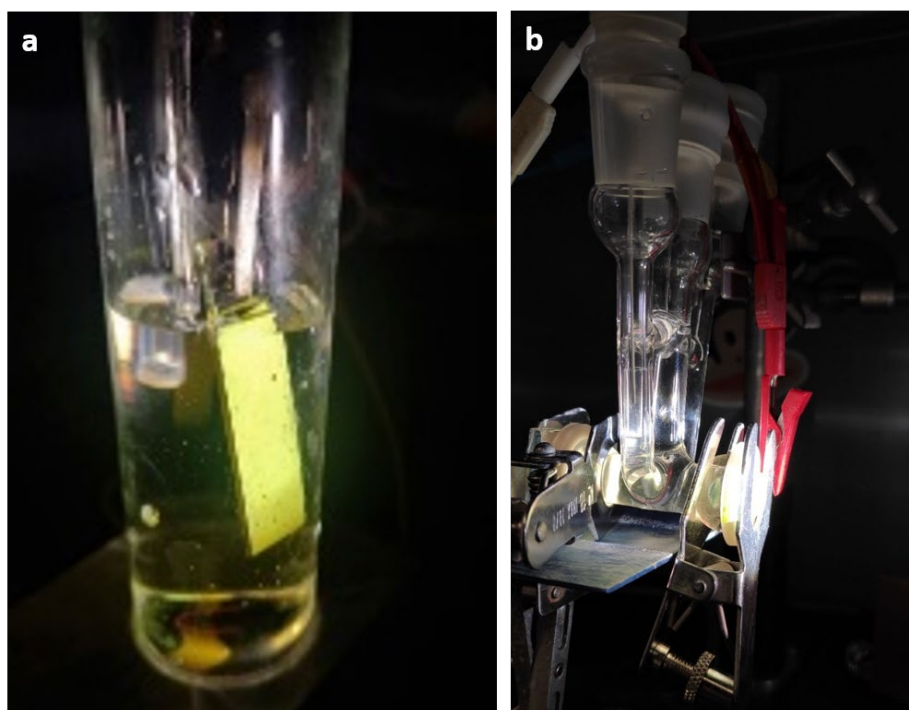


Figure 26. BiVO<sub>4</sub> photoanodes. a) Photo-assisted electrodeposition of CoPi catalyst on a 3 cm<sup>2</sup> BiVO<sub>4</sub> photoanode, in 0.1M KPi electrolyte (pH 7) under AM1.5G front illumination (FI). b) Photocurrent measurement with a standard three-electrode cell: Ag/AgCl (reference electrode), Pt wire (counter electrode), Mo:BiVO<sub>4</sub> photoanode (working electrode), in 1M KPi electrolyte (pH 7), under AM1.5G, BI and inert gas bubbling.

All the experiments were carried out at pH 7 and in the presence of 1M KPi electrolyte solution (see detailed protocol in Appendix 5.4).

Then, hole scavengers<sup>143,144</sup> such as H<sub>2</sub>O<sub>2</sub> and N<sub>2</sub>SO<sub>3</sub> were introduced in the pH 7 electrolytic solution to evaluate the maximum photocurrent that a photoanode can achieve (with negligible charge recombination), and to predict the expected photocurrent quantified after the addition of a catalyst to the BiVO<sub>4</sub> photoanode. Hence, the use of a sacrificial agent permits investigations of the photoelectrochemical properties of the BiVO<sub>4</sub> electrodes without complications from slow surface reactions and surface recombination



**Set-up:** All (photo)electrochemical measurements were carried out using a SP-300 potentiostat (Biologic), controlled by EC-Lab software, using in a standard three-electrode setup (Figure 27, Appendix 5.3 and 5.4). The measurements were performed in a back-illumination (BI) configuration: the glass was the first layer positioned facing the light, subsequently, the ITO (or FTO) and the BiVO<sub>4</sub> layer were back-illuminated. The reverse configuration is designed as front illumination (FI).

Note that for the two-electrode configuration used for the electrochemical measurements made in Chapter 3 and 4, counter electrode and the reference electrode are connected to each other.

Several LSVs were performed by varying the concentration of H<sub>2</sub>O<sub>2</sub>: 0 – 20 – 40 – 80 – 120 mmol.L<sup>-1</sup> in KPi 0.1 mol.L<sup>-1</sup> (see Appendix 5.6), or by adding 0.1 M of Na<sub>2</sub>SO<sub>3</sub> in KPi 0.5M (See Sec. 2.6). Among the two hole scavengers, sodium sulfite was chosen for the photoanode characterization study due to the better current-voltage behavior; H<sub>2</sub>O<sub>2</sub> shows almost the same magnitude of anodic photocurrent as Na<sub>2</sub>SO<sub>3</sub> but much larger and therefore less suitable cathodic and anodic dark current.<sup>145</sup>

Three operating modes were used, always following the same test sequence: “chop” mode, “dark” mode, and “light” mode, with a scanning speed of 10 mV.s<sup>-1</sup> and a potential varying between -0.5 and 1 V vs Ag/AgCl reference electrode Figure 27. The order of measurements was always the same.

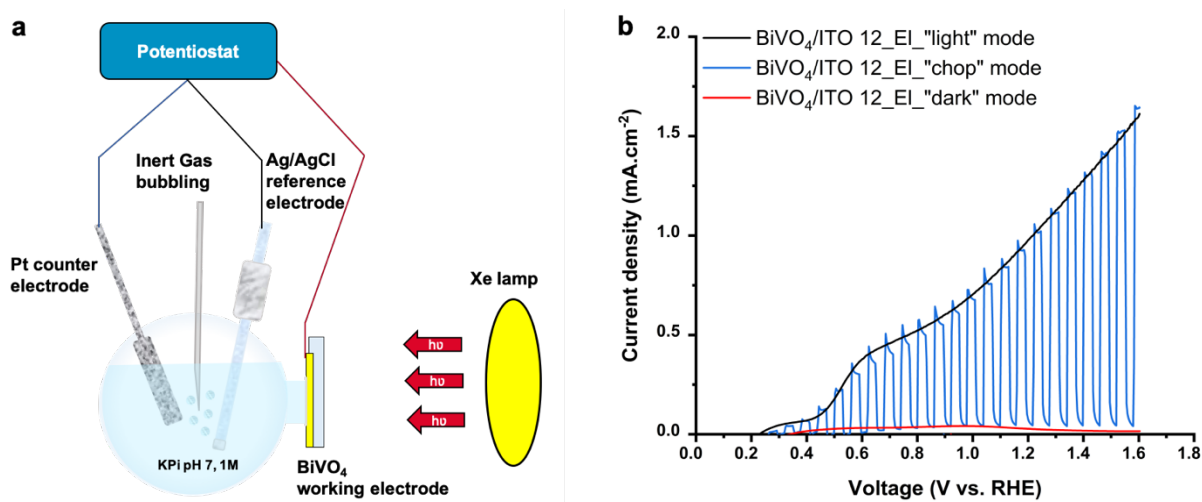


Figure 27. Photoelectrochemical Set-up and measurements. a) Detailed scheme of a three electrodes configuration cell (Ag/AgCl reference electrode, Pt counter electrode and BiVO<sub>4</sub> working electrode) together with a Xenon arc lamp (AM 1.5G filter), BI configuration. b) Linear sweep voltammograms of BiVO<sub>4</sub>/ITO 12 (illuminated surface: 0.46 cm<sup>2</sup>), recorded at 10 mV.s<sup>-1</sup> in 1M KPi electrolyte (pH 7) under AM1.5G BI. The blue line corresponds to “chop” mode, the red line to “dark” mode, and the black line to “light” mode.

The **light source** used in all the photoelectrochemical analysis was a Xenon arc lamp (Oriel 67001), precision-tuned to 280 W. To better simulate sunlight, a 1.5 global air mass filter (AM1.5G) was used. Light intensity was then calibrated, by defocusing the light beam, to 100 mW.cm<sup>-2</sup> (equivalent to 1 sun) using a photodiode. All components were purchased from Newport Corporation.

## 2.6 Results and discussion

The influence of the TCO on the photocurrent delivered by the n-type BiVO<sub>4</sub> semiconductor is illustrated in Figure 28. The three specimens were produced by electrodeposition.

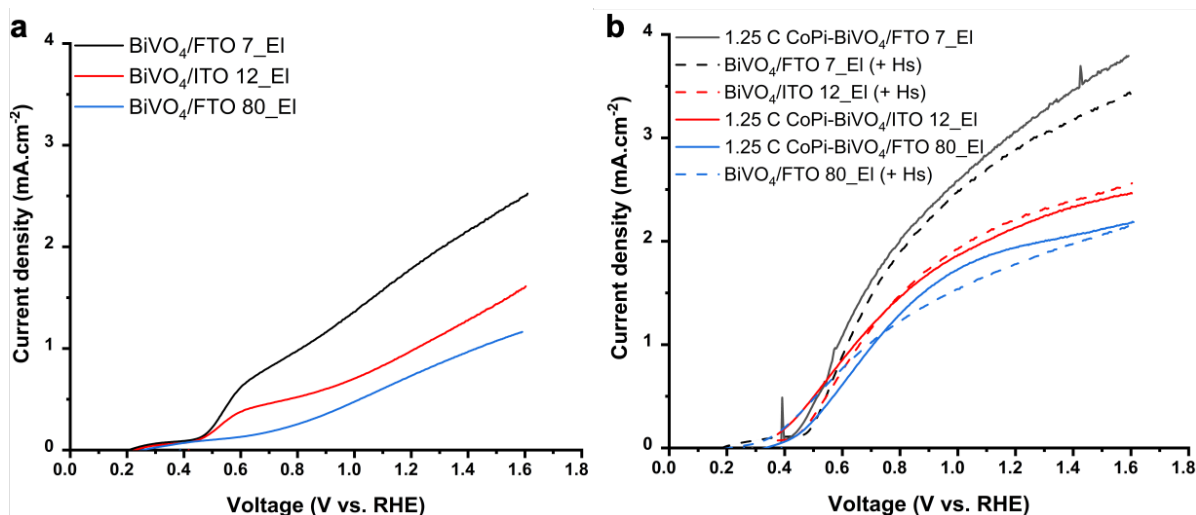


Figure 28. Photoelectrochemical assessment of 3 cm<sup>2</sup> BiVO<sub>4</sub> photoanodes made by electrodeposition (illuminated surface: 0.46 cm<sup>2</sup>). a) LSV scans for BiVO<sub>4</sub>/FTO 80 (blue line), BiVO<sub>4</sub>/ITO 12 (red line), BiVO<sub>4</sub>/FTO 7 (black line) in 1M KPi electrolyte (pH 7), under AM1.5G, BI. b) LSV scans for CoPi-BiVO<sub>4</sub>/FTO 80 (solid blue line), CoPi-BiVO<sub>4</sub>/ITO 12 (solid red line), CoPi-BiVO<sub>4</sub>/FTO 7 (solid black line) in 1M KPi electrolyte (pH 7), under AM1.5G, BI. LSV scans for BiVO<sub>4</sub>/FTO 80 with hole scavenger (dashed blue line), BiVO<sub>4</sub>/ITO 12 with hole scavenger (dashed red line), BiVO<sub>4</sub>/FTO 7 with hole scavenger (dashed black line) in KPi 0.5M, under AM1.5G, BI. Hole scavenger (Hs): Na<sub>2</sub>SO<sub>3</sub> 0.1 M.

Comparing the three samples: BiVO<sub>4</sub>/FTO 7, BiVO<sub>4</sub>/ITO 12, and BiVO<sub>4</sub>/FTO 80, show that **the BiVO<sub>4</sub> electrode made on the most conductive support, FTO 7, featuring the highest photocurrent value**, whether without (Figure 28a) or adding a CoPi catalyst or in a hole scavenger solution (Figure 28b). The photocurrent is strongly connected to the sheet resistance of the support (7 Ω.sq<sup>-1</sup> in the case of FTO 7), which is lower than for other supports (12 Ω.sq<sup>-1</sup> and 80 Ω.sq<sup>-1</sup> for ITO 12 and FTO 80 respectively). This higher conductivity, already observed to favour the electrodeposition synthesis method, hence also results in higher photoelectrochemical activity.

The addition of a *sacrificial agent* (0.1 M Na<sub>2</sub>SO<sub>3</sub> in 0.5 M KPi) increases the photocurrent promoting rapid oxidation (versus a slower catalytic process) by photogenerated holes at the surface of the BiVO<sub>4</sub> photoanode, and simultaneously reducing photodegradation. In the three series of dashed lines illustrated in Figure 28b, the use of Na<sub>2</sub>SO<sub>3</sub> as a hole scavenger represents the photocurrent activity of an efficient CoPi-BiVO<sub>4</sub> electrode (CoPi charge density = 0.42 C.cm<sup>-2</sup>).

**The *catalyst* plays an important role in optimizing the performance of photoanodes** by increasing the reaction rate (decreasing the activation energy and stabilizing the transition state) and improving charge separation.

This makes the photoelectrochemical processes more energetically favorable. The catalyst affects the kinetics of a reaction, without being consumed in it, but not the thermodynamics. It also increases not only the photocurrent, but also the PEC long-term stability and selectivity (reducing the presence of impurities in the final product).

The results presented in Figure 28b demonstrate that the catalyst effectively mitigates charge recombination, leading to a notable increase in the obtained photocurrent values compared to the results in Figure 28a.

In this case, the highest photocurrent was claimed to be 3.12 mA.cm<sup>-2</sup> at 1.23 V (vs. RHE) on the nanoporous CoPi-BiVO<sub>4</sub>/FTO 7\_EI photoanode (black line in Figure 28b).



All the photocurrents measured at 1.23V vs RHE are highlighted (grey lines) in the following Table 5.

Table 5. Photocurrent measurements

Sample	$J_{ph}$ @ 1.23 V vs. RHE (mA.cm <sup>-2</sup> )	
	In KPi 1 M	In 0.1 M Na <sub>2</sub> SO <sub>3</sub> in KPi 0.5M
CoPi-BiVO <sub>4</sub> /FTO 7_EI	3.12	-
BiVO <sub>4</sub> /FTO 7_EI	1.86	2.94
2.5 % Mo:BiVO <sub>4</sub> /FTO 7_Sc	0.63	0.84
1.25 % Mo:BiVO <sub>4</sub> /FTO 7_Sc	0.77	0.86
BiVO <sub>4</sub> /FTO7_Sc	0.38	0.56
CoPi-BiVO <sub>4</sub> /FTO 80_EI	1.96	-
BiVO <sub>4</sub> /FTO 80_EI	0.77	1.81
CoPI-BiVO <sub>4</sub> /ITO 12_EI	2.18	-
BiVO <sub>4</sub> /ITO 12_EI	1.02	2.38

As XRD analyses have confirmed a monoclinic clinobisvanite structure on all photoanodes, which is the most favorable crystal structure for increasing the catalytic activity in photoelectrochemical applications.<sup>146</sup> Here, the discussion will primarily center on the difference between the results obtained from various samples based on their different thicknesses and microstructures.

The activity of the BiVO<sub>4</sub> photoanode is limited by the absorption range of incident light, charge separation and diffusion, and the availability of holes for OER catalysis. To overcome these limitations, bulk properties are generally modulated through the introduction of a *dopant into the lattice*. In this work, the doping of BiVO<sub>4</sub> with molybdenum (Mo) facilitates the creation of oxygen vacancies<sup>147</sup> and the introduction of monovalent defects or charge trap states, primarily influencing charge diffusion and recombination mechanisms. The dopant acts as electron traps<sup>148</sup> (for the photo-excited electrons), preventing photoinduced charge recombination in order to encourage the oxidation process required in heterogeneous catalysis where the holes are transferred to the surface.

The optimal amount of monovalent defects or electron (or hole) trap states depends on the doping percentage. Figure 29a shows a comparison between three different electrodes fabricated by spin coating, varying the quantity of doped agents (0%, 1.25% Mo, 2.5% Mo vs V), where Mo is added to the BiVO<sub>4</sub> film during a sol-gel synthesis (see Sec. 2.2). The optimal Mo percentage, i.e. giving the highest photocurrent, is 1.25% (Figure 29).

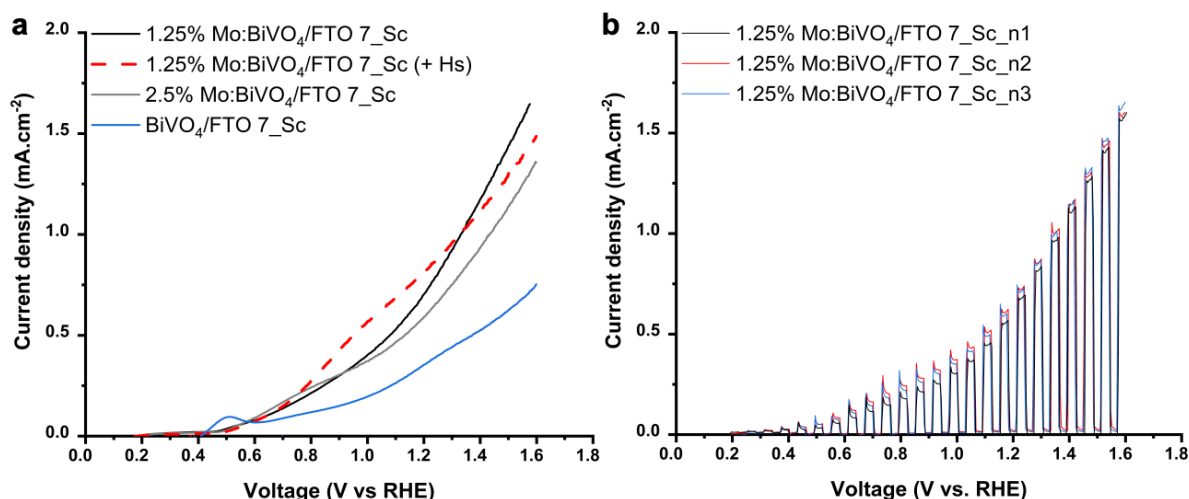


Figure 29. Photoelectrochemical characterization of BiVO<sub>4</sub> photoanodes made by sol-gel spin coating. a) BiVO<sub>4</sub>/FTO 7 (blue line), 1.25% Mo:BiVO<sub>4</sub>/FTO 7 (black line), 2.50% Mo:BiVO<sub>4</sub>/FTO 7 (grey line), 1.25% Mo:BiVO<sub>4</sub>/FTO 7 in hole scavenger solution (dashed red line). b) Repeatability of the photoelectrochemical measurements: current density, measured in chop light modes, of three 1.25% Mo:BiVO<sub>4</sub>/FTO 7 electrodes, made with the same process. The repeatability of performances have been verified for all the samples treated.

A higher concentration of Mo (2.5% vs V) shows lower charge separation efficiency, resulting in reduced PEC activity. As molybdenum serves as charge recombination sites, this may be attributed to an inhomogeneous distribution of Mo ions in the lattice or an excessive doping metal content that tends to occupy space charge, thus could interact negatively with the penetration depth of light rays into BiVO<sub>4</sub>.<sup>149</sup>

The graphs reported in Figure 29 show that **the best photoelectrochemical results are obtained by adding molybdenum in the BiVO<sub>4</sub> sol-gel solution** to prepare doped photoelectrodes. This is connected with the diffusion coefficient and the electron diffusion length (equal to 10 nm for undoped BiVO<sub>4</sub> photoanodes) that increase in presence of Mo in the material. Seabold et al. state that Mo doping improves the diffusion coefficient by four times and increases the electron diffusion length to 300 nm, which, in this case, is also the optimal thickness of the empirically determined Mo:BiVO<sub>4</sub> film with a charge separation efficiency of 90% and an absorbed photon-to-current efficiency (APCE) of 80%.<sup>117</sup>

In photoelectrochemical tests with doped (2.5% and 1.25% Mo) BiVO<sub>4</sub> electrodes, it was observed that, in the presence of a *hole scavenger*, the maximum photogenerated current at 1.23 V vs. RHE is 0.86 mA.cm<sup>-2</sup>. Meanwhile, without a hole scavenger,  $J_{ph}$  for 1.25% Mo:BiVO<sub>4</sub>/FTO 7 and for 2.5% Mo:BiVO<sub>4</sub>/FTO 7, in electrolytic solution without hole scavenger, are 0.77 and 0.635 mA.cm<sup>-2</sup>, respectively. These results suggest that **additional modifications to the surface of the photoanode**, such as variations in texture thickness and roughness, **can contribute to achieving better photocurrent results**, converging toward the 0.86 mA.cm<sup>-2</sup> measured in the presence of the hole scavenger.

**The performance of photoanodes fabricated by electrodeposition consistently exceeds that of photoanodes produced by spin coating** (Table 5). The two processes differ mainly in the structural characteristics of the BiVO<sub>4</sub> film, notably the thickness and roughness as well as the homogeneity of the layer (see Sec. 2.2.2)

These discrepancies are illustrated by the SEM pictures (Figure 30) of three samples selected to discuss the impact of structural characteristics on photoelectrochemical processes:

- BiVO<sub>4</sub>/FTO 7 made by electrodeposition (BiVO<sub>4</sub>/FTO 7\_EI)
- BiVO<sub>4</sub>/FTO 7 made by spin coating (BiVO<sub>4</sub>/FTO 7\_Sc)
- BiVO<sub>4</sub>/ITO 12 made by electrodeposition (BiVO<sub>4</sub>/ITO 12\_EI )

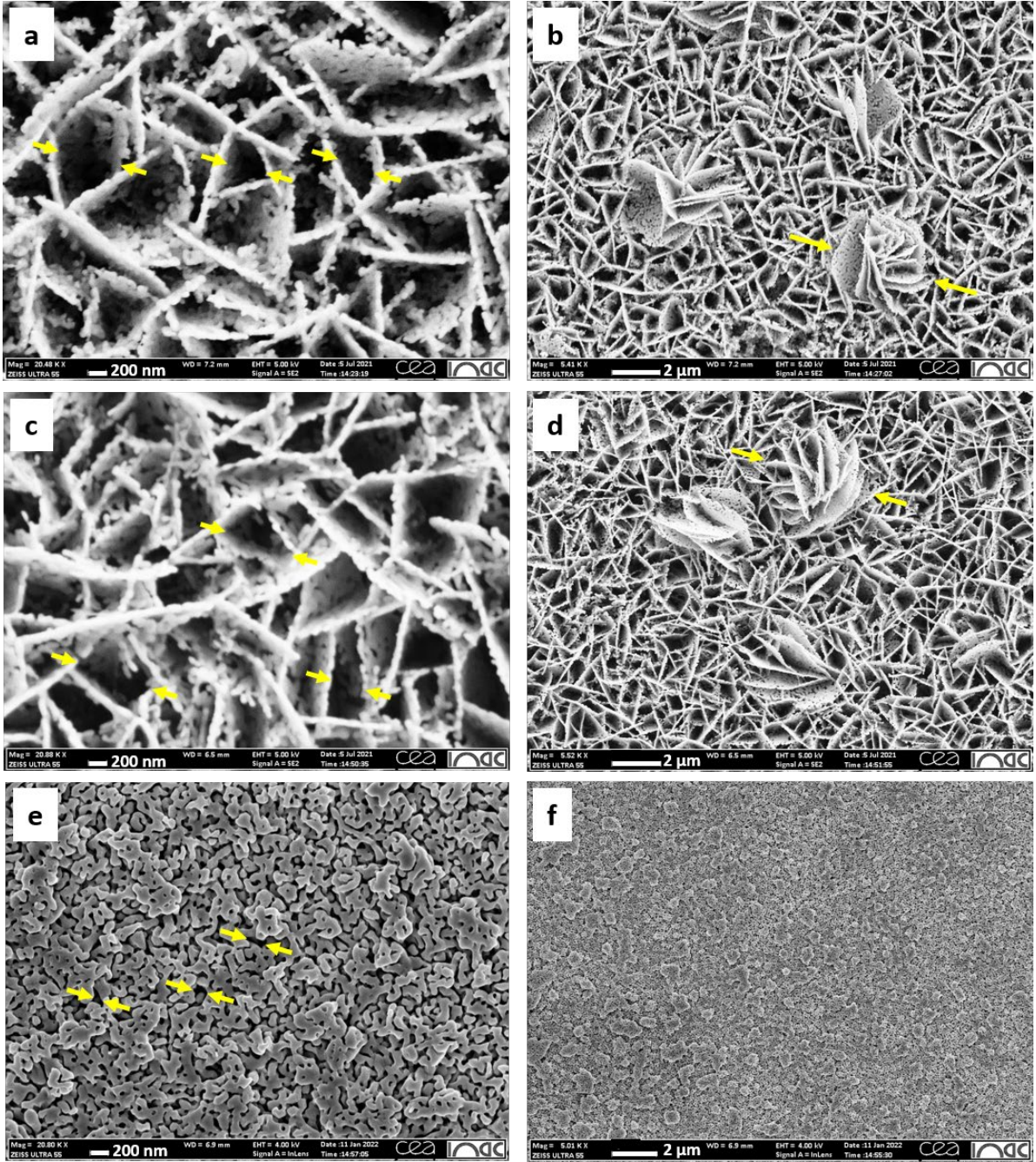


Figure 30. SEM images of BiVO<sub>4</sub> photoanodes. a) and b) BiVO<sub>4</sub>/FTO 7\_El. c) and d) BiVO<sub>4</sub>/ITO 12\_El. e) and f) BiVO<sub>4</sub>/FTO 7\_sc. The yellow arrows point a characteristic size of the pores (picture (a), (c) and (e)) or flower-like clusters (picture (b) and (d)).

The main structure of the semiconductors generated with the electrodeposition method consists of intertwined thin blades of BiVO<sub>4</sub> with occasional formation of over-deposited domains resembling flowers on top, originating from the electrodeposited BiOI. The drop-casting of V<sub>2</sub>O<sub>5</sub> increases the surface area of the BiVO<sub>4</sub> layer compared to the BiOI layer. From the images, it is observed that an elevated number of flowers (with a diameter on the order of approx. 5µm) is mainly present on the photoanodes with higher photoelectrocatalytic activity, it is most significant when the electrodeposition process is applied on FTO 7 supports; the flowers are absent in photoanodes fabricated by sol-gel spin coating.



The surface morphology of BiVO<sub>4</sub>/FTO 7\_Sc shows particles agglomeration with a less homogeneous structure, this is due to the centrifugal force acting on the substrate during the high-speed spin-coating fabrication process.

The BiVO<sub>4</sub> electrodes fabricated by electrodeposition (BiVO<sub>4</sub>/support\_El), which exhibited a more porous and dissected faces (suggesting a higher specific surface area) than the BiVO<sub>4</sub> samples produced by spin coating (BiVO<sub>4</sub>/support\_Sc), show superior values of the photocurrent with a thicker active layer, reported in Table 5. There weren't sufficient number of pictures to carry out an in-depth image analysis, but on the available shots, BiVO<sub>4</sub>/ITO 12\_El displayed the largest pore size of 683 nm, followed by BiVO<sub>4</sub>/FTO 7\_El with 507 nm, and finally, the spin-coated photoanode with 160 nm (BiVO<sub>4</sub>/FTO 7\_Sc).

**The observed effect of texture on the photocurrent is, at first glance, consistent with a greater concentration of catalytic sites, for enhancing reactivity and facilitating charge carrier separation, and a greater accessibility of the latter, thanks to the porous network developed by the electrolytic deposition.**

### 3 Role of optical processes: numerical sensitivity approach

The analysis of the macroscopic and crystallographic structure for several types of photoanodes is fundamental to discuss their integration as electrodes in PEC cells. Pivotal importance in this context stems from understanding and predicting the limiting conditions in PEC devices, particularly the behavior at the liquid junction between the photoanode and the electrolytic solution. In Sec. 2.6, the differences in photocurrent observed between the various photoanode specimens were discussed in relation to their conductivity (the lower the sheet resistance of the TCO, the higher the photocurrent), and their texture, on the basis of knowledge related to flow in porous media, heterogeneous catalysis, electrochemistry.

This section focuses on studying how optical, electrical and surface properties combined influence the performance of photoanodes. The aim is to highlight possible couplings and limiting phenomena that need to be taken into account when scaling up. Indeed, few studies consider the effective properties of materials used in a PEC device in operation, and in particular the optical phenomena which, unlike electrochemical phenomena (electrocatalysis, porous media, ionic migration, etc.) are specific to PEC and responsible for the conversion of photons into electrons, during the propagation and absorption of light.

This study is based on the optical characterizations described in Sec. 2.4 and numerical simulations to analyse the experiments (by allowing the identification of parameters by inverse method) and to study the sensitivity of heterogeneous photoanodes to the design of the multilayer assembly and especially to the texture of the BiVO<sub>4</sub> layer.

The system under consideration is based on the specificities of the photoanodes manufactured and characterized experimentally in Sec. 2.6, and is shown in Figure 31.

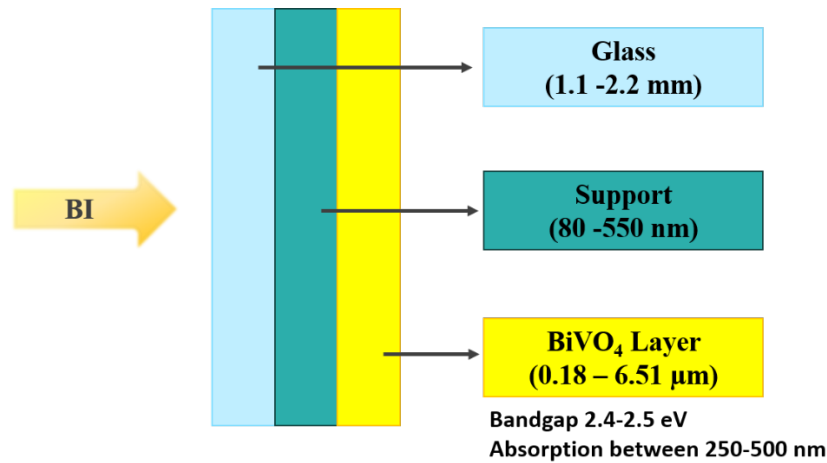


Figure 31. Structure of simulated photo-anode including conductive TCO layer (FTO 7, FTO 80 or ITO 12).

\*The BI configuration shown in this scheme was adopted for the calculation of the photocurrents  $J_{ph}$ , in coherence with the experimental set-up of Figure 27.

This section focuses on the phenomenology affecting light propagation in manufactured photoanodes, to unveil how textural irregularities influence the photocurrent delivered by 'large' BiVO<sub>4</sub> photoanodes.

A preliminary study, carried out during the internship of A. Chauvet<sup>150</sup>, was dedicated to the testing and comparison of different optical simulation tools, detailed below. These optical tools were then used to determine the apparent optical properties of BiVO<sub>4</sub> in coated layers, then to carry out a numerical sensitivity simulation study to investigate, on a small scale, the impact of photoactive layer thickness and roughness, which were found to differ according to the deposition process and its parameters.

### 3.1 Optical codes

The opensource Transfer Matrix code (TM) (based on MATLAB) and the CROWM optical simulator (developed by the University of Ljubljana) were used to estimate the photocurrent density  $J_{ph}$  produced, in theory, by the BiVO<sub>4</sub> photoanodes, considering either a flat (TM and CROWM) or a rough surface (CROWM) with a given texture. The  $J_{ph}$  predictions given by the two models, where appropriate on the two types of surface, were compared to each other, and with experimental data (obtained under a given imposed potential), and with the State of Art.

#### 3.1.1 Transfer Matrix

Transfer Matrix (TM)<sup>151</sup> is a calculation method implemented in Matlab to evaluate optical interference and absorption in multilayer stacks. It calculates the transmission and the reflection at each interface in a stack of thin films, the attenuation in each layer and the photocurrent density ( $J_{ph} - \text{mA}\cdot\text{cm}^{-2}$ ) for absorbing materials.

To predict the device's performance is also possible to determine the generation rate  $\left(\frac{n_{excitations}}{s \times cm^3}\right)$  at each of position in the device and the spatial distribution and the intensity of the electric field in a material. The TM MATLAB program was published by McGehee's Group of Stanford Materials Science & engineering<sup>152</sup>.

To study multilayer assemblies, the model makes several assumptions about interfaces<sup>153</sup>:

- ◆ each layer is homogeneous and isotropic. Thanks to this assumption, it is possible to describe the linear optical response of each layer using a scalar complex refractive index.

- ◆ The interfaces between the various layers are all considered to be flat and parallel to the light wave.
- ◆ The incident light on the semiconductor is considered normal, can be efficiently described using plane waves and does not take scattering effects into account.
- ◆ Exciton scattering contributes to photocurrent and dissociates into charge carriers at interfaces.
- ◆ All charges generated contribute to the steady-state photocurrent, implying that there is no charge trapping inside the photoanode.

Furthermore, the TM code has eliminated the use of complex parameters such as magnitude, incident and deviation angle, as well as dissociation probability, assuming an Internal Quantum Efficiency (IQE) of 100%.

In any device with a layered structure, light absorption is affected by optical interference if the thickness of each layer is comparable to the wavelength of light <sup>154</sup>.

In our numerical parametric study, light is assumed to be incident from the left-hand side on a multilayered structure with a perfectly flat surface. The corresponding model in Transfer Matrix is shown in Figure 32.

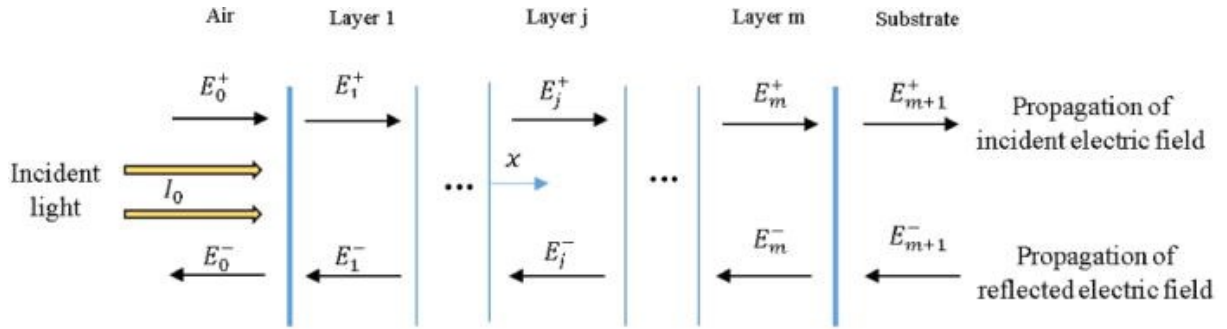


Figure 32. Principle of Transfer Matrix calculation in a stack of thin layers.<sup>154</sup>

It is easily transferable to the multilayered structure of the BiVO<sub>4</sub> photoanodes: Air/BiVO<sub>4</sub>/ITO or FTO film/Glass, showed in Figure 31.

In the diagram of a multilayer structure (Figure 32)  $I_0$  is the intensity of incident radiation,  $E_j^+$  and  $E_j^-$  are the magnitudes of electric field components in the incident and reflected electromagnetic radiation in the  $j^{\text{th}}$  layer, in the left and right directions, respectively. The variable  $x$  represents the position in the active layer, measured from the first interface on the left<sup>154</sup>.

Each  $j$ -layer has a thickness  $d$  and its optical properties are described by its complex refractive index, (Eq.17) which is a function of the wavelength of the incident light.<sup>153</sup>

$$\tilde{n}_j = n_j + k_j \quad \text{Eq. 17}$$

The total electric field  $E_j(x)$  entering in the layer  $j^{\text{th}}$  is given by:

$$E_j(x) = E_j^+(x) + E_j^-(x) \quad \text{Eq. 18}$$

The energy absorbed at position  $x$ , correlated to the number of photons absorbed  $Q_j(x)$  in the  $j^{\text{th}}$  layer, is proportional to the square of the electric field:

$$Q_j(x) = \frac{1}{2} c \epsilon_0 \alpha_j n_j |E_j(x)|^2 \quad \text{Eq. 19}$$

$$\alpha_j = \frac{4\pi k_j}{\lambda} \quad \text{Eq. 20}$$

Here  $c$  is the speed of light,  $\epsilon_0$  is the vacuum permittivity,  $\alpha_j$  the absorption coefficient, and  $\lambda$  the wavelength of the light, while  $k_j$  and  $n_j$  stand respectively for the extinction coefficient and the refractive index of the  $j^{\text{th}}$  layer.

The specific rate of generation of free charge carriers resulting from the absorption of a wavelength of light is calculated as follows:

$$G_j(x, \lambda) = \left( \frac{\lambda}{hc} \right) Q_j(x) \quad \text{Eq. 21}$$

Therefore, the total rate of generation of charge carriers at a position  $x$  in the  $j^{\text{th}}$  layer is:

$$G_j(x) = \int_{\lambda_1}^{\lambda_2} G_j(x, \lambda) d\lambda \quad \text{Eq. 22}$$

from which the short-circuit current density  $J_{sc}$  ( $\text{mA}\cdot\text{cm}^{-2}$ ) can be calculated :

$$J_{sc} = q G_j(x) \times (L_e + L_h) \quad \text{Eq. 23}$$

where  $L_e$  and  $L_h$  are the electron and hole diffusion lengths, which in the code correspond to the user-defined stepsize (in nm) between each point calculated in the spectrum.

The short circuit current equation is used considering a perfectly passivated surface and a uniform generation rate. For photoactive materials, the calculated value of  $J_{sc}$  represents the generated photocurrent  $J_{ph}$ , as expected under the assumed simulation conditions

In addition, the TM method makes it possible to determine the amount of light transmitted, reflected, or absorbed at the various interfaces of the multilayered system. The intensities transmitted and reflected by the thin-film stacks are calculated using the total transmittance  $\mathbf{T}$  and total reflectance  $\mathbf{R}$ , defined as follows:

$$R = \frac{I_R}{I_I} = |r|^2 = \left| \frac{E_0^-}{E_0^+} \right|^2 \quad \text{Eq. 24}$$

$$T = \frac{I_T}{I_I} = \frac{n_{m+1}}{n_0} \times |t|^2 = \frac{n_{m+1}}{n_0} \times \left| \frac{E_{m+1}^+}{E_0^+} \right|^2 \quad \text{Eq. 25}$$

$r$  and  $t$  are respectively the complex Fresnel reflection and transmission coefficients, while  $n_{m+1}$  and  $n_0$  are the refractive indices of the incident and outgoing media.

The total absorbance  $\mathbf{A}$  of the assembly depends on the square of the absolute value of the electric field  $\mathbf{E}$ , as well as on the absorption coefficient  $\alpha$  and the refractive index  $\mathbf{n}$ . It is defined as follow:

$$A = 1 - T - R$$

Eq. 26

The TM code has been used in numerous publications<sup>155,156</sup> where further details are given. One of the main advantages of this tool is its ability to simulate and predict the optical behavior of complex structures, as a function of the effective properties of the constituent materials, laying the foundations for optimized design and a less limited optical system.

### 3.1.2 CROWM

CROWM<sup>157</sup> (Combined Ray Optics and Wave Optics Models) is an optical simulator developed by the faculty of Electrical Engineering of the University of Ljubljana and already used at CEA/LITEN to simulate the properties of photovoltaic cells. It is based on more refined models than the Transfer Matrix method, and designed not only to handle flat and thin (*i.e.* coherent) layers, but also to simulate multiple thick (incoherent) layers.

Thick layers can be flat or textured with arbitrary 1D or 2D textures in the micrometer up to the millimeter range, defined with lateral and vertical parameters.

The program deals with the combination of incoherent geometrical optics and coherent wave optics. A schematic of a general photoactive structure that can be simulated by CROWM is represented in Figure 33.

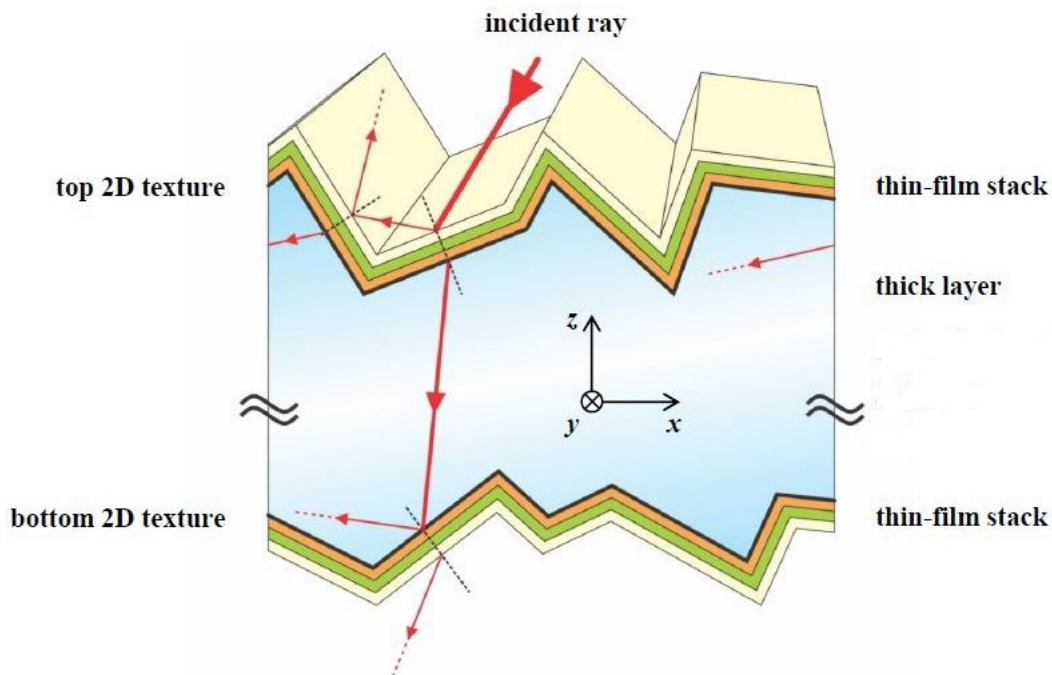


Figure 33. Schematic of the general device structure that can be simulated with CROWM.<sup>158</sup>

This example shows light propagation through a stack of materials with locally flat surfaces and through a single thick incoherent layer (in the range of 10  $\mu\text{m}$  – 10 mm).

It is important to point out that the thin-layer stacks in the considered material follow the fully coherent Transfer Matrix formalism. Thick textured layers, on the other hand, are analyzed by the three-dimensional incoherent ray tracing based on geometrical optics.<sup>150</sup>

More precisely, using the coherent Transfer Matrix equations, thin films are considered to be parallel to each other. This formalism is a one-dimensional approach to wave optics, taking into account only destructive and constructive interference to simulate light propagation at arbitrary angles of incidence. Moreover, there is no lateral shift in the rays transmitted and reflected by



the thin films, they always emerge from the same zone where the incident ray initially struck the thin-film structure.

On the other hand, for the incident medium and thick layers, a two-dimensional ray-tracing method is adopted. The optical equations consider that the incident illumination (with a defined angle of incidence that depends on the zenith and the azimuth) is split into several rays, which are then traced in the material, assuming a totally incoherent propagation of light without any interference effects. This is justified by the fact that the thickness of the front layer and the size of the texture features are significantly larger ( $> 10 \mu\text{m}$ ) than the wavelength of the light.<sup>158</sup>

Finally, the two approaches - geometrical ray tracing and thin-film wave optics - are combined to produce a high-performance optical simulator.<sup>159</sup>

The basic quantity used to define the light rays/waves propagating in the simulated structure is the electric field  $\mathbf{E}$ . Considering each ray propagating through the incident medium (two-dimensional ray tracing method) to the textured surface (thick front layer of the material), the electric field for each ray is derived from the following equations:

$$\mathbf{E} = \mathbf{E}_{in} \times \exp\left(\frac{-i \times 2\pi \times \mathbf{n}_{in} \times \mathbf{d}}{\lambda}\right) \quad \text{Eq. 27}$$

$$\mathbf{E}_{in} = \sqrt{\mathbf{P}_{in} \left(\frac{2\eta_0}{\mathbf{n}_{in}}\right)} \quad \text{Eq. 28}$$

$$\eta_0 = \sqrt{\mu_0/\epsilon_0} \quad \text{Eq. 29}$$

In the 1<sup>st</sup> equation (Eq. 27)  $i$  is the imaginary unit,  $\mathbf{d}$  is the distance traveled by the ray in the incident medium to the interface point, and  $\lambda$  represents the wavelength (in vacuum) of the considered spectral component.  $\mathbf{E}_{in}$  is the incident electric field,  $\mathbf{P}_{in}$  is the time-averaged incident power per unit area of the ray,  $\mathbf{n}_{in}$  is the refractive index of the incident medium (air),  $\eta_0$  is the vacuum impedance,  $\mu_0$  is the magnetic constant, also known as the vacuum permeability,  $\epsilon_0$  is the electric constant, also known as the vacuum permittivity.

On the other hand, light is considered as a wave passing through a medium or interfaces where only transverse waves are capable of interacting constructively or destructively with each other. Moreover, the incident illumination is divided into transverse-magnetic (TM) and transverse-electric (TE) polarized illumination, defined with respect to the  $xy$  horizontal plane, the latter is parallel to the layer interfaces. Hence, the transverse electric fields  $\mathbf{E}_T$  of the incident waves are computed from the electric fields of the outgoing rays ( $\mathbf{E}^{TE}, \mathbf{E}^{TM}$ ), taking into account the complex propagation angle  $\theta_i$ :

$$\mathbf{E}_{T,in}^{TE} = \mathbf{E}^{TE} \quad \text{Eq. 30}$$

$$\mathbf{E}_{T,in}^{TM} = \mathbf{E}^{TM} \times \cos\theta_i \quad \text{Eq. 31}$$

As the morphology of the texture, the optical absorption in the material and the resulting reflectance and transmittance through the photoactive BiVO<sub>4</sub> influence the intensities and directions of the rays, the CROWM approach is highly relevant for our study.

The typical film stack of Figure 31 can be simulated with CROWM as comprising one or more incoherent thick layers and an arbitrary number of thin films with a thickness between 1 nm and 1 μm, smaller than the lateral and vertical features of the textures. An example of dataset is given in Figure 34.

The thin films are assumed to be locally flat. One-dimensional or two-dimensional surface textures are applied to the top surface and/or bottom surface of the incoherent thick layers. The lateral and vertical features of the textures are of the order of micrometres or more. Textures are assumed to be continuous and periodic in  $x$  and  $y$  directions. The incident medium (typically air) and the transmitting medium are considered incoherent (*i.e.* infinitely thick).

<pre> air (0 nm) [T1]====[ (flat interface) ]===== [T1]====[ (flat interface) ]===== glass (1100000 nm) [T2]====[Flat_ITO]=====   ITO(theorique) (370 nm) [T2]====[Flat_ITO]===== BiVO4 layer on ITO (4600 nm) [T3]====[Texture_BiVO4 layer on I [T3]====[Texture_BiVO4 layer on I air (0 nm) </pre>	<pre> air (0 nm) [T1]====[Texture_BiVO4 layer on I [T1]====[Texture_BiVO4 layer on I BiVO4 layer on ITO (4600 nm) [T2]====[Flat_ITO]=====   ITO(theorique) (370 nm) [T2]====[Flat_ITO]===== glass (1100000 nm) [T3]====[ (flat interface) ]===== [T3]====[ (flat interface) ]===== air (0 nm) </pre>
--	--

Figure 34. Example of CROWM optical simulator dataset. Case of a BiVO<sub>4</sub> photoanode, respectively under back illumination (BI, left)) and front illumination (FI, right).

CROWM was mainly used to calculate the total reflectance and transmittance of the conductive material, as well as the absorbance in each of the individual films. Other output parameters considered are the power density reflected, transmitted, or absorbed on the light path through the material, and the short-circuit current density calculated according to the following equation<sup>160</sup>:

$$J_{sc} = \frac{q}{hc} \int P_{spc}(\lambda) \times A_{layer}(\lambda) \times \lambda \times d\lambda \quad \text{Eq. 32}$$

$q$  is the elementary charge,  $h$  is Planck's constant,  $c$  is the speed of light,  $\lambda$  is the wavelength,  $P_{spc}(\lambda)$  is the total incident power given at the current wavelength in the spectrum file (AM1.5G) and  $A_{layer}(\lambda)$  is the absorption of the considered layer at the current wavelength.

For the BiVO<sub>4</sub> photoanode simulation in this study, the short-circuit current  $J_{sc}$  corresponds to the photocurrent  $J_{ph}$  generated, assuming that all absorbed photons contribute to charge carrier generation *i.e.*:  $\text{EQE} = A$ .

More details on the program, its results and input data can be found in the software manual<sup>158</sup> and Lipovšek's group articles<sup>161, 162</sup>.

Ultimately, Transfer Matrix and CROWM tools provide various indicators for evaluating the features of a film stack. This work focuses on the evaluation of the (maximal) photoactive current density  $J_{ph}$  and the comparison of the resulted obtained according to the hypotheses considered.

## 3.2 Simulation of the synthesized BiVO<sub>4</sub> photoanodes

### 3.2.1 Identification of BiVO<sub>4</sub> properties

In order to evaluate photoactive current density with CROWM, it is important to define not only the illumination spectrum file and ray tracing parameters, but also the textural/structural characteristics and the complex refractive index  $n + ik$ .

$n$  (the real part) and  $k$  (the imaginary part) are key parameters underlying the numerical sensitivity study, used as initial conditions in CROWM and TM.

Each layer of the BiVO<sub>4</sub> photoanode has different  $n$  and  $k$  indices, as they are related to the chemical composition, the structure, and the light behavior in each film.

As shown in Figure 34, BiVO<sub>4</sub> electrodes have been treated as stacks of successive layers of Air, photoactive film of BiVO<sub>4</sub>, conductive FTO or ITO substrate, and glass. The light is assumed to be directed on the BiVO<sub>4</sub> layer (FI), as for the Reflectance and Transmittance measurements, used for the calculation of the BiVO<sub>4</sub> refractive index  $n$ . Table 6 gathers the expressions and/or known values of  $n$  and  $k$  indices<sup>163,164</sup>, as well as the thickness corresponding to each layer.

Table 6. Input parameters for the calculation of the BiVO<sub>4</sub> refractive index.

Layer	$k$	$n$	Thickness (nm)
Air	0	1	0
BiVO <sub>4</sub>	$k = \frac{\alpha_1 \lambda}{4\pi}$ $\alpha_1 = 2.302 \frac{A_{BiVO_4}}{d}$	$n = \frac{1 + R_{BiVO_4}}{1 - R_{BiVO_4}} + \sqrt{\frac{4R_{BiVO_4}}{(1 - R_{BiVO_4})^2} - k^2}$	300 - 6000
ITO 12 FTO 80 FTO 7	$k^* = \frac{\alpha_1^* \lambda}{4\pi}$ $\alpha_1^* = 2.302 \frac{A_{supp}}{d}$	$n = \frac{1 + R_{supp}}{1 - R_{supp}} + \sqrt{\frac{4R_{supp}}{(1 - R_{supp})^2} - k^2}$	370/80/550
Glass	0	~ 1.45	$2.2 \times 10^6$ $1.1 \times 10^6$

In order to determine the actual refractive index  $n$  of the BiVO<sub>4</sub> layer, the indices of the conductive substrate layers were readjusted according to the formulae in Table 6, based on measurements achieved on the substrates alone. Then an identification procedure was used to determine those, unknown, of BiVO<sub>4</sub> in each type of sandwich. Again, the values of  $n$ ,  $k$  reported in Table 6 for BiVO<sub>4</sub> were used as first guess to initialize the optimization procedure.

The calculations are carried out assuming  $A_{BiVO_4} = A_{tot} - A_{support}$  and  $R_{tot} = R_{BiVO_4}$ .

The refractive index of the BiVO<sub>4</sub> was obtained using an inverse method. The latter consists of coupling the experimental transmission and reflection data (see Sec. 2.4) with the Transfer Matrix code (Figure 35) and the Matlab function *fminsearch*.

More precisely, an initial value of the BiVO<sub>4</sub> refractive index ( $n_0$ ) was defined, adapted from Sarkar et al.<sup>163</sup> (Eq. 33) from which a multidimensional nonlinear minimization algorithm (Nelder-Mead Method, available in Matlab) was applied to make the simulated total reflectance

of the multilayer material ( $R_j simulated$ ) fit the experimental one ( $R_j experimental$ ), by minimizing the mean square roots error  $Z$  (Eq. 34).

$$n_0 = \frac{1 + R_{BiVO_4}}{1 - R_{BiVO_4}} + \sqrt{\frac{4R_{BiVO_4}}{(1 - R_{BiVO_4})^2} - k^2} \quad \text{Eq. 33}$$

$$Z = \sum_{j=1}^n (R_j simulated - R_j experimental)^2 \quad \text{Eq. 34}$$

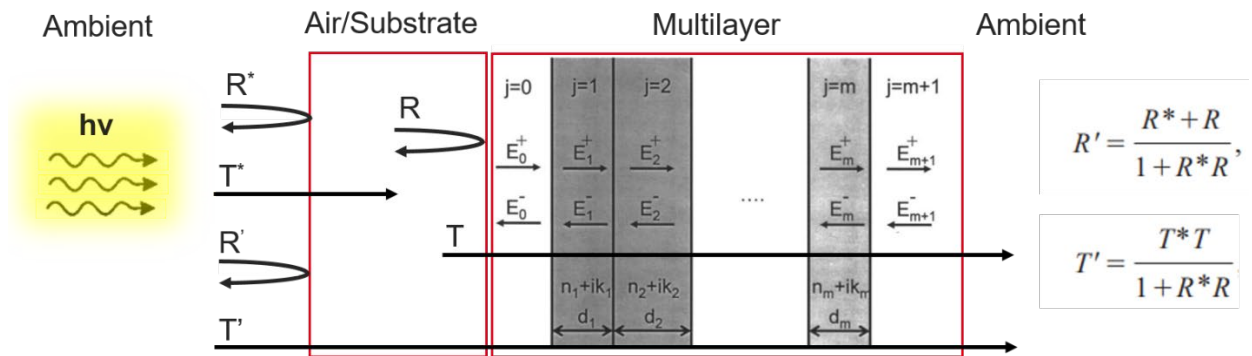


Figure 35. Geometry of the multilayer stack (air, photoactive film of  $BiVO_4$ , conductive FTO or ITO substrate, glass) used in the optical electric field calculation underlining the Reflectance and the Transmittance in the material. FI: the light is first directed on the  $BiVO_4$  layer, then on the substrate.

The graphs below show the  $n$ - $k$  indices of the three types of electrodes manufactured and fully characterized ( $BiVO_4/FTO7\_El$ ,  $BiVO_4/FTO7\_Sc$ ,  $BiVO_4/ITO12\_El$ ), and considered for the numerical sensitivity study and the absorbance values derived from the reflectance and transmittance measurements detailed in Sec. 2.4.

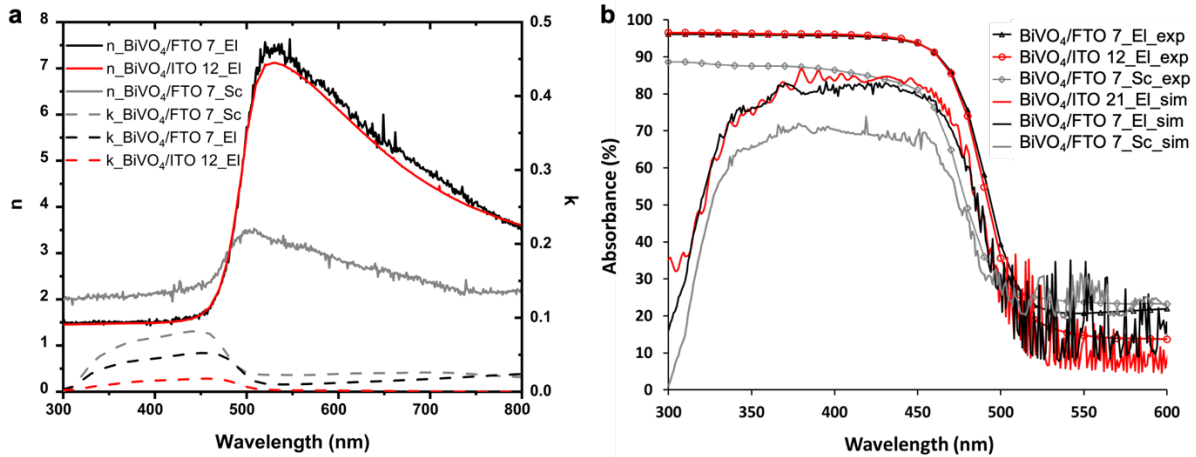


Figure 36. Study of the optical properties. a)  $n$ - $k$  index of  $BiVO_4/FTO7\_El$  (black line),  $BiVO_4/FTO7\_Sc$  (grey line),  $BiVO_4/ITO12\_El$  (red line). The refractive index  $n$  is represented by solid lines, the extinction coefficient  $k$  is represented by dashed lines. b) Experimental Absorbance measurements:  $BiVO_4/FTO7\_El\_exp$  (dotted black line),  $BiVO_4/FTO7\_Sc\_exp$  (dotted grey line),  $BiVO_4/ITO12\_El\_exp$  (dotted red line). Transfer Matrix measurements on flat surface:  $BiVO_4/FTO7\_El\_sim$  (black line),  $BiVO_4/FTO7\_Sc\_sim$  (grey line),  $BiVO_4/ITO12\_El\_sim$  (red line).

Thus, R, T, and A depend on the thickness of the active layer and of the conductivity and thickness of the supports. Indeed, the electrode produced via sol-gel spin-coating that are generally thinner than those made by electrodeposition (e.g. 0.7  $\mu\text{m}$  for BiVO<sub>4</sub>/FTO 7\_Sc vs. 1.3  $\mu\text{m}$  for BiVO<sub>4</sub>/FTO 7\_El and 4.3  $\mu\text{m}$  for BiVO<sub>4</sub>/ITO 12\_El), shows fewer absorption of photons between 300 and 500 nm (dotted and solid grey lines in Figure 36b) than photoanodes fabricated by electrodeposition (dotted and solid black and red lines). It is therefore highlighted that even the simulated values of Absorbance (from 300 to 800 nm), calculated with Transfer Matrix on flat textures show the same trend as the experimental Absorbance results. Also CROWM simulations support these conclusions, as detailed in Sec. 3.2.2.

Furthermore, different  $n$ ,  $k$  values are identified for the BiVO<sub>4</sub> layers of the three photoanodes (Figure 36a), with a higher and quite similar extinction coefficient  $k$  for the “thick” layers deposited by spin coating, and a smaller refractive index  $n$ . Note that  $n$  is primarily influenced by the synthesis method rather than the conductivity of the TCO coated glass.

For the sake of comparison, simulations of the photocurrent generated by a given architecture were carried out using either the  $n, k$  indices adjusted on the BiVO<sub>4</sub>/FTO 7\_El samples, or those adjusted on the BiVO<sub>4</sub>/FTO 7\_Sc samples. The results (see Table 7) consistently show a higher photocurrent ( $J_{ph, flat}$ ) when the optical properties are measured on the electrodeposited layer, suggesting that, **whatever its thickness, the layer obtained by this process is more "photoactive" than the denser spin-coated layer** (see SEM picture in Figure 30, Figure 44 in Appendix).

Table 7. Influence of the deposition process on the photocurrent (estimated by TM simulations on flat textures). The values predicted using the correct match of stack and  $n, k$  indices are underlined.

Sample	Using n-k calculated for BiVO <sub>4</sub> /FTO 7_El	Using n-k calculated for BiVO <sub>4</sub> /FTO 7_Sc
BiVO <sub>4</sub> /FTO 7_El	<u><math>J_{ph, flat} = 9.25 \text{ mA.cm}^{-2}</math></u>	$J_{ph, flat} = 11.84 \text{ mA.cm}^{-2}$
BiVO <sub>4</sub> /FTO 7_Sc	$J_{ph, flat} = 6.28 \text{ mA.cm}^{-2}$	<u><math>J_{ph, flat} = 8.39 \text{ mA.cm}^{-2}</math></u>

Even if the extinction coefficient  $k$  is higher for photoanodes made by spin coating (Figure 36a), the lower thickness of the active layer leads to a lower final value of generated photocurrent.

### 3.2.2 Estimation of the photocurrent

Once the typical optical indices of the different synthesized BiVO<sub>4</sub> deposits have been identified, it is possible to simulate the currents generated by the various photoanodes under 1 sun illumination. For this estimation, a back illumination configuration (BI, Figure 34a, Air/Glass/Support/Active Layer/Air) has been adopted, this allows to correlate the theoretical  $J_{ph}$  results with the LSVs results of Table 5 (Sec. 2.6).

In addition to the optical indices, the BiVO<sub>4</sub> real textures are the 2<sup>nd</sup> input parameter necessary for CROWM simulations. The local thickness values determined by profilometry (see Sec. 2.3.3) were used to generate a *text file* containing texture specifications. The measured profile at the core of the photoanode is replicated, hence defining the lateral borders ( $X_{max}$ ,  $Y_{max}$ ) and the ray tracing step ( $d_{RT}$ ): respectively 500, 500, 0.01 (all dimensions in  $\mu\text{m}$ ).

Table 8 show a comparison of the results obtained with Transfer Matrix (similar to that used in most PEC models<sup>77,165</sup>) and CROWM considering either a flat or the rough surface.

Table 8. Thicknesses ( $H$ ,  $h_p$ ) and roughness ( $R_a$ ) of the characterized samples, photocurrent values obtained with Crowm and TM, as a function of the structure of the active layer (real texture ( $J_{ph}$ ) and flat texture ( $J_{ph, flat}$ )).

	SEM	Profilometer		CROWM		TM
Sample	H (nm)	$h_p$ (nm)	Ra ( $\mu\text{m}$ )	$J_{ph}$	$J_{ph, flat}$	$J_{ph, flat}$
CoPi-BiVO <sub>4</sub> /FTO 7_El	1045	2365	1.05	13.41	11.87	11.03
BiVO <sub>4</sub> /FTO 7_El	2279	1299	0.20	9.64*	9.25	8.22
2.5 %Mo:BiVO <sub>4</sub> /FTO 7_Sc	599	-	-	-	7.37	6.77
1.25 % Mo:BiVO <sub>4</sub> /FTO 7_Sc	578	388	0.11	10.05	5.48	4.95
BiVO <sub>4</sub> /FTO 7_Sc	661	706	0.54	4.18*	8.39	7.64
CoPI-BiVO <sub>4</sub> /FTO 80_El	2561	4740	2.34	18.37	11.86	11.05
BiVO <sub>4</sub> /FTO 80_El	1462	4585	2.30	18.28*	12.17	10.99
BiVO <sub>4</sub> (150mC.cm <sup>-2</sup> )/FTO 80_El	900	1082	0.13	6.54	4.78	3.94
CoPI-BiVO <sub>4</sub> /ITO 12_El	2264	3421	0.68	10.30	4.86	4.52
BiVO <sub>4</sub> /ITO 12_El	2432	4289	1.27	9.18*	5.68	5.15

\*Average value of the photocurrents measured an three different points on the photoanode to assess the homogeneity of the deposit.

\*\* The values of  $n$  and  $k$  used for the calculations of  $J_{ph}$  are those of BiVO<sub>4</sub> photoanodes, synthesized on the TCO coated glasses by the two explained synthesis methods (Sc, El). The presence of molybdenum and CoPi is not considered when determining  $n$  and  $k$ .

A good agreement between TM and CROWM simulations is observed, when a flat surface is considered.

The simulation results are also consistent with the increased activity observed for photoanodes fabricated by electrodeposition, and underscores the role of a catalyst or doping agent in enhancing photoanode performance. As mentioned in Sec. 2.6, the texture of the photoanode influences the photocurrent generated by the oxidation of the electrolytic solution. While the photocurrent values obtained with CROWM in Table 8, assuming EQE = A, are higher than the experimental ones (see Table 5), they show the same trends. In almost all studied cases, it is observed that **increased thickness and roughness, and consequently a larger surface area, positively contributes to enhancing the photocurrent values**, the latter being higher than for photoanodes with flat surfaces.

The results obtained for photoanodes made by spin coating do not always follow this criterion, due to the inhomogeneity of the layer, strongly influencing both theoretical and experimental photoelectrochemical results. For instance, for rough BiVO<sub>4</sub>/FTO7\_Sc anodes,  $J_{ph,real}$  is 4.18 mA.cm<sup>-2</sup> and 10.05 mA.cm<sup>-2</sup>, with and without a doping agent respectively. These significantly different values underline the substantial contribution of the doping agent in modifying the texture (or surface recombination at the electrolyte/layer interface). Conversely, for **flat photoanodes made by spin coating, the principal limiting factor is the thickness of the layers, and the higher the thickness the higher currents**. When all charges have been absorbed, the current density reaches a limiting value (this is confirmed by the numerical sensitivity study explained in the Sec. 3.3). Higher thickness results in a greater distance between the generated charges and the collection region, increasing charge recombination.

There is also a slight difference between the  $J_{ph}$  of the photoanodes fabricated on ITO and FTO supports. In this case, the difference in photocurrent does not depend on the optical parameters, since  $n$  and  $k$  are similar for both photoanodes considered, but rather on the thickness of the substrate and the electrodeposited active layer.



CROWM helps identify influencing parameters, such as thickness and optical properties, in this type photoanode. An in-depth study of the contribution of the structure (roughness and thickness) of photoanodes on the variation of photocurrent density is presented in the following.

### 3.3 Numerical Sensitivity Study

Karuturi et al.<sup>166</sup> used surface roughening to enhance the performance of their PK/Si/Ti/Pt photocathode. The texturing of the light harvesting Si surface enhances the photon absorption, by increasing the path of the photons and their bouncing on the surface of the material (which minimizes reflexions towards the external environment), while the texturing of the catalytic surface, on the opposite side of the cell, allows to increase the surface of active sites.

The photoelectrode, with a planar surface area of  $0.3 \text{ cm}^2$ , showed an efficiency of up to 17% STH (water splitting current density up to  $14 \text{ mA/cm}^2$ ).

As previously illustrated in Sec. 2.6, the electrodes obtained by electrodeposition, which are rougher, develop a higher electrolysis photocurrent than electrodes fabricated by spin-coating. It is likely that this difference is linked to the texturing of the  $\text{BiVO}_4$  layer, which, for “large textures” (order of magnitude of the wavelength), increases the specific surface area and minimizes photon leakage to the outside environment by trapping them in grooves.

In this section, simulation is used to study the effect of texturing on three photoanodes similar to those presented in Sec. 3.2.2. in terms of material (nature and thickness of layers), the distance and depth between the periodical sinusoidal microgrooves on hypothetical surface being varied (Figure 37).

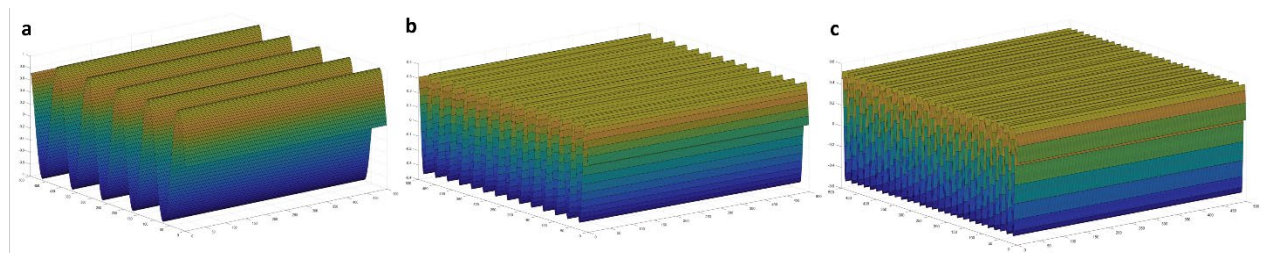


Figure 37. Periodic model textures simulated with CROWM (amplitude, period) in  $\mu\text{m}$  respectively equal to (0.97; 97.45), (0.35; 35.29) and (3.22; 6.43) from left to right.

The numerical sensitivity study comprises two main stages: definition of sample textures and calculation of photocurrent density.

It focus on the macroscopic, structural analysis of the three samples, already considered in the previous sections:

- a  $\text{BiVO}_4$  photoanode prepared by spin coating on FTO 7 (sample  $\text{BiVO}_4/\text{FTO 7\_Sc}$  in Table 5 and Table 8),
- a  $\text{BiVO}_4$  photoanode prepared by electrodeposition on FTO 7 ( sample  $\text{BiVO}_4/\text{FTO 7\_El}$  in Table 5 and Table 8),
- and a  $\text{BiVO}_4$  photoanode prepared by electrodeposition on ITO 12 (sample  $\text{BiVO}_4/\text{ITO 12\_El}$  in Table 5 and Table 8).

The three samples differ in conductivity or type of support, and/or type of synthesis method, as well as in substrate and photoactive layer thickness (measurement protocol in Sec. 2.3.3).

In each case, the incident light arrives through the glass layer, as in Sec. 2.5 and 3.2.

These configurations allow to study the influence of the non-uniformity of deposition.

### 3.3.1 Definition of the “model” textures

The “model” textures were defined from the actual textures measured on the photoanode, at least in terms of the depths of the periodic thickness oscillations (see Figure 38).

For a given photoanode assembly, the local thickness of the BiVO<sub>4</sub> photoactive layer, implemented in CROWM via a MATLAB routine, is calculated as follow:

$$h_{total\ textured\ BiVO_4} = h_p + a \times \sin\left(\frac{2\pi}{T}x\right) \quad \text{Eq. 35}$$

where  $h_p$  is the averaged thickness of the BiVO<sub>4</sub> photoactive layer (used for comparison in “flat” simulations),  $a$  and  $T$  are respectively the amplitude and the period of the sinusoidal function. In each case, the considered amplitude of the oscillations ( $a$  in  $\mu\text{m}$ ) was 25, 50 and 75% of the mean thickness of the BiVO<sub>4</sub> layer (Eq. 35) and their spacing ( $T$  in  $\mu\text{m}$ ) was varied between 0.01 and 100 times the amplitude (all the data are in SI). Note that the model textures with the lowest period  $T$  are more representative of the tightly-packed deposit facies observed on the profilometer.

In the texture file, all dimensions are expressed in  $\mu\text{m}$ , then the area considered for the numerical sensitivity study is  $500 \times 500 \mu\text{m}^2$ , the ray-tracing step is  $0.01 \mu\text{m}$ .

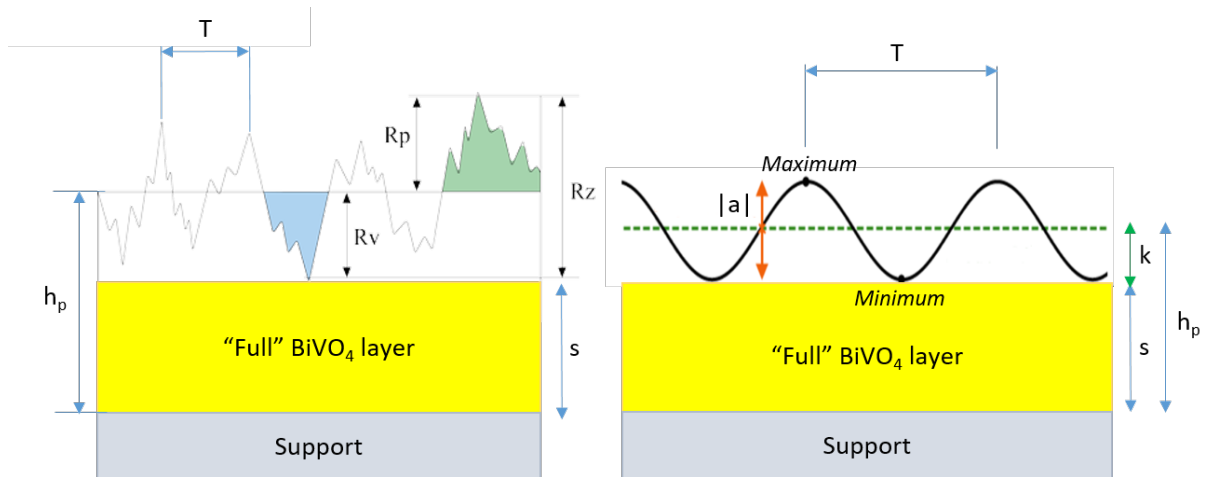


Figure 38. BiVO<sub>4</sub> layer schematized in real and theoretical (sinusoidal) conditions.

To summarize, variations in the period  $T$  and in the amplitude  $a$  allowed for the validation of structures with different thicknesses and roughnesses aimed to simulate defects and gaps, in order to explore the impact of photoanode heterogeneity on generated photocurrent.

After that, photocurrent density values  $J_{ph}$  were calculated with the proposed sinusoidal textures and  $J_{ph}$  at the limit condition: flat surface (thickness  $h_p$ ).

The roughness values calculated thanks to the experimental results were the point of reference for defining the limit parameters of the treated textures.

The  $a$  value reported in the Table 11 are defined considering the maximum profile valley depth  $R_v = \min(Z(x))$ , and the maximum profile peak height  $R_p = \max(Z(x))$  derived from the profilometry measurements (Figure 22)

### 3.3.2 Results

Figure 39 and Figure 40 show the evolution of the photocurrent predicted by CROWM in the case of a thick and a thin BiVO<sub>4</sub> layer deposit on a FTO7 support, *i.e.* as achieved by EL or SC



respectively. A thicker layer of BiVO<sub>4</sub> on a more resistive ITO 12 substrate is reported in Appendix 5.9, Figure 48. For each curve, an overall trend line is plotted to facilitate comparison between configurations. These curves do not represent averages of each series, but only make it possible to erase the sometimes significant fluctuations observed in the simulation results. The graphs clearly reveal a higher dispersion in the results, related to the chosen synthesis method from which more or less homogeneous layers have been obtained. For each curve, an overall trend line is plotted to facilitate comparison between configurations. These curves do not represent averages of each series but rather help to erase the sometimes significant fluctuations observed in the simulation outcomes. From the graphs, it clearly emerges that the dispersion of the results is related to the chosen synthesis method; more precisely, varying the synthesis method yields active layers that are more or less homogeneous. These variations respectively reflect lower and greater dispersion of the results.

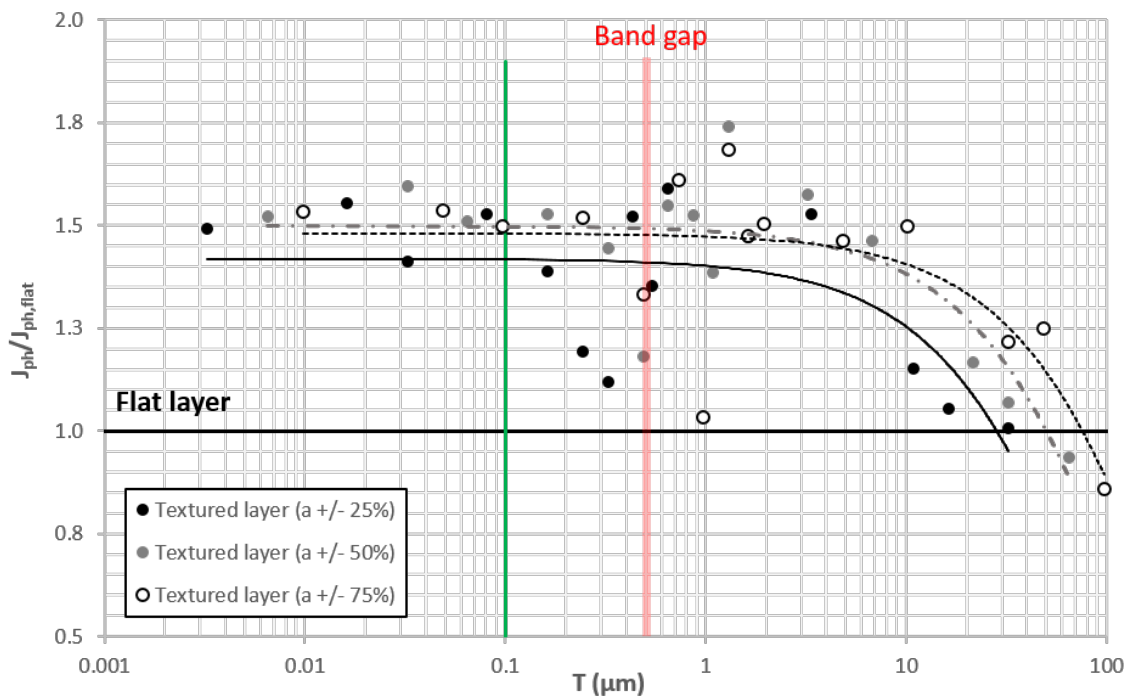


Figure 39. Evolution of photocurrent with microgroove characteristics for a BiVO<sub>4</sub> layer of average thickness 1.3 μm ( $a = 0.32 / 0.65 / 0.97 \mu\text{m}$ ) deposited (by electrodeposition) on an FTO7 substrate. The band-gap of the material is represented by the red line (at  $0.514 \mu\text{m}$ ), the diffusion length by the green line, and the current corresponding to the flat layer by the black line at  $J/J_{\text{flat}} = 1$  ( $J_{\text{flat}} = 9.25 \text{ mA/cm}^2$ ).

In Figure 39, the photocurrent values obtained from sinusoidal textures are always higher than those obtained considering a flat texture, which may reflect the fact that by promoting photon trapping, roughness increases absorption and consequently the photocurrent. For this thick BiVO<sub>4</sub> layer, the effect of the sinusoidal texture amplitude,  $a$ , seems moderate ( $J_{\text{ph}} / J_{\text{ph,flat}} \cong 1.5$  in all cases). On the other hand, as the spacing between the grooves increases, *i.e.* at high values of  $T$ , the positive effect of the sinusoid attenuates, as shown by the decrease in the predicted photocurrent values. The **photocurrent plateau on the left part of the curve** seems to coincide with  $T$  values below the diffusion length in BiVO<sub>4</sub>, materialized by the green line at 100 nm.

Additional calculations are necessary, involving variations in the input parameters, to verify the numerical or physical origin of the oscillations.

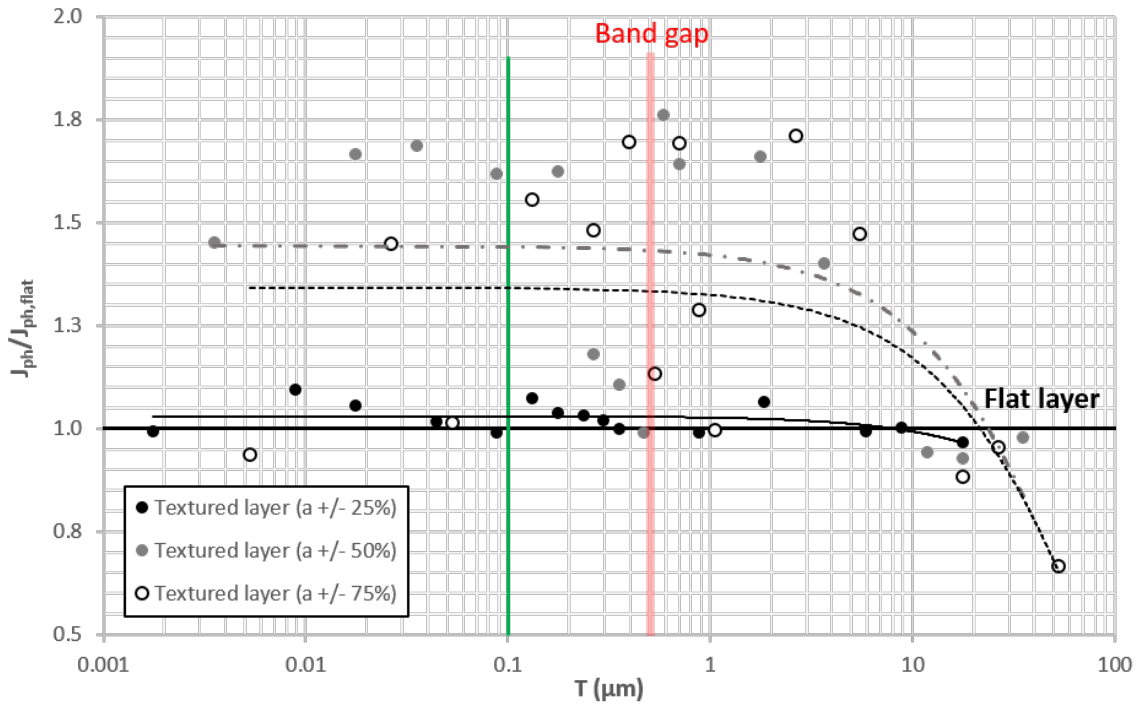


Figure 40. Evolution of photocurrent with microgroove characteristics for a  $\text{BiVO}_4$  layer of average thickness  $0.7 \mu\text{m}$  ( $a = 0.18 / 0.35 / 0.53 \mu\text{m}$ ) deposited (by spin coating) on an FTO7 substrate. The band-gap of the material is represented by the red line (at  $0.514 \mu\text{m}$ ), the diffusion length by the green line and the current corresponding to the flat layer by the black line at  $J/J_{\text{flat}} = 1$  ( $J_{\text{flat}} = 8.39 \text{ mA/cm}^2$ ).

In Figure 40, typical of a thinner layer, the same trends are globally observed. However, the configuration differs from Figure 39 in two points.

First, the effect of  $a$  is much more pronounced, with nearly no impact for the smallest values of  $a$  ( $J_{\text{ph}} / J_{\text{ph,flat}} \cong 1$ ). Larger fluctuations of the photocurrent values are also exhibited, still considering the trendlines as reference. The decrease of the photocurrent for large values of the period  $T$  is still observed.

**In both graphs, the most favorable results in terms of predicted photocurrent (considering the trendline) are generally observed for  $T < L_d$ . For  $T \gg L_d$  the photocurrent values tend to decrease up to the  $J_{\text{ph,flat}}$  values.** The effect of  $a$  is less obvious. The plateau at  $J_{\text{ph}} / J_{\text{ph,flat}} \cong 1.5$  seems to be shared by the thick and the thin layers, provided  $a$  is greater than the band gap of  $\text{BiVO}_4$ . Far below (when  $a \ll \text{band gap}$ ) (black curve in Figure 40), no positive effect of texturing is observed. On the other hand, when  $a$  is close to the band gap, strong oscillations are observed. At this stage, it is hard to determine whether these fluctuations are physical or due to numerical simplifications.

In the Appendix 5.9 the graph of the  $\text{BiVO}_4/\text{ITO 12\_El}$  photoanode, follows the same trend as observed in Figure 39, the synthesis process of the two compared samples is the same.

**This simulation study, considering an hypothetical texture, confirms that the thickness of the layer is the main limiting factor**, which in turn, as observed by profilometry, determined the surface roughness, the latter having an additional positive impact on the electrocatalytic process.

## 4 Conclusions and perspectives

Different BiVO<sub>4</sub> photoanodes have been fabricated and characterized in terms of their physical and optical properties, and resulting photocurrent for water electrolysis. Table 9 compares the generated photocurrent in PEC cells based on different BiVO<sub>4</sub> photoanodes as a function of illuminated area and operating time.

Table 9. Generated photocurrent in photoelectrochemical devices: this study vs State of Art

	<b>Illuminated area (cm<sup>2</sup>)</b>	<b>Duration (h)</b>	<b><math>J_{ph}^*</math> (mA.cm<sup>-2</sup>)</b>	<b>Ref.</b>
CoPi-BiVO <sub>4</sub>	0.46 3 (electrode)	0.4	3.12	This work (Chapter 2)
Fe(Ni)OOH-Mo:BiVO <sub>4</sub>	0.25	5	5.82	Qiu <i>et al.</i> <sup>64</sup>
FeOOH/NiOOH - WO <sub>3</sub> /(W,Mo):BiVO <sub>4</sub>	2.25 (electrode)	168	5.35	Shi <i>et al.</i> <sup>167</sup>
NiOOH/Co <sub>3</sub> O <sub>4</sub> /BiVO <sub>4</sub>	3 (electrode)	90	6.4	Zhang <i>et al.</i> <sup>168</sup>
CoPi-BiVO <sub>4</sub> / WO <sub>3</sub> NRs biased by PV	1	0.16	6.72	Pihosh <i>et al.</i> <sup>63</sup>
2 CoPi-W:BiVO <sub>4</sub> and 2 Si SHJ	50	0.16	1.7	Ahmet <i>et al.</i> <sup>68</sup>

\*The photocurrent densities ( $J_{ph}$ ) are measured @ 1.23 V vs RHE.

Initial attempts in overcoming the performance limitations for large area BiVO<sub>4</sub> photoanodes are detailed by Ahmet *et al.* This work shows the coupling of two cobalt phosphate-coated tungsten-doped BiVO<sub>4</sub> photoanodes with series-connected silicon heterojunction solar cells. In this context, new limiting factors such as local pH gradients and cell design are identified to achieve higher photocurrent results.

This chapter, focused on analyzing the influence of electrode texture on the photocurrent delivered by the BiVO<sub>4</sub> photoanodes. Through optical simulations, the optical properties of the materials was defined useful for simulating the real textures of the photoanodes in CROWM. Subsequently, a numerical sensitivity study was conducted by simulating sinusoidal structures with selected amplitudes and periods (corresponding to periodic grooves) to identify how thickness and roughness limit the photoelectrochemical efficiency of the photoanodes.

From the experimental results, it was deduced that the performance of photoanodes manufactured by electrodeposition consistently exceeds that of photoanodes made by spin coating.

However, when comparing electrodes fabricated with the same process (i. e. electrodeposition), it was observed that the conductivity of the support plays a key role, and BiVO<sub>4</sub> electrodes made on FTO 7 glass coated substrate, generate greater photocurrent. Furthermore, the presence of catalysts and doping agents plays optimize the performance of photoanodes. Microscopy also confirmed that photoanodes made through electrodeposition exhibit a very porous structure, with a large concentration of active sites.

Optical simulations on real structures confirmed a dependence of performance on texture thickness and roughness, converging on a higher photocurrent generated by photoanodes

fabricated by electrodeposition; this result is also evident in experimental and simulated absorbance measurements.

The sensitivity study is a further confirmation of these conclusions.

Here, the most favorable results in terms of expected photocurrent (considering the trend line) occurred for  $T < L_d$  in both graphs (if  $a \geq \text{bandgap}$ ). Moreover, for the photoanodes made with electrodeposition, the photocurrent plateau observed on the left part of the Figure 39 allow to confirm higher  $J_{ph}$  values (for this type of electrodes).

In addition, the numerous oscillations in the Figure 40 and Figure 48 prevents us at this stage from concluding on an optimal texture to seek to maximize the photocurrent.

More investigations regarding active surface ( $\text{BiVO}_4/\text{ITO}$  12 surface area measured in appendix 5.5), as well as precise measurements of surface porosity and study of the impact of the tortuosity of the charge transport pathways, could be important to have more detailed results on the textures of heterogeneous structures and to identify further limiting phenomena.

Optical simulations in the presence of an electrolyte and considering the chemical reaction would allow for a better interpretation of these phenomena.

Beyond optical considerations only, the photoelectrolysis reaction, that is not taken into account by CROWM and TM, begins when the energy of the photons absorbed by the photoanode is equal to or greater than the bandgap of the semiconductor to generate electron-hole pairs. The excited electrons migrate from the valence band to the conduction band and afterward to the cathode, while the holes participate in the oxidation water reaction (anode side). At the same time, the diffusion length influences the efficiency of charge separation, the latter depends on various factors such as the macroscopic and microscopic structure, and the photoanode synthesis method.

It is likely that to reduce the oscillations in the photocurrent, it would be necessary to integrate the electron-hole interaction of a specific electrochemical reaction into the model, considering these two parameters (*band-gap* and  $L_d$ ) between the limiting factors.

## 5 Appendix

### 5.1 Chemicals

All the chemicals, unless specified otherwise, were bought from Sigma-Aldrich and used without further purification.

### 5.2 Table of manufactured photoanodes

Table 10. List of the characterized samples

Sample	SEM	XRD	PEC measurements		R-T	Thickness	ECSA
			without hole scavenger	with hole scavenger			
Ref. Al <sub>2</sub> O <sub>3</sub>	-	1	-	-	-	-	-
FTO 7		1			2	1	
FTO 80		1			2	1	
ITO 12		1			2	1	1
<b>Sol-Gel Spin Coating</b>							
BiVO <sub>4</sub> /FTO 7	1	1	3	3	2	1	
1.25 Mo:BiVO <sub>4</sub> /FTO 7	1		3	3	1	1	
2.5 Mo:BiVO <sub>4</sub> /FTO 7	1		3	3	1	1	
BiVO <sub>4</sub> /FTO 80		1	3	2	1		
1.25Mo:BiVO <sub>4</sub> /FTO 80			2	2	1		
2.5Mo:BiVO <sub>4</sub> /FTO 80			3	3	1		
<b>Electrodeposition</b>							
BiVO <sub>4</sub> /FTO 7	1	1	2	2	2	1	
CoPi-BiVO <sub>4</sub> /FTO 7	1	1	2	2	1	1	
BiVO <sub>4</sub> /FTO 80	1	3	2	2	2	3	
CoPi-BiVO <sub>4</sub> /FTO 80	1	1	3	2	1	1	
BiVO <sub>4</sub> /ITO 12	1	1	2	2	2	1	1
CoPi-BiVO <sub>4</sub> /ITO 12	1	1	2	2	1	1	

### 5.3 Ag/AgCl reference electrode

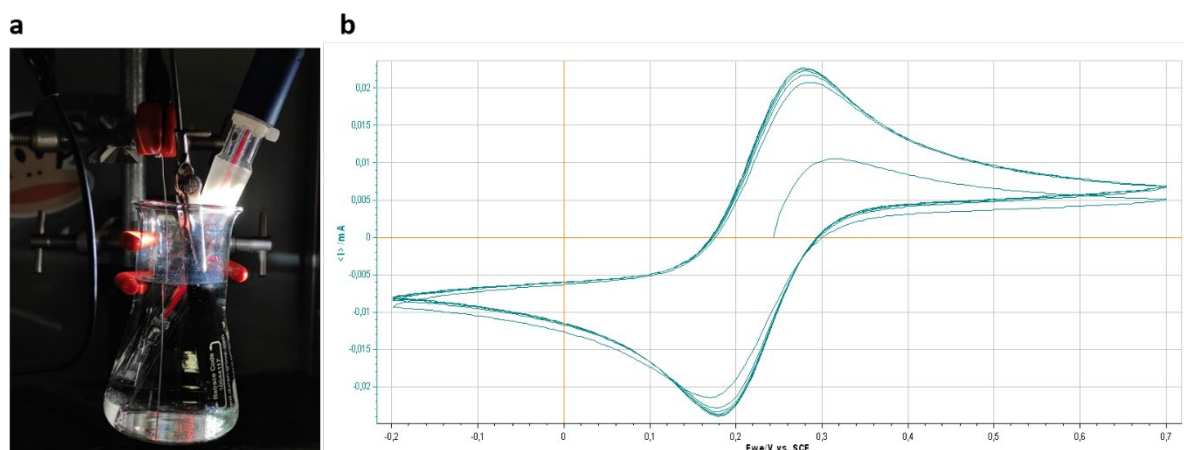


Figure 41. a) Preparation and b) calibration of Ag/AgCl 3 M KCl reference electrode.

Ag/AgCl in KCl has a simple structure and cost of fabrication lower than other reference electrodes. It was largely utilized in (photo)electrochemistry.

To prepare an Ag/AgCl reference electrode, a layer of AgCl is deposited on a silver wire. A silver wire (working electrode) is first cleaned, then surface activated by cyclic voltammetry (potential sweep from -0.3 to 1.2V vs. SCE) in a three-electrode configuration set-up (Figure 41a), using a carbon rod as counter electrode, a saturated calomel electrode (SCE) as reference electrode, and 0.5M H<sub>2</sub>SO<sub>4</sub> electrolytic solution,

The cycles are repeated until the peaks overlap 5 times in a row.

After that, the cleaned activated silver wire is immersed in a 0.1M FeCl<sub>3</sub> solution for 5 min. Finally, it is stored in a glass tube fitted with a frit and containing a saturated 3 M KCl solution. The electrode must rest in this environment for at least 24 hours before it can be used.

A calibration before the first manipulation have to be performed to ensure that the reference electrode is in good condition.

The calibration procedure takes place with a SP-300 potentiostat from Biologic in the typical three-electrode configuration, where a freshly polished glassy carbon rod is used as working electrode and a Pt wire as counter electrode.

The electrolyte solution is a 10 mM equimolar solution of potassium ferro-ferricyanide (K<sub>3</sub>/K<sub>4</sub>[Fe(CN)<sub>6</sub>]) in 0.1 M phosphate buffer (pH 7), with oxidation potential  $E_{Fe^{3+}/Fe^{2+}}^0 = 0.4247 V$  vs. *NHE* (normal hydrogen electrode).<sup>169</sup> A cyclic voltammetry was performed with scan rate of 100 mV/s and scan range from -0.4 V to 0.8 V vs. ref. Within this range, a redox couple for the  $Fe^{3+}/Fe^{2+}$  conversion was observed.

The value of the potential of this redox couple ( $E_{Fe^{3+}/Fe^{2+}}$ ), with respect to the Ag/AgCl 3M KCl reference electrode that have to be calibrated, was then deduced from the average position of the two electrochemical peaks (Figure 41b). Finally, the standard potential of the reference electrode  $E_{Ag/AgCl}^0$  was calculated with the following equation:

$$E_{Ag/AgCl}^0 = E_{Fe^{3+}/Fe^{2+}}^0 - E_{Fe^{3+}/Fe^{2+}} \quad \text{Eq. 36}$$

It has been observed a change over time in its potential, due to the incorporation of foreign elements in the KCl solution during operation or the obstruction of the Vycor glass frit.

As a consequence, the Ag/AgCl 3M KCl reference electrode was daily calibrated in order to ensure optical accuracy and to have the exact value of the  $E_{Ag/AgCl}^0$  before each photot electrochemical test.

All recorded potentials were subsequently converted to the reversible hydrogen electrode (RHE) potentials using Eq. 37.

$$E_{RHE} = E_{Ag/AgCl} + E_{Ag/AgCl}^0 + 0.059 \times pH \quad \text{Eq. 37}$$

## 5.4 KPi electrolytic solution

The 1M electrolytic phosphate buffer solution at pH 7 was prepared dissolving 27.218 g of potassium dihydrogen phosphate (KH<sub>2</sub>PO<sub>4</sub>) and 52.254 g of dipotassium hydrogen phosphate (K<sub>2</sub>HPO<sub>4</sub>) in 400 ml of distilled water. Then, it was adjusted to pH 7.0 using a sodium hydroxide solution, mixed and diluted with distilled water until 500 ml.

The hole scavenger solution was prepared adding 0.1M Na<sub>2</sub>SO<sub>3</sub> (5.042 g) in 0.5M of electrolytic phosphate buffer solution.

The 0.5M electrolytic phosphate buffer solution at pH 7 was prepared dissolving 13.609 g of potassium dihydrogen phosphate (KH<sub>2</sub>PO<sub>4</sub>) and 26.127 g of dipotassium hydrogen phosphate (K<sub>2</sub>HPO<sub>4</sub>) in 400 ml of distilled water. Then, it was adjusted to pH 7.0 using a sodium hydroxide solution, mixed and diluted with distilled water until 500 ml.

## 5.5 Electrochemical active surface area

The measured electrochemical active surface area (ECSA)<sup>170,171</sup> of a BiVO<sub>4</sub>/ITO 12 photoanode, made by electrodeposition, is 1.9 cm<sup>2</sup>.

The ECSA was calculated by the following equation:

$$ECSA = \frac{C_{DL}}{C_S} \quad \text{Eq. 38}$$

$C_S$  (0.07 mF.cm<sup>-2</sup>) is the specific capacitance of the ITO glass substrate, calculated from Figure 42a.

$C_{DL}$  is the double layer capacitance determined recording cyclic voltammograms at various scan rates ( $\nu$  from 0.005 to 0.5 V.s<sup>-1</sup>) within a potential region where no redox processes take place (between 0.4 V and 0.5 V vs Ag/AgCl), extracting the capacitive current  $I_C$  from the anodic and cathodic scans of the recorded voltammograms, and subsequently extracting  $C_{DL}$  (e<sup>-8.89</sup> F) from the trend line equation of the resulting  $\log(I)$  vs  $\log(\nu)$  plot (Figure 42b).



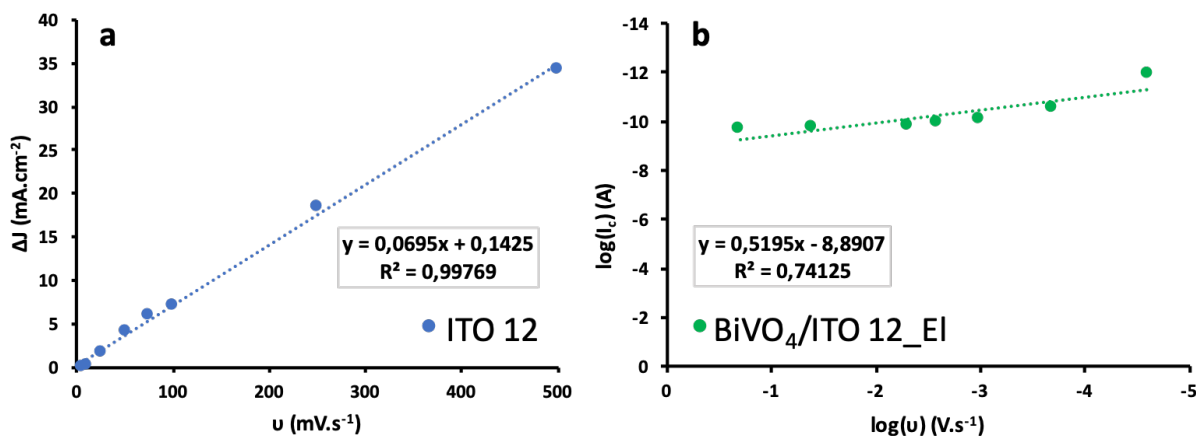


Figure 42. Capacitance calculation in order to determine the ECSA. a) Linear plot of current density of ITO 12 vs. scan rate. b) Logarithmic plot of the capacitive current of BiVO<sub>4</sub>/ITO 12\_EI vs. scan rate.

## 5.6 Photoelectrochemical tests using H<sub>2</sub>O<sub>2</sub> as hole scavenger

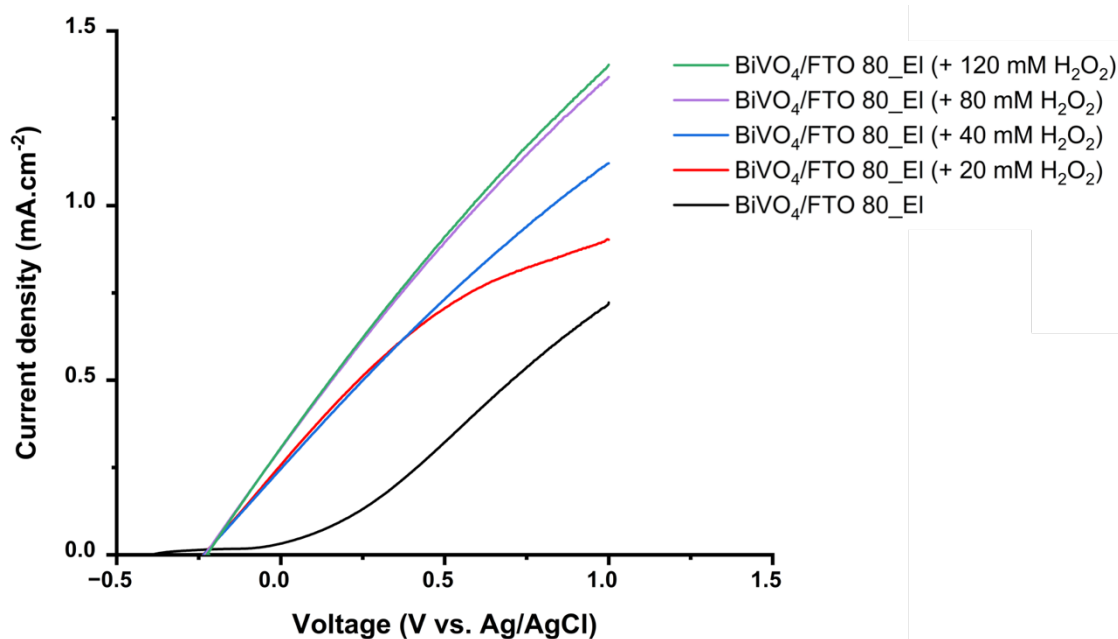


Figure 43. Linear sweep voltammograms of BiVO<sub>4</sub> photoanodes (illuminated surface 2.7 cm<sup>2</sup>) at different concentrations of hole scavenger (H<sub>2</sub>O<sub>2</sub>), under AM1.5G FI. BiVO<sub>4</sub>/FTO 80 in KPi 0.1M (black line), BiVO<sub>4</sub>/FTO 80 with 20 mM H<sub>2</sub>O<sub>2</sub> in KPi 0.1M (red line), BiVO<sub>4</sub>/FTO 80 with 40 mM H<sub>2</sub>O<sub>2</sub> in KPi 0.1M (blue line), BiVO<sub>4</sub>/FTO 80 with 80 mM H<sub>2</sub>O<sub>2</sub> in KPi 0.1M (green line), BiVO<sub>4</sub>/FTO 80 with 120 mM H<sub>2</sub>O<sub>2</sub> in KPi 0.1M (violet line).

All the photoanodes were made by electrodeposition: total charge density of 150 mC.cm<sup>-2</sup>. The photoelectrochemical set-up used in this experiment is explained in the manuscript of Duc Nguyen Ngoc<sup>136</sup>.

## 5.7 Scanning Electron Microscopy

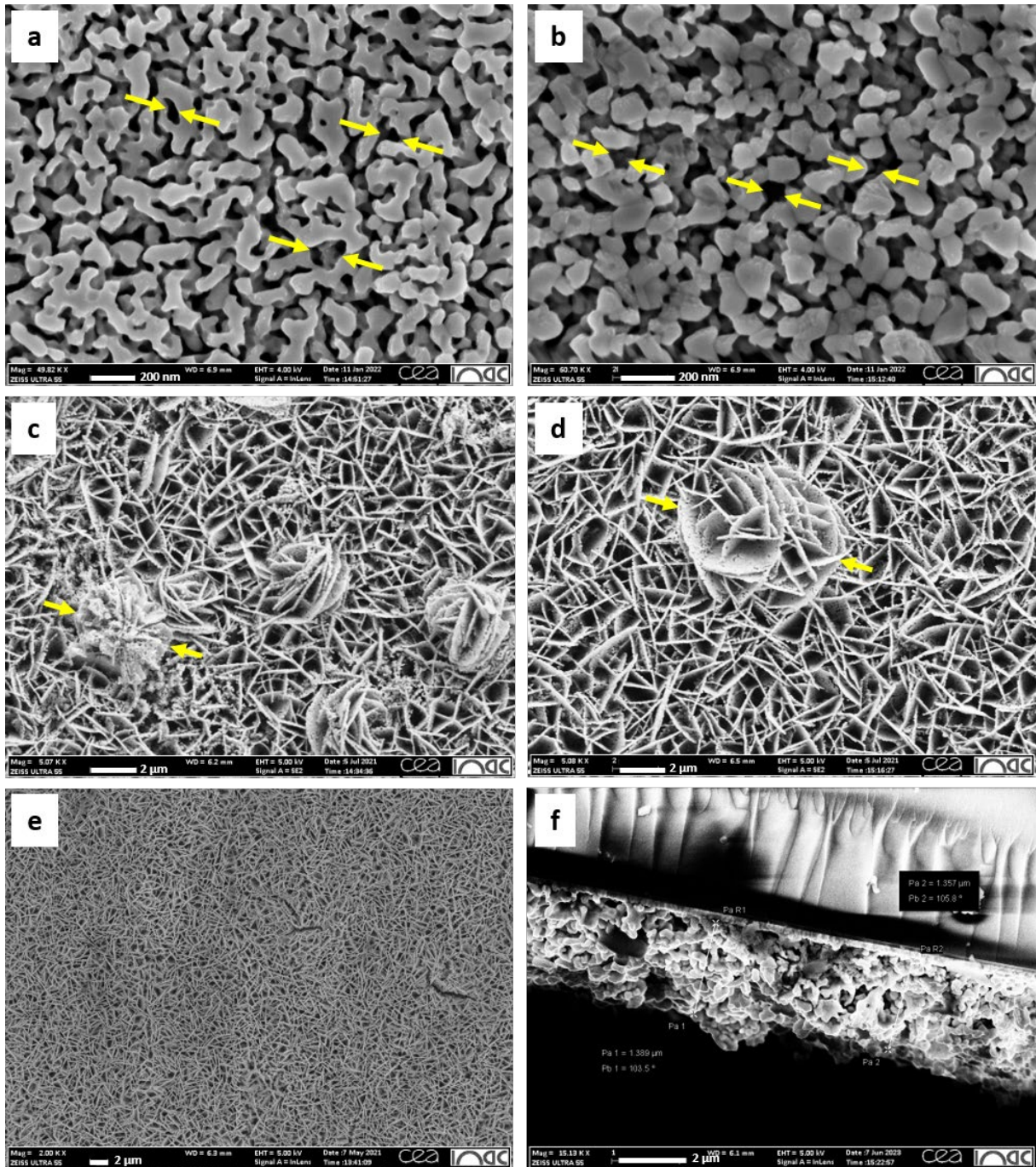


Figure 44. SEM images of BiVO<sub>4</sub> photoanodes. a) 1.25% Mo:BiVO<sub>4</sub>/FTO 7\_Sc. b) 2.5% Mo:BiVO<sub>4</sub>/FTO 7\_Sc. c) CoPi-BiVO<sub>4</sub>/FTO 7\_El. d) CoPi-BiVO<sub>4</sub>/FTO 80\_El. e) BiVO<sub>4</sub>/FTO 80\_Sc, as discussed in Sec. 2.6, no flowers are present. f) Section of BiVO<sub>4</sub>/FTO 80\_Sc for thickness measurements.

## 5.8 X ray diffraction: theoretical aspects

X-rays are electromagnetic radiation with wavelengths ranging from 0.01 to 10 nanometers; because their wavelengths are similar to the interatomic spacing in crystals, they are ideal tool for studying the geometry and shape of molecular and atomic structures. When the X-ray beam encounters the three-dimensional arrangements of atoms in crystalline and polycrystalline materials (e.g., BiVO<sub>4</sub> photoanode), it can either be absorbed or scattered.

The absorption of X-rays results in a photoelectric event occurring when the energy of a photon is transferred to a core-level electron, ejecting it from the atom. The majority of scattered X-rays interact destructively, canceling each other out. However, in specific directions, the beams interfere constructively, reinforcing each other. These reinforced diffracted X-rays (elastic scattering) create an X-ray diffraction pattern specific to the crystal structure considered. The constructive interference of monochromatic X-rays and a (poly)crystalline sample follows Bragg's Law<sup>172</sup> (Eq. 39):

$$n\lambda = 2d_{hkl}\sin\theta \quad n\lambda = 2d_{hkl}\sin\theta \quad \text{Eq. 39}$$

$$d_{hkl} = \frac{2\pi}{|Q_{hkl}|} \quad \text{Eq. 40}$$

where  $\lambda$  represents the photons wavelength, and  $\theta$  is half of the angle formed between the incident angle and the exit wave, as illustrated in Figure 45a.

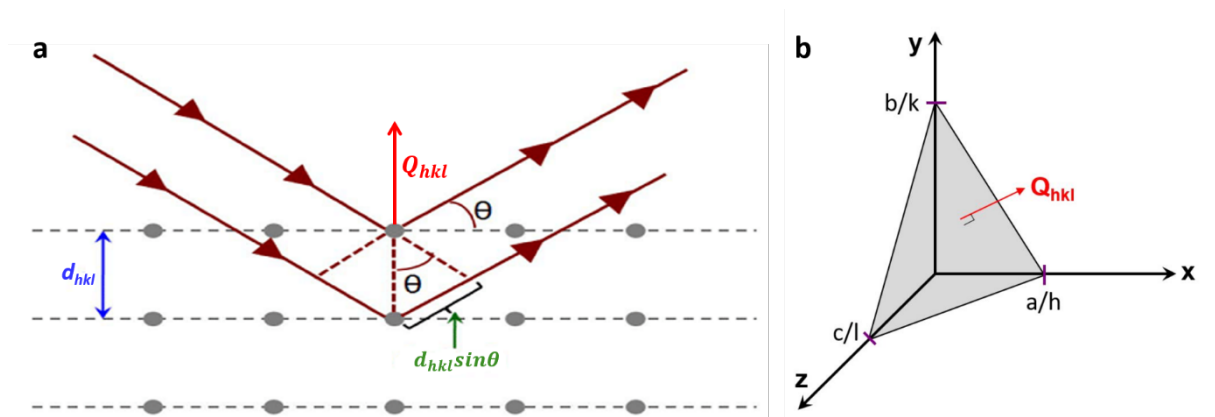


Figure 45. a) Bragg condition of diffraction. b)  $(hkl)$  plane, its intersection with the  $x$ ,  $y$  and  $z$  axis at, respectively  $a/h$ ,  $b/k$  and  $c/l$ . Lattice vector  $Q_{hkl}$  perpendicular to the plane.

The inter-reticular distance,  $d_{hkl}$ , i.e. the distance between two parallel planes), which is related to the lattice parameters ( $a, b, c$  and  $\alpha, \beta, \gamma$ ) via the Eq. 40.

$Q_{hkl}$  denotes the lattice vector perpendicular to the  $(hkl)$  plane family it characterizes.

**Remark.** It is important to underline that that in a crystal, the different families of parallel and equidistant planes can be identified using the Miller indices  $(h, k, l)$ :  $(100)$  represents a plane orthogonal to direction  $\mathbf{h}$ ,  $(010)$  a plane orthogonal to direction  $\mathbf{k}$  direction, and  $(001)$  a plane orthogonal to direction  $\mathbf{l}$ .  $(h, k, l)$  represents the family for which the plane closest to the origin (but not containing it) intercepts the  $x$ ,  $y$ ,  $z$  axis at  $a/h$ ,  $b/k$ ,  $c/l$ , respectively (Figure 45b).

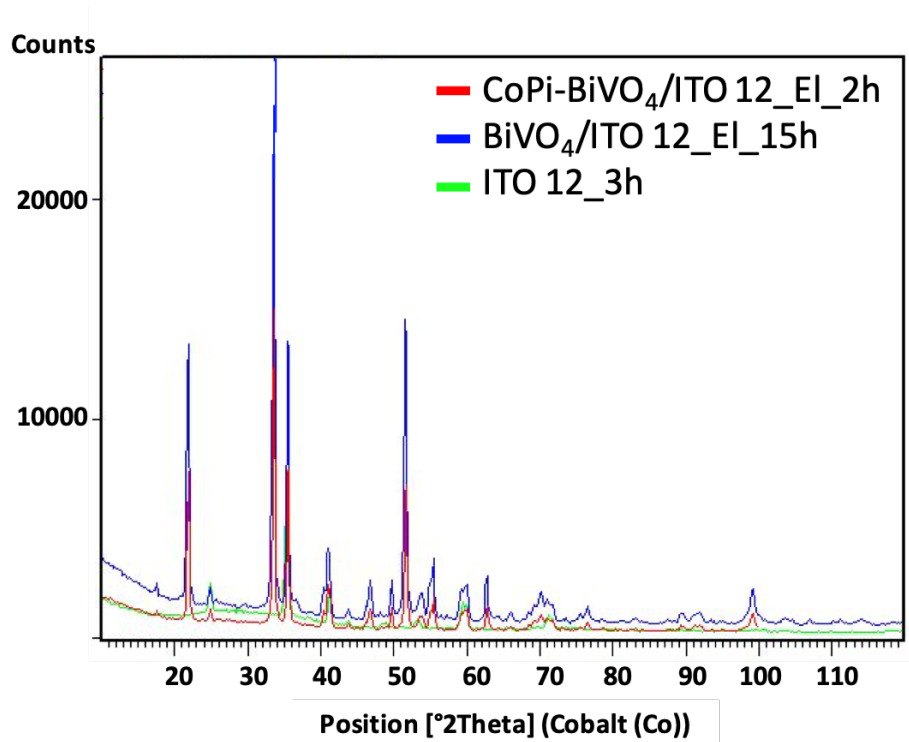


Figure 46. XRD patterns of CoPi-BiVO<sub>4</sub>/ITO 12\_EI (red line), BiVO<sub>4</sub>/ITO 12\_EI (blue line) and ITO 12 coated glass (green line).

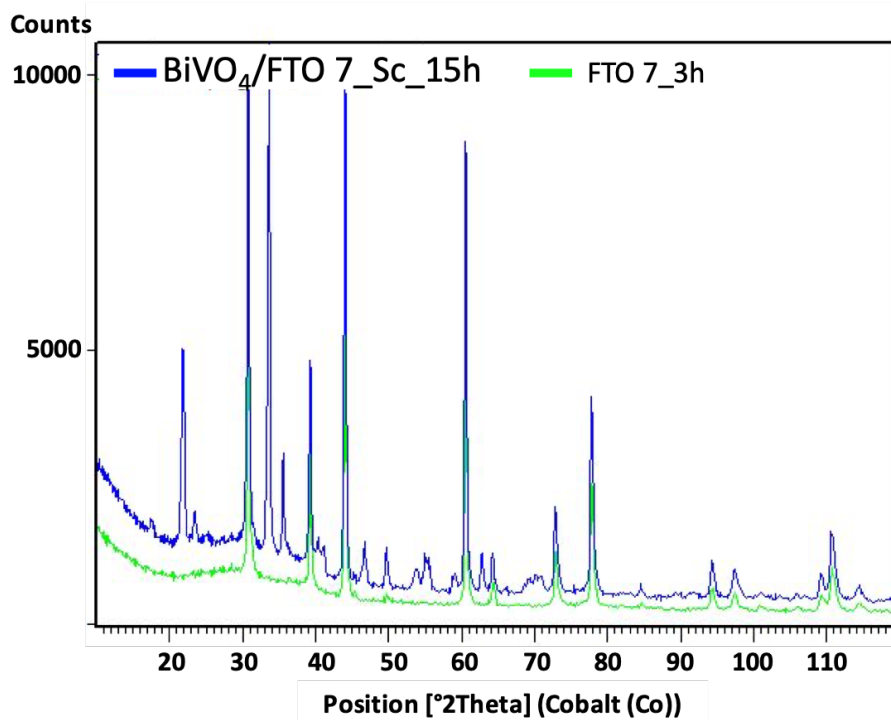


Figure 47. XRD patterns of BiVO<sub>4</sub>/FTO 7\_Sc (blue line) and FTO 7 coated glass (green line).

## 5.9 Numerical Sensitivity Study: supplementary information

Table 11. Values of T and a considered for the sensitivity analyses performed.

BiVO <sub>4</sub> /FTO 7_EI			BiVO <sub>4</sub> /FTO7_EI			BiVO <sub>4</sub> /FTO7_EI		
<b>a1 = 25%h</b>	<b>a2 = 50%h</b>	<b>a3 = 75%h</b>	<b>a1 = 25%h</b>	<b>a2 = 50%h</b>	<b>a3 = 75%h</b>	<b>a1 = 25%h</b>	<b>a2 = 50%h</b>	<b>a3 = 75%h</b>
0.325	0.650	0.975	0.176	0.353	0.529	1.072	2.144	3.217
<b>T(μm)</b>	<b>T(μm)</b>	<b>T(μm)</b>	<b>T(μm)</b>	<b>T(μm)</b>	<b>T(μm)</b>	<b>T(μm)</b>	<b>T(μm)</b>	<b>T(μm)</b>
0.003	0.006	0.010	0.002	0.004	0.005	0.011	0.021	0.032
0.016	0.032	0.049	0.009	0.018	0.026	0.054	0.107	0.161
0.032	0.065	0.097	0.018	0.035	0.053	0.107	0.214	0.322
0.081	0.162	0.244	0.044	0.088	0.132	0.268	0.536	0.804
0.162	0.325	0.487	0.088	0.176	0.265	0.536	1.072	1.608
0.244	0.487	0.731	0.132	0.265	0.397	0.804	1.608	2.413
0.325	0.650	0.975	0.176	0.353	0.529	1.072	2.144	3.217
0.433	0.866	1.299	0.235	0.471	0.706	1.430	2.859	4.289
0.541	1.083	1.624	0.294	0.588	0.882	1.787	3.574	5.361
0.650	1.299	1.949	0.353	0.706	1.059	2.144	4.289	6.433
1.624	3.248	4.873	0.882	1.764	2.647	5.361	10.72	16.08
3.384	6.767	10.15	1.838	3.676	5.514	11.17	22.34	33.51
10.83	21.66	32.48	5.881	11.76	17.64	35.74	71.48	107.2
16.24	32.48	48.73	8.822	17.64	26.47	53.61	107.2	160.8
32.48	64.97	97.45	17.64	35.29	52.93	107.2	214.4	321.7



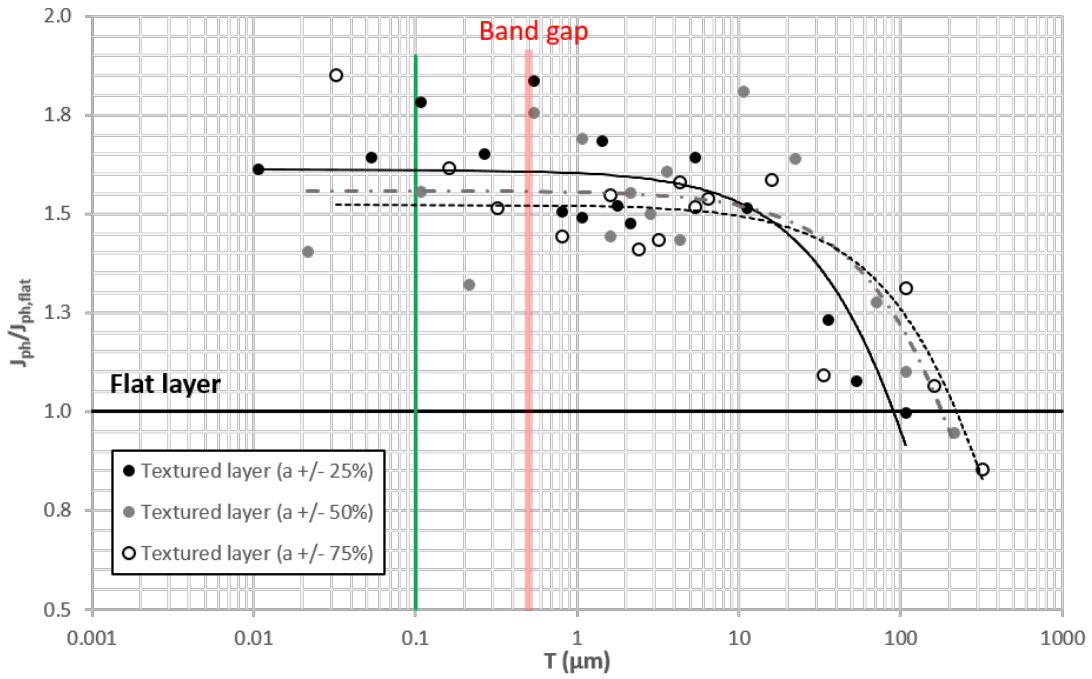


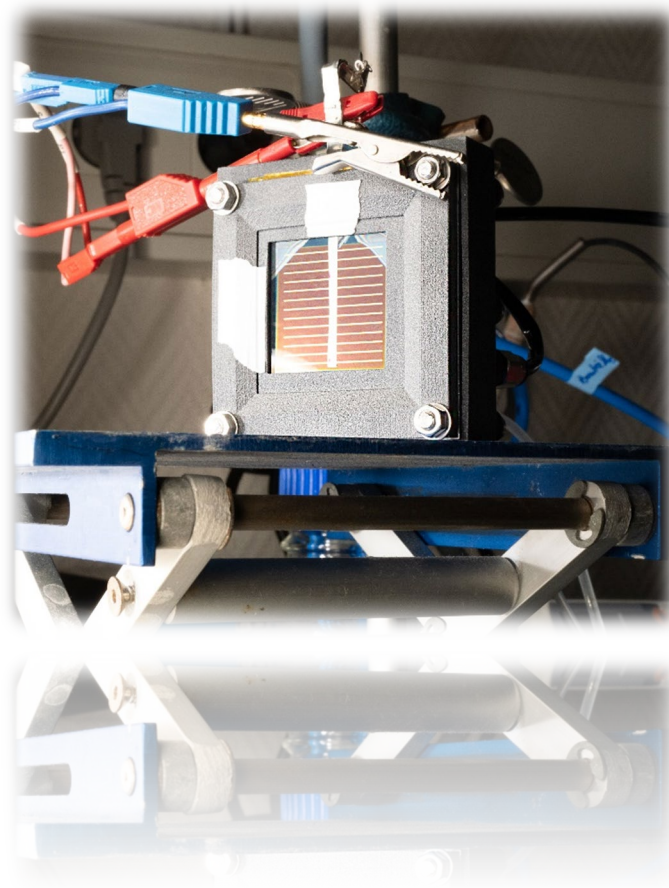
Figure 48. Evolution of photocurrent with microgroove characteristics for a BiVO<sub>4</sub> layer of average thickness 4.3 μm ( $a = 1.07 / 2.14 / 3.22 \mu\text{m}$ ) deposited (by electrodeposition) on an ITO 12 substrate. The band-gap of the material is represented by the red line (at 0.514 μm) and the current corresponding to the flat layer by the black line ( $J_{\text{flat}} = 5.68 \text{ mA/cm}^2$ ).





## Chapter 3:

### **Thermally integrated, scalable, 3D-printed photoelectrochemical cells and modules based on perovskite / silicon tandem solar cells for high-efficiency hydrogen production**



## Chapter 3:

# Thermally integrated, scalable, 3D-printed photoelectrochemical cells and modules based on perovskite / silicon tandem solar cells for high-efficiency hydrogen production

In Chapter 2, various BiVO<sub>4</sub> photoanodes were fabricated, characterized and tested. This has enabled us to unravel a major point in PEC scaling, associated with the impact of the large-scale materials development process on their performance.

In the remainder of this thesis, the focus will be on the "process" aspects associated with device scaling. To this end, the work performed with materials (light absorbers, catalysts for water electrolysis, membranes for gas separation) that are already state-of-the-art for their specific function, and whose fabrication is well mastered, at least for sizes of 10 cm<sup>2</sup>.

Progressing towards a higher TRL, Chapter 3 looks at the integration of the necessary steps from "light capture" to "H<sub>2</sub> production", first in a cell of around 7 cm<sup>2</sup>, combining a Si/Pk tandem solar cell and a Nafion-based PEM for water electrolysis, sharing the same active surface.<sup>173</sup>

Then a numbering-up strategy is proposed, based on monolithic IPEC modules of around 350 cm<sup>2</sup> (scale factor approx. 50), each comprising 9 IPEC cells, thanks in particular to the mutualization and arrangement of fluid circuits.<sup>174</sup>

The contents of this chapter will shortly be submitted for publication to a peer review journal.

### 1 Introduction

The direct conversion of solar energy and water into chemical energy via the production of a fuel, such as hydrogen, is a topic that has recently gained substantial interest.

Solar energy can be used to directly drive the water splitting redox reactions, in order to reduce the complexity of the actual devices, eliminating the need for separated power generation and electrolyser systems.

Many different technologies have been investigated so far to produce hydrogen from sunlight and water. To reach maturity, such technologies should be at the same time *i*) efficient (in terms of *STH* efficiency), *ii*) stable under intermittent operation and over years of operation, and *iii*) scalable, which means that they should rely on Earth-abundant materials and cost- and energy-effective processes.<sup>175</sup> The main challenge is to achieve high *STH* efficiency with low cost materials (light absorbers, catalysts, membranes) and to overcome barriers that limit the scalability and the stability of such new technologies.

Possible architectures include Photovoltaic-Electrolyser (PVE) cells, Photocatalytic (PC) cells, Photoelectrochemical (PEC) cells.

Today, the most efficient way to produce solar hydrogen, with up to 30% *STH*, is through the combination of III-V absorbers in a multijunction (i.e. InGaP/GaAs/GaInNAsSb) cell

connected with electrolysers. This mature technology guarantee high performance stability<sup>48</sup> but it is associated with high investment costs<sup>176</sup>. A monolithic buried junction device using the same high efficiency high-cost components reaches 19% STH, though with lower stability because of the corrosion of III-V semiconductor materials in contact with liquid electrolytes.<sup>44,177</sup>

Alternatively, the use of PC inorganic metal oxide particles either as slurries or deposited onto solid substrates has demonstrated long term stability and potential for scalability (with a recent demonstration over 100 m<sup>2</sup>).<sup>70</sup> But this type of device has so far been limited to a low STH yield and requires the downstream separation of O<sub>2</sub> and H<sub>2</sub>.<sup>178</sup> The maximum STH efficiency achieved on a large-scale photocatalytic water splitting system (4 cm × 4 cm photocatalyst wafer) was of 6.2%, with highly concentrated natural solar light intensity (~ 161 sun).<sup>179</sup>

Photoelectrochemical (PEC) cells combine the versatility of electrochemical devices with the possibility to separate the H<sub>2</sub> and O<sub>2</sub> gas respectively produced in the cathodic and anodic compartments. They can accommodate a variety of materials with precise control of the interfaces between supports, semiconductors for light harvesting and charge separation, and catalysts. Low-cost semiconductors<sup>180</sup> for PEC water splitting have recently reached STH peaks of 10 %, while the US Department of Energy (DoE) recommends and targets STH efficiencies of at least 20% for systems to be commercially viable<sup>181</sup>. Techno-economic analysis demonstrated that PEC technology can become competitive with current H<sub>2</sub> production from fossil resources by 2050.<sup>182-184</sup> Among photoelectrochemical devices, the Integrated-PEC (IPEC) cells<sup>47</sup> were considered highly important, in which they combine photovoltaic modules, such as tandem cells and electrolysers. They are currently considered the most promising technology for short-term deployment, with reduced projected costs.

Tandem cells coupling halogenated hybrid perovskites with silicon solar cell represent a new generation of solar devices. This integration aims to minimize thermalization losses and takes advantage of the bandgap energy range of these materials. Recent works report the association of a perovskite / silicon tandem solar cell with an electrolysis device, with a *STH* close to 18-19% in early 2020<sup>185,186</sup>, up to 20% in 2021<sup>187,188</sup>, and reaching 21.5% in 2023<sup>66</sup>. Currently, the theoretical maximum STH value for a tandem PEC system is 29.7%.<sup>189</sup>

To date, studies on the integration of PK / Si tandems in electrolysers have focus mainly on STH efficiency, neglecting other aspects of future commercial applications. First of all, no data is reported on performance repeatability, and very few studies consider device scalability. The technological readiness level of the reported devices is still low: proof of concept has been established for laboratory-scale devices so far (ranging in surface area from a few mm<sup>2</sup> up to 1.42 cm<sup>2</sup>) whose stability is tested under continuous and constant illumination for up to 20 h. It is necessary to bring such a concept to a higher TRL, starting with a fully integrated and scalable device with a surface area greater than 1 cm<sup>2</sup>.

This work presents a thermally optimized, monolithic IPEC cell that effectively combines a perovskite / silicon tandem solar cell with an innovative hybrid metal / polymer PEM electrolyser. The device is an integrated cell from both electrical, thermal and fluidic points of view (efficient gas separation), which facilitates scale-up and prefigures industrial deployment of compact solar fuel generators. The IPEC cell was first realized and tested at small scale (*i.e.* single cell with 7.6 cm<sup>2</sup> solar active surface) then scaled-up to a 68.4 cm<sup>2</sup> solar active surface, by designing an original 21 × 22 cm<sup>2</sup> IPEC module.<sup>173,174</sup> Five of these IPEC modules were finally combined, with a total active area of 342 cm<sup>2</sup>, enabling a more in-depth study of the stability and repeatability of their performance under real-life conditions. More specifically, the gain enabled by thermal integration via the machining of a heat exchanger on the cathode side

of the IPEC was first assessed. An analysis of the repeatability of the results for each IPEC cell and IPEC module was then carried out, *i*) in the laboratory, comparing their photoelectrochemical performance during "day-night" cycles and the ageing of the photovoltaic module, and *ii*) outdoors, during autonomous operation for 72 hours<sup>190</sup>, on the 45 IPEC cells divided into five IPEC modules.

These results provide a unique database on the expected dispersion in scale-up and numbering up (encompassing dispersion linked to mass production and variability linked to the actual environment of each cell in a scaled device). They also enable us to position our device within the current state of the art.

## 2 Materials and methods

### 2.1 Component description

#### 2.1.1 Tandem solar cell fabrication and encapsulation

*Silicon bottom cell fabrication.* Silicon heterojunction bottom cells are processed starting from commercially available n-type float-zone (100) oriented both side polished silicon wafers (chemical mechanical polishing), 4 inch size, with a thickness between 260 and 300  $\mu\text{m}$  and a resistivity between 1 and 5  $\Omega\cdot\text{cm}$ . A wet cleaning with hydrofluoric acid (HF) and hydrochloric acid (HCl) is performed to remove native oxide and contaminants, before the deposition of intrinsic amorphous silicon layers (a few nanometers thick) on both sides of the wafer, by plasma enhanced chemical vapour deposition (PECVD) at 200 °C with  $\text{SiH}_4$  and  $\text{H}_2$  gases. Doped amorphous silicon layers are then deposited by PECVD on each side of the wafer, adding phosphine gas ( $\text{PH}_3$ ) for the n-doped a-Si:H layer and diborane ( $\text{B}_2\text{H}_6$ ) for the p-doped a-Si:H. The back-side electrode, made of indium tin oxide (ITO), is then deposited by sputtering. The recombination layer, also made of ITO, is then deposited by physical vapor deposition (PVD). Thickness and carrier density are adjusted to provide enough recombination centers in the bulk of the layer while maintaining an acceptable transparency in the infrared range.

*Perovskite top cell fabrication.* Silicon heterojunction bottom cell wafers are laser cut to  $5 \times 5 \text{ cm}^2$  size. A layer of 200 nm silver is then thermally evaporated to form the back-side electrode. The electron transport layer (ETL) is prepared from a commercially available tin oxide ( $\text{SnO}_2$ ) nanoparticles colloidal suspension diluted in deionized water. Perovskite and hole transport layers are prepared in a glovebox the day before deposition, as follows. The formamidinium lead iodide ( $\text{FAPbI}_3$ ), lead bromide ( $\text{PbBr}_2$ ) and cesium iodide ( $\text{CsI}$ ) mother solutions are prepared by dissolving lead iodide ( $\text{PbI}_2$ ) and formamidinium iodide ( $\text{FAI}$ ) in a N,N-dimethylformamide/dimethylsulfoxide mixture (DMF/DMSO) at 40 °C,  $\text{PbBr}_2$  in DMF/DMSO mixture at 40 °C and  $\text{CsI}$  in DMSO at ambient temperature. The solution of  $\text{Cs}_x\text{FA}_{1-x}\text{Pb}(\text{I}_{1-y}\text{Br}_y)_3$  is prepared the next day, mixing in a vial the  $\text{FAPbI}_3$ ,  $\text{PbBr}_2$  and  $\text{CsI}$  solutions so that  $x = 0.05$  and  $y = 0.17$ . The hole transport layer (HTL) is prepared as follows: poly (triaryl amine) (PTAA) is dissolved in toluene and lithium bis(trifluoromethylsulphonyl)imide (Li-TFSI) in acetonitrile at ambient temperature, then Li-TFSI solution and 4-tert-butylpyridine (tBP) are added to the PTAA solution, and the resulting mixture is kept at 65 °C overnight. Right before the top cell fabrication, a 30 min UV-ozone surface treatment is applied to the recombination ITO. Cells are immediately introduced into the glovebox to perform further steps under inert nitrogen atmosphere. The  $\text{SnO}_2$  colloidal suspension is spin-coated on the recombination ITO, followed by annealing at 80 °C for 1 min on a hot plate. The perovskite layer is then deposited by spin-coating, with a chlorobenzene quenching step to promote perovskite crystallization. Annealing is performed on a hot plate at 100 °C for 1 h. The HTL is then formed on top of the perovskite by spin-coating the PTAA

solution. The transparent front side electrode is obtained by sputtering at ambient temperature to form a 100 nm thick ITO layer. A 200 nm thick gold grid, thermally evaporated, is finally added. Devices are then stored in the dark in ambient air before use.

*Solar cells encapsulation.* A conductive metal ribbon (3M 3007 solar tape) is manually pressed on the solar cells front and back sides. The  $5 \times 5 \text{ cm}^2$  glass lids are cleaned using acetone, isopropanol and water and dried in an oven for 1 h. An epoxy glue is manually spread over the cells front side before carefully placing the glass lid on top. Glue thickness is adjusted to around 120  $\mu\text{m}$  thanks to tape separators placed at the cells corners. Crosslinking is then triggered by 400 nm incident photons provided by a DELOLUX source (LED) for 2 min. Cells are stored in the dark and in ambient air before use.

### 2.1.2 PEM electrolyser

The proton exchange membrane (PEM) electrolyser consists of two current collector plates with flow channels (cathodic and anodic) between which the membrane electrode assembly (MEA) is interposed, on either side of which the gas release reactions take place. All components are placed in an anodic box, which is essential for closing the device and managing water distribution and collection.

Catodic and anodic plates, as well as the anodic box, are manufactured using 3D printing<sup>191</sup>, to maximize the cell's compactness, with metal being replaced by polymer where the function of the component allows. This makes it possible to reduce the weight of the cell, develop alternative energy conversion devices and break the restrictions of traditional hydrogen manufacturing methods for hydrogen generators.

The anodic box is made of polyoxymethylene (POM), a technical thermoplastic.

The anodic flow-plate features a machined flow channel consisting of six serpentines, each 1 mm wide, which distribute the preheated water evenly over the entire anode surface. The serpentine flow channel is manufactured from polypropylene (PP) by Fused Deposition Modeling (FDM). A 200 nm thick electrically conductive gold layer was deposited on the flow area of the PP plate using the electron-beam physical vapour deposition (EBPVD) technique.

The MEA was prepared using a Nafion NRE-212 membrane (50  $\mu\text{m}$  thick, Alfa Aesar), iridium black (Alfa Aesar) as the anode catalyst with a fixed loading of  $5.7 \text{ mg}\cdot\text{cm}^{-2}$ , and 0.5  $\text{mg}\cdot\text{cm}^{-2}$  60% Pt-Vulcan/carbon cloth gas diffusion electrode (FuelCellStore) as cathode. The anode catalyst ink was deposited by drop-casting onto a  $12.3 \text{ cm}^2$  area of a decal substrate poly(tetrafluoroethylene) (PTFE)-coated fiberglass cloth (Plastic Elastomer) until the desired catalyst loading was reached. The cathode electrode and the coated decal substrate were assembled by sandwiching the Nafion membrane and hot-pressing it at 120 °C for 90 s under 5 MPa. The anode catalyst was transferred to the Nafion membrane by peeling off the decal substrate following the hot-pressing process.

The cathodic plate is made of 316L stainless steel by additive manufacturing (AM) using Laser Powder Bed Fusion (LPBF) technology, also known as Selective Laser Melting (SLM). The laser is used to melt and solidify metal powder in a specific area, which is then molded into a layer-by-layer stack. After each cycle, the powder is raked or rolled onto the previous consolidated layer. Thanks to this technique, it was possible to integrate thirteen parallel channels into the metal mass. These channels, with their 2.3 mm side, are distributed across the entire width of the plate, the outer face of which is designed to host the solar cell, and thus enable optimum distribution of the water to be preheated. The integrated pin flow channel

design, facing the MEA, was chosen for its enhanced performance compared to “conventional” flow channels due to reduced ohmic resistance <sup>192</sup>.

A Pt-coated titanium grid (254  $\mu\text{m}$  thick, 12.25  $\text{cm}^2$ , FuelCellStore) was added on the anode side without pressing during the PEM electrolyser cell assembling. The cell is closed with silicon gaskets (GETELEC), nuts and bolts.

### 2.1.3 IPEC cell and module

In the IPEC cell, the PEM electrolyser and the perovskite / silicon tandem solar cell (PV) are electrically connected via the external surface of their cathode sides. This direct integration is enhanced by the intercalation of an indium sheet between the two sides. The face-to-face contact does not induce any additional series resistance to that measured at the solar cell terminals. To conduct the holes to the water oxidation sites, the positive terminal (anode) of the tandem solar cell is connected to the anode of the electrolyser via a low-resistivity tin-plated copper ribbon, a silver wire and a platinum wire. Finally, a mask in polyamide 11 (PA11) is positioned around the PV to precisely define the irradiated surface.

The IPEC module has been developed to integrate nine individual IPEC cells. The module anodic box is manufactured in a single piece to optimize thermal integration, limit both the number of steps for fluidic assembly and the risk of leaks. The nine IPEC cells are electrically independent and in series 3 by 3 in terms of fluid management.

The details of the main components of the IPEC cell and module are summarized in Table 12.

Table 12. Components of the IPEC cell and module

Component	Detailed description
<b>Anodic box</b>	Polyoxymethylene (POM), 7 × 7 $\text{cm}^2$ (cell), 21 × 22 $\text{cm}^2$ (module)
<b>Anodic plate</b>	Current collecting plate with flow channels, 3D-printed polypropylene (PP): active flow area of 3.5 × 3.5 $\text{cm}^2$ , 6 machined serpentine channels of 1 mm width Electrically conductive coating: sputtered bilayer of Cr/Au (5 nm/200 nm)
<b>Pt wire</b>	4 cm length, 1 mm diam. (Alfa Aesar), ensures electrical contact between anode and solar cell
<b>Pt/Ti grid</b>	Platinum-coated titanium grid (254 $\mu\text{m}$ thick, 3.5 × 3.5 $\text{cm}^2$ , FuelCellStore)
<b>Membrane Electrode Assembly</b>	Anode catalyst: 5.7 $\text{mg cm}^{-2}$ Ir black (Alfa Aesar) Nafion NRE-212 membrane (50 $\mu\text{m}$ thick, Alfa Aesar) Gas diffusion cathode: 0.5 $\text{mg}\cdot\text{cm}^{-2}$ 60% Pt-Vulcan/carbon cloth (FuelCellStore) Active surface area of 3.5 × 3.5 $\text{cm}^2$
<b>Gaskets</b>	Silicon (GETELEC) of thickness: 300 $\mu\text{m}$ anode side, 200 $\mu\text{m}$ cathode side, 1 mm between anodic plate and anodic box
<b>Cathodic plate</b>	Current collecting plate with flow channels, 3D-printed 316L stainless steel: external area 6.5 × 6.5 $\text{cm}^2$ , active flow area of 3.5 × 3.5 $\text{cm}^2$ , flow channels consisting of 1 mm width-cubic pins, internal heat exchanger with 13 machined flow channels of 2.3 mm diameter

<b>In sheet</b>	Indium film 100 $\mu\text{m}$ -thick (Chimie Tech Services), ensures electrical contact between cathodic box and solar cell backside
<b>Solar cell</b>	Perovskite / silicon tandem solar cell: $3 \times 3 \text{ cm}^2$ on a $5 \times 5 \text{ cm}^2$ substrate, metallization shading of ca. 15 % of the illuminated surface, $7.6 \text{ cm}^2$ active area
<b>Mask</b>	Polyamide 11 (PA11): external area $6.5 \times 6.5 \text{ cm}^2$ , internal area $10.24 \text{ cm}^2$

## 2.2 Characterization and performance measurement

### 2.2.1 Photovoltaic efficiency measurement

A class A solar simulator (Oriel 92190, Xe source and AM1.5 filter) is used to simulate solar irradiation in continuous mode. Current-voltage  $I(V)$  curves of the illuminated cells are recorded using a Keithley 2602A source measure unit (SMU). Calibration is performed with a standard silicon solar cell (monocrystalline silicon solar cell, WPVS) from Fraunhofer ISE and a spectrophotometer (Aescusoft). The electrical connection of the cells is ensured either by gold probes positioned on the front side and a metal chuck on the back-side, or (in the case of encapsulated devices) using crocodile clamps placed on the metal ribbons. An  $8.5 \text{ cm}^2$  mask is used in all cases. Unless otherwise stated, results are not corrected for the shading losses due to metal contacts (estimated at around 15 %).

Acquisitions are monitored with a homemade Labview software. Several  $I(V)$  sweeps are performed under continuous illumination and under the following conditions, until the efficiency stabilizes: reverse scans (from 2.2 V to  $-1.5 \text{ V}$ ) with one scan every 10 s, steps: 50 mV, dwell time: 20 ms, scan speed:  $1.36 \text{ V}\cdot\text{s}^{-1}$ , number of power line cycles (NPLC) set to 1, cell kept at open circuit between measurements.

### 2.2.2 Active area measurement

The aperture of all masks was determined using ImageJ software and a calibrated scale for accuracy. The aperture of the standard mask used to characterize the photovoltaic cells (according to 2.2.1) was  $8.5 \text{ cm}^2$ . The aperture of the mask placed on the solar cells integrated into the IPEC cells was  $10.2 \text{ cm}^2$ . The active area of IPEC cells was determined by contrast analysis, to identify the area where all layers of the solar cells are present ( $9.0 \text{ cm}^2$ , corresponding to the PVD hard mask), from which the shaded areas are subtracted (Figure 55 in Appendix). These have variable surface, depending on the alignment of the ribbon on the metallization. On average, a shaded area of  $1.4 \text{ cm}^2$  was obtained, leading to an active area of  $7.6 \text{ cm}^2$  for the IPEC cells (Table 17 in Appendix).

### 2.2.3 (Photo)Electrochemical measurements

The set-up for electrochemical measurements, along to the electrochemical reaction cell, includes two peristaltic pumps (PP1300, WVR), an ultrapure water (Milli-Q) reservoir with temperature controller (Pilot ONE HUBER circulation thermostat), and a computer-controlled potentiostat (SP-300 Bio-Logic with a  $\pm 10 \text{ A}/[0, 5] \text{ V}$  booster). For a series of specific measurements, two separate water circuits were installed, one to pump water into the internal heat exchanger of the cathodic plate and the other directly to the anodic flow side. Before starting operation and measuring, water was pumped for 30 min into the IPEC cell at a flow rate of  $5 \text{ mL}\cdot\text{min}^{-1}$ . A REGLO-CPF Digital reciprocated pump with piston pump-head RHOCKC was used to deliver  $17 \text{ mL}\cdot\text{min}^{-1}$  for an IPEC module. A Hioki Memory HiLogger



(LR8431-20) and several temperature sensors were used to control the temperature of the various parts of the IPEC cell or module.

The performance of MEA in PEM electrolyser was evaluated by recording their polarization curves from 0 to 1.6 V with a scan rate of  $10 \text{ mV}\cdot\text{s}^{-1}$ . The curves were *iR*-corrected by carrying out automatically ohmic drop compensation by the EC-Lab software using the electrochemical impedance technique (ZIR).

A Solaronix Solar simulator (M205 500-1300 We SN:120125-16; FADEC Software – Multiple Light Engine Version) was used for the photoelectrochemical measurements. The IPEC cell (or module) is positioned facing the light beam. The IPEC device and the potentiostat are connected in series as follows: the working electrode port of the potentiostat connected to the top contact (+) of the solar cell, the bottom contact (–) of the solar cell connected to the cathode (–) of the electrolyser, the counter electrode port of the potentiostat connected to the anode (+) of the electrolyser. The reference electrode port of the potentiostat is connected to the counter electrode port in order to measure the current passing through the closed system. No additional potential was applied. Chronoamperometry (CA) measurements were carried out under a fixed irradiation power density (1 sun) and under light/dark cycles.

The operating voltage and current of the tandem integrated in the IPEC cell were measured using a multimeter (RS:123-3245, range 2V, resolution 1 mV, error:  $\pm 0.5 \%$ ).

#### **2.2.4 Gas flow measurements**

For single IPEC cells and PEM electrolyzers, (photo)electrochemical measurements are coupled with a gas detection device (MilliGascounter type MGC-1 PMMA, RITTER) to quantify the  $\text{H}_2$  volume and flow rate. The MGC-1 is specially adapted to small gas flow rates with an error smaller than  $\pm 1 \%$  in the range  $1 \text{ mL}\cdot\text{h}^{-1}$  to  $1000 \text{ mL}\cdot\text{h}^{-1}$ .

Gas flow values for a single IPEC module were estimated from the electrical current, assuming a constant Faradaic efficiency of 74 % for each cell.

For the assembly of IPEC modules, the  $\text{H}_2$  flow-rate was measured by a BROOKS SLA5850S mass flowmeter.

#### **2.2.5 Outdoor stability tests**

Outdoor experiments were carried out on IPEC modules tested in the field, at the Joint Research Center (JRC) from the European Commission, Ispra (Italy), in conditions close to ISOS-O-1 conditions (the solar cells delivering their power to the electrolyser). The values of Global Horizontal Irradiance (GHI) were recorded from the ESTI Meteo Tower in Ispra (JRC Ispra ||  $45^\circ 48' 43.4'' \text{ N} - 8^\circ 37' 37.4'' \text{ E}$  || altitude: 220 m), positioned approximately 100 m from the IPEC modules. To calculate the *STH* efficiency, a correction factor was applied to GHI values in order to account for the tilt angle between the IPEC plane and the horizontal plane and obtain the power density striking the IPEC modules. This correction factor, equal to 0.9, was estimated from comparison between calculated horizontal and tilted irradiances (Figure 56 in Appendix).

### **2.3 Data analysis and calculation of solar to hydrogen efficiency**

All calculations have been carried out considering standard conditions of pressure and temperature ( $25^\circ\text{C}$  and 1.013 bar, from Environmental Protection Agency (EPA) and Standard Ambient Temperature and Pressure (SATP) reference<sup>193</sup>).

The *STH* efficiency is calculated according to the following equation<sup>1</sup>:

$$STH = \frac{I_{op} \times E^{\circ} \times FE}{E_{sun} \times A} \quad \text{Eq. 41}$$

where:  $I_{op}$  is the operating current in A,  $E^{\circ}$  is the voltage (here, 1.23 V),  $FE$  is the Faradaic efficiency,  $E_{sun}$  is the incident solar energy in  $W.m^{-2}$ ,  $A$  is the active area of the solar cell in  $m^2$ .

Another definition,  $STH^*$ , is given by the following equation<sup>2</sup> that compares the produced energy in the form of  $H_2$  to the energy of the incident light on the surface of the device:

$$STH^* = \frac{n_{H_2} \times \Delta G_r}{E_{sun} \times A \times t} \quad \text{Eq. 42}$$

where:  $n_{H_2}$  is the total amount (in mol) of hydrogen produced,  $\Delta G_r$  is the reaction's Gibbs free energy ( $237 \text{ kJ.mol}^{-1}$ ) of the water splitting reaction at 298 K (corresponding to 1.23 V, the thermodynamic voltage of water splitting),  $t$  (in s) is the duration of the hydrogen production experiment.

### 3 Results and discussions

#### 3.1 IPEC cell description and motivation for thermal integration

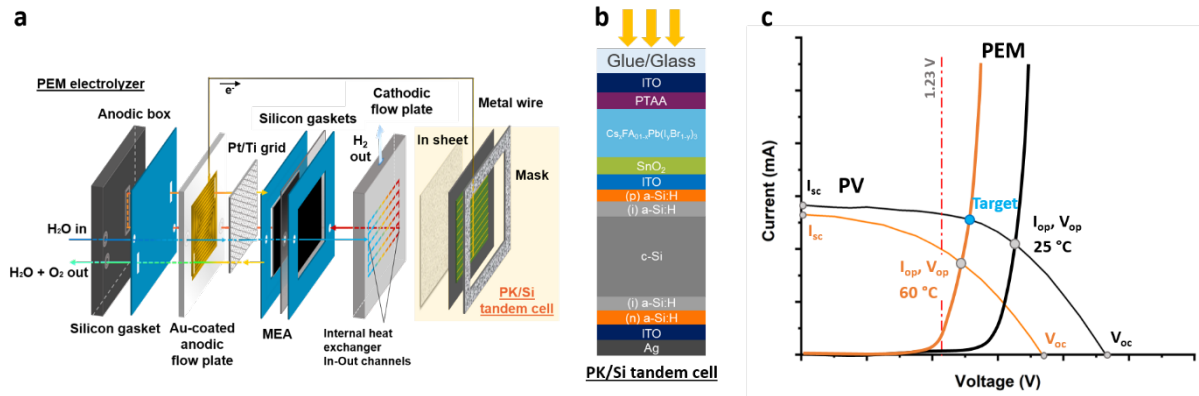


Figure 49. IPEC cell description and its operating points as a function of temperature. a) Scheme of PEM electrolyzer with internal heat exchanger and perovskite / silicon tandem cell integrated on the cathode. b) Details of perovskite / silicon solar cell architecture. c) Crossing points of the I(V) curves of the tandem cell and of the PEM electrolyzer operating with water at different temperatures (black: 25°C, orange: 60°C).

Figure 48 describes the building blocks of the IPEC cell: a monolithic perovskite / silicon tandem solar cell (Figure 49b) was integrated with n-i-p architecture on the cathode of a PEM electrolyzer (Figure 49a). This allows to drive the water splitting reaction under illumination, by means of the photovoltage produced by the tandem solar cell.

The tandem solar cell is made of a 1.58 eV bandgap halide perovskite absorber sandwiched between charge transport layers ( $SnO_2$  for electrons and doped poly (triaryl amine) (PTAA) polymer for holes) and transparent conducting oxide electrodes, connected in series to a silicon heterojunction bottom cell via an indium tin oxide (ITO) recombination layer, that enables the

charge recombination of electrons (from the perovskite top cell) and holes (from the bottom cell). Figure 49c shows the current-voltage  $I(V)$  curves measured under illumination. Typical voltages reached at the maximum power point are of the order of 1.3 - 1.4 V (Figure 57 in Appendix), above the thermodynamic voltage for water splitting (1.23 V).

The PEM electrolyser described in Figure 49a was built by additive manufacturing to enable the integration of a heat exchanger into the cathodic flow plate and to optimize fluid distribution. The membrane electrode assembly (MEA) is sandwiched between two gaskets and two 3D printed flow-plates. A Pt-coated titanium grid improves electrical contact and water distribution at the anode. The anodic flow plate is adapted from literature<sup>194,192</sup>, where the printed serpentine flow channels facilitate a fast and uniform water distribution, this is confirmed by CFD (Computational Fluid Dynamics) simulations. Polypropylene (PP) was selected for its low cost, flexibility (to facilitate final sealing of the assembly), chemical compatibility with PEM water electrolysis components, and availability from a wide range of suppliers. The cathodic flow plate is a 3D-printed stainless steel monolithic plate<sup>191</sup> with a pin structure designed both to maximize electrical contact with the MEA and to accommodate the gas flow ( $H_2$ ). A heat exchanger was also implemented in this cathodic flow plate through additional internal channels (see Figure 58 in Appendix), which preheats the water (before sending it to the anode) while cooling the tandem solar cell. The stack is assembled in a polyoxymethylene (POM) anodic box and tightened with nuts and bolts. Figure 49c shows a typical  $I(V)$  curve of such a PEM electrolyser.

The operating point of the IPEC cell sits at the crossing point of the  $I(V)$  curves of the PEM electrolyser and the solar cell, as shown in Figure 49c.

In general, only the crossing point at 25 °C is considered, whereas in practice under illumination, the device temperature rarely remains at 25 °C. The IR range of the solar spectrum (which is not fully absorbed by the 1.12 eV silicon bottom cell) results in a significant heating of the system. For instance, it is known that solar panels temperature can reach at least 60 °C outdoors. In this work, the  $I(V)$  curves of tandem solar cells were measured both on a hot plate after temperature stabilization (near 60 °C) and at room temperature (Figure 48c); the curves measured at 60 °C are more representative of the real IPEC cells working conditions. As operating temperature increases, even if water splitting reactions are favoured thanks to the reduction in thermodynamic and kinetic barriers, a significant voltage drop is observed on the tandem solar cells, which could prevent reaching a sufficiently high potential for hydrogen production. An ideal situation could be achieved if the PEM electrolyser could operate at 60 °C and the tandem solar cell at 25 °C. In this case, the operating current and therefore the hydrogen production would be maximized (Figure 49c). These considerations motivated us to integrate a heat exchanger into the electrolyser, as already done in some IPEC cells operating under concentrated illumination.<sup>47</sup>

### 3.2 Influence of heat exchanger on IPEC cell efficiency

Figure 50a (left) shows the path of the water inside the heat exchanger to the anode, and Figure 50a (right) the temperatures recorded along the water circuit, on the tandem solar cell and the cathodic plate, when the IPEC cell was exposed to 1 sun illumination. Several cycles of around 10 h each were performed. The stabilized working temperature of water at the anode ( $T_4$ ) was ca. 40 °C, with the water inlet temperature to the heat exchanger ( $T_1$ ) always 10 °C lower than the water outlet temperature from the heat exchanger ( $T_2$ ), revealing preheating of the water in the exchanger before entering the anode. Equilibrium was reached between the cathodic plate temperature ( $T_5$ ) and the water outlet temperature from the heat exchanger ( $T_2$ ). However, the operating temperature of the tandem solar cell ( $T_6$ ) was around 55 °C, always higher than  $T_4$  and  $T_5$ , meaning that in practice the ideal case described in Figure 49c was not achieved. A

more efficient heat exchanger would have to be implemented in order to effectively decrease the temperature of the tandem solar cell to a value equal to or lower than that of the electrolyser. Nevertheless, our strategy was relevant since a heat transfer was observed from the cathodic plate to the anode, resulting in improved efficiency for the IPEC cell, as shown in Figure 50c and Table 13. The progressive increase in  $T_1$  was explained by the fact that water outlet at the anode ( $T_4$ ) was directed to the inlet water tank feeding the cathodic plate.

The performance of the IPEC cell under 1 sun, with and without water flow inside the heat exchanger, is compared in Table 13. The heat exchanger operation (*i.e.* with water flow) led to an increase in operating current from 46 to 70 mA, with corresponding hydrogen flow rates of 0.2 to 0.4 mL·min<sup>-1</sup>. As a result, the STH\* was more than doubled, from 3.2 % to 8.0 %. This can be explained, at least in part, by the heating of the PEM electrolyser. By switching from 25 °C to 50 °C, the performance of the PEM electrolyser (biased at a fixed voltage of 1.50 V, in the dark) was improved, as shown in Figure 50b. At 50 °C, an operating current ( $I_{op}$ ) of 800 mA and a corresponding hydrogen flow rate of 6 mL·min<sup>-1</sup> were obtained, compared to 250 mA and 2 mL·min<sup>-1</sup> at 25 °C. Moreover, under 1 sun, with no external heating other than the illumination source, the operating current stabilized close to 1 A with a hydrogen flow rate of around 8 mL·min<sup>-1</sup>. This is likely due to the more homogeneous heating achieved by the uniform surface irradiation than by the hot water flow alone. The slight shift in operating voltage ( $V_{op}$ ) with heating (decreasing from 1.49 to 1.44 V) is also consistent with the PEM electrolyser operating at a higher temperature. The Faradaic efficiency (FE) is 74 % on average (see Table 18 in Appendix) in IPEC cell compared to more than 98 % in PEM electrolyser (dark) at 1.5 V.

The positive impact of the thermal integration on IPEC cell performance was systematically observed (see Table 19 in Appendix), although the STH efficiency did not always strictly reach the same value. This could be explained by the dispersion in the I(V) shape of the solar cells. On a batch of forty five solar cells, some variations in the I(V) curves were recorded, particularly in the area of the crossing point with the PEM electrolyser curve. This resulted in some dispersion of the expected STH efficiency, calculated from the current delivered by the tandem solar cells at 1.45 V (and taking a constant FE of 74 %). The calculated STH efficiency ranged from 7.5 to 10.8 % (see Figure 59 in Appendix).

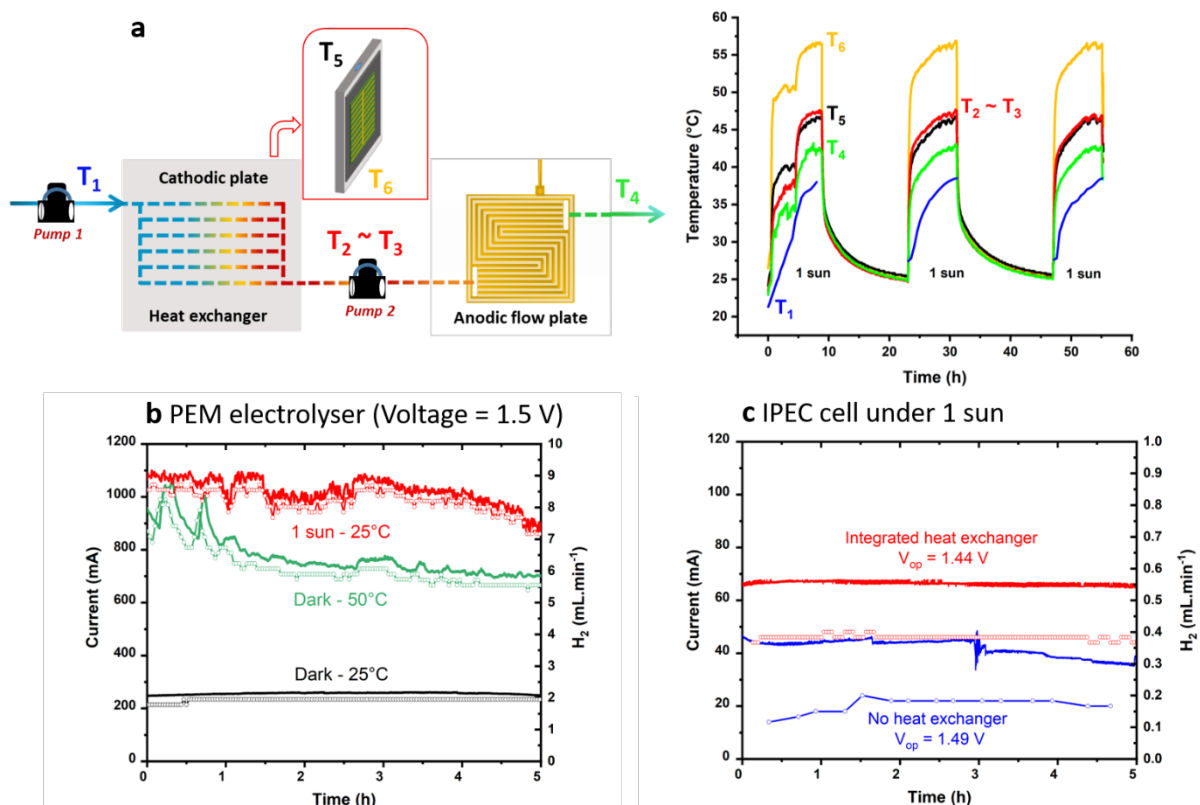


Figure 50. IPEC cell thermal integration. a) Detailed scheme of the water circuit of the IPEC cell (left) and recorded temperatures (right). T1 (blue): water inlet in the heat exchanger. T2 (red): water outlet from the heat exchanger. T3 (red): water inlet in the anodic compartment. T4 (green): water outlet from the anodic compartment. T5 (black): temperature of the cathode plate. T6 (yellow): temperature of the tandem solar cell. b) Water splitting current (solid line) and H<sub>2</sub> flow rate (solid line + circles) of the PEM electrolyser under different heating conditions (through the exchanger with water at different temperatures or under illumination). c) Water splitting current (solid line) and H<sub>2</sub> flow rate (solid line + circles) of the IPEC cell without (blue) or with (red) heat exchanger.

Table 13. Detailed results of the PEM electrolyser and IPEC cell performances. V<sub>op</sub> and I<sub>op</sub>: operating voltage and current (respectively) recorded at the electrolyser's terminals. t: duration of the hydrogen production, Vol. H<sub>2</sub>: corresponding hydrogen produced during the experiments of Figure 50. STH and STH\* are calculated using two methods as described in the Materials and methods section.

	Dark/illuminated mode	Initial inlet water temperature (°C)	V <sub>op</sub> (V)	I <sub>op</sub> (mA)	t (h)	Vol. H <sub>2</sub> (L)	STH (%)	STH* (%)
PEM electrolyser	Dark	25	1.50	250	6	0.69	-	-
PEM electrolyser	Dark	50	1.50	800	6	2.41	-	-
PEM electrolyser	1 sun	25	1.50	1000	6	2.94	-	-
IPEC cell**	1 sun	25	1.49	46	5	0.05	3.6	3.3
IPEC cell	1 sun	25	1.44	70	6	0.13	8.4	8.0

\*\*without water flow in the heat exchanger

### 3.3 IPEC cell stability and efficiency under light (1 sun)-dark cyclic illumination

The stability of the IPEC cells under cyclic 1 sun illumination was evaluated, following the so-called ISOS-LC-1 protocol from the perovskite photovoltaics community,<sup>195</sup> but with the solar cell delivering its power to the electrolyser. 8-hour light cycles was performed followed by a recovery time of at least 16 h in the dark. A slow decay in operating current was systematically

observed under illumination (Figure 51a and Figure 60 (in Appendix)). The behavior during recovery in the dark is different for cycles 1-2 and 2-3. In both experiments, while the starting point of cycle 2 stands at the ending point of cycle 1, the starting point of cycle 3 is lower than the ending point of cycle 2, as if the cell were degrading in the dark. This could indicate that different degradation modes occur initially and after the second cycle.

The I(V) curves of each component of the IPEC were compared before/after the three light cycles (Figure 51b). Significant degradation was observed for the solar cell: open circuit voltage ( $V_{oc}$ ), fill factor and series resistance are markedly affected, possibly indicating a degradation in the perovskite material and its interface layers (ETL and HTL). The increase in current produced by the tandem solar cell close to short circuit could originate from a shunted perovskite subcell, and/or from the change in current balance due to perovskite material degradation. As the perovskite / silicon tandem solar cell is the least mature component of the IPEC cell, it is not surprising that it is the least stable.

In order to optimize the operating current  $I_{op}$ , the perovskite thickness was adjusted to be in a bottom-limited configuration (providing a better fill factor). But as the perovskite material degrades, this may no longer be true, and shunts in the perovskite top cell may appear on the I(V) curve, with a slope impacting the short-circuit current. Regarding the PEM electrolyser, the I(V) curve shifts towards higher potentials (reflecting an increase in resistance, overpotential and/or mass transport limitations). The mechanisms at the origin of this phenomenon have to be better investigated (starting with a study of membrane degradation over time). Overall, the expected operating point is shifted toward lower current, which is consistent with the experimental results. The performance of the IPEC cell under light (1 sun)-dark cyclic illumination is compared in Table 14. STH efficiency drops to half of its initial value after three 8 h illumination cycles, from 8.6 to 4.5 %, in accordance with the observations from Figure 51b.

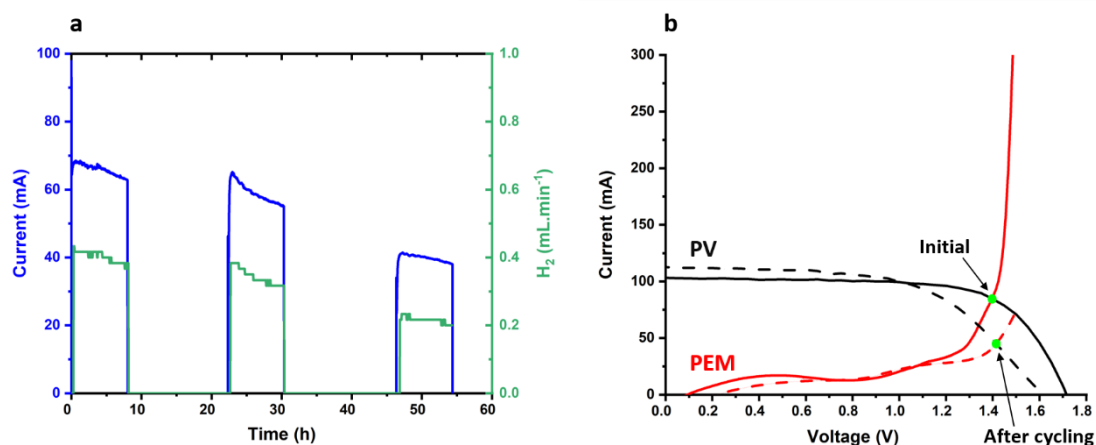


Figure 51. IPEC cell stability under light / dark cycles. a) Operating current (in blue) and hydrogen flow rate (in green). b) I(V) curves of the PEM electrolyser (red) and of the tandem solar cell (black) before (plain) and after (dashed) the three 8h-long illumination cycles.

Table 14. Performance of the IPEC cell over three cycles of 8 h under 1 sun (inlet water temperature: 25 °C,  $V_{op}$  and  $I_{op}$ : operating voltage and current recorded at the electrolyser's terminals, t: duration of the hydrogen production, Vol. H<sub>2</sub>: corresponding hydrogen produced during the experiments of Figure 51, STH and STH\*: solar-to-hydrogen efficiencies calculated using two methods as described in the Materials and methods section).

Cycle	$V_{op}$ (V)	Average $I_{op}$ (mA)	t (h)	Vol. H <sub>2</sub> (L)	STH (%)	STH* (%)
1		66	8	0.19	8.6	8.6
2		59	8	0.16	7.2	7.2

3	From 1.45 to 1.53	40	8	0.10	4.5	4.4
---	-------------------	----	---	------	-----	-----

### 3.4 IPEC module efficiency

Figure 52a (left) shows an exploded view of water circulation in the module. Cold water ( $T_1$ ) enters the heat exchanger (cathodic plate) of each IPEC successively and gradually heats up until its maximal temperature at the outlet of the last IPEC cathode. The preheated water ( $T_2$ ) is then divided into three identical flows, each of which passing through a series of three anodes, where it is oxidized into  $O_2$  and protons. The reason for dividing the water flow into three equal parts is to limit the overvoltage potentially associated with the accumulation of  $O_2$  bubbles.<sup>196</sup> Figure 52a (right) shows that the heat exchanger of the IPEC module under 1 sun operates in the same way as that of the IPEC cell. The temperatures stabilize at values comparable to those for the IPEC cell in Figure 50a (left): close to 60 °C for the tandem solar cells ( $T_6$ ) and 50 °C for the water in the anodic compartment of PEM electrolyser ( $T_3$ ).

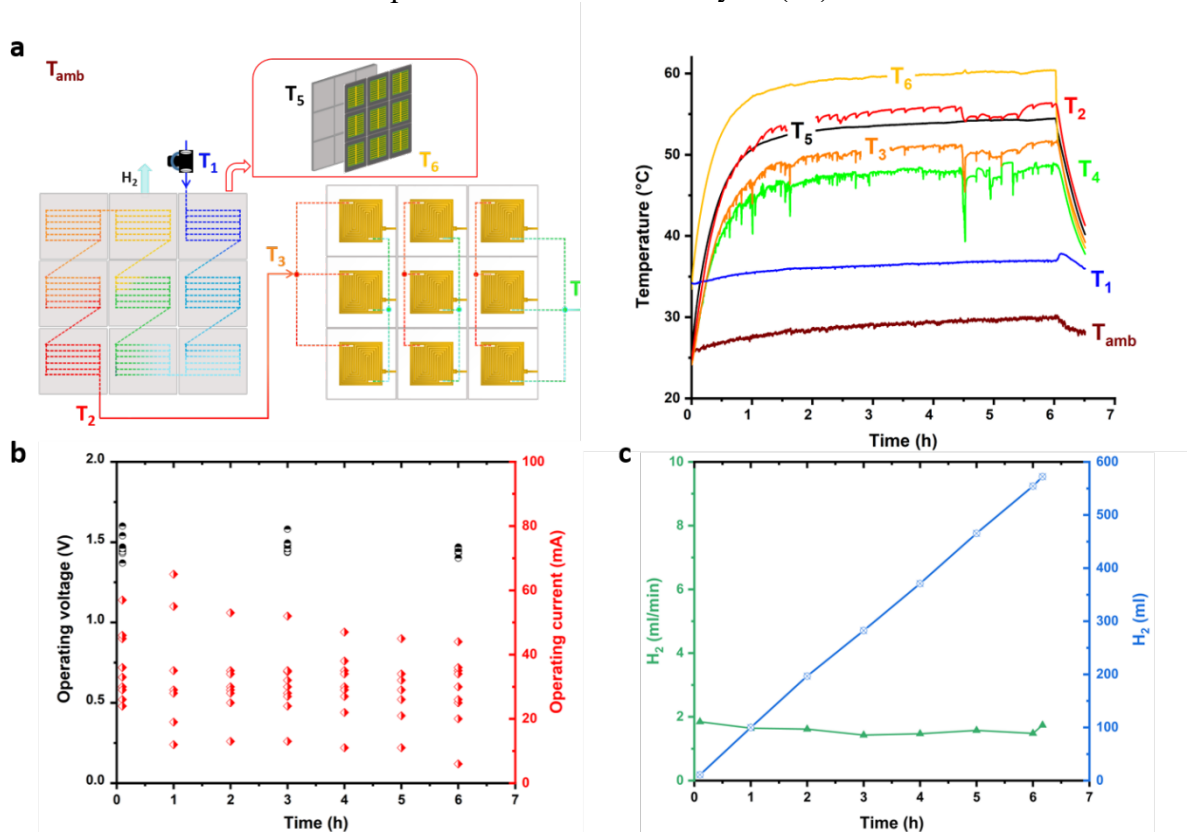


Figure 52. IPEC module thermal integration and performance (68.4 cm<sup>2</sup> active area). a) Detailed scheme of the water circuit in the IPEC module (left) and recorded temperatures (right).  $T_1$  (blue): water inlet in the heat exchanger.  $T_2$  (red): water outlet from the heat exchanger.  $T_3$  (red): water inlet in the anodic compartment.  $T_4$  (green): water outlet from the anodic compartment.  $T_5$  (black): temperature of the cathodic plate.  $T_6$  (yellow): temperature of the tandem solar cell. b) Operating points ( $V_{op}$  and  $I_{op}$ ) of the nine IPEC cells in the IPEC module before and during constant 1 sun illumination. c) Calculated  $H_2$  volume and flow rate produced by the IPEC module.

Figure 52b shows the operating currents of the nine IPEC cells constituting the IPEC module, initially and during a 6-hour stability test under continuous 1 sun illumination (see details in Appendix, Table 20). Initial operating currents range from 24 to 57 mA and are lower than those observed for the IPEC cell (70 mA, Table 13), which can be explained by the already



marked ageing of the tandem solar cells used in previous experiments. Under these conditions, according to the measured currents, the IPEC module delivers an estimated amount of 552 mL of hydrogen in 6 h, corresponding to a hydrogen flow rate of around 2 mL·min<sup>-1</sup> (Figure 52c).

The corresponding STH efficiencies are reported in Table 15. Assuming a constant FE of 74 %, the measured currents result in a STH efficiency of 3.7 %, about two times less than would be expected from nine fresh and stable IPEC cells (as in Table 13). Therefore, the volume of H<sub>2</sub> produced by the best achievable IPEC module (made with nine fresh tandem solar cells) could reach 1.21 L over 6 h under 1 sun.

Table 15. Performance of the IPEC module (68.4 cm<sup>2</sup> active area) over 6 h under 1 sun (inlet water temperature: 25 °C, Average I<sub>op</sub>: average I<sub>op</sub> recorded at each electrolyser's terminals during 6 h, t: duration of the hydrogen production, Vol. H<sub>2</sub>: corresponding calculated hydrogen produced during the experiments of Figure 52, STH and STH\*: solar-to-hydrogen efficiencies calculated as described in the Materials and methods section). Values for the best expected IPEC module (consisting of 9 fresh and stable IPEC cells) are also given.

	Average I <sub>op</sub> (mA)	t (h)	Calculated Vol. H <sub>2</sub> (L)	STH (%)	Estimated STH* (%)
IPEC module from Figure 52	282	6	0.56	3.7	3.6
9 IPEC cells as in Table 13	630 (70 x 9)	6	1.21 (~ 0.13 x 9)	8.3	8.0

### 3.5 IPEC module stability outdoors and origin of degradation

Several IPEC modules were tested in an autonomous device dedicated to the production of green methane.<sup>190</sup> The conditions of this 72-hour demonstration, conducted at the JRC center in Ispra<sup>a</sup>, differ significantly from the laboratory tests described previously on several major points.

First, the modules had to operate in real sunlight and climate conditions (ISOS-O-1 protocol<sup>195</sup>). They all shared the same water inlet and hydrogen outlet circuits. In addition, they were coupled to a bioreactor carrying out the continuous conversion of CO<sub>2</sub> with “as produced” hydrogen into green methane (without any compression, heating or storage step prior use).<sup>197</sup> This reactor, based on a selected strain of Archaea microorganisms allowing the Sabatier (Eq. 43) reaction to be carried out under mild temperature and pressure conditions, imposed very strict criteria on the residual O<sub>2</sub> composition of the gas produced. Consequently, the H<sub>2</sub> flow at the IPEC outlet was regulated by a control system that respects these constraints and allows H<sub>2</sub> to evacuate above a pressure of 20 mbar (see Chapter 3 or *Maragno et al.*<sup>190</sup> for more details).



The device was sized for an average hydrogen conversion capacity of 0.5 L·h<sup>-1</sup> (8 mL·min<sup>-1</sup>). To this end, five IPEC modules, able of delivering around 16 mL·min<sup>-1</sup> of H<sub>2</sub> initially, were assembled based on the data reported in Table 13 and taking into account the effect of aging. Forty five tandem solar cells were selected within several batches, the selection criterion being

<sup>a</sup> European Commission, Directorate-General for Research and Innovation, Fuel from the sun: Artificial Photosynthesis – EIC Horizon Prize – Commissariat à l'énergie atomique et aux énergies alternatives (CEA), Publications Office of the European Union, 2022, <https://data.europa.eu/doi/10.2777/18380>

the current delivered by the solar cell under 1 sun at a given fixed voltage of 1.45 V (close to operating point). This value stands a few tens of mV above the typical maximum power point of n-i-p perovskite / silicon tandem solar cells under 1 sun (see Figure 57 in Appendix), in a region where the I(V) curve follows an exponential shape, with a steep slope. To improve this current (increase the maximum power point voltage), the parameters of certain batches were modified, adjusting the concentration of the perovskite solution (from 1.2 to 1.4 mol·L<sup>-1</sup>, see Figure 61 in Appendix) to increase the thickness of the perovskite layer and shift the tandem into a bottom cell limited configuration. The p-layer concentration (PTAA solution) was also increased from 6 to 12 g·L<sup>-1</sup> as it led to a slightly better maximum power point voltage (see Figure 61 in Appendix). Unfortunately, such improvements were lost once the tandems were encapsulated: the current delivered by the solar cells at 1.45 V after encapsulation were all in the same range, as displayed on Figure 53b (blue points). The mechanical stress linked to crosslinking of the glue, imposing stress to the interfaces, could be a clue to explain this result<sup>198</sup>, as an increased series resistance was observed after encapsulation.

Figure 53a presents the volume of hydrogen produced by the five IPEC modules over time, and the corresponding irradiance. As hydrogen is measured close to the bioreactor inlet, significant dead volumes have to be taken into account, which explains the delay between irradiance onset and hydrogen detection. In total, around 7 L of hydrogen were evolved by the five IPEC modules over the 72 h test. For comparison with the previous ageing cycles performed in simulated 1 sun conditions, production periods with steady hydrogen production were selected (Figure 53a). The corresponding volumes, reported for an 8-hour period, per module, for the production periods indicated in Figure 53a, are reported in Table 16. They are consistent with the values observed for the IPEC module comprising aged tandems from Figure 52 and Table 15 (0.55 L in 6 h). Thus, between 0.66 and 0.72 L of hydrogen were produced by each module in 8 h, under a natural illumination with irradiance of several hundreds of watts per square meter. Corresponding STH\* are reported in Table 16 and range between 3.8 and 9.3 %, depending on the outdoor conditions. Overall, the STH\* from the whole 72 hour outdoor test for the five IPEC modules was 6.3 %.

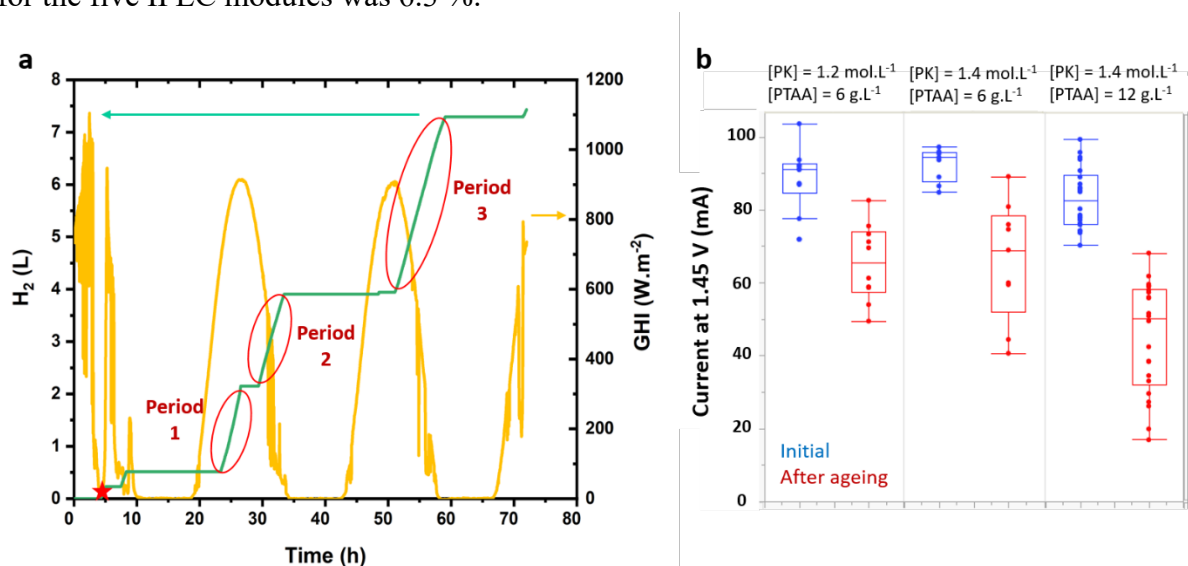


Figure 53. Outdoor functioning of five IPEC modules (342 cm<sup>2</sup> active area). a) Evolved hydrogen (in red) and corresponding Global Horizontal Irradiance (GHI, in orange) recorded in the field. Three periods (shown in red) were selected for STH efficiency calculations. b) Current delivered by the tandem solar cells at 1.45 V under 1 sun: point before (blue) and after outdoor ageing (red), from batches with variations in perovskite top cell conditions (perovskite and p-layer concentrations). To perform these measurements, the solar cells were dismantled from the IPEC modules and measured under a calibrated solar simulator.

Table 16. Amount of hydrogen produced outdoor by each IPEC module, measured over real periods (shown in red in Figure 53) and calculated for 8-hour periods for comparison with IPEC cell data. The total amount of hydrogen produced by the five IPEC modules over the 72 hour test is also reported. STH\* values are calculated from measured hydrogen volumes and corrected global horizontal irradiance, as explained in the Materials and methods section.

	Calculated Vol. H <sub>2</sub> (L) for 8 h	Measured Vol. H <sub>2</sub> (L)	STH* (%)
Period 1 Average irradiance 850 W.m <sup>-2</sup>	0.72	0.33	3.8
Period 2 Average irradiance 297 W.m <sup>-2</sup>	0.62	0.33	9.3
Period 3 Average irradiance 389 W.m <sup>-2</sup>	0.66	0.64	7.6
72 hour outdoor test, 5 IPEC modules (342 cm <sup>2</sup> )	/	7.43	6.3 (without GHI correction: 7.0 %)

Figure 53b shows the evolution of the current of the tandem solar cells at 1.45 V under 1 sun (representative of the operating current) before and after outdoor ageing. To obtain these values, the tandem solar cells were disconnected from the IPEC modules and characterized under the calibrated solar simulator. While variations in perovskite and PTAA thickness led to devices with initial current values in the same range, the highest current losses observed after ageing occur in the case of the thickest p-layer. Analysis of the I(V) curves indicates that degradation results in an increase in open-circuit resistance and a reduction of the fill factor (Figure 62 in Appendix). As the open-circuit voltage remains stable, the perovskite material is not degraded. Thus, degradation of the tandem solar cell seems to originate at the perovskite/p-layer interface or within the p-layer.

The tandem solar cells were encapsulated with glass and a glue with high gas barrier properties, hence the main stress factors affecting them during outdoor ageing should be light, heat, their combination and cycling. From our previous experience, moisture ingress was observed, that quickly made the tandem edges turn yellow due to perovskite decomposition, but only after heavy rain. Here, devices are more likely affected by illumination and thermal stress.

Some studies report the thermal oxidation and morphological changes in PTAA thin films (aged at 65 °C in air)<sup>199</sup> that could potentially induce lower conductivity and impact the fill factor when integrated into solar cells. Delamination at interfaces due to thermal expansion coefficients mismatch was also reported.<sup>200</sup> Yaghoobi *et al.* studied the thermal stability of n-i-p perovskite solar cells with doped PTAA and highlighted the impact of PTAA molecular weight and doping on device stability, through modification of the passivation of the perovskite/p-layer interface.<sup>201</sup> Similarly, Rombach *et al.*<sup>200</sup> assigned the degradation of n-i-p perovskite solar cells to PTAA doping, which affects the perovskite/PTAA interface. Therefore, our assumption that the solar cells degrade at the perovskite/p-layer interface or within the p-layer is consistent with previous detailed investigations on similar devices. Better stability could be reached by tuning the tandems interfaces and performing in-depth analysis of the degradation pathways.

## 4 Comparison with State-of-the-Art

Figure 54 and Table 21 (in Appendix) show the performance of the devices from this study compared with the largest and most efficient solar hydrogen production systems selected from literature.

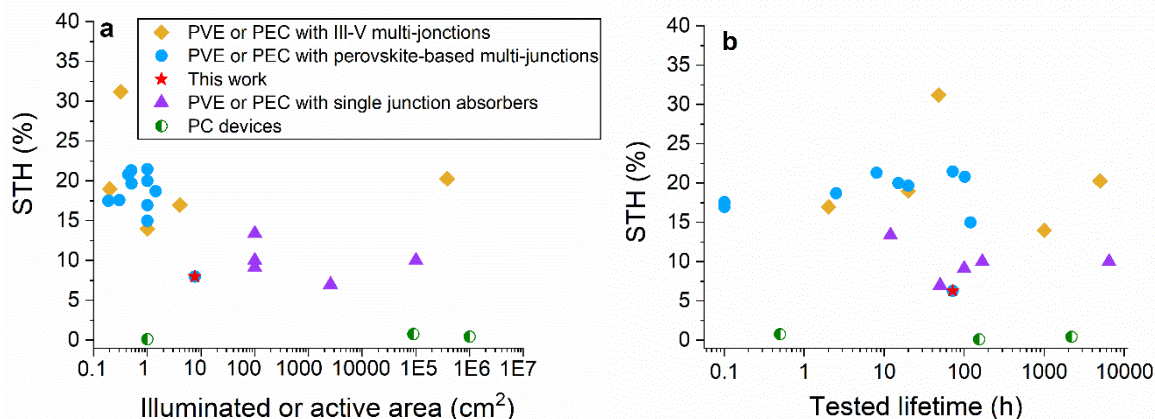


Figure 54. Performance of selected reports from literature regarding photocatalytic systems (PC), photovoltaic cells coupled to electrolyzers (PVE), photoelectrochemical cells and integrated photoelectrochemical cells (PEC and IPEC), with single junction absorbers (silicon or CIGS), multi-junctions (with III-V absorbers), and perovskite-based tandems. a) STH efficiency as a function of absorber active area. b) STH efficiency and tested lifetime (results gathered for various ageing conditions: light cycling, continuous illumination or outdoor). The red stars correspond to the devices from this study: IPEC cell from Table 13 (7.6 cm<sup>2</sup>, 8 % STH\*) and IPEC modules aged outdoors (342 cm<sup>2</sup>, 6.3 % STH\*) from Table 16.

Today, the largest systems deployed are using mature and abundant silicon-based absorbers. However, such systems have an intrinsic efficiency limitation due to the single junction optical absorption.<sup>202</sup> Maximum reported STH efficiencies so far are close to 15 %. Alternately, large-scale devices can be obtained with cheap abundant photocatalysts (PC). Their lower efficiency, in the range of a few percents, is mitigated by the possibility of scaling-up the system. The use of PC inorganic metal oxide particles, in slurry form or deposited onto solid substrates, has demonstrated long-term stability and scale-up potential (with a recent demonstration over 100 m<sup>2</sup>).<sup>70</sup> However, this type of device has so far been limited to a low STH efficiency and requires downstream separation of O<sub>2</sub> and H<sub>2</sub>.<sup>178</sup>

The US Department of Energy (DoE) recommends and targets STH efficiencies of at least 20 % for systems to be commercially viable.<sup>181</sup> This motivated the development of multi-junction water splitting devices. Today, the most efficient way to produce solar hydrogen, with up to 30 % STH efficiency, is through the combination of III-V absorbers in a multi-junction (i.e. InGaP/GaAs/GaInAsSb) cell connected with electrolyzers. This mature technology guarantees high performance<sup>48</sup> but it is associated with high investment costs<sup>176</sup>. A monolithic buried junction device using the same high efficiency high-cost components reaches a STH efficiency of 19 %, but with lower stability because of the corrosion of III-V semiconductor materials in contact with liquid electrolytes.<sup>44,177</sup> Such multi-junctions were used in kilowatt scale devices by Holmes-Gentle *et al.*<sup>203</sup> Perovskite-based multi-junctions have proved high STH efficiency (over 20 %) at a potentially low cost. However, no data is available beyond 1.42 cm<sup>2</sup>. Here, it is demonstrated that larger photoelectrochemical devices can be obtained using larger perovskite / silicon tandems (7.6 cm<sup>2</sup>) and up to 342 cm<sup>2</sup> through a numbering-up approach. It should be noted that there is no technological obstacle to adapting this strategy to larger cells, such as the ones recently reported.<sup>204</sup>

Higher STH efficiencies could have been obtained if the operating point of the IPEC cells had perfectly matched the maximum power point of the solar cells, which was not the case here, contrary to previous work from literature. Indeed, although the perovskite and PTAA layers were adjusted, the initial gains obtained at the maximum power point could not be translated into the encapsulated tandems, probably due to the mechanical stress arising from the adhesive crosslinking. In fact, today, the record power conversion efficiencies of perovskite / silicon tandems are obtained with p-i-n architectures, probably due to the better quality of the interfaces that can be achieved with the materials implemented in such architectures (self-assembled monolayers, buffer layers...). The combination of p-i-n-based architectures with optimized encapsulation and more efficient heat transfer is expected to show significant progress in STH efficiency<sup>205</sup>. Progress towards the commercialization of solar panels made of perovskite / silicon tandem cells<sup>206</sup> will undoubtedly help in this direction.

## 5 Conclusions and perspectives

This chapter develops and discusses the performance of IPEC cells depending on their size, level of integration, and under controlled-laboratory to real life operating conditions, some of them partially shown in the *Chapter 1*.

The performance of the IPEC cell under simulated illumination is very close to that reported by *Kistler et al.*<sup>67</sup> on a system of similar design and smaller size. It is interesting to note that this cell, which had no thermal integration, operated with water at 60°C, which supports the thermal integration approach considered here, for cells operating without solar concentration.

Given the drop in performance observed between IPEC cells of 0.44 and 1 cm<sup>2</sup> active surface, it is also remarkable to note the maintenance of performance during module integration (IPEC modules) and under real operating conditions (IPEC modules integrated in the demonstrator), which supports the proposed numbering-up approach, exploiting the flexibility of 3D printing. It should be noted that there is no technological obstacle to adapting this strategy to larger cells (10x10 cm<sup>2</sup> tandem cells are currently being developed, i.e. modules close to m<sup>2</sup>).

In conclusion, the following work not only demonstrates results regarding the scaling up of perovskite-based integrated photoelectrochemical devices and their lifetime assessment in real environment, but also provides an example of a modular and scalable system that enables rapid testing and characterization of components, thanks to reversible integration. Additive manufacturing has enabled the implementation in a single electrode of the gas separation function and a heat exchanger.

This study confirms the benefits of thermal integration in improving STH efficiency, obtaining almost doubled values with the embedded heat exchanger in direct contact with the back side of the solar cell. With a more efficient thermal transfer, effectively cooling the solar cell, even better results could be achieved.

Our study provides noteworthy insights into the practical deployment of integrated photoelectrochemical devices. The data were collected repeatedly on over forty-five IPEC cells, showing the expected scatter in STH efficiencies due to variability in solar cell I(V) curves. The modular approach presented here enabled us to rapidly scale-up the device to 342 cm<sup>2</sup> of active surface area, even though individual components remained on a scale of a few cm<sup>2</sup>. The development of larger components, and especially of tandem solar cells,<sup>206</sup> will also directly contribute to upscaling the IPEC devices. This numbering up strategy is in line with the recent concept of golden hydrogen for adaptable and decentralized hydrogen production units.<sup>207</sup>

The approach presented here paves the way for further investigations of other promising materials, such as light absorbers, electrocatalysts, or membranes, in order to compare performance, stability, repeatability, and to highlight the limitations of such new systems.

## 6 Appendix

### 6.1 Determination of solar cells active area

Active area is defined as the area where all layers of the solar cells are stacked, taking into account the shading from opaque metallization (evaporated gold and additional metal ribbon) deposited on the front side. ImageJ software and a contrast determination method were used to determine  $A_{\text{stack}}$ , the area where all layers are stacked (in average,  $9.0 \text{ cm}^2$ ), from which the  $A_{\text{shaded}}$  subtracted, the average area occupied by metallization (in average,  $1.4 \text{ cm}^2$ ).

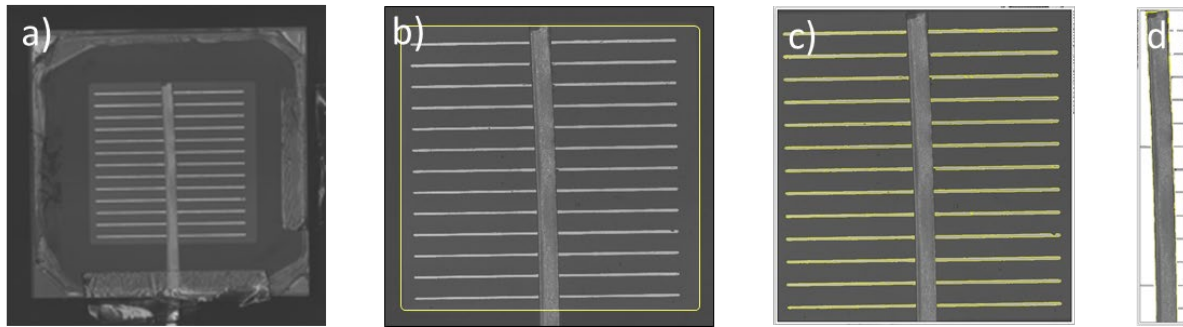


Figure 55. Determination of the active area of a perovskite / silicon tandem solar cell. a) Initial image of the solar cell's front side, showing the  $5 \times 5 \text{ cm}^2$  substrate with the  $3 \times 3 \text{ cm}^2$  central zone where all layers are present. This central zone is defined by the  $3 \times 3 \text{ cm}^2$  front side ITO hard mask. b) In yellow, the area selection corresponding to  $A_{\text{stack}}$ , as determined with ImageJ. c) Within this central zone, in yellow, the area selection corresponding to gold metallization. d) In yellow, the area corresponding to the metal ribbon.  $A_{\text{shaded}}$  is determined summing the areas from c) and d).

Table 17. Determination of perovskite / silicon tandem solar cells active area.

	$A_{\text{stack}} \text{ (cm}^2\text{)}$	$A_{\text{shaded}} \text{ (cm}^2\text{)}$	<b>Active area</b> $(A_{\text{stack}} - A_{\text{shaded}}) \text{ (cm}^2\text{)}$	<b>% shaded</b> $(A_{\text{shaded}}/A_{\text{stack}})$
Cell 1	9.0	1.6	7.5	17.2
Cell 2	9.1	1.4	7.7	15.7
Cell 3	9.0	1.2	7.8	13.4
<b>Average</b>	<b>9.0</b>	<b>1.4</b>	<b>7.6</b>	<b>15.4</b>



## 6.2 Determination of the correction factor for the horizontal irradiance

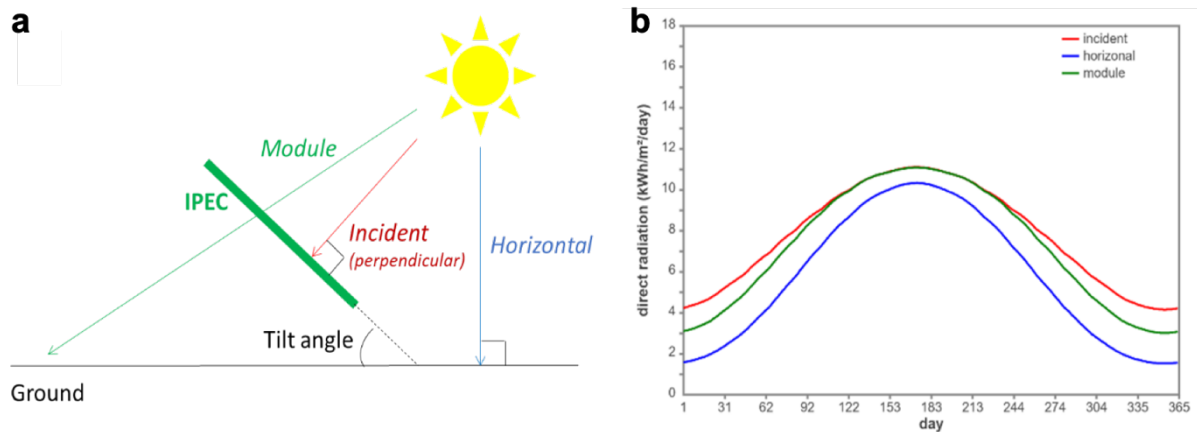


Figure 56. Direct radiation striking a tilted plane. a) Scheme of the IPEC modules, tilted  $25^\circ$  against the horizontal. b) Calculated direct radiation on the IPEC modules (in green), on the horizontal plane (in blue), and on the plane always perpendicular to the sun thanks to a light tracker. The latitude was  $45^\circ$  N. Day on the abscissa is the number of days since January 1<sup>st</sup>. The ratio of irradiances used to correct the GHI for  $STH^*$  calculation is 0.9. Figure and calculations adapted from <sup>208</sup>.

## 6.3 Typical maximum power point voltages of perovskite / silicon solar cells under 1 sun

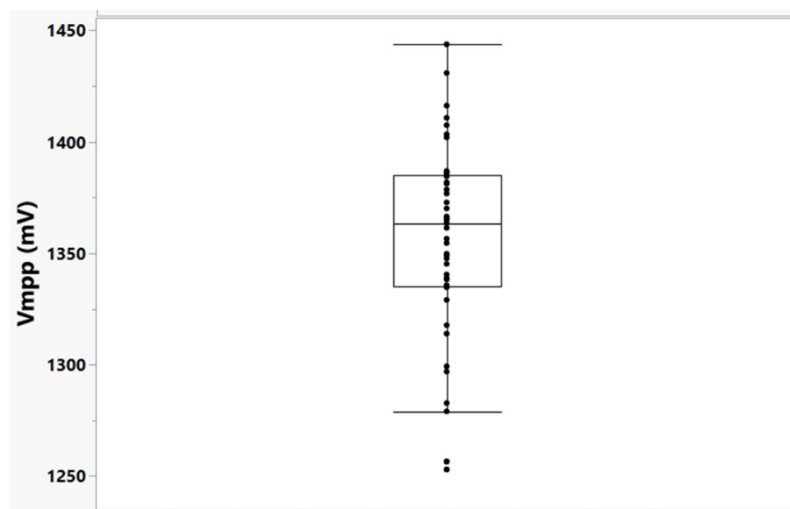


Figure 57. Typical voltages reached at the maximum power point for the perovskite / silicon tandem solar cells under 1 sun (minimum value: 1253 mV, maximum value: 1444 mV, median value: 1364 mV).

### 6.4 Structure of the 3D-printed cathode with the heat exchanger

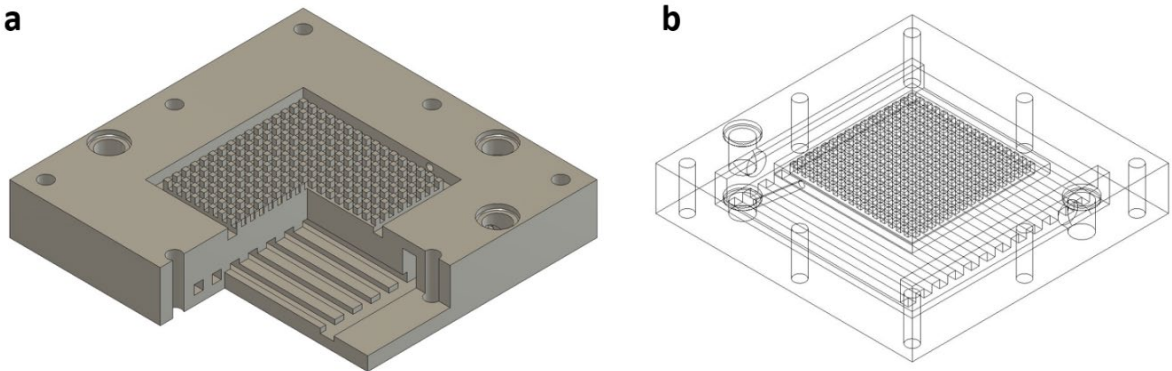


Figure 58. Design of the 3D-printed metallic flow plate showing the heat exchanger channels and the central rough conductive surface.

### 6.5 Faradaic efficiency during various IPEC cell performance tests

Table 18. Faradaic efficiency in IPEC cells under 1 sun illumination, during long and short operational periods. The average value of FE is used for the STH efficiency calculations.

	<b>Faradaic efficiency (FE) (%)</b>
IPEC cell (Table 13)	74
Cycle 1 (Table 14)	80
Cycle 2 (Table 14)	76
Cycle 3 (Table 14)	70
Cycle 1 (Table 19)	75
Cycle 2 (Table 19)	68
Cycle 3 (Table 19)	71
<b>Average</b>	<b>74</b>

## 6.6 Influence of heat exchanger on IPEC cell performance

Table 19. IPEC cell performance under cycles of continuous 1 sun illumination, without or with heat exchanger. Active area 7.3 cm<sup>2</sup> in the case without heat exchanger.

Cycle	V <sub>op</sub> (V)	Average I <sub>op</sub> (mA)	t (h)	Vol. H <sub>2</sub> (L)	STH (%)	STH* (%)
<b>without heat exchanger</b>						
1	1.44	69	5	0.06	4.6	4.6
2		76	8	0.09	3.8	3.8
3		65	10	0.07	2.5	2.5
<b>with heat exchanger</b>						
1	From	60	8	0.16	7.3	7.3
2	1.44 to	57	8	0.14	6.6	6.4
3	1.5	45	8	0.12	6.9	5.1

## 6.7 Estimation of STH efficiency from I(V) curves of perovskite / silicon tandem solar cells

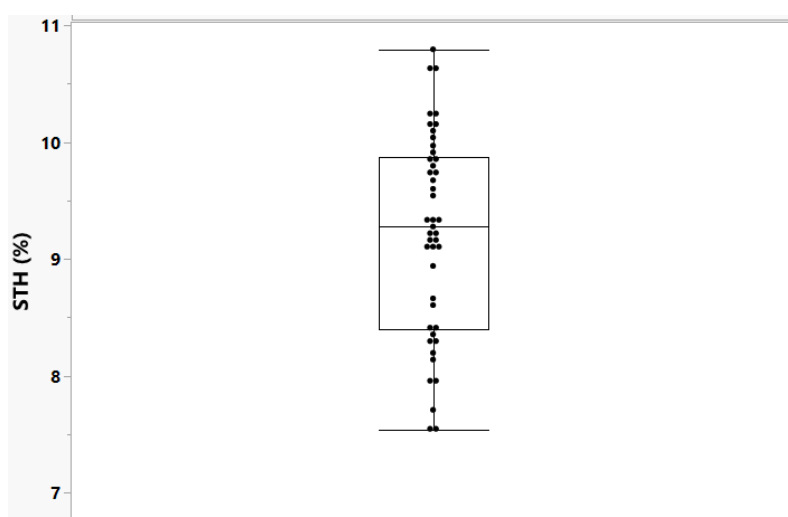


Figure 59. Estimated initial STH efficiency for the forty five IPEC cells from the current densities of the solar cells (disconnected from the PEM electrolyser) measured at 1.45 V under 1 sun. The Faradaic efficiency was taken at 74 %. STH range from 7.5 up to 10.8 %.

## 6.8 IPEC cell stability under light/dark cycles (repeated)

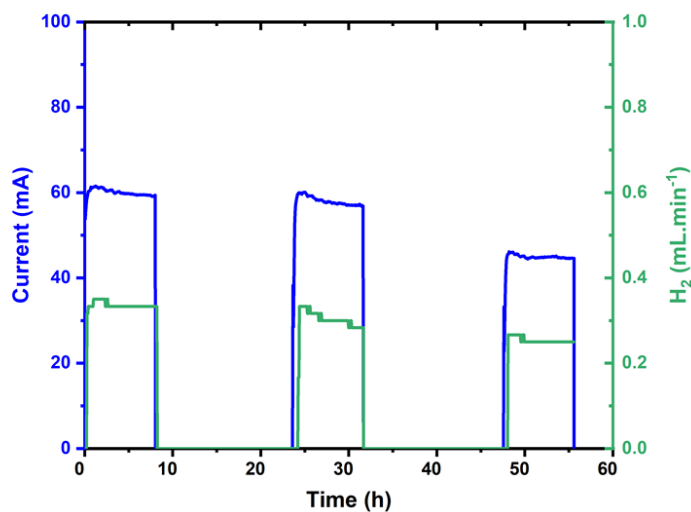


Figure 60. IPEC cell stability under light / dark cycles (repeated experiment from Figure 51). Operating current (in blue) and hydrogen flow rate (in green).

## 6.9 Operating current of the nine IPEC cells from the IPEC module

Table 20. Operating currents of the nine IPEC cells comprising the IPEC module. The corresponding STH efficiencies were calculated with a Faradaic efficiency of 74 %. Values of operating currents are given at the beginning and at the end of the 6 h stability run under continuous illumination from Figure 52.

Solar cell	Initial		Final	
	$I_{op}$ (mA)	STH (%)	$I_{op}$ (mA)	STH (%)
1	36	4.3	35	4.2
2	45	5.4	34	4.1
3	26	3.1	30	3.6
4	57	6.8	44	5.3
5	30	3.6	6	0.7
6	33	4.0	36	4.3
7	46	5.5	25	3.0
8	24	2.9	20	2.4
9	29	3.5	26	3.1
<b>Average</b>	<b>36</b>	<b>4.3</b>	<b>28</b>	<b>3.4</b>

## 6.10 Impact of variations in perovskite and p-layer thicknesses on performance

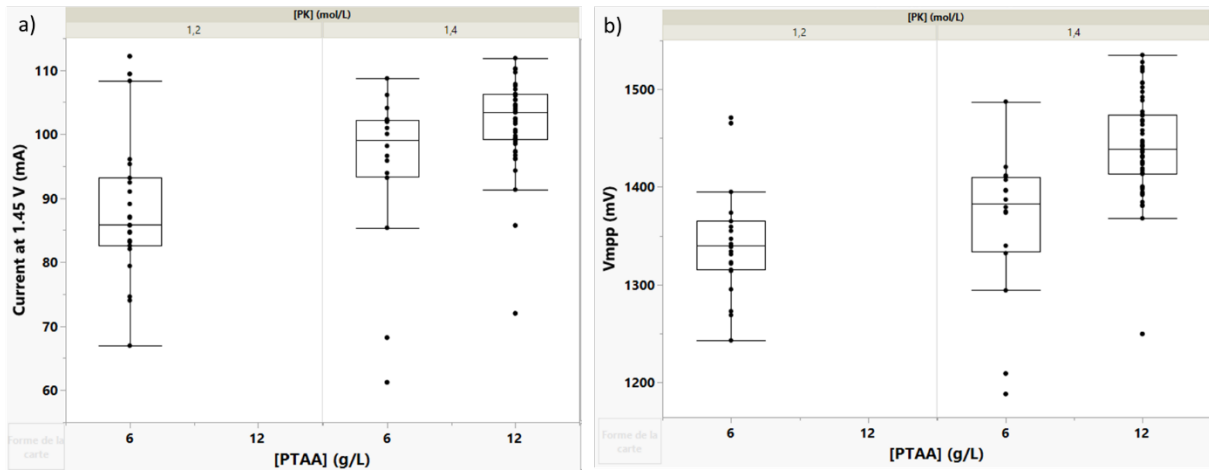


Figure 61. a) Current delivered at 1.45 V (close to operating point) by the perovskite / silicon tandem solar cells under 1 sun. b) Corresponding maximum power point voltage. Results are shown here for devices before encapsulation.

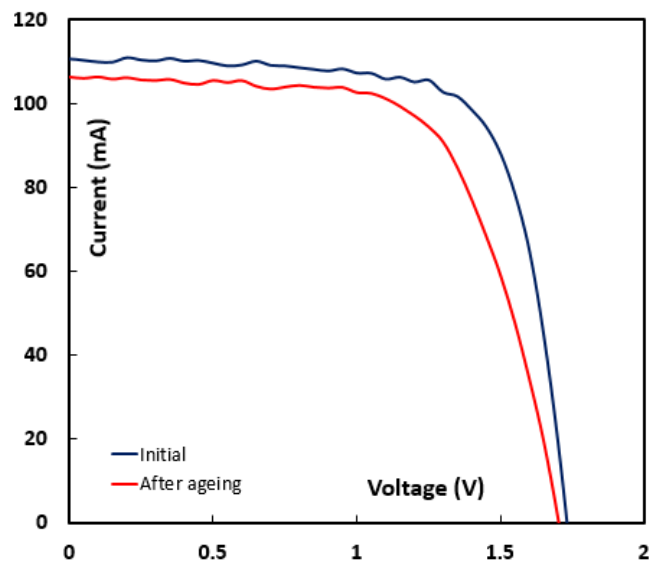


Figure 62. Typical I(V) curve of a perovskite / silicon tandem solar cell before (in blue) and after ageing (in red).

## 6.11 Details of reports from literature used to build the graphs from Figure 54

Table 21. Comparison of best IPEC cells and modules from this study with State of Art devices: illuminated or absorber active area, STH efficiency and tested lifetime (results are gathered for various ageing conditions: light cycling, continuous illumination or outdoor).

Device type	Illuminated or active area (cm <sup>2</sup> )	STH (%)	Tested lifetime (h)	Ref.
PVE or PEC with III-V multi-junctions	0.2	19	20	Cheng <i>et al.</i> <sup>177</sup>
	0.316	31.2	48	Jia <i>et al.</i> <sup>209</sup>
	1	11-14	1000	Kistler <i>et al.</i> <sup>67</sup>
	4	17	2	Haussener <i>et al.</i> <sup>47</sup>
	8	N.A.	96	Kistler <i>et al.</i> <sup>210</sup>
	385 000	20.3	~ 5000	Holmes <i>et al.</i> <sup>203</sup>
PVE or PEC with perovskite-based multi-junctions	0.1875	17.52	0.1	Park <i>et al.</i> <sup>211</sup>
	0.3	17.6	0.1	Karuturi <i>et al.</i> <sup>186</sup>
	0.44	20.8	102	Fehr <i>et al.</i> <sup>65</sup>
	0.5	21.32	8	Pan <i>et al.</i> <sup>212</sup>
	0.5091	19.68	20	Wang <i>et al.</i> <sup>213</sup>
	1	17	0.1	Sharma <i>et al.</i> <sup>214</sup>
	1	20	15	Wang <i>et al.</i> <sup>187</sup>
	1	21.5	72	Datta <i>et al.</i> <sup>66</sup>
	1	15	120	Song <i>et al.</i> <sup>215</sup>
	1.42	18.7	2.5	Gao <i>et al.</i> <sup>216</sup>
	<b>7.6</b>	<b>8</b>	<b>72</b>	<b>IPEC cell from this work (Table 13)</b>
<b>342</b>	<b>6.3<sup>+</sup></b>	<b>72</b>	<b>IPEC modules from this work (Table 16 and Chapter 4 for more details)</b>	
PVE or PEC with single junction absorbers	100	9.1	100	Pehlivan <i>et al.</i> <sup>217</sup>
	100	10	168	Calnan <i>et al.</i> <sup>218</sup>
	100	13.4	12	Calnan <i>et al.</i> <sup>218</sup>
	2600	7	50	Calnan <i>et al.</i> <sup>218</sup>
	100000	10	6500	Lee <i>et al.</i> <sup>219</sup>
PC devices	1	0.13	154	Reisner <i>et al.</i> <sup>220</sup>
	90 000	0.76	0.5	Nishiyama <i>et al.</i> <sup>70</sup>
	1 000 000	0.45	~ 2200	Nishiyama <i>et al.</i> <sup>70</sup>
Integrated PV (Si) – PEM module*	64	1.33	5	Becker <i>et al.</i> <sup>69</sup>

<sup>+</sup>The performances are measured outdoors.

\*The performances of this device are not reported in Figure 54.





## Chapter 4:

### **A scalable integrated solar device for the autonomous production of green methane**



## Chapter 4:

# A scalable integrated solar device for the autonomous production of green methane

After scaling up the IPEC using the numbering strategy described in Chapter 3, the challenge associated with implementing and testing a stand-alone device for green methane production was the transposition to real sunlight and climatic conditions, as well as operation.

Note that the development of the biological reactor (choice of strains, culture medium and design), carried out by the LCBM BEE biology team, is the subject of a specific article, also under revision. Only the interfaces with the IPEC and the associated operating modes were developed within the framework of the thesis.

The continued successful use of solar hydrogen produced by the IPEC modules to convert CO<sub>2</sub> into a highly catalytic fuel proves that a TRL of 5 has been achieved.

This chapter is an article currently under review<sup>190</sup>

## 1 Introduction

The demand for sustainable and clean energy technologies has intensified over recent decades and is at the heart of the transition to an energy system less dependent on fossil fuels. Solar fuels, which harness the abundant and renewable energy from the sun to produce storable and transportable energy carriers, offer a promising solution to address these challenges. Despite significant progress in solar fuel technologies<sup>221</sup>, the transition from laboratory-scale experiments to practical, scalable, and economically viable systems remains a critical area of research and only few prototypes have been demonstrated that can efficiently generate solar fuels under real-life conditions<sup>70,222</sup>.

Methane, the primary component of natural gas, holds great potential as a solar fuel due to its high specific energy, wide use, and established infrastructure for storage and distribution. Solar methane, as biomethane and synthetic methane, has a major role to play on the energy transition, by reducing both the need for natural gas in domestic or industrial usages and fossil fuels in transportation. The direct electrocatalytic conversion of CO<sub>2</sub> into valuable molecules, such as methane, is still challenging and exhibits poor performances both energetically and in terms of selectivity and conversion yield<sup>223</sup>. Today the most energetically favorable process to transform CO<sub>2</sub> into synthetic CH<sub>4</sub> is the Sabatier reaction:



This reaction has aroused a great interest in the framework of power-to-gas (P2G) technologies<sup>224,225</sup>. It requires significant excess of H<sub>2</sub>, that is generally supplied by alkaline

electrolysis, connected to the electrical grid. Alkaline electrolysis is among the most mature water electrolysis technology, knowing water electrolysis has a low CO<sub>2</sub> footprint only if coupled to renewable sources of, as stated in the conclusion of<sup>226</sup>, that exhibits one of the lowest greenhouse gas (GHG) footprint provided that electricity comes from renewable or nuclear source.<sup>226</sup> Alternatively, solar hydrogen can be used to feed the Sabatier reaction with low overall environmental footprint. Among the many different technologies investigated during the last decades to produce solar hydrogen<sup>15</sup>, photo-electrochemical (PEC) cells combine the versatility of electrochemical devices for water splitting to the light harvesting and charge separation properties of semiconductor materials. Techno-economic analysis shows that solar H<sub>2</sub> production from PEC technology could become competitive by 2050<sup>183,184</sup>. However, to reach maturity, such technologies should be at the same time efficient in terms of solar-to-hydrogen (STH) conversion efficiency, stable over years under intermittent operation, and scalable, which means that they should rely on Earth-abundant materials and cost- and energy-effective processes<sup>175</sup>. This will also require a substantial integration effort<sup>227</sup> to ensure optimized management of charge and heat,<sup>47,228</sup> mass transfer, as well as the safe management of large H<sub>2</sub> and O<sub>2</sub> amounts. Currently, the most efficient photovoltaic-driven electrolysis systems, with up to 30 % STH, rely on expensive III-V/Si multijunctions under concentrated light, associated to platinum-group metal based electrolyzers<sup>65,209,229</sup>. Alternatively, integrated photoelectrochemical approaches that intimately couple photovoltaic cells to electrolyzers (designated as IPEC, following the denomination proposed by Haussener<sup>52</sup>) have reached efficiencies up to 10% STH<sup>52</sup> (and see Fig. 21a in ref.<sup>2</sup>).

The direct coupling of solar H<sub>2</sub> production with the Sabatier reaction has never been investigated. Actually, the Sabatier reaction is a balanced exothermic reaction ( $\Delta_rH^0 = -165 \text{ kJ}\cdot\text{mol}^{-1}$ ) which is industrially implemented in catalytic plug flow reactors, that operate at steady-state, elevated temperature (600 to 700 K), and with precise process control to minimize power demand, and guarantee high selectivity and efficiency of the catalyst. These conditions are hardly compatible with an intermittent supply of H<sub>2</sub>, as delivered by stand-alone PEC cells, unless the process contains a hydrogen storage tank acting as a buffer for continuous hydrogen supply. Alternately, anaerobic methanogens are able to convert CO<sub>2</sub> into CH<sub>4</sub> under mild conditions of pressure and temperature. Eq. 44 is *de facto* part of the metabolism of methanogens that use H<sub>2</sub> as a primary energy and electron source to achieve CO<sub>2</sub> conversion in a non-reversible and selective way. While combining solar H<sub>2</sub> production with biomethanation poses additional challenge in terms of process integration and safety, this would allow a significant reduction in the carbon impact of green methane production units, with a minimal energy cost. Presented here is the EASI Fuel device, featuring integrated photoelectrochemical (IPEC) cells with a combined light-harvesting surface area of 342 cm<sup>2</sup>. These cells generate solar hydrogen to supply a resource-efficient bioreactor.<sup>230</sup> where green methane is produced from CO<sub>2</sub> by methanogens. The EASI Fuel device was one of the three finalists of the European Innovation Council challenge "Horizon Prize - Fuel from the sun: Artificial Photosynthesis " which acknowledged its originality and high standard of integration<sup>b</sup>. its design is discussed in terms of integration and future scaling as well as measured performance during long-term runs under natural solar irradiation, hence demonstrating achievement of a Technology Readiness Level (TRL) of 5.

---

<sup>b</sup> European Commission, Directorate-General for Research and Innovation, Fuel from the sun : Artificial Photosynthesis – EIC Horizon Prize – Commissariat à l'énergie atomique et aux énergies alternatives (CEA), Publications Office of the European Union, 2022, <https://data.europa.eu/doi/10.2777/18380>

## 2 Results and discussion

### 2.1 A compact and integrated design for intensification and scalability

The principle of the EASI Fuel device for solar methane production is depicted in Figure 63. The originality of the developed system lies in the interfacing of a solar water splitting system, self-sufficient for hydrogen production from water under sunlight, with a methanogenic bioreactor for methane formation from CO<sub>2</sub> (Equation 1) in a continuous way and near ambient pressure and temperature.

#### 2.1.1 Integrated Photoelectrochemical Cells.

Solar hydrogen is produced by a series of 45 IPEC cells ( $6.5 \times 6.5 \text{ cm}^2$ ) assembled in 5 monolithic modules ( $21 \times 22 \text{ cm}^2$ ).

Each IPEC cell consists in the association of a silicon / perovskite (Si/PK) tandem solar cell and a hybrid polymer-metal proton exchange membrane (PEM) electrolyser (Figure 64). The  $9.0 \text{ cm}^2$  Si/PK solar cell (n-i-p architecture)<sup>231</sup> with a solar active area of  $7.6 \text{ cm}^2$  ensures photons collection in the 300-1200 nm range thanks to a perovskite top-cell (optical band gap 1.58 eV, UV-visible absorption until 750 nm) deposited onto a silicon heterojunction bottom-cell (optical band gap 1.12 eV, UV-visible-near IR absorption until 1200 nm) and connected in series through an ITO (Indium Tin Oxide) recombination layer. As depicted in Figure 64, the voltage addition of both sub-cells reaches 1.35 - 1.45 V at the maximum power point under 1 sun enabling overall water splitting in a PEM electrolyser based on a typical Ir black/Nafion NRE-112/Pt-C membrane electrode assembly (MEA) prepared by hot pressing. A Au-coated 3D-printed polypropylene flow-plate, as described previously by Cronin and coworkers<sup>194</sup> and a platinized titanium grid as current collector were used at the anode side. At the cathode side, a 3D-printed metallic flow plate in stainless steel (316 L type), with built-in pin flow channels,<sup>192</sup> also acts as both current collector and electrical contact for the Si/PK tandem solar cell.

Additionally, a heat exchanger was integrated in the bulk of the cathodic flow plate, in order to exploit heat generated at the solar cell to raise the water temperature<sup>47</sup> to approx. 50°C, at a typical flow rate between 1 and 5 L.h<sup>-1</sup>, before it is delivered at the anode side, as described in detail elsewhere.<sup>227</sup> In each monolithic module comprising 9 IPEC cells (total solar active area of  $68.4 \text{ cm}^2$ , Figure 64), the fluid management was designed both to connect the 9 heat exchangers in series, hence maximizing the water temperature, and to evenly distribute the pre-heated water flux to 3 series of 3 IPEC cells.<sup>c,d</sup>

---

<sup>c</sup> Pellat, M., Roux, G., Charton, S., Maragno, A. R. A., Photoelectrochemical converter for producing dihydrogen WO 2023057374. (2023).

<sup>d</sup> Pellat, M., Roux, G., Artero, V., Charton, S., Maragno, A. R. A., Matheron, M., Photoelectrochemical converter for producing dihydrogen WO 2023057376. (2023).

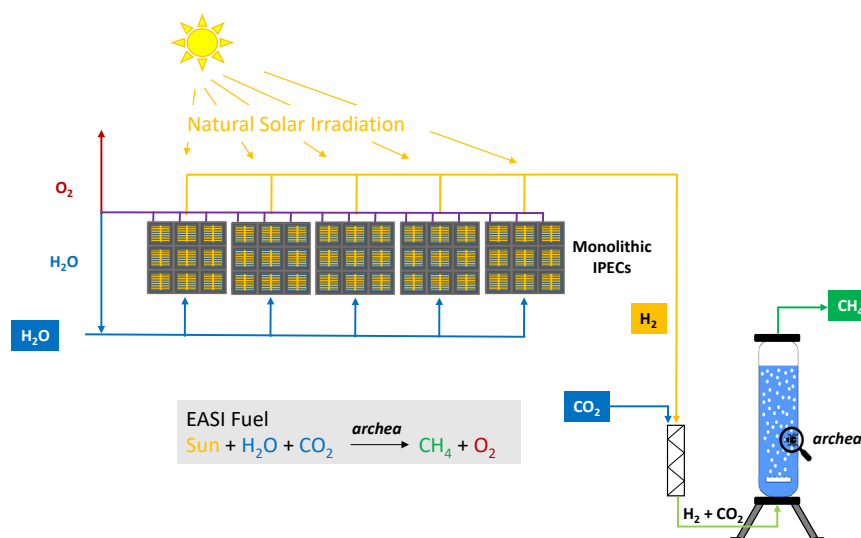


Figure 63. Top: Schematic view of the EASI Fuel device with IPEC modules in series and bioreactor; Bottom: Picture of the EASI Fuel device installed for a 3-day demonstration test at the JRC in Ispra in July 2022.

This design allows to limit the holdup of  $\text{O}_2$  bubbles and electrical resistance created by such bubbles in the anodic compartment.<sup>232</sup>

Wireless electrical integration of the Si/PK solar cell was ensured with a 100  $\mu\text{m}$ -thick indium sheet between its rear electrode and the cathodic flow plate of the electrolyser, enabling the direct use of the photogenerated electrons at the cathode. Positive charges delivered by the PK top cell are transferred to the anode of the electrolyser via a Pt wire. The cell fixation on the cathodic plate has been strengthened with a plastic 3D-printed mask that precisely defines the illuminated surface of the solar tandem cell (9.0  $\text{cm}^2$ ). The 9 IPEC cells in each module are therefore electrically independent, so that the failure of one solar cell or PEM electrolyser, or shading effects likely to occur outdoor, do not affect the performance of the others.



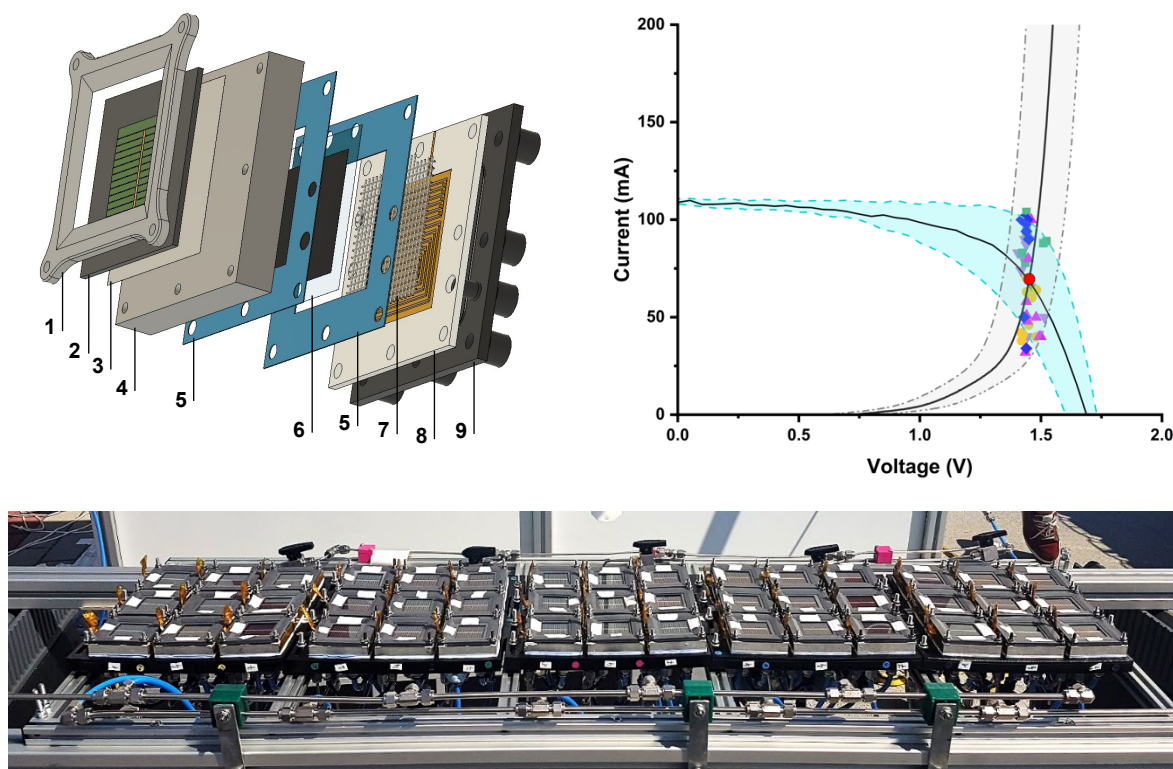


Figure 64. Top left: exploded view of an IPEC cell: 1. mask, 2. Si/PK solar cell, 3. indium sheet, 4. 3D-printed cathodic flow plate with integrated heat exchanger, 5. silicone gasket, 6. membrane-electrode assembly, 7. platinumized Ti grid, 8. gold-coated anodic flow plate, 9. plastic support; Top right: the solid black lines corresponds to the I-V curves of the components of a typical IPEC cell (Si/PK tandem solar cell of 7.6 cm<sup>2</sup> active area, and corresponding PEM electrolyser) whose intersection materializes the operating point (filled red dot). The filled colored symbols (■◆▲▼●) represents the actual operating points of the 45 IPEC cells, measured before the 72 h outdoor test at the JRC, in Ispra, in July 2022. Each colored symbol corresponds to one of the 5 IPEC modules; the shaded blue and grey area represent the dispersion of I-V curves for solar and PEM cells, respectively. Bottom: picture of the 5 monolithic modules installed on the EASI Fuel device.

The operating point of each IPEC cell lies at the crossing between the I-V curve of its Si/PK cell and that of the PEM electrolyser. Figure 64 shows the distribution of the operating points of the 45 IPEC cells assembled in the 5 modules used in the EASI Fuel device, as measured prior to long term testing at Ispra. An equivalent graph, representing the distribution of operating points before long term testing in Grenoble, is shown in Appendix (Figure 70, right). All operating points lie close to 1.45 V. The variation in photocurrent is due to the exponential shape of the I-V curves in this voltage range (see Figure 68).

### 2.1.2 Strain selection and bioreactor.

The anaerobic methane-producing *Methanococcus maripaludis* has been selected for its easy and fast growth under H<sub>2</sub>/CO<sub>2</sub> feed, at ambient temperature (20-40°C).<sup>233</sup> A specific bubble column bioreactor (BCR) was designed and realized<sup>230</sup> to implement the conversion of solar H<sub>2</sub> and CO<sub>2</sub> into green CH<sub>4</sub> (Figure 74 in Appendix). Its innovative, frugal, robust and modular architecture meets both the need for maximizing the bioavailability of the gas to the microorganisms,<sup>234</sup> and for notably reducing the energy consumption, as compared *e.g.* to the direct upscaling of lab-scale mechanically stirred bioreactor (Continuous Stirred-Tank Reactor or CSTR)<sup>235</sup>. Beyond the significant increase of H<sub>2</sub> residence time and gas-liquid exchange surface, provided by dispersing the gas in the form of small bubbles in the culture medium, the biological conversion of the H<sub>2</sub>/CO<sub>2</sub> mixture into CH<sub>4</sub> is further optimized by recycling the

outlet gas flux at the bottom of the reactor, where it is redispersed as bubbles, thanks to a porous metal diffuser and a high recirculation flow of  $10 \text{ L}\cdot\text{h}^{-1}$ .

The reactor was tested for long periods of times, and its sensitivity to various parameters, including temperature, inlet pressure, inlet gas flow, and of course intermittent supply of  $\text{H}_2/\text{CO}_2$  mixture to simulate day-night cycles, was evaluated with bottle gas supply. The achieved selectivity and efficiency of  $\text{CO}_2$  conversion into  $\text{CH}_4$  determined by chromatographic analysis were remarkable with an output gas mainly composed of methane (volume fraction  $X_{\text{CH}_4}$  of 87 vol%) and no side product other than  $\text{H}_2$  ( $X_{\text{H}_2} = 11 \text{ vol}\%$ ) and  $\text{CO}_2$  ( $X_{\text{CO}_2} < 2 \text{ vol}\%$ ) under operational conditions ( $P = 2 \text{ bar}$ ,  $T = 37^\circ\text{C}$ ,  $X_{\text{O}_2} = 0 \text{ vol}\%$ ). The strain exhibited stable performances for over one month without addition of fresh growth medium. The detrimental effect of  $\text{O}_2$  on these oxygen-sensitive microorganisms was prevented by the use of an  $\text{O}_2$ -scavenger system, ensuring a maximum  $\text{O}_2$  concentration below 0.05% in the  $\text{H}_2$  flow along the experiment.



Figure 65. Left: side view of the EASI Fuel device showing the bioreactor in the front (see Figure 74 in Appendix for an enlargement) and the feed water tank in the back; Center: back view showing the control panel; Right : side view showing 4 of the 5 IPEC modules for solar  $\text{H}_2$  production.

### 2.1.3 System Integration : from light capture to fuel production

The autonomous device combines the electrical, thermal and fluidic integration of the 5 IPEC modules (Figure 65, 45 IPEC cells in total) with the bioreactor, together with an automation system allowing for autonomous operation and for the collection of process monitoring relevant data. The process and instrumentation diagram (PID) of the device is provided in Figure 66. Autonomy of the system is ensured by an OPTO 22 type PLC with several analog and digital input/output modules.

A specific and in house control and command program was developed under the Pack Display Basic<sup>®</sup> software suite. Its operation is structured around the programming of 4 control loops (for the regulation of the IPEC modules water flow, the overpressure of the  $\text{H}_2$  produced, the composition of the  $\text{H}_2/\text{CO}_2$  inlet mixture, and the pressure within the bioreactor, respectively), followed by 5 safety actions (concerning the  $\text{O}_2$  content in the gas mixture fed to reactor, the IPECs pressure, the default of water supply to the modules, the bioreactor pressure and the temperature of the  $\text{O}_2$  traps, respectively) and two nominal “day” and “night” operation modes to adjust the electrical consumption to the intermittent  $\text{H}_2$  production.



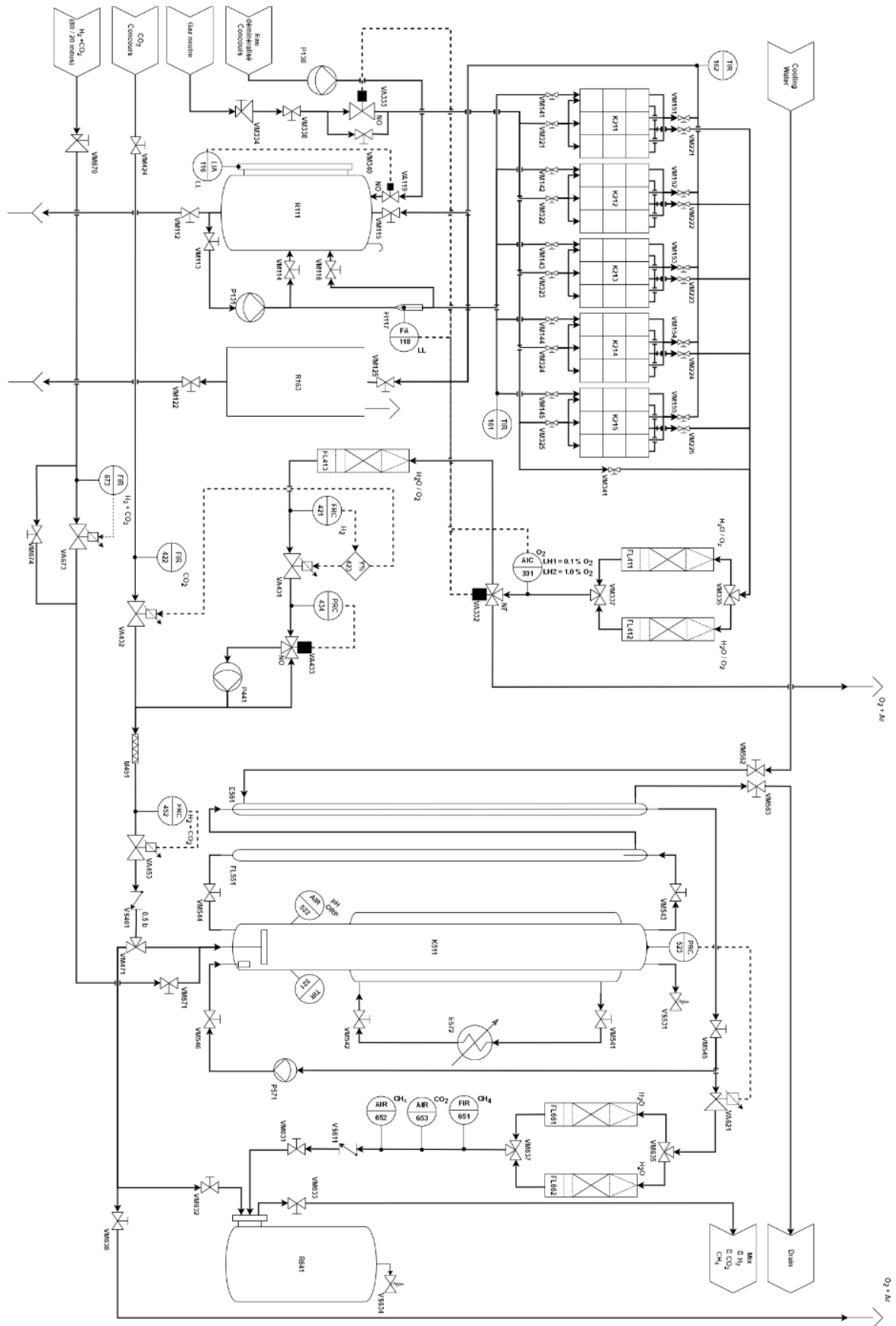


Figure 66. Process and instrumentation diagram of the EASI Fuel device (see Table 25 in Appendix for the PID nomenclature).

Deionized water is supplied continuously to the IPEC modules from a 300 L tank (Figure 66, left) by a flow controlled pump. The on-line removal of possible oxygen trace in the solar hydrogen, before being mixed with CO<sub>2</sub>, to avoid the risk of O<sub>2</sub> contamination in the reactor, was the main challenge encountered to couple solar H<sub>2</sub> production and biomethanation. The water content in the output gas of the IPEC modules must also be limited because of the sensors sensitivity to humidity. Two catalytic filters (activated copper oxide and aluminum oxide for O<sub>2</sub> removal and zeolites for dehumidification) in parallel are used in this aim<sup>e</sup>. The oxygen content is then measured and a third catalytic filter is placed to remove any residual O<sub>2</sub> in the H<sub>2</sub> gas. Once purified, H<sub>2</sub> accumulates upstream from an adjustable pressure valve, until it reaches a sufficient pressure (down to 20 mbar) and is then mixed in real time with CO<sub>2</sub>. The mixing plate consists of a pressure reducer, a flow controller and a static mixer. The gas composition is adjusted to the stoichiometry required for the reaction (Eq. 44), e.g. 80 vol% H<sub>2</sub> – 20 vol% CO<sub>2</sub>. The mixture is then transferred, by a volumetric pump, to the bioreactor at a pressure slightly higher than the one prevailing inside the bubble column, therefore avoiding the need for a compressor.

As the bioreactor nominally operates between 25°C and 35°C, no additional heating was found necessary in the summer period. A reversible Peltier thermoelectric module was however included in the device to maintain the temperature between 25°C and 40°C if needed. The continuous conversion of H<sub>2</sub> and CO<sub>2</sub> into CH<sub>4</sub> and H<sub>2</sub>O causes the pressure in the reactor to change, especially as the 3 gases have different solubilities in the aqueous culture medium. Consequently, a constant pressure of 1.5 bar is maintained in the bioreactor by means of a pressure gauge located in the headspace. For the 2 L liquid column used in the demonstrator, and at the chosen operating pressure and temperature (1.5 bar, 35°C), the maximum gas retention in the reactor is 0.72 L. The outlet gas is dehumidified with zeolites filters, then volumetrically quantified and analysed using infrared sensors in order to determine the CH<sub>4</sub> and CO<sub>2</sub> fractions. Finally, it is stored in a flexible tank (Musthane®) made from rubber-coated fabric, with a maximum volume of 10 L and admissible pressure of 2 bar.

Designed at TRL 5, the EASI Fuel device is autonomous, occupies about 2 m<sup>2</sup> and is able to steadily deliver 12 Wh.day<sup>-1</sup> of methane fuel in a summer day. The device was subjected to ATEX certification by an approved body (APAVE) before its installation and commissioning in Ispra. Only the auxiliary elements, such as pumps, flow-regulators, sensors, whose consumption has been minimized (and could be mutualized at larger scale), used the electrical network.

## 2.2 Real-life tests to assess the device versatility and resilience

The device autonomously operated outdoor for two periods of 72 hours each. The first trial period took place on July 4-7 during summer 2022 in Ispra (Italy), within the framework of the EIC Challenge « Fuel from the Sun: Artificial Photosynthesis » grand finale, while the second test was performed on October 4-7 in autumn 2022 in Grenoble (France). Detailed results and the overall performance achieved during these two demonstrations in real conditions are shown in Figure 67 and Figure 69 (in Appendix), and discussed below.

Figure 67 presents the time-evolution of the green fuel (CH<sub>4</sub> + H<sub>2</sub>) production during the summer test in Ispra, along with the corresponding transient global horizontal irradiance, which was recorded from the ESTI Meteo Tower. Additional graphs depicting the production of solar

---

<sup>e</sup> In the version of the prototype used in Grenoble for the autumn testing campaign, an additional gas-liquid separator was added prior two O<sub>2</sub>/H<sub>2</sub>O filters.

H<sub>2</sub> in Ispra (Figure 71 in Appendix), as well as the time-evolutions of green fuel (Figure 69 in Appendix) are given in the supplementary information section.

During the 3-day summer measurement campaign, the actual duration of methane production was limited to 18 h 15 min, mainly due to the weather conditions (in particular, the system had to be shut down on the first day due to heavy rain to protect the Si/PK tandem solar cells.), and due to the malfunction of the dehumidification system impeding the oxygen sensor and related triggering of the safety system installed on the device. As a result, the time required to reach a nominal state of the entire system was relatively long compared with the duration of the test campaign, with the onset of H<sub>2</sub> production observed after 4 h 14 min of operation. This time was taken as the starting point for determining the system performance (Table 22 and Figure 67). The 2<sup>nd</sup> and the 3<sup>rd</sup> days exhibited a more regular trend, with similar average values for both global normal irradiance (800 W.m<sup>-2</sup>) and global horizontal irradiance (500 W.m<sup>-2</sup>). On the 3<sup>rd</sup> day, the pressure threshold of the solenoid valve, responsible for directing hydrogen flow into the reactor, was reduced from 50 mbar to 20 mbar to compensate for the aging of the tandem solar cells. The system continued to operate remarkably well with such a low overpressure. During this first testing campaign, the device demonstrated its capacity to adapt to a wide range of operating conditions, including the alternative day-night H<sub>2</sub> gas supply, and to stop and restart according to the weather conditions, thanks to the remarkable stability of the Archaea culture.

Table 22. System specifications and achieved performance at the JRC in Ispra in July 2022. The reported data were calculated by subtracting the gas volume already present in the reactor (0.14 L) at the beginning of the measurement campaign. Total incident solar energy  $E_{GHI}$  and solar-to-hydrogen yield  $STH_{GHI}$  are based on the values of Global Horizontal Irradiance (GHI, direct and diffuse incident irradiance measured on a horizontal plane); the same applies for the solar-to-fuel yield  $STF_{CHI}$ . The  $[Photon\ Flux^{3rd\ day}]_{1\ sun}$  and the Quantum Efficiency  $[QE_{Fuel}^{3rd\ day}]_{1\ sun}$  are calculated for the 3<sup>rd</sup> day of production when the irradiance was closer to 1 sun during the operating hours.

Date (2022)	JRC in Ispra			
	July 4	July 5	July 6	July 7
Number of IPEC modules	5			
Total test / production time (h)	72 / 18.25			
Daily production time (h)	2.22	7.29	8.17	0.57
Average GHI (W.m <sup>-2</sup> )	105	557	437	716
Max GHI (W.m <sup>-2</sup> )	969	914	909	793
$E_{GHI}$ (Wh.m <sup>-2</sup> )	237	4082	3600	442
$STH_{GHI}$ (%)	17.13*	6.53	7.42	2.46**
Average H <sub>2</sub> production per hour of operation (L.h <sup>-1</sup> )	0.37			
$r_{H_2}$ (mol.m <sup>-2</sup> .h <sup>-1</sup> )	0.49			
Weighted average of $STH_{GHI}$ (%)	7.00			
Average CH <sub>4</sub> production per hour of operation (L.h <sup>-1</sup> )	0.075			
$[Photon\ Flux^{3rd\ day}]_{1\ sun}$ (mol.m <sup>-2</sup> )	69.40			
$[QE_{Fuel}^{3rd\ day}]_{1\ sun}$ (%)	4.54			
$r_{Fuel}$ (mol.m <sup>-2</sup> .h <sup>-1</sup> )	0.11			
$STF_{GHI}$ (%)	5.48 <sup>+</sup>			

<b>Average concentration of O<sub>2</sub> in the H<sub>2</sub> flow during operating time (%)</b>	0.049	0.022	0.028	0.021
<b>Max O<sub>2</sub> detected in the H<sub>2</sub> flow during the day (%)</b>	> 1 %	> 1 %	0.055	0.034
<b>Reactor Pressure (bar abs)</b>	1.20	1.41	1.40	1.34
<b>Average H<sub>2</sub> Pressure (bar abs)</b>	0.969	0.995	0.988	0.975
<b>Max H<sub>2</sub> Pressure (bar abs)</b>	1.433	1.558	1.554	1.411
<b>Max instantaneous power consumed (W)</b>	132	132	134	133

\* This high STH value on July 4<sup>th</sup>, although consistent with preliminary results obtained from laboratory tests on “fresh” IPECs (unpublished results), has not been included in the average yield, due to uncertainties related to the actual production time.

\*\* Similarly, the data for July 7<sup>th</sup> were not included in the calculation of the weighted average STH, due to the short duration time and instability of the system during the first 30 minutes of the early morning operation.

† X<sub>CH<sub>4</sub></sub>: 89 vol%, X<sub>H<sub>2</sub></sub>: 11 vol%

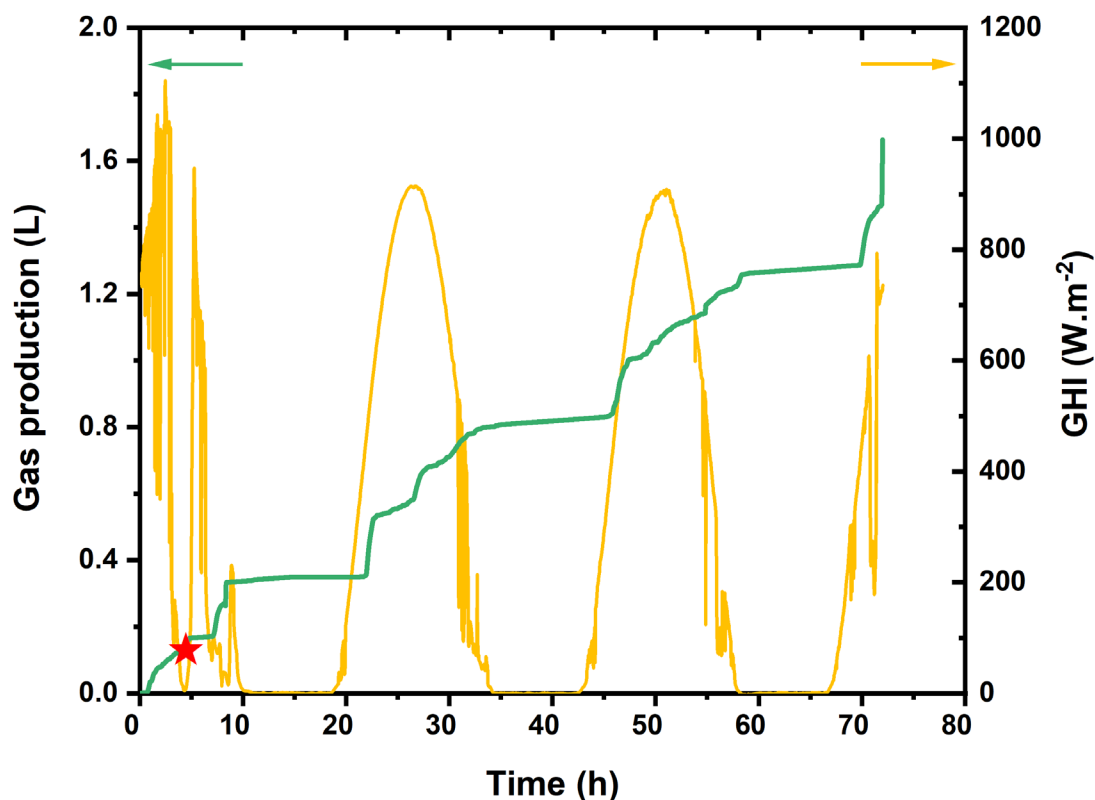


Figure 67. Outdoor test of EASI Fuel device (Ispra): cumulated volume of gas produced (in green), Global Horizontal Irradiance (GHI, in yellow). Red symbol: beginning of the measurement campaign.

The test in Grenoble (Figure 69 in Appendix) was achieved with aged (*i.e.* degraded) Si/PK tandem solar cells and after their decoupling from all IPEC cells, individual testing (see Figure 68), and reassembly of 36 IPEC cells with the best performing Si/PK tandem solar cells. It had a total duration of methane production of 28 h 20 min. During this second campaign, in addition to continuous monitoring with a non-dispersive infrared (NDIR) sensor, the composition of the gas leaving the bioreactor was determined using gas chromatography. Both measurements proved consistent, indicating a fuel composition of X<sub>CH<sub>4</sub></sub> = 89 vol% and X<sub>H<sub>2</sub></sub> = 1 vol%, similar

to that considered to determine the methane production rates and solar-to-fuel yields in Ispra (Table 22) and in Grenoble. During this second campaign, the temperature could also be monitored at different places of the EASI Fuel device (Figure 70, left in Appendix).

## 2.3 Discussion on device performance

### 2.3.1 Solar-to-Hydrogen and Solar-to-Fuel yield

During the first test campaign, the 5 monolithic IPEC modules, with a total capture area of 342 cm<sup>2</sup>, produced hydrogen at a rate of 0.37 L.h<sup>-1</sup>. This corresponds to an average STH<sub>GHI</sub> of 7.0 %, over 72 h of continuous outdoor testing, with 18 h 15 min of solar irradiation. To the best of our knowledge, this is one of the very few examples<sup>66,203</sup> of devices producing solar hydrogen tested under such real life conditions. The STH performance measured under such conditions ranks well with the current state of the art for similar integrated solar-to hydrogen devices<sup>47,203,217,236</sup> working under non-concentrated solar conditions. Importantly, outdoor-measured STH values of fixed-array devices are expected to be lower than those determined in lab conditions since the outdoor irradiance is lower at sunrise and sunset. In addition, the area of the solar cells used here is significantly larger than most integrated devices reported so far which show better performance (typically below 1 cm<sup>2</sup>)<sup>65,236</sup>.

This average value actually captures the significant degradation of the tandem Si/PK solar cells (see below) with a significantly higher STH<sub>GHI</sub> achieved in day 1 (~17 %) compared to the subsequent days (~ 7% on day 2 and 3, ~2.5% on day 4) as reported in Table 22.

The total volume of hydrogen produced by the IPEC cells (approximately 7 L over the 72 consecutive hours of the first testing campaign) was gradually converted into a green fuel primarily consisting of CH<sub>4</sub> and unreacted solar H<sub>2</sub>, by reaction with bottled CO<sub>2</sub> in the bioreactor. The solar-to-fuel yield was calculated at 5.5% over the 72 hours of testing, a value that stands out among other reported systems for converting CO<sub>2</sub> into hydrocarbons<sup>237-245</sup>. While systems producing formic acid, CO or syngas have been reported with higher STF efficiencies, they were of small size, not tested outdoor and not optimized toward a high conversion of CO<sub>2</sub>. The EASI fuel device also ranks well in performance compared to solar photothermal CO<sub>2</sub> conversion into syngas.<sup>246</sup>

The tests performed in Grenoble showed results consistent with the progressive degradation of Si/PK tandem with a solar-to-fuel yield of 2.7 %. Meanwhile, the average CH<sub>4</sub> production per hour of operation was 0.04 L.h<sup>-1</sup>, and the fuel product rate was 0.06 mol.m<sup>-2</sup>.h<sup>-1</sup>. This performance was achieved under an average GHI of 537 W.m<sup>-2</sup> (typical sunshine in autumn in this region), a cumulative E<sub>GHI</sub> of 14246 Wh.m<sup>-2</sup>, for a total operating time greater than in ISPRA but with a reduced number of IPEC modules (36 IPEC cells corresponding to 4 IPEC modules) equipped with aged solar cells. Finally there is a proportional relationship between the two measurement campaigns.

### 2.3.2 Solar cells degradation: a major bottleneck that limits green CH<sub>4</sub> production

While the sequence of tests had no impact on the conversion of CO<sub>2</sub> into methane, which performed remarkably well for months,<sup>230</sup> the performances of the IPEC cells continuously decreased during the testing periods, which was attributed to the degradation of the solar cells (as already observed for other types of IPEC<sup>210</sup>). The impact of this degradation is particularly visible in Figure 68. This graph presents the evolution of the current density produced by the tandem Si/PK cells at 1.45 V and measured under calibrated 1 sun conditions, before integration in the IPEC cells and after each outdoor testing campaign (for these measurements, the solar cells were dismantled from the IPEC cells). The operating current density decay observed after ageing is consistent with and explains the decrease in STH measured over time

(Table 22). Actually, the I-V curves of the solar cells recorded after outdoor ageing (Figure 72 in Appendix) show significant fill factor (FF) losses that impact the current density delivered by the solar cells when integrated into the IPEC cells. Interestingly, these losses seem correlated to the position of the tandems in the IPEC modules (see Figure 73 and Table 24, both in Appendix): losses are minimized (18 %) for tandems placed close to the water inlet, while solar cells at the end of the heat exchanger suffer from major degradations (up to 65 %), suggesting that among stress factors, not only illumination but also heat might play a major role in outdoor ageing.

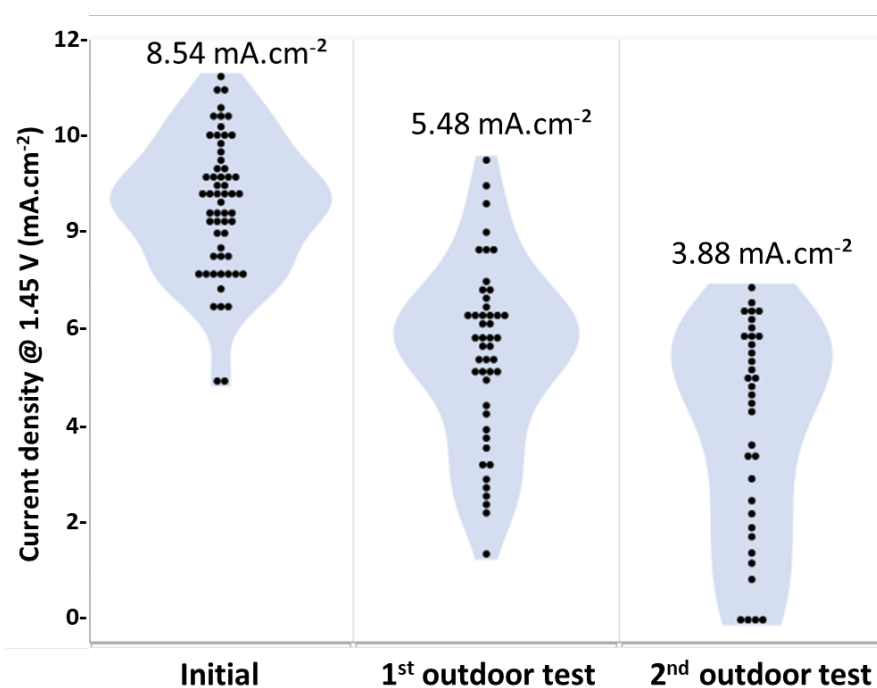


Figure 68. Evolution of current density produced under 1 sun at 1.45 V (close to IPEC cells operating point) by the 45 tandem Si/PK solar cells integrated into the EASI Fuel device. For the measurements, the solar cells were decoupled from the electrolysers. Average current density values are indicated on the top of each dataset.

## 2.4 Market potential

While the EASI Fuel device exploits bottled CO<sub>2</sub> gas, the deployment of solar fuel technologies will require the coupling of the conversion units to either point source supply or air capture plants. Methanogenesis is considered as a promising route for biogas upgrading<sup>247</sup>. Electrochaeta project investigates biomethane production with H<sub>2</sub> produced electrochemically, targeting a 10 MW device based on thermophilic strains of Archea, which benefited from EU fundings in 2020<sup>f</sup>. Accordingly, the best market opportunity for the EASI Fuel technology appears to be coupling solar methane production with a methanisation unit. This approach takes advantage of the large biosourced CO<sub>2</sub> output from methanisation units, which is already compatible with the biological methanation process in the EASI Fuel device. Additionally, it leverages the existing operational connection of such biogas plants to the natural gas distribution network.

<sup>f</sup> Electrochaeta project. <http://www.electrochaeta.com/technology/>

A preliminary economic assessment was carried out in 2021. It was based on the coupling of the EASI Fuel system with a 2MW methane production unit providing a continuous flow of around 200 Nm<sup>3</sup>/h of CO<sub>2</sub> without significant seasonal variations, such as the Biomethan facility in the South of France<sup>g</sup>, to provide an average production of approx. 100 m<sup>3</sup>/h of additional CH<sub>4</sub> thanks to the solar device. The estimated production cost of this green CH<sub>4</sub> was 3.5 times higher than the purchase price of biomethane in France over the same period, with the PEC and bioreactor making an equivalent contribution to this cost. The study also highlighted that coupling the EASI Fuel system with an intermediate H<sub>2</sub> storage, to delay one half of the daily production at night, could reduce the price by up to 40%, thanks to the induced reduction in bioreactor investment and exploitation costs.<sup>h</sup> In addition, the thermal coupling of the EASI Fuel bioreactor with the biomethaniser will ease managing heat variations in the two devices, both of which needing to operate at similar temperature with intermittent energy sources.

In France, the deployment of methanisation is still in progress. The AFG (Association France Gaz) expects a global market of 50 TWh for biogas injected in the French natural gas network by 2030.<sup>i</sup> Taking into account the constraints for the minimal size of the biomethaniser unit (at least 1 MW) and the land constraint for techno-economic viability (a few hectares available), a good estimate of the minimum potential in the French context is around 10% of the global offer, hence around 5 TWh for France, and the valorisation of 500,000 m<sup>3</sup> (820 tons) of CO<sub>2</sub> per year.

In Italy, where biogas is more developed but where most units are dedicated to electricity production<sup>248</sup>, there is an opportunity to convert some of these units to biomethane production. By transforming some of the co-produced CO<sub>2</sub> to methane thanks to solar hydrogen, the EASI Fuel device will extend the biomethane capacity of the converted plant, obviously increasing the opportunity to convert the current electricity dedicated biogas plant to a biomethane plant.

### 3 Conclusion and perspectives

The EASI Fuel device demonstrates solar methane production at a technological readiness level (TRL) of 5 according to the EU definition<sup>j</sup>. It relies on solar H<sub>2</sub> production in IPEC cells where thermal and fluidic integration allowed to intensify both performance and stability compared to classical PV + EC systems via a limitation of the solar cells heating (which affects their efficiency and lifespan)<sup>249</sup> and the preheating of water which lowers the voltage of the electrolysis cells. The proper selection and adaptation of a mesophilic methanogen strain and its growth medium to near ambient temperature and at moderate pressure, coupled with the inventive design of a frugal bioreactor were the key to the direct chaining of solar H<sub>2</sub> production. Such a biological system provides significant flexibility for the direct conversion of solar hydrogen into methane and the EASI Fuel device opens up the possibility of producing high-purity methane in environments where access to electricity is limited. The current demonstration has been made with solar cells that, though not at the state of the art regarding their performance and stability, bear the promise for greater STH, STF and device lifetime. To improve device performance and stability, it is necessary to enhance the shape of the Si/PK

---

<sup>g</sup> [www.biomethan.fr](http://www.biomethan.fr)

<sup>h</sup> The results of this evaluation are detailed in the EIC challenge application file, which can be made available on request. Assumptions were based on 2022 prices, which are no longer relevant since the war in Ukraine and the global energy context.

<sup>i</sup> <https://www.francegaz.fr/wp-content/uploads/CP-LAFG-devient-France-gaz-1.pdf>

<sup>j</sup> [https://ec.europa.eu/research/participants/data/ref/h2020/wp/2014\\_2015/annexes/h2020-wp1415-annex-g-trl\\_en.pdf](https://ec.europa.eu/research/participants/data/ref/h2020/wp/2014_2015/annexes/h2020-wp1415-annex-g-trl_en.pdf)



tandem solar cells' characteristic curve to maximize the operating voltage. This improvement has been initiated by modifying the thickness and composition of the perovskite and p-layers of the perovskite sub-cell<sup>227</sup> and to optimize the encapsulation process<sup>45</sup>. Progress brought by the community regarding perovskite / silicon tandem solar cells have steadily been reported, with recent power conversion efficiencies of 32.5,<sup>250</sup> 33.7<sup>k</sup> and 33.9<sup>l</sup> %, now surpassing the theoretical limit for single junctions. Long lasting performance has also been demonstrated, for example in studies with year-long outdoor operational lifetimes.<sup>249</sup>

Future optimisations regarding the development of noble metal-free catalysts and use of fluorine-free membranes will also further lower the environmental impact and increase the economical viability of this technology. In the short term, the use of stable, cheap but less efficient single-junction absorbers such as silicon, although not economically attractive,<sup>251</sup> could be a relevant option to demonstrate the scalable and reliable coupling of direct solar hydrogen generation and methanogenesis. Furthermore, additive manufacturing technologies should in the future allow to increase the degree of integration of this hybrid solar fuel generator by extending the concept of monoblock geometry, here limited to the PEM module, to the overall device. This will enable to further reduce the weight of the structure, minimize the need for materials and connectors, and increase its compactness, hence paving the way for new industrial and domestic applications of solar fuels.

Finally, positioning the Easi Fuel device for CH<sub>4</sub> production within the state of the art presents an intricate challenge, being it a world-first in coupling IPEC cells with a biological methanation process. An example of two distinct systems achieving equivalent Solar-to-Fuel (STF) values is illustrated in Table 23.

Table 23. Comparison of the Easi Fuel Device with a “large scale” Solar Reactor.

Easi Fuel functional device	Solar Reactor <sup>246</sup>
<ul style="list-style-type: none"> <li>• <b>STF<sub>GHI</sub>: 5.3 ± 0.2 % (Solar CH<sub>4</sub>)</b></li> <li>• Average GHI 453.4 W.m<sup>-2</sup> (Outdoor)</li> <li>• 3 day/night cycles</li> <li>• <b>Solar active surface ~ 360 cm<sup>2</sup></b></li> </ul>	<ul style="list-style-type: none"> <li>• <b>STF: 4.1 ± 0.8 % (Solar Syngas)</b></li> <li>• Solar concentration ratio ~ 2100 W.m<sup>-2</sup></li> <li>• 51.1 min operating time</li> <li>• <b>Sun-tracking reflectors area : 507 m<sup>2</sup></b></li> </ul>

## 4 Experimental procedures

### 4.1 Monitoring of gas production and Safety limits

#### 4.1.1 O<sub>2</sub> monitoring and safety.

At the outlet of the IPEC modules and before the mixing operation with CO<sub>2</sub>, the device is equipped with a compact oxygen transmitter that uses proven sensor technology (oxy.IQ2 oxygen sensor) to measure the volume fraction of O<sub>2</sub> in the gas produced by the IPEC. More in detail, the oxygen sensor is an advanced galvanic fuel cell (0 - 1000 ppm); the transmitter is

<sup>k</sup> <https://www.pv-magazine.com/2023/05/30/kaust-claims-33-7-efficiency-for-perovskite-silicon-tandem-solar-cell/>

<sup>l</sup> <https://www.pv-magazine.com/2023/11/03/longi-claims-33-9-efficiency-for-perovskite-silicon-tandem-solar-cell/>

installed after two O<sub>2</sub>/H<sub>2</sub>O reducing filters (CRS - 202295-5S) in parallel, which, under normal operating conditions, allow to reach O<sub>2</sub> content of less than 5 ppb, and H<sub>2</sub>O content of less than 20 ppb. The measurement of the O<sub>2</sub> concentration is monitored to enable system shutdown in case of a filters failure, which would compromise process integrity.

To ensure the device security, two safety thresholds have been programmed in the O<sub>2</sub> sensor. The first threshold corresponds to 1% of the lower explosive limit (LEL) of hydrogen in air, and is the threshold above which the device may present a risk to humans. If this threshold is exceeded, all hydrogen production is evacuated from the demonstrator, and a purge with neutral gas (argon) is performed throughout the hydrogen production area to evacuate any contaminated gas from the demonstrator. The second threshold, set at a concentration of 0.1 vol% O<sub>2</sub> in H<sub>2</sub>, corresponds to the point at which the process is at risk. At this threshold, the biological system can be severely degraded, adversely affecting methane production. When this threshold is exceeded, hydrogen production is directed away from the device so as not to introduce oxygen into the biological part of the demonstrator. Moreover, to prevent any risk of deterioration of the biological part, a third O<sub>2</sub>/H<sub>2</sub>O filter (CRS - 202295-5S) is positioned downstream of the O<sub>2</sub> sensor to ensure maximum reduction of the oxygen content (O<sub>2</sub> < 0.1 vol%). Finally, initial experiments carried out on the device showed that the moisture contained in the gas, coming from the IPEC modules, tended to condense before passing through the filters, greatly reducing filtration efficiency. For the autumn testing campaign, the device was therefore fitted with a liquid gas separator upstream of the filtration system to capture any source of liquid water. As an additional safety measure, and to avoid the accumulation of the oxygen produced by the IPEC modules, a potential source of explosion, the water leaving the electrolyser was collected in an open air recovery tank ("R163" tank in Figure 66).

#### **4.1.2 Produced gas control and supply.**

In addition to sensors dedicated to safety, the system is equipped with various sensors required for monitoring and data acquisition. All gas flows are measured using BROOKS SLA5850S thermal mass flowmeters, with the exception of the gas flow produced at the reactor outlet, which is measured using Bronkhorst EL-FLOW F-201CV thermal mass flowmeters. Pressure is measured using KELLER serie 23 absolute pressure transmitters. The residual CH<sub>4</sub> and CO<sub>2</sub> composition in the gas produced is obtained by infrared measurement (NDIR) using 2 smartGas FLOW evo sensors (CH<sub>4</sub> sensor : F3-043108-05000 and CO<sub>2</sub> sensor : F3-214507-05000), respectively calibrated over a range of 0 to 100%vol and 0 to 50vol%. The bioreactor chamber is also equipped with measuring instruments to monitor the condition of the biological system. The bioreactor is equipped with a Mettler Toledo INPRO3253i probe for simultaneous measurement of pH, redox potential and temperature of the culture medium. The thermal sensors for mass flow and gas composition measurement (NDIR) are sensitive to the humidity that may be contained in the gas. To protect this equipment, moisture traps (CRS - 202230-SS) are installed at the outlet of the bioreactor outlet. Finally, all signals measured on the device are transmitted to the programmable controller for recording or use in plant automation.

For information, all bottle of gas used to test the device were supplied by the gas manufacturer "Air Products" with a certified purity level > 99.999%. For verification and calibration of the CO<sub>2</sub> infrared sensor, the gas used was a mixture of CO<sub>2</sub> and N<sub>2</sub> in equivalent proportions (50/50 vol%). For calibrating the CH<sub>4</sub> infrared sensor, the gas used was pure methane. The device is also equipped with an argon-based inert gas cylinder and an 80/20 vol% H<sub>2</sub> - CO<sub>2</sub> gas mixture, used to maintain biological cultures between experiments.

## 4.2 Irradiance monitoring

In Ispra, the values of Global Horizontal Irradiance (GHI) were recorded from the ESTI Meteo Tower (J.R.C. Ispra || 45° 48' 43.4' N - 8° 37' 37.4' E || altitude: 220 m), positioned approximately 100 m from the EASI Fuel Device. Incident power in the IPEC plane was not recorded. Solar to fuel efficiencies are calculated against GHI and are therefore likely to be overestimated by maximum 10 % (Figure 75 in Appendix), as horizontal irradiance is lower than normal irradiance. To keep the reader aware of that, *STH* and *STF* are explicitly denoted with a GHI subscript.

The photon flux was registered with a In-Plane spectroradiometer mounted on the EKO Sun Tracker STR-32G, that followed an azimuth-elevation algorithm and was therefore not in a fixed configuration like the IPEC modules. Consequently, the  $[QE_{Fuel}^{3rd\ day}]_{1\ sun}$  for the fixed array of IPEC modules is likely to be underestimated, depending on the photon flux.

On the other hand, in Grenoble, the Global Horizontal Irradiance was measured by a static Kipp & Zonen CMP10 pyranometer.

Thus, the comparison between the two test campaigns can be made by considering the results depending on the Global Horizontal Irradiance (Table 22, Figure 69 in Appendix), calculated during both the summer and autumn campaigns.

## 4.3 Data analysis and performance calculation

All calculations have been carried out considering standard conditions of pressure and temperature (earlier IUAPC definition, 0°C and 1.013 bar).

The solar to hydrogen efficiency<sup>70</sup> is calculated according to the following Equation:

$$STH = \frac{\text{Output energy as } H_2}{\text{Energy of incident solar light}} = \frac{n_{H_2} \times \Delta G_r}{E_{sun} \times A} \quad \text{Eq. 45}$$

$n_{H_2}$  is the amount (in mole) of Hydrogen,  $\Delta G_r$  is the reaction's Gibbs free energy (237  $kJ.mol^{-1}$ ) for water splitting reaction at 298 K, corresponding to 1.23 V, that is the thermodynamic water splitting voltage.  $E_{sun}$  is the total incident solar energy ( $Ws\ cm^{-2}$ ) and  $A$  is the irradiated active surface ( $cm^2$ ).

The product rate (i.e. quantity of product)<sup>50</sup> per irradiated active surface ( $A$  in  $m^2$ ) and time ( $h$  of production) can be expressed by:

$$r_{product} = \frac{n_{product}}{A \times t} \quad \text{Eq. 46}$$

This equation is used to calculate both the  $H_2$  produced from electrochemical water splitting, and the fuel produced during the production hours.

Volume of produced fuel inside the reactor. The effective production of hydrogen in Ispra started at  $t_0 + 4\ h\ 14\ min$  (1:14 pm). Consequently, all the methane produced before 1:14 pm was discarded for the final calculations. A similar procedure, taking into account the slope variation of the curve "Gas production (NL) vs. Time (h)", as well as the  $H_2$  flow rate, was applied when analyzing the results of the measurement campaign carried out in Grenoble.

The Quantum Efficiency for methane production is the product of the amount of CH<sub>4</sub> in mol ( $n_{CH_4}$ ) with the number of electrons required to transform CO<sub>2</sub> into CH<sub>4</sub>, ( $N_e = 8$ ), divided by the number of incidents photons reaching the active area of the IPEC cells ( $N_{ph} \times A$ ).in ( $mol.m^{-2} \times m^2$ )

$$QE_{CH_4} = \frac{N_e \times n_{CH_4}}{N_{ph} \times A} \quad \text{Eq. 47}$$

To define the efficiency of the device, the solar to fuel yield is expressed as the ratio of the chemical energy produced and the incident solar energy  $E_{sun}$ .

$$STF_{GHI} = \frac{\text{Chemical energy}}{\text{Solar energy}} = \frac{\text{mol}_{fuel\ produced} \times HHV_{fuel\ produced} (J.mol^{-1})}{E_{sun}(Wh.m^{-2}) * A (m^2) * 3600(J.Wh^{-1})} \quad \text{Eq. 48}$$

The total higher heating value of the produced fuel is derived from the following equations:

$$HHV_{fuel\ produced} = HHV_{CH_4} \times X_{CH_4} + HHV_{H_2} \times X_{H_2} \quad \text{Eq. 49}$$

$HHV$  is the higher heating value corresponding to  $890,800 J.mol^{-1}$  for the green methane and to  $285,667 J.mol^{-1}$  for the unreacted hydrogen.

$X_{CH_4}$  and  $X_{H_2}$  are respectively the volume fractions of methane and hydrogen in the gas at the reactor outlet.

## 5 Appendix

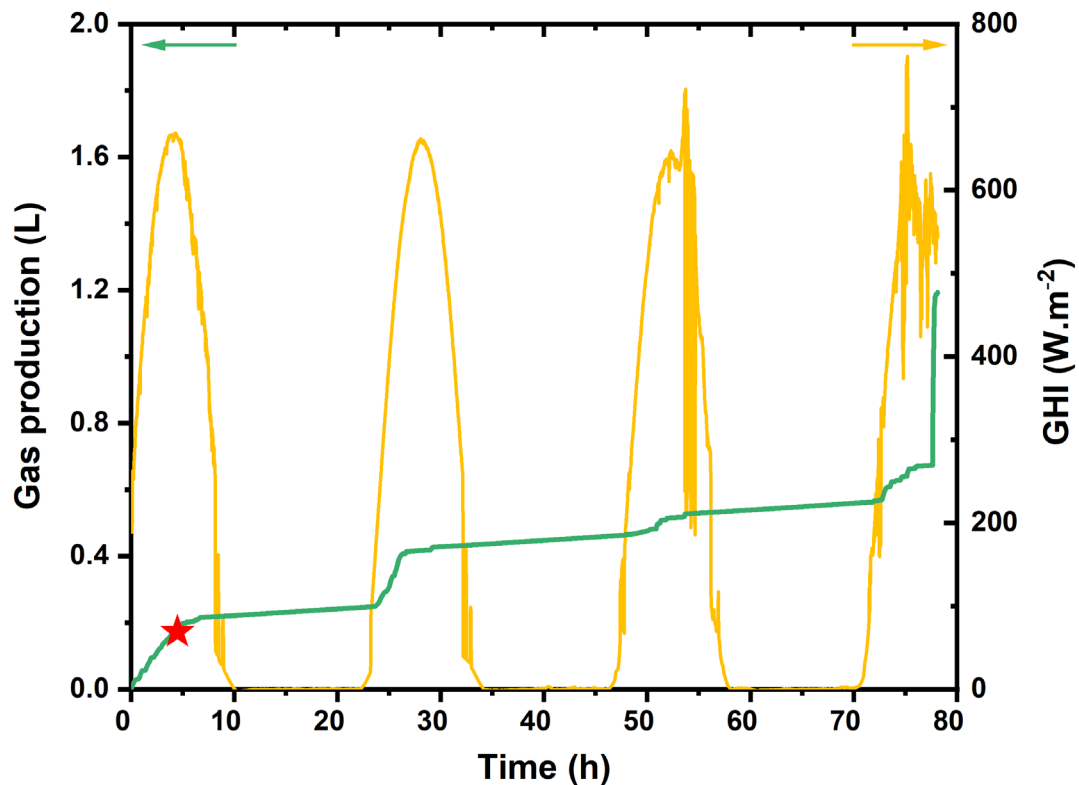


Figure 69. Outdoor test of EASI Fuel device in Grenoble (second campaign, in autumn): cumulated volume of gas produced (in green), Global Horizontal Irradiance (GHI, in yellow). Red star : beginning of the solar production. The initial gas volume of 0.18 L, present within the reactor before this point, was omitted in the STF calculation.

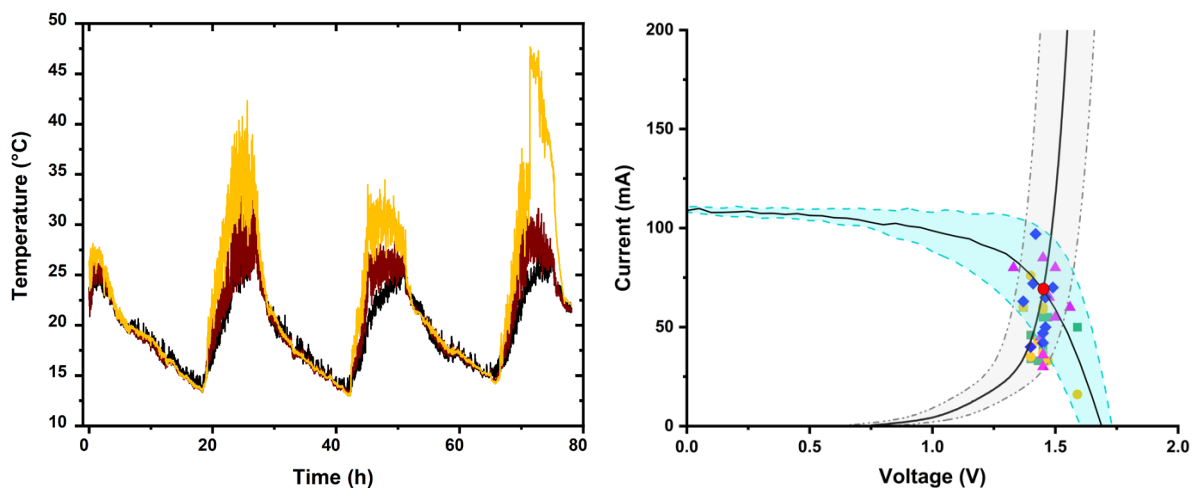


Figure 70. Left : temperature monitoring during the outdoor test of EASI Fuel device in Grenoble (second campaign, in autumn): measured ambient temperature close to the mixing plate (in black), measured ambient temperature close to the IPEC modules (in brown), measured temperature on the tandem solar cells (in yellow). Right : determination of operating point (red dot) of an IPEC cell at the intersection of the I-V curve of a tandem Si/PK solar cell, and the I-V curve of a PEM electrolyser (plain black trace). The cloud of filled colored symbols (■◆▲●) represents the experimental operating points of the 36 IPEC cells, measured before the 72 h outdoor test at CEA, in Grenoble, in October 2022. Each color corresponds to one of the 4 IPEC modules. The shaded blue and grey area represent the dispersion of I-V curves for solar and PEM cells, respectively.

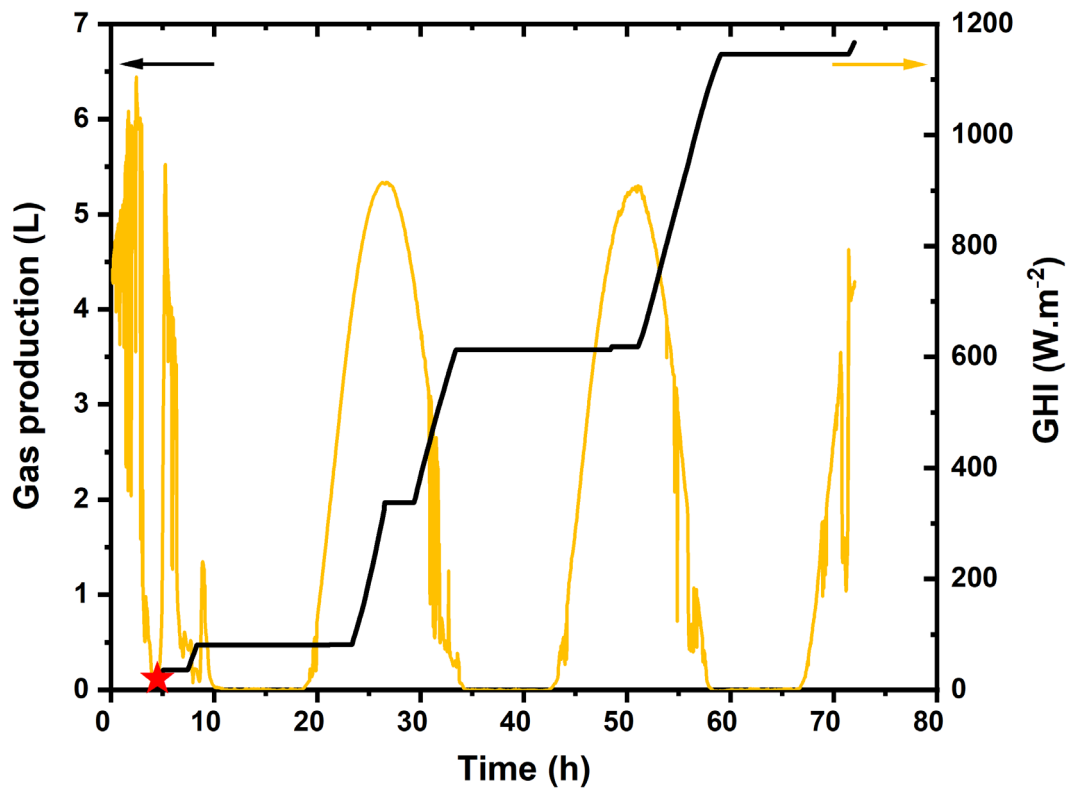


Figure 71. Outdoor test of EASI Fuel device in Ispra (first campaign, in summer): cumulated volume of solar H<sub>2</sub> produced (in black), Global Horizontal Irradiance (GHI, in yellow). Red star: beginning of the summer measurement campaign.

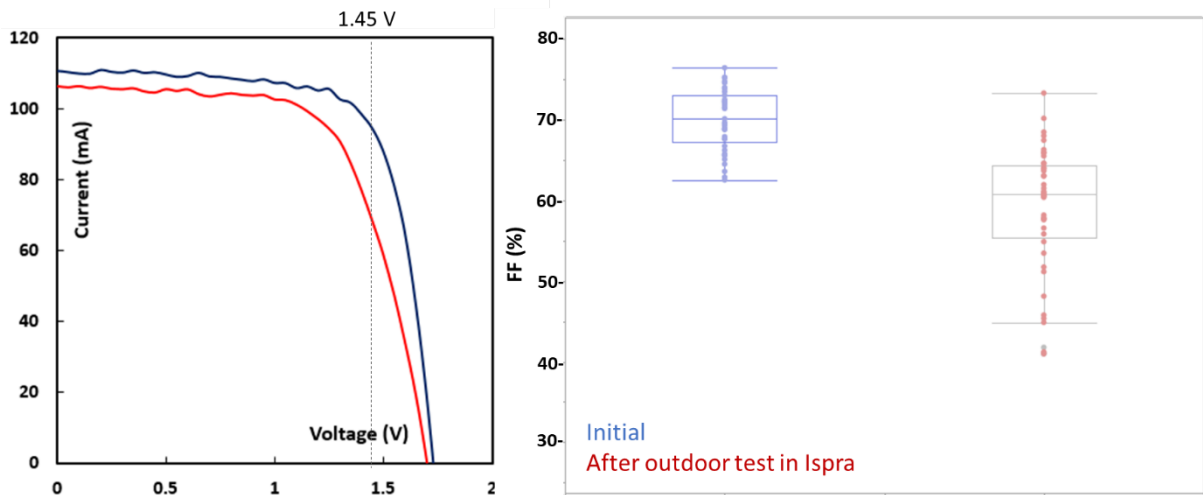


Figure 72. Typical evolution of I-V curves of a tandem Si/PK solar cell before / after outdoor test in Ispra, and statistics on fill factor for the whole dataset. To perform these measurements, the solar cells were decoupled from the electrolyzers.

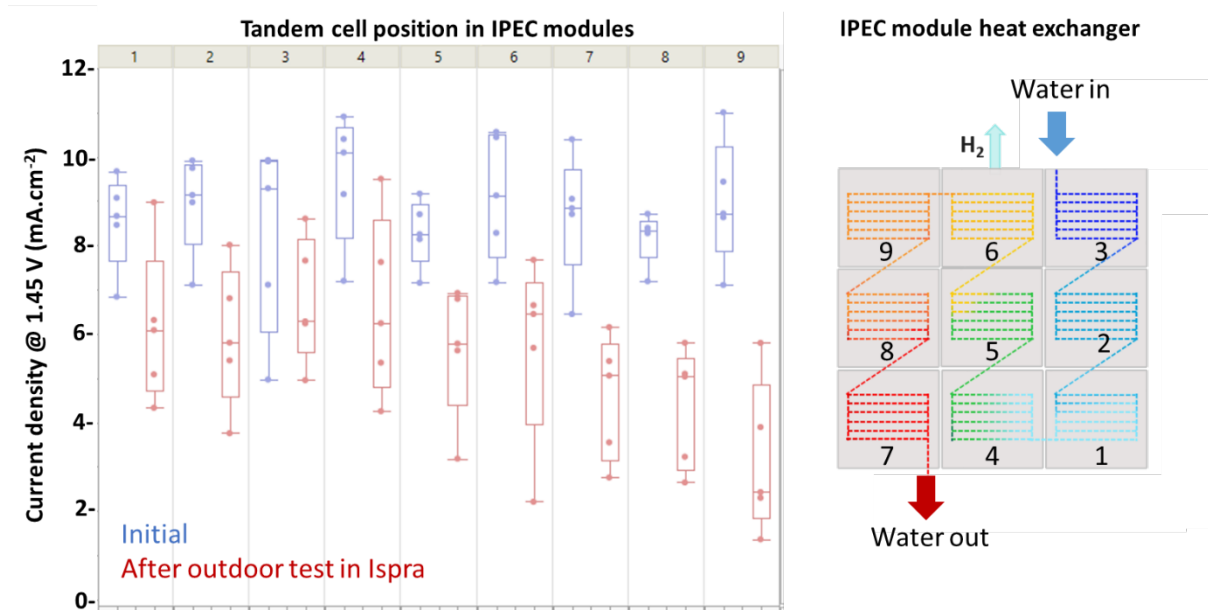


Figure 73. Evolution of current density produced by the tandem Si/PK solar cells under 1 sun at 1.45 V (close to operating point) before (in blue) and after (in red) outdoor test in Ispra. To perform these measurements, the solar cells were decoupled from the electrolyzers. Data from the 45 tandems are represented as a function of their location within the IPEC modules, shown on the right.

Table 24. Average current density produced by the tandem Si/PK solar cells at 1.45 V and under 1 sun before / after the outdoor test in Ispra, as a function of the location of the solar cells within the IPEC modules. To perform these measurements, the solar cells were decoupled from the electrolyzers.

Position	1	2	3	4	5	6	7	8	9
<b>Initial (mA.cm<sup>-2</sup>)</b>	8.55	8.98	8.24	9.56	8.29	9.12	8.69	8.18	8.98
<b>After (mA.cm<sup>-2</sup>)</b>	6.16	5.96	6.75	6.60	5.67	5.74	4.59	4.37	3.16
<b>Loss (%)</b>	28	34	18	31	32	37	47	47	65



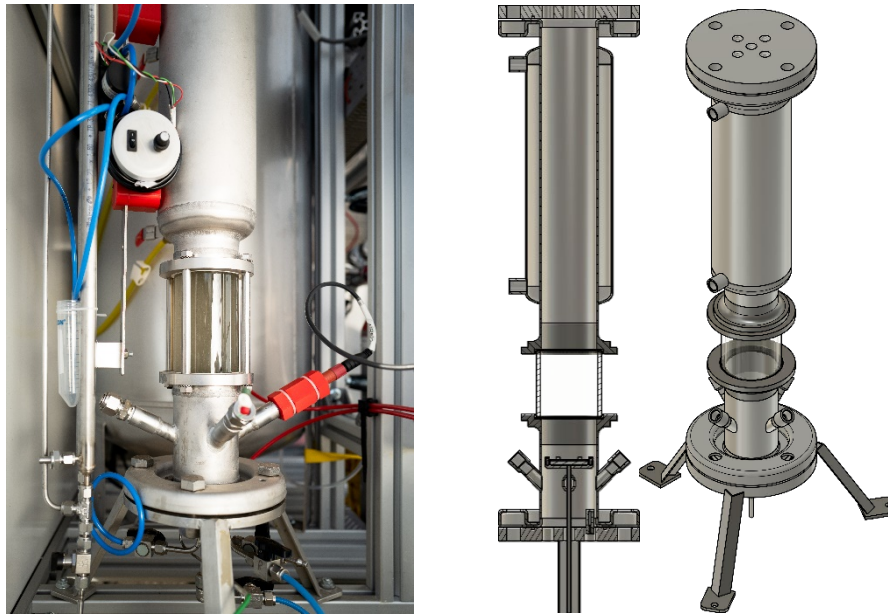


Figure 74. View of the bioreactor. Left: Actual view. Centre: CAD sectional view. Right: CAD isometric view.

Table 25. EASI Fuel device PID nomenclature

<b>TAG</b>	<b>Equipment</b>	<b>Supplier - Ref</b>
R111	Demineralized water supply tank	SECTORIEL - 425020006INX
R163	Demineralized water drainage tank	DENIOS - 266183W
VM112	Low drain valve for R111	HAM-LET - H800SSSL6MM
VM113	Electrolyser supply valve from R111	HAM-LET - H800SSSL6MM
VM114	Recirculation valve for R111	HAM-LET - H800SSSL6MM
VM115	Electrolysis water return valve in R111	HAM-LET - H800SSSL6MM
LIA116	Visual level for R111	RS PRO - 174-8427
FI117	Float flowmeter	KOBOLD - KSK-1015H P08 S0
FA118	Low flow sensor	KOBOLD - KSK-1015H P08 S0
VA119	Solenoid valve for water filling R111	BURKERT - TYPE 6281
VM116	Electrolyser bypass valve	HAM-LET - H300USSLV6MMRS
VM122	Low drain valve for R163	DENIOS - 266183W
VM125	Electrolysis water return valve in R163	HAL-LET - H800SSSL6MM
P130	Water supply pump for R111 tank	W ROBINSON AND SONS - 022-422
P131	Electrolyser water supply pump	SCHWARZER PRECISION - SP 622 EC-BL
VM141	Water inlet valve - electrolyser n°1	HAM-LET - H800SSSL6MM
VM142	Water inlet valve - electrolyser n°2	HAM-LET - H800SSSL6MM
VM143	Water inlet valve - electrolyser n°3	HAM-LET - H800SSSL6MM
VM144	Water inlet valve - electrolyser n°4	HAM-LET - H800SSSL6MM
VM145	Water inlet valve - electrolyser n°5	HAM-LET - H800SSSL6MM
VM151	Water outlet valve - electrolyser n°1	HAM-LET - H800SSSL6MM
VM152	Water outlet valve - electrolyser n°2	HAM-LET - H800SSSL6MM

VM153	Water outlet valve - electrolyser n°3	HAM-LET - H800SSSL6MM
VM154	Water outlet valve - electrolyser n°4	HAM-LET - H800SSSL6MM
VM155	Water outlet valve - electrolyser n°5	HAM-LET - H800SSSL6MM
TIR161	Electrolyser inlet water temperature	RS PRO - 397-1264
TIR162	Electrolyser inlet water temperature	RS PRO - 397-1264
K211	Electrolyser n°1	NON-COMMERCIAL EQUIPEMENT
K212	Electrolyser n°2	NON-COMMERCIAL EQUIPEMENT
K213	Electrolyser n°3	NON-COMMERCIAL EQUIPEMENT
K214	Electrolyser n°4	NON-COMMERCIAL EQUIPEMENT
K215	Electrolyser n°5	NON-COMMERCIAL EQUIPEMENT
VM221	Gas outlet valve - electrolyser n°1	HAM-LET - H800SSSL1/8
VM222	Gas outlet valve - electrolyser n°2	HAM-LET - H800SSSL1/8
VM223	Gas outlet valve - electrolyser n°3	HAM-LET - H800SSSL1/8
VM224	Gas outlet valve - electrolyser n°4	HAM-LET - H800SSSL1/8
VM225	Gas outlet valve - electrolyser n°5	HAM-LET - H800SSSL1/8
VM321	Inert gas inlet valve - electrolyser n°1	HAM-LET - H800SSSL1/8
VM322	Inert gas inlet valve - electrolyser n°2	HAM-LET - H800SSSL1/8
VM323	Inert gas inlet valve - electrolyser n°3	HAM-LET - H800SSSL1/8
VM324	Inert gas inlet valve - electrolyser n°4	HAM-LET - H800SSSL1/8
VM325	Inert gas inlet valve - electrolyser n°5	HAM-LET - H800SSSL1/8
AIC331	Oxygen composition analyzer	PANAMETRICS - OXY. IQ
VA332	Automatic drain valve (NF)	BURKERT - TYPE 0330
VA333	Inert gas supply valve (NO)	BURKERT - TYPE 0330
VM334	Inert gas pressure regulator	AIR LIQUIDE - REF 15658
VM335	3-way valve inlet O <sub>2</sub> , H <sub>2</sub> O filter	HAM-LET - H800SSSL1/8T
VM337	3-way valve outlet Filter O <sub>2</sub> , H <sub>2</sub> O	HAM-LET - H800SSSL1/8T
VM338	Inert gas isolation valve	HAM-LET - H800SSSL6MM
VM340	By-pass valve VA333	HAM-LET - H800SSSL6MM
FL411	H <sub>2</sub> O / O <sub>2</sub> filter	CRS - 202295-SS
FL412	H <sub>2</sub> O / O <sub>2</sub> filter	CRS - 202295-SS
FL413	H <sub>2</sub> O / O <sub>2</sub> filter	CRS - 202295-SS
FRC421	H <sub>2</sub> flowmeter	BROOKS - SLA5850S
FIR422	CO <sub>2</sub> flowmeter	BROOKS - SLA5850S
Y%423	H <sub>2</sub> /CO <sub>2</sub> proportional calculator	NON-COMMERCIAL EQUIPEMENT
VM341	By-pass valve Electrolyser	HAL-LET - H800SSSL6MM
VM424	Manual CO <sub>2</sub> isolation valve	HAL-LET - H800SSSL6MM
VA431	H <sub>2</sub> flow control valve	BROOKS - SLA5850S
VA432	CO <sub>2</sub> flow control valve	BROOKS - SLA5850S
VA433	3-way H <sub>2</sub> supply valve (NC)	BURKERT - TYPE 0330
PRC434	H <sub>2</sub> overpressure control pressure switch	KELLER - SERIE 23
P441	H <sub>2</sub> booster pump	SCHWARZER PRECISION - SP 622 EC-BL-DU

M451	Static mixer	COLE-PARMER - KOFLO 1/4-21 316 SS TUBE MIXER
FRC452	H <sub>2</sub> + CO <sub>2</sub> flowmeter	BROOKS - SLA5850S
VA453	H <sub>2</sub> + CO <sub>2</sub> flow control valve	BROOKS - SLA5850S
VS461	Gas check valve	H400ASSL6MM3PSI
VM471	H <sub>2</sub> / CO <sub>2</sub> gas supply manual drain valve	HAM-LET - H800SSSL6MMT
K511	Bioreactor	NON-COMMERCIAL EQUIPEMENT
TIR521	Bioreactor temperature measurement	METTLER-TOLEDO - INPRO3253i/SG/120
AIR522	pH and ORP measurement	METTLER-TOLEDO - INPRO3253i/SG/120
PRC523	Pressure measurement	KELLER - SERIE 23
VS531	Safety valve	HAM-LET - H900SSL6MMSL
VM541	Double jacket isolation valve	HAM-LET - H700SSL6MMTLD
VM542	Double jacket isolation valve	HAM-LET - H700SSL6MMTLD
VM543	Isolation valve in Gas/Liquide separator	HAM-LET - H800SSSL6MM
VM544	Isolation valve in Gas/Liquide separator	HAM-LET - H800SSSL6MM
VM545	K511 production output isolation valve	HAM-LET - H800SSSL6MM
VM546	Isolation valve recirculation gas	HAM-LET - H800SSSL6MM
FL551	Gas/Liquide separator	NON-COMMERCIAL EQUIPEMENT
E561	Gas condenser	NON-COMMERCIAL EQUIPEMENT
VM562	Water isolation valve condenser	HAM-LET - H700SSL6MMTLD
VM563	Water isolation valve condenser	HAM-LET - H700SSL6MMTLD
P571	Gas recirculation pump	SCHWARZER PRECISION - SP 622 EC-BL-DU
E572	K511 thermoregulator	NON-COMMERCIAL EQUIPEMENT
VS611	Gas check valve	HAM-LET - H400SSL6MM1/3PSI
VA621	Pressure control valves in K511	BROOKS - SLA5820S
VM631	R641 product gas isolation valve	HAM-LET - H800SSSL6MM
VM632	R641 inerting gas isolation valve	HAM-LET - H800SSSL6MM
VM633	Tank drain valve R641	HAM-LET - H800SSSL6MM
VS634	Safety valve	HAM-LET - H900SSL6MMSL
VM635	3-way valve inlet H <sub>2</sub> O filter	HAM-LET - H800SSSL1/8T
VM637	3-way valve outlet H <sub>2</sub> O filter	HAM-LET - H800SSSL1/8T
VM638	Gas circuit purge valve	HAM-LET - H800SSSL6MM
R641	CH <sub>4</sub> storage tank	MUSTHANE - CUSTOMISED EQUIPMENT
FIR651	Production gas flowmeter	BRONKHORST - EL-FLOW F-201CV
AIR652	CH <sub>4</sub> analyzer	SMARTGAS - F3-043108-05000
AIR653	CO <sub>2</sub> analyzer	SMARTGAS - F3-214507-05000
FL661	Moisture filter	CRS - 202230-SS
FL662	Moisture filter	CRS - 202230-SS
VM670	Pressure regulator for industrial H <sub>2</sub> / CO <sub>2</sub> gases	AIR LIQUIDE - REF 15658

VM671	K511 H <sub>2</sub> / CO <sub>2</sub> industrial gas supply valve	HAM-LET - H800SSSL6MM
VA673	Flow control valve industrial H <sub>2</sub> / CO <sub>2</sub> gases	BRONKHORST - EL-FLOW F-201CV
FIR673	Mixing flow sensor for industrial gases H <sub>2</sub> / CO <sub>2</sub>	BRONKHORST - EL-FLOW F-201CV
VM674	H <sub>2</sub> /CO <sub>2</sub> industrial gas bypass valve	HAM-LET - H800SSSL6MM

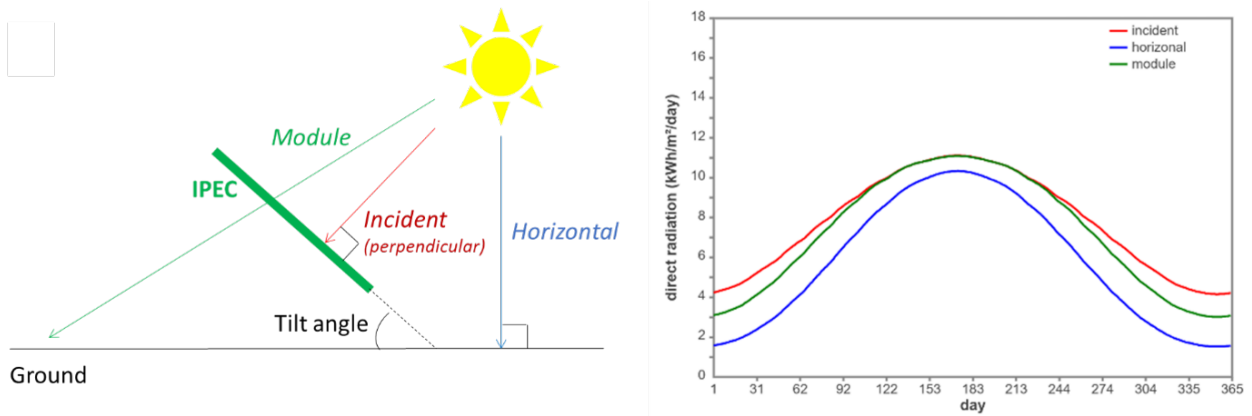


Figure 75. Influence of the reference surface on the incident power density measurement (adapted from C.B.Honsberg and S.G.Bowden, “Solar Radiation on a Tilted Surface” page on [www.pveducation.org](http://www.pveducation.org)).

Note that transposition from Global Horizontal Irradiance (GHI) to Global Normal Irradiance (GNI) or Direct Normal Irradiance (DNI) relies on complex mathematical models, that have to take into account scattering and albedo.



## Chapter 5:

### Conclusions and perspectives



## Chapter 5:

### Conclusions and perspectives

The research discussed in this manuscript employs a progressive Technology Readiness Level approach.

The *first chapter* focuses on the "sustainable" global context in which the thesis takes place, presenting the policies introduced nowadays to reduce CO<sub>2</sub> emissions, the photoelectrochemical devices for H<sub>2</sub> production, an energy vector at the center of the sustainable circular economy, and the limiting factors for scale-up purposes. A key role in my study is given by chemical engineering, the analysis of transport phenomena related to the applications described in the manuscript, through numerical models and simulations, helps us to develop scaled-up devices.

*Chapter 2* focuses on BiVO<sub>4</sub> photoanodes (TRL 3) This semiconductor indeed find potential applications in PEC cells.

The impact of possible heterogeneities in large-scale preparation processes on the performance of these photoactive materials was studied. It was identified how the porosity and/or roughness of the BiVO<sub>4</sub> layer can either limit or promote nanoscale transport phenomena, such as photons and charge carriers, as well as photocurrent generation.

The fabricated BiVO<sub>4</sub> photoanodes exhibit a mainly monoclinic crystallographic structure (clinobisvanite), a bandgap of 2.4 – 2.5 eV and a light absorption range of 250 – 500 nm. Photoelectrochemical characterizations confirm that the performance of photoanodes manufactured by electrodeposition systematically exceeds that of spin-coated photoanodes, both deposition processes being transposable on a large scale. Moreover, they highlight the benefits of dopants for improving electron mobility, and of catalysts for enhancing the reaction kinetics. The highest measured photocurrent was 3.12 mA.cm<sup>-2</sup> at 1.23 V (vs. RHE) on a CoPi-BiVO<sub>4</sub> photoanode made by electrodeposition on FTO 7 glass coated substrate. Although the electrodes were not optimized (this was not the aim of the study), this value measured on electrodes with an active surface of 3 cm<sup>2</sup> of which only 0.46 cm<sup>2</sup> was illuminated is consistent with the state of the art, announcing a photocurrent of 6.5 cm<sup>2</sup>, in PV-biased configuration, for a fully illuminated CoPi-BiVO<sub>4</sub> photoanode of 1cm<sup>2</sup>.<sup>63</sup>

In all cases, a very good reproducibility of the results was evidenced. The conductivity of the support was confirmed to be the main parameter affecting the photocurrent.

**The best performing BiVO<sub>4</sub> photoanodes were manufactured via electrodeposition on the most conductive support (FTO)**, they have a photocatalytic layers of thickness of around 1.3 μm, with a small surface rugosity (around 0.20 μm). Microscopy revealed a **very porous structure**, likely to result in a large concentration of active catalytic sites, and a more homogeneous texture compared to the samples prepared by spin coating.

Complementing the experimental analysis, a numerical study was carried out. The aim of these optical simulation was to better understand the transport and conversion of light in "model" geometries with the same textures as electrodeposited and spin-coated photo-anodes, to be compared with similar objects but with flat textures. A parametric study on model sinusoidal textured surfaces was also achieved in an attempt to decorrelate the effect of the amplitude and the period of the surface of the photoactive layer. Optical simulations on real structures are consistent with experimental observations, highlighting the effect of the roughness of the



BiVO<sub>4</sub> layer, and confirm the higher performance of the photoanodes fabricated by electrodeposition. A clear effect of the texture on the absorption spectrum is evidenced.

**The simulation considering sinusoidal periodic grooves also suggest that a greater margin for optimization is possible on active layers typical of electro-disposition** (same optical indices and same average thickness as for FTO 7\_El photoanodes). The results moreover guide us in our understanding on how thickness and roughness may limit the photoactivity of the BiVO<sub>4</sub> anodes. Interestingly, on the best performing configuration (FTO 7\_El, average BiVO<sub>4</sub> thickness 1.3 μm) it appears that reducing the groove spacing below the photons diffusion length ( $T < L_d$ ) results in a 50% increase in the photocurrent relative to the flat surface, and this plateau current appears to be insensitive the groove depth.

Further investigations, including active surface measurements, along with precise assessments of surface porosity and its impact of charge or reactant transport (as *e.g.* tortuosity, apparent diffusivity, etc.) and catalytic activity, could provide more comprehensive results and reveal additional limiting factors. Optical simulations conducted in the presence of an electrolyte and considering chemical reactions would enhance the interpretation of these phenomena.

In *Chapter 3*, the attention was shift to integrated PEC cells, exploring their scalability to evaluate the benefits of fluidic, electrical and thermal integration.

This investigation addresses the drawbacks and proposes potential enhancements required for the implementation of industrial-scale technology. The coupling of an in-house design PEM cell and a PK/Si tandem solar cell makes it possible to achieve stable and quantitative H<sub>2</sub> production, thanks to effective water management, efficient separation of the hydrogen and oxygen flows, and robust electrical contacts. **The relevance of the thermal, electrical and fluidic integration was first evidenced on an IPEC cell, and then transposed to an IPEC module with, roughly, a factor 10 in the active area.**

**For the first time, experiments have been carried out on a large number of specimens (over 60 cells and 5 modules), enabling us to quantify the impact of dispersion on performance.**

As in *Chapter 2*, **the achieved STH efficiencies are consistent with the recent state of the art** ( $5 \leq \text{STH} \leq 21\%$ ), generally reporting the best performance measured on devices with significantly smaller size (active solar surface  $\sim 1 \text{ cm}^2$ ), and under short periods of controlled irradiation. The results obtained on both the IPEC cells (STH up to 8.4 %) and the IPEC modules (up to STH 6.3 %) demonstrate that **the proposed integrated design limits the loss of performance due to scaling and/or transposition to real conditions.**

Finally, **the ageing of the solar cells has been identified as the main factor limiting the performance of the IPEC and their stability.** Among the potential areas for improvement, adjustments to the PK thickness and the doping of the PTAA layer have been identified and are being tested.

*Chapter 4* outlines the implementation process of 5 IPEC modules and their integration into the EASI Fuel (European Autonomous Solar Integrated fuel station).

This autonomous solar technology enables the continuous conversion of H<sub>2</sub> (produced under sunlight by the IPEC cells) and CO<sub>2</sub> into methane within a methanogenesis Archaea-based bioreactor. Last step of our bottom-up approach, **the functioning of these 5 IPEC modules in the EASI Fuel device, allowed to take up the challenges of water photoelectrolysis on a larger scale (400 cm<sup>2</sup> of illuminated surface) and under real weather conditions (TRL 5).**

The EASI Fuel device successfully operates under variable outdoor conditions and prove stable operation for more than 100 hours to date.

The direct coupling of the alternative source of H<sub>2</sub> to a continuous reactor using biological material, to which this thesis actively contributes, represents a world-first with a remarkable STH up to 6.7 % and a  $5.3 \pm 0.2$  % solar to fuel yield (STF). Further optimizations are possible, in particular to increase the life of the tandem solar cells (see *Chapter 3*) and reduce the energy costs of the system.

The approach adopted in this thesis, based on the identification of the main factors limiting the performance of different PEC and semiconductor concepts, rather than motivated by the search for the best performance, has enable us to test and validate optimization strategies for the scale-up. The knowledge acquired could also serve as basis for future material optimization study, e.g. on multiphysics modelling and simulation, only partially addressed here, with a view to scaling up other types of photoactive technologies, ultimately helping to discover and promote the development of the most promising ones for solar fuel production.

# References

1. Sharp, I. D., Atwater, H. A. (Harry A. & Lewerenz, H.-J. *Integrated Solar Fuel Generators*. *The Royal Society of Chemistry* (2018). doi:10.1039/9781788010313
2. Kim, J. H., Hansora, D., Sharma, P., Jang, J. W. & Lee, J. S. Toward practical solar hydrogen production – an artificial photosynthetic leaf-to-farm challenge. *Chem. Soc. Rev.* **48**, 1908–1971 (2019).
3. *Climate Change: Evidence and Causes*. *Climate Change* (The National Academies Press, 2020). doi:10.17226/25733
4. Martin, R. *et al.* *Ghg Emissions of All World Countries Jrc Science for Policy Report*. *Publications Office of the European Union* (2023). doi:10.2760/235266
5. Alsarhan, L. M., Alayyar, A. S., Alqahtani, N. B. & Khdary, N. H. Circular carbon economy (Cce): A way to invest co2 and protect the environment, a review. *Sustain.* **13**, (2021).
6. Masson-Delmotte, V. *et al.* *Climate Change 2021: the Physical Science Basis*. (2021).
7. Ovaere, M. & Proost, S. Cost-effective reduction of fossil energy use in the European transport sector: An assessment of the Fit for 55 Package. *Energy Policy* **168**, 113085 (2022).
8. IEA. *Renewable Energy Market Update: Outlook for 2023 and 2024 - International Energy Agency*. (2023).
9. Barber, J. & Tran, P. D. From natural to artificial photosynthesis. *J. R. Soc. Interface* **10**, (2013).
10. Nocera, D. G. The Artificial Leaf. *Acc. Chem. Res.* **45**, 767–776 (2012).
11. Chen, Z., Dinh, H. N. & Miller, E. Photoelectrochemical water splitting: standards, experimental methods, and protocols. 126 (2013). doi:10.1007/978-1-4614-8298-7
12. Amjad, U. E. S. *et al.* Methane Steam Reforming on the Pt/CeO<sub>2</sub> Catalyst: Effect of Daily Start-Up and Shut-Down on Long-Term Stability of the Catalyst. *Ind. Eng. Chem. Res.* **58**, 16395–16406 (2019).
13. Ashraf, M. A. *et al.* Experimental Insights into the Coupling of Methane Combustion and Steam Reforming in a Catalytic Plate Reactor in Transient Mode. *Ind. Eng. Chem. Res.* **60**, 196–209 (2021).
14. Collodi, G. Hydrogen production via steam reforming with CO<sub>2</sub> capture. *Chem. Eng. Trans.* **19**, 37–42 (2010).
15. SAYAMA, K. & MISEKI, Y. Research and development of solar hydrogen production. *Synth. English Ed.* **7**, 79–91 (2014).
16. International Renewable Energy Agency. Hydrogen. Available at: <https://www.irena.org/Energy-Transition/Technology/Hydrogen#:~:text=As at the end of,around 4%25 comes from electrolysis.> (Accessed: 7th January 2024)
17. Kalamaras, C. M., Efstathiou, A. M., Al-Assaf, Y. & Poullikkas, A. Hydrogen Production Technologies: Current State and Future Developments. *Conf. Pap. Energy* **2013**, (2013).

18. Fuel Cells and Hydrogen 2 Joint Undertaking. Fuel Cells and Hydrogen 2 Joint Undertaking - Annual Work Plan and Budget. *Eur. Comm.* (2018).
19. Usman, M. R. Hydrogen storage methods: Review and current status. *Renew. Sustain. Energy Rev.* **167**, 112743 (2022).
20. Nielander, A. C., Shaner, M. R., Papadantonakis, K. M., Francis, S. A. & Lewis, N. S. A taxonomy for solar fuels generators. *Energy Environ. Sci.* **8**, 16–25 (2015).
21. Bard, A., Faulkner, L. & White, H. *Electrochemical methods: fundamentals and applications*. (2022).
22. Wei, J. *et al.* Heterostructured Electrocatalysts for Hydrogen Evolution Reaction Under Alkaline Conditions. *Nano-Micro Lett.* **10**, 75 (2018).
23. Kou, T., Wang, S. & Li, Y. Perspective on High-Rate Alkaline Water Splitting. *ACS Mater. Lett.* **3**, 224–234 (2021).
24. Luo, Y. *et al.* Morphology and surface chemistry engineering toward pH-universal catalysts for hydrogen evolution at high current density. *Nat. Commun.* **10**, (2019).
25. Liu, Y. *et al.* Corrosion engineering towards efficient oxygen evolution electrodes with stable catalytic activity for over 6000 hours. *Nat. Commun.* **9**, 1–10 (2018).
26. Yoon, Y., Kim, H., Kim, S.-K., Jeong Kim, J. & Jae Jeong Kim, C. Acid-durable, high-performance cobalt phosphide catalysts for hydrogen evolution in proton exchange membrane water electrolysis. (2021). doi:10.1002/er.6936
27. Nozik, A. J. Photochemical diodes. *Appl. Phys. Lett.* **30**, 567–569 (1977).
28. Li, J. & Wu, N. Semiconductor-based photocatalysts and photoelectrochemical cells for solar fuel generation: A review. *Catal. Sci. Technol.* **5**, 1360–1384 (2015).
29. Zhang, H., Liu, J., Xu, T., Ji, W. & Zong, X. Recent Advances on Small Band Gap Semiconductor Materials ( $\leq 2.1$  eV) for Solar Water Splitting. *Catalysts* **13**, (2023).
30. Nasir, S. N. S. *et al.* Direct extrapolation techniques on the energy band diagram of BiVO<sub>4</sub> thin films. *Phys. B Condens. Matter* **604**, 412719 (2021).
31. Zanatta, A. R. Revisiting the optical bandgap of semiconductors and the proposal of a unified methodology to its determination. *Sci. Rep.* **9**, 11225 (2019).
32. De Jamblinne De Meux, A., Pourtois, G., Genoe, J. & Heremans, P. Method to quantify the delocalization of electronic states in amorphous semiconductors and its application to assessing charge carrier mobility of p-type amorphous oxide semiconductors. *Phys. Rev. B* **97**, 1–10 (2018).
33. Solymar, L., Walsh, D. & Syms, R. R. A. *Principles of semiconductor devices. Electrical Properties of Materials* (2018). doi:10.1093/oso/9780198829942.003.0009
34. Schweicher, G., Olivier, Y., Lemaire, V. & Geerts, Y. H. What currently limits charge carrier mobility in crystals of molecular semiconductors? *Isr. J. Chem.* **54**, 595–620 (2014).
35. Bolton, J. R. The photochemical conversion and storage of solar energy: An historical perspective. *Sol. Energy Mater. Sol. Cells* **38**, 543–554 (1995).
36. Grätzel, M. Photoelectrochemical cells. *Nature* **414**, 338–344 (2001).
37. Gu, D. M., Zhang, J. Z., Zhang, M., Geng, Y. & Su, Z. M. Dye regeneration mechanisms of dye sensitized solar cells: Quantum chemical studies on the interaction

- between iodide and O/S-containing organic dyes. *Dye. Pigment.* **132**, 136–141 (2016).
38. Ren, Y. *et al.* Hydroxamic acid pre-adsorption raises the efficiency of cosensitized solar cells. *Nature* **613**, 60–65 (2023).
  39. Goto, Y. *et al.* A Particulate Photocatalyst Water-Splitting Panel for Large-Scale Solar Hydrogen Generation. *Joule* **2**, 509–520 (2018).
  40. Wang, Q. *et al.* Scalable water splitting on particulate photocatalyst sheets with a solar-to-hydrogen energy conversion efficiency exceeding 1%. *Nat. Mater.* **15**, 611–615 (2016).
  41. Ru Ng, A. Y., Boruah, B., Chin, K. F., Modak, J. M. & Soo, H. Sen. Photoelectrochemical Cells for Artificial Photosynthesis: Alternatives to Water Oxidation. *ChemNanoMat* **6**, 185–203 (2020).
  42. Fujishima, A. & Honda, K. Electrochemical Photolysis of Water at a Semiconductor Electrode. *Nature* **238**, 37 (1972).
  43. Khaselev, O. & Turner, J. A. A monolithic photovoltaic-photoelectrochemical device for hydrogen production via water splitting. *Science (80-. )*. **280**, 425–427 (1998).
  44. Reece, S. Y. *et al.* Wireless Solar Water Splitting Using Silicon-Based Semiconductors and Earth-Abundant Catalysts. *Science (80-. )*. **334**, 645 (2011).
  45. McKone, J. R., Lewis, N. S. & Gray, H. B. Will solar-driven water-splitting devices see the light of day? *Chemistry of Materials* **26**, 407–414 (2014).
  46. Wang, Z. *et al.* Host/Guest Nanostructured Photoanodes Integrated with Targeted Enhancement Strategies for Photoelectrochemical Water Splitting. *Adv. Sci.* **9**, 1–16 (2022).
  47. Tembhurne, S., Nandjou, F. & Haussener, S. A thermally synergistic photoelectrochemical hydrogen generator operating under concentrated solar irradiation. *Nat. Energy* **4**, 399–407 (2019).
  48. Zahran, Z. N. *et al.* Perfect Matching Factor between a Customized Double-Junction GaAs Photovoltaic Device and an Electrolyzer for Efficient Solar Water Splitting. *ACS Appl. Energy Mater.* **5**, 8241–8253 (2022).
  49. Nguyen, D. N., Fadel, M., Chenevier, P., Artero, V. & Tran, P. D. Water-Splitting Artificial Leaf Based on a Triple-Junction Silicon Solar Cell: One-Step Fabrication through Photoinduced Deposition of Catalysts and Electrochemical Operando Monitoring. **20**, 59 (2023).
  50. Andrei, V., Wang, Q., Uekert, T., Bhattacharjee, S. & Reisner, E. Solar Panel Technologies for Light-to-Chemical Conversion. *Acc. Chem. Res.* **55**, 3376–3386 (2022).
  51. Nocera, D. G. The artificial leaf. *Acc. Chem. Res.* **45**, 767–776 (2012).
  52. Tembhurne, S. & Haussener, S. Integrated Photo-Electrochemical Solar Fuel Generators under Concentrated Irradiation. *J. Electrochem. Soc.* **163**, H988–H998 (2016).
  53. Kistler, T. A. *et al.* Integrated Membrane-Electrode-Assembly Photoelectrochemical Cell under Various Feed Conditions for Solar Water Splitting. *J. Electrochem. Soc.* **166**, H3020–H3028 (2019).
  54. Du, N. *et al.* Anion-Exchange Membrane Water Electrolyzers. *Chem. Rev.* **122**, 11830–

- 11895 (2022).
55. Maeda, K. Photocatalytic water splitting using semiconductor particles: History and recent developments. *J. Photochem. Photobiol. C Photochem. Rev.* **12**, 237–268 (2011).
  56. Hong, W. *et al.* High-Performance Silicon Photoanode Enhanced by Gold Nanoparticles for Efficient Water Oxidation. *ACS Appl. Mater. Interfaces* **10**, 6262–6268 (2018).
  57. Fujita, T. *et al.* Nanoporous Metal Papers for Scalable Hierarchical Electrode. *Adv. Sci.* **2**, 2–7 (2015).
  58. Akay, Ö. *et al.* Electrolysis in reduced gravitational environments: current research perspectives and future applications. *npj Microgravity* **8**, (2022).
  59. Reyes Cruz, E. A. *et al.* Molecular-Modified Photocathodes for Applications in Artificial Photosynthesis and Solar-to-Fuel Technologies. *Chem. Rev.* **122**, 16051–16109 (2022).
  60. Fischer, F. Photoelectrode, photovoltaic and photosynthetic microbial fuel cells. *Renew. Sustain. Energy Rev.* **90**, 16–27 (2018).
  61. Luo, J. *et al.* Water photolysis at 12.3% efficiency via perovskite photovoltaics and Earth-abundant catalysts. *Science (80-. ).* **345**, 1593–1596 (2014).
  62. Andrei, V., Reuillard, B. & Reisner, E. Bias-free Solar Syngas Production by Integrating a Molecular Cobalt Catalyst with Perovskite–BiVO<sub>4</sub> Tandems. *Nat. Mater.* **19**, 189 (2020).
  63. Pihosh, Y. *et al.* Photocatalytic generation of hydrogen by core-shell WO<sub>3</sub>/BiVO<sub>4</sub> nanorods with ultimate water splitting efficiency. *Sci. Reports 2015 51* **5**, 1–10 (2015).
  64. Qiu, Y. *et al.* Efficient solar-driven water splitting by nanocone BiVO<sub>4</sub>-perovskite tandem cells. *Sci. Adv.* **2**, (2016).
  65. Fehr, A. M. K. *et al.* Integrated halide perovskite photoelectrochemical cells with solar-driven water-splitting efficiency of 20.8%. *Nat. Commun.* **14**, (2023).
  66. Datta, K. *et al.* Efficient Continuous Light-Driven Electrochemical Water Splitting Enabled by Monolithic Perovskite-Silicon Tandem Photovoltaics. *Adv. Mater. Technol.* **8**, 2201131 (2023).
  67. Kistler, T. A., Um, M. Y. & Agbo, P. Stable Photoelectrochemical Hydrogen Evolution for 1000 h at 14% Efficiency in a Monolithic Vapor-fed Device. *J. Electrochem. Soc.* **167**, 066502 (2020).
  68. Ahmet, I. Y. *et al.* Demonstration of a 50 cm<sup>2</sup> BiVO<sub>4</sub> tandem photoelectrochemical-photovoltaic water splitting device. *Sustain. Energy Fuels* **3**, 2366–2379 (2019).
  69. Becker, J. P. *et al.* A modular device for large area integrated photoelectrochemical water-splitting as a versatile tool to evaluate photoabsorbers and catalysts. *J. Mater. Chem. A* **5**, 4818–4826 (2017).
  70. Nishiyama, H. *et al.* Photocatalytic solar hydrogen production from water on a 100-m<sup>2</sup> scale. *Nature* **598**, 304–307 (2021).
  71. Cobo, S. *et al.* A Janus cobalt-based catalytic material for electro-splitting of water. *Nat. Mater.* **11**, 802–807 (2012).

72. Selberherr, S. *Analysis and Simulation of Semiconductor Devices*. (1984). doi:10.1007/978-3-7091-8752-4
73. Bedoya-Lora, F. E., Holmes-Gentle, I. & Haussener, S. Multiphysics model for assessing photoelectrochemical phenomena under concentrated irradiation. *Electrochim. Acta* **462**, 142703 (2023).
74. Scassellati, P. Contribution to the simulation of photo-electrochemical cells. (Politecnico di Torino, 2021).
75. Carver, C. *et al.* Modelling and development of photoelectrochemical reactor for H<sub>2</sub> production. *Int. J. Hydrogen Energy* **37**, 2911–2923 (2012).
76. Haussener, S. *et al.* Modeling, simulation, and design criteria for photoelectrochemical water-splitting systems. *Energy Environ. Sci.* **5**, 9922–9935 (2012).
77. Andrade, L., Lopes, T., Ribeiro, H. A. & Mendes, A. Transient phenomenological modeling of photoelectrochemical cells for water splitting - Application to undoped hematite electrodes. *Int. J. Hydrogen Energy* **36**, 175–188 (2011).
78. Berger, A. & Newman, J. An Integrated 1-Dimensional Model of a Photoelectrochemical Cell for Water Splitting. *J. Electrochem. Soc.* **161**, E3328–E3340 (2014).
79. Singh, M. R., Haussener, S. & Weber, A. Z. Chapter 13: Continuum-scale Modeling of Solar Water-splitting Devices. *RSC Energy Environ. Ser.* **2019-January**, 500–536 (2019).
80. Yang, X. S., Koziel, S. & Leifsson, L. Computational optimization, modelling and simulation: Recent trends and challenges. *Procedia Comput. Sci.* **18**, 855–860 (2013).
81. Falciani, G. & Chiavazzo, E. An overview on modelling approaches for photochemical and photoelectrochemical solar fuels processes and technologies. *Energy Convers. Manag.* **292**, (2023).
82. Lee, D. K. & Choi, K. S. Enhancing long-term photostability of BiVO<sub>4</sub> photoanodes for solar water splitting by tuning electrolyte composition. *Nat. Energy* **3**, 53–60 (2018).
83. He, Y., Gamba, I. M., Lee, H. C. & Ren, K. On the Modeling and Simulation of Reaction-Transfer Dynamics in Semiconductor-Electrolyte Solar Cells. <http://dx.doi.org/10.1137/130935148> **75**, 2515–2539 (2015).
84. Kim, J. H. & Lee, J. S. Elaborately Modified BiVO<sub>4</sub> Photoanodes for Solar Water Splitting. *Adv. Mater.* **31**, 1–35 (2019).
85. Wang, L., Zhang, Y., Li, W. & Wang, L. Recent advances in elaborate interface regulation of BiVO<sub>4</sub> photoanode for photoelectrochemical water splitting. *Mater. Reports Energy* **3**, 100232 (2023).
86. Yao, X. *et al.* Scale-Up of BiVO<sub>4</sub> Photoanode for Water Splitting in a Photoelectrochemical Cell: Issues and Challenges. *Energy Technol.* **6**, 100–109 (2018).
87. Liu, C. *et al.* Cobalt-phosphate-modified Mo:BiVO<sub>4</sub> mesoporous photoelectrodes for enhanced photoelectrochemical water splitting Chemical routes to materials. *J Mater Sci* **54**, 10670–10683 (2019).
88. Tembhurne, S. & Haussener, S. Integrated Photo-Electrochemical Solar Fuel Generators under Concentrated Irradiation. *J. Electrochem. Soc.* **163**, H988–H998



- (2016).
89. Datta, K. *et al.* Efficient Continuous Light-Driven Electrochemical Water Splitting Enabled by Monolithic Perovskite-Silicon Tandem Photovoltaics. *Adv. Mater. Technol.* **8**, (2023).
  90. Rahman, M. Z., Raziq, F., Zhang, H. & Gascon, J. Key Strategies for Enhancing H<sub>2</sub> Production in Transition Metal Oxide Based Photocatalysts. *Angew. Chemie Int. Ed.* **62**, e202305385 (2023).
  91. Ho-Kimura, S., Moniz, S. J. A., Handoko, A. D. & Tang, J. Enhanced photoelectrochemical water splitting by nanostructured BiVO<sub>4</sub>-TiO<sub>2</sub> composite electrodes. *J. Mater. Chem. A* **2**, 3948–3953 (2014).
  92. Hilliard, S. Water splitting photoelectrocatalysis: the conception and construction of a photoelectrocatalytic water splitting cell. (Université Pierre et Marie Curie - Paris VI, 2016).
  93. Sfaelou, S., Pop, L. C., Monfort, O., Dracopoulos, V. & Lianos, P. Mesoporous WO<sub>3</sub> photoanodes for hydrogen production by water splitting and PhotoFuelCell operation. *Int. J. Hydrogen Energy* **41**, 5902–5907 (2016).
  94. Zhang, L. *et al.* Significantly enhanced photocurrent for water oxidation in monolithic Mo:BiVO<sub>4</sub>/SnO<sub>2</sub>/Si by thermally increasing the minority carrier diffusion length. *Energy Environ. Sci* **9**, 2044 (2016).
  95. Butler, K. T. *et al.* Ultrafast carrier dynamics in BiVO<sub>4</sub> thin film photoanode material: interplay between free carriers, trapped carriers and low-frequency lattice vibrations. *J. Mater. Chem. A* **4**, 18516–18523 (2016).
  96. Hou, C. *et al.* An effective route for growth of WO<sub>3</sub>/BiVO<sub>4</sub> heterojunction thin films with enhanced photoelectrochemical performance. *J. Ind. Eng. Chem.* **104**, 146–154 (2021).
  97. Pihosh, Y. *et al.* Photocatalytic generation of hydrogen by core-shell WO<sub>3</sub>/BiVO<sub>4</sub> nanorods with ultimate water splitting efficiency. *Sci. Rep.* **5**, 11141 (2015).
  98. Cooper, J. K. *et al.* Indirect Bandgap and Optical Properties of Monoclinic Bismuth Vanadate. *J. Phys. Chem. C* **119**, 2023 (2015).
  99. Cooper, J. K. *et al.* Electronic structure of monoclinic BiVO<sub>4</sub>. *Chem. Mater.* **26**, 5365–5373 (2014).
  100. Kim, T. W. & Choi, K. S. Nanoporous BiVO<sub>4</sub> photoanodes with dual-layer oxygen evolution catalysts for solar water splitting. *Science (80- )*. **343**, 990–994 (2014).
  101. Gan, J. *et al.* Tandem photovoltaic – photoelectrochemical GaAs / InGaAsP – WO<sub>3</sub> / BiVO<sub>4</sub> device for solar hydrogen generation. *Jpn. J. Appl. Phys.* **55**, 1–5 (2016).
  102. Zhao, Z., Li, Z. & Zou, Z. Electronic structure and optical properties of monoclinic clinobisvanite BiVO<sub>4</sub>. *Phys. Chem. Chem. Phys.* **13**, 4746–4753 (2011).
  103. Tücks, A. & Beck, H. P. The photochromic effect of bismuth vanadate pigments. Part I: Synthesis, characterization and lightfastness of pigment coatings. *J. Solid State Chem.* **178**, 1145–1156 (2005).
  104. Trinh, D. T. T., Khanitchaidecha, W., Channei, D. & Nakaruk, A. Synthesis, characterization and environmental applications of bismuth vanadate. *Res. Chem. Intermed.* **45**, 5217–5259 (2019).

105. Noor, M. *et al.* Effect of pH variation on structural, optical and shape morphology of BiVO<sub>4</sub> photocatalysts. *ICECE 2018 - 10th Int. Conf. Electr. Comput. Eng.* 81–84 (2018). doi:10.1109/ICECE.2018.8636721
106. Bierlein, J. D. & Sleight, A. W. Ferroelasticity in BiVO<sub>4</sub>. *Solid State Commun.* **16**, 69–70 (1975).
107. Pookmanee, P., Kojinok, S., Puntharod, R., Sangsrichan, S. & Phanichphant, S. Preparation and characterization of BiVO<sub>4</sub> powder by the sol-gel method. *Ferroelectrics* **456**, 45–54 (2013).
108. Bhattacharya, A. K., Mallick, K. K. & Hartridge, A. Phase transition in BiVO<sub>4</sub>. *Mater. Lett.* **30**, 7–13 (1997).
109. Zhou, D., Pang, L. X., Wang, D. W. & Reaney, I. M. BiVO<sub>4</sub> based high k microwave dielectric materials: a review. *J. Mater. Chem. C* **6**, 9290–9313 (2018).
110. Tolod, K. R. *et al.* Insights on the surface chemistry of BiVO<sub>4</sub> photoelectrodes and the role of Al overlayers on its water oxidation activity. *Appl. Catal. A Gen.* **605**, 117796 (2020).
111. Kim, J. H. & Lee, J. S. Elaborately Modified BiVO<sub>4</sub> Photoanodes for Solar Water Splitting. *Adv. Mater.* **31**, 1806938 (2019).
112. Liang, Y., Tsubota, T., A Mooij, L. P. & van de Krol, R. Highly Improved Quantum Efficiencies for Thin Film BiVO<sub>4</sub> Photoanodes. *J. Phys. Chem. C* **115**, (2011).
113. Tokunaga, S., Kato, H. & Kudo, A. Selective preparation of monoclinic and tetragonal BiVO<sub>4</sub> with scheelite structure and their photocatalytic properties. *Chem. Mater.* **13**, 4624–4628 (2001).
114. Tolod, K., Hernández, S. & Russo, N. Recent Advances in the BiVO<sub>4</sub> Photocatalyst for Sun-Driven Water Oxidation: Top-Performing Photoanodes and Scale-Up Challenges. *Catalysts* **7**, 13 (2017).
115. Kim, H., Bae, S., Jeon, D. & Ryu, J. Fully solution-processable Cu<sub>2</sub>O-BiVO<sub>4</sub> photoelectrochemical cells for bias-free solar water splitting. *Green Chem.* **20**, 3732–3742 (2018).
116. Lin, Z., Hu, J., Zhang, B., Wu, L. & Wang, J. Illuminated from back or front? Insight into factors affecting the efficiency of BiVO<sub>4</sub> photoanode. *Appl. Catal. A Gen.* **652**, 119024 (2023).
117. Seabold, J. A., Zhu, K. & Neale, N. R. Efficient solar photoelectrolysis by nanoporous Mo:BiVO<sub>4</sub> through controlled electron transport. *Phys. Chem. Chem. Phys.* **16**, 1121–1131 (2014).
118. Rettie, A. J. E. *et al.* Combined charge carrier transport and photoelectrochemical characterization of BiVO<sub>4</sub> single crystals: Intrinsic behavior of a complex metal oxide. *J. Am. Chem. Soc.* **135**, 11389–11396 (2013).
119. Ju, S. *et al.* Simultaneous Improvement of Absorption and Separation Efficiencies of Mo:BiVO<sub>4</sub> Photoanodes via Nanopatterned SnO<sub>2</sub>/Au Hybrid Layers. *ACS Sustain. Chem. Eng.* **7**, 17000–17007 (2019).
120. Hernández, S., Gerardi, G., Bejtka, K., Fina, A. & Russo, N. Evaluation of the charge transfer kinetics of spin-coated BiVO<sub>4</sub> thin films for sun-driven water photoelectrolysis. *Appl. Catal. B Environ.* **190**, 66–74 (2016).

121. Ma, Y., Pendlebury, S. R., Reynal, A., Le Formal, F. & Durrant, J. R. Dynamics of photogenerated holes in undoped BiVO<sub>4</sub> photoanodes for solar water oxidation. *Chem. Sci.* **5**, 2964–2973 (2014).
122. Öz, S., Singh, T., Resalati, S., Kim, G. M. & Babu, V. Industrial perspectives on the upscaling of perovskite materials for photovoltaic applications and its environmental impacts. *Met. Halide Perovskites Gener. Manip. Detect. Light* 117–142 (2023). doi:10.1016/B978-0-323-91661-5.00018-0
123. Mustafa, H. A. M. & Jameel, D. A. Modeling and the main stages of spin coating process: A review. *J. Appl. Sci. Technol. Trends* **2**, 91–95 (2021).
124. Poddighe, M. & Innocenzi, P. Hydrophobic thin films from Sol–Gel processing: A critical review. *Materials (Basel)*. **14**, (2021).
125. Nasirpouri, F., Alipour, K., Daneshvar, F. & Sanaeian, M.-R. Electrodeposition of anticorrosion nanocoatings. *Corros. Prot. Nanoscale* 473–497 (2020). doi:10.1016/b978-0-12-819359-4.00024-6
126. Arya, S. & Mahajan, P. CIGS-Based Solar Cells. *Sol. Cells* 77–100 (2023). doi:10.1007/978-981-99-7333-0\_3
127. Deligianni, L., Ahmed, S. & Romankiw, L. T. The next frontier: Electrodeposition for solar cell fabrication. *Electrochem. Soc. Interface* **20**, 47–53 (2011).
128. Lee, W. H., Kang, J., Park, H. S., Nam, K. M. & Cho, S. K. Photoelectrochemical response of Au-decorated CuBi<sub>2</sub>O<sub>4</sub> photocathode in bicarbonate solution. *J. Electroanal. Chem.* **838**, 172–177 (2019).
129. Sun, Z. *et al.* Construction of organic–inorganic hybrid photoanodes with metal phthalocyanine complexes to improve photoelectrochemical water splitting performance. *New J. Chem.* **46**, 9111–9118 (2022).
130. Wang, Z., Huang, X. & Wang, X. Recent progresses in the design of BiVO<sub>4</sub>-based photocatalysts for efficient solar water splitting. *Catal. Today* **335**, 31–38 (2019).
131. Guo, L., Li, X. & Chen, G. Techniques of electrode fabrication. *Electrochem. Environ.* 55–98 (2010). doi:10.1007/978-0-387-68318-8\_3
132. Hilliard, S. *et al.* Mesoporous thin film WO<sub>3</sub> photoanode for photoelectrochemical water splitting: A sol-gel dip coating approach. *Sustain. Energy Fuels* **1**, 145–153 (2017).
133. Luo, W. *et al.* Solar hydrogen generation from seawater with a modified BiVO<sub>4</sub> photoanode †. (2011). doi:10.1039/c1ee01812d
134. Sayama, K. *et al.* Photoelectrochemical decomposition of water on nanocrystalline BiVO<sub>4</sub> film electrodes under visible light. **3**, 48–79 (2003).
135. Sayama, K. *et al.* Photoelectrochemical decomposition of water into H<sub>2</sub> and O<sub>2</sub> on porous BiVO<sub>4</sub> thin-film electrodes under visible light and significant effect of Ag Ion treatment. *J. Phys. Chem. B* **110**, 11352–11360 (2006).
136. Ngoc, D. N. Engineering of a viable artificial leaf for solar fuel. (2023).
137. Le, H. V. *et al.* Decoration of AgOx hole collector to boost photocatalytic water oxidation activity of BiVO<sub>4</sub> photoanode. *Mater. Today Energy* **21**, (2021).
138. Hamd, W. *et al.* Mesoporous a-Fe<sub>2</sub>O<sub>3</sub> thin films synthesized via the sol-gel process for light-driven water oxidationw. *Phys. Chem. Chem. Phys* **14**, 13224–13232 (2012).

139. Liu, C. *et al.* Cobalt–phosphate-modified Mo:BiVO<sub>4</sub> mesoporous photoelectrodes for enhanced photoelectrochemical water splitting. *J. Mater. Sci.* **54**, 10670–10683 (2019).
140. Li, Y. *et al.* High Fill Factor and Reduced Hysteresis Perovskite Solar Cells Using Small-Molecule-Engineered Nickel Oxide as the Hole Transport Layer. *ACS Appl. Energy Mater.* **6**, 1555–1564 (2023).
141. Veeco Instruments Inc. *DEKTAK 150 Surface Profiler User's Manual.* (2007).
142. Saadati, M., Akhavan, O. & Fazli, H. Single-layer MoS<sub>2</sub>-MoO<sub>3-x</sub> heterojunction nanosheets with simultaneous photoluminescence and co-photocatalytic features. *Catalysts* **11**, (2021).
143. Le, H. V. *et al.* Decoration of AgOx hole collector to boost photocatalytic water oxidation activity of BiVO<sub>4</sub> photoanode. *Mater. Today Energy* **21**, 100762 (2021).
144. Ye, H., Lee, J., Jang, J. S. & Bard, A. J. Rapid screening of bivo<sub>4</sub>-based photocatalysts by scanning electrochemical microscopy (SECM) and studies of their photoelectrochemical properties. *J. Phys. Chem. C* **114**, 13322–13328 (2010).
145. Nair, V., Perkins, C. L., Lin, Q. & Law, M. Textured nanoporous Mo:BiVO<sub>4</sub> photoanodes with high charge transport and charge transfer quantum efficiencies for oxygen evolution †. *1412 | Energy Environ. Sci* **9**, 1412 (2016).
146. Byun, S. *et al.* Compositional engineering of solution-processed BiVO<sub>4</sub> photoanodes toward highly efficient photoelectrochemical water oxidation. *Nano Energy* **43**, 244–252 (2018).
147. Zhang, X., Huang, Y., Ma, F., Zhang, Z. & Wei, X. Influences of vacancies on the structural, electronic and optical properties of monoclinic BiVO<sub>4</sub>. *J. Phys. Chem. Solids* **121**, 85–92 (2018).
148. Nguyen, T. D. *et al.* Co<sup>2+</sup> substituted for Bi<sup>3+</sup> in BiVO<sub>4</sub> and its enhanced photocatalytic activity under visible LED light irradiation. *RSC Adv.* **9**, 23526–23534 (2019).
149. Wang, Y. *et al.* Microwave synthesis and photocatalytic activity of Tb<sup>3+</sup> doped BiVO<sub>4</sub> microcrystals. *J. Colloid Interface Sci.* **483**, 307–313 (2016).
150. Chauvet, A. *Contribution to the simulation of thin-film Photo-anode Optical Properties.* (2021).
151. Peumans, P., Yakimov, A. & Forrest, S. R. Small molecular weight organic thin-film photodetectors and solar cells. *J. Appl. Phys.* **93**, 3693–3723 (2003).
152. Burkhard, G. F. & Hoke, E. T. Transfer Matrix Optical Modeling. 1–6 (2011).
153. Pettersson, L. A. A., Roman, L. S. & Inganäs, O. Modeling photocurrent action spectra of photovoltaic devices based on organic thin films. *J. Appl. Phys.* **86**, 487–496 (1999).
154. Mehdizadeh Rad, H., Zhu, F. & Singh, J. Profiling exciton generation and recombination in conventional and inverted bulk heterojunction organic solar cells. *J. Appl. Phys.* **124**, (2018).
155. Someda, C. G. *Electromagnetic waves.* 577 (2006).
156. Rafieipour, P., Mohandes, A., Moaddeli, M. & Kanani, M. Integrating transfer matrix method into SCAPS-1D for addressing optical losses and per-layer optical properties in perovskite/Silicon tandem solar cells. (2023).

157. Lipovšek, B., Krč, J. & Topič, M. Optical model for thin-film photovoltaic devices with large surface textures at the front side. *Inf. MIDEEM* **41**, 264–271 (2011).
158. Lipovšek, B., Krč, J. & Topič, M. *CROWM User Manual*. (2021).
159. Lipovšek, B., Krč, J., Topič, M. & Member, S. Optimization of Microtextured Light-Management Films for Enhanced Light Trapping in Organic Solar Cells Under Perpendicular and Oblique Illumination Conditions. *IEEE J. PHOTOVOLTAICS* **4**, (2014).
160. Zhang, X., Sun, X. H. & Jiang, L. Di. Absorption enhancement using nanoneedle array for solar cell. *Appl. Phys. Lett.* **103**, 211110 (2013).
161. Lipovšek, B. *et al.* Detailed optical modelling and light-management of thin-film organic solar cells with consideration of small-area effects. *Opt. Express* **25**, A176 (2017).
162. Holman, Z. C. *et al.* Parasitic absorption in the rear reflector of a silicon solar cell: Simulation and measurement of the sub-bandgap reflectance for common dielectric/metal reflectors. *Sol. Energy Mater. Sol. Cells* **120**, 426–430 (2014).
163. Sarkar, S., Das, N. S. & Chattopadhyay, K. K. Optical constants, dispersion energy parameters and dielectric properties of ultra-smooth nanocrystalline BiVO<sub>4</sub> thin films prepared by rf-magnetron sputtering. *Solid State Sci.* **33**, 58–66 (2014).
164. Rai, R. & Singh, B. K. Absorbance and Transmittance measurement of CsI thin films. **58**, 838–839 (2013).
165. Cendula, P., Steier, L., Losio, P. A., Grätzel, M. & Schumacher, J. O. Analysis of optical losses in a photoelectrochemical cell: A tool for precise absorptance estimation. *Adv. Funct. Mater.* **28**, 1–9 (2018).
166. Karuturi, S. K. *et al.* Over 17% Efficiency Stand-Alone Solar Water Splitting Enabled by Perovskite-Silicon Tandem Absorbers. *Adv. Energy Mater.* **10**, (2020).
167. Shi, X. *et al.* Efficient photoelectrochemical hydrogen production from bismuth vanadate-decorated tungsten trioxide helix nanostructures. *Nat. Commun.* **5**, 1–8 (2014).
168. Zhang, Y. *et al.* Engineering BiVO<sub>4</sub> and Oxygen Evolution Cocatalyst Interfaces with Rapid Hole Extraction for Photoelectrochemical Water Splitting. *ACS Catal.* **13**, 5938–5948 (2023).
169. O'Reilly, J. E. Oxidation-reduction potential of the ferro-ferricyanide system in buffer solutions. *Biochim. Biophys. Acta - Bioenerg.* **292**, 509–515 (1973).
170. De Tovar, J. *et al.* Light-driven water oxidation using hybrid photosensitizer-decorated Co<sub>3</sub>O<sub>4</sub> nanoparticles. *Mater. Today Energy* **9**, 506–515 (2018).
171. McCrory, C. C. L. *et al.* Benchmarking Hydrogen Evolving Reaction and Oxygen Evolving Reaction Electrocatalysts for Solar Water Splitting Devices. *J. Am. Chem. Soc.* **137**, 4347–4357 (2015).
172. Medjahed, A. A. Structure-properties correlation in hybrid perovskite for photovoltaics. (Université Grenoble Alpes, 2021).
173. Pellat, M. *et al.* Photoelectrochemical converter for producing dihydrogen. (2023).
174. Pellat, M., Roux, G., Shopie, C. & Maragno, A. R. A. Photoelectrochemical converter for producing dihydrogen. (2023).

175. Walter, M. G. *et al.* Solar water splitting cells. *Chem. Rev.* **110**, 6446–6473 (2010).
176. Zahran, Z. N., Tsubonouchi, Y. & Yagi, M. Solar-Driven H<sub>2</sub> Production in PVE Systems. *Sol. Fuels* 341–373 (2023). doi:10.1002/9781119752097.ch10
177. Cheng, W. H. *et al.* Monolithic Photoelectrochemical Device for Direct Water Splitting with 19% Efficiency. *ACS Energy Lett.* **3**, 1795–1800 (2018).
178. Goto, Y. *et al.* A Particulate Photocatalyst Water-Splitting Panel for Large-Scale Solar Hydrogen Generation. *Joule* **2**, 509 (2018).
179. Zhou, P. *et al.* Solar-to-hydrogen efficiency of more than 9% in photocatalytic water splitting. *Nature* **613**, 66–70 (2023).
180. Chen, Q., Fan, G., Fu, H., Li, Z. & Zou, Z. Tandem photoelectrochemical cells for solar water splitting. **3**, 1487267 (2018).
181. Miller, E. L. Photoelectrochemical water splitting. *Energy Environ. Sci* **8**, 2809 (2015).
182. Pinaud, B. A. *et al.* Technical and Economic Feasibility of Centralized Facilities for Solar Hydrogen Production via Photocatalysis and Photoelectrochemistry. *Energy Environ. Sci.* **6**, 1983 (2013).
183. Ardo, S. *et al.* Pathways to electrochemical solar-hydrogen technologies. *Energy Environ. Sci* **11**, 2768 (2018).
184. Detz, R. J., Reek, J. N. H. & Van Der Zwaan, B. C. C. The future of solar fuels: when could they become competitive? *Energy Environ. Sci* **11**, 1653 (2018).
185. Gao, J. *et al.* Solar Water Splitting with Perovskite/Silicon Tandem Cell and TiC-Supported Pt Nanocluster Electrocatalyst. *Joule* **3**, 2930–2941 (2019).
186. Karuturi, S. K. *et al.* Over 17% Efficiency Stand-Alone Solar Water Splitting Enabled by Perovskite-Silicon Tandem Absorbers. *Adv. Energy Mater.* **10**, 1–9 (2020).
187. Wang, Y. *et al.* Direct Solar Hydrogen Generation at 20% Efficiency Using Low-Cost Materials. *Adv. Energy Mater.* **11**, (2021).
188. Pan, S. *et al.* An over 20% solar-to-hydrogen efficiency system comprising a self-reconstructed NiCoFe-based hydroxide nanosheet electrocatalyst and monolithic perovskite/silicon tandem solar cell. *J. Mater. Chem. A* **9**, 14085–14092 (2021).
189. Chiu, Y.-H., Lai, T.-H., Kuo, M.-Y., Hsieh, P.-Y. & Hsu, Y.-J. Photoelectrochemical cells for solar hydrogen production: Challenges and opportunities APL Materials PERSPECTIVE scitation.org/journal/apm Photoelectrochemical cells for solar hydrogen production: Challenges and opportunities. **7**, 80901 (2019).
190. Maragno, A. R. A. *et al.* A scalable integrated solar device for the autonomous production of green methane. *Submitt. Joule*
191. Lee, C. Y., Taylor, A. C., Nattestad, A., Beirne, S. & Wallace, G. G. 3D Printing for Electrocatalytic Applications. *Joule* **3**, 1835–1849 (2019).
192. Yang, G. *et al.* Fully printed and integrated electrolyzer cells with additive manufacturing for high-efficiency water splitting. *Appl. Energy* **215**, 202–210 (2018).
193. Haynes, W. M. *CRC Handbook of Chemistry and Physics. Journal of the American Pharmaceutical Association* (CRC Press, 2015).
194. Chisholm, G., Kitson, P. J., Kirkaldy, N. D., Bloor, L. G. & Cronin, L. 3D printed flow plates for the electrolysis of water: An economic and adaptable approach to device

- manufacture. *Energy Environ. Sci.* **7**, 3026–3032 (2014).
195. Khenkin, M. V. *et al.* Consensus statement for stability assessment and reporting for perovskite photovoltaics based on ISOS procedures. *Nat. Energy* **5**, 35–49 (2020).
  196. Vogt, H. & Balzer, R. J. The bubble coverage of gas-evolving electrodes in stagnant electrolytes. *Electrochim. Acta* **50**, 2073–2079 (2005).
  197. Gr', G. *et al.* Development of a CO<sub>2</sub>-biomethanation reactor for producing methane from green H<sub>2</sub>. (2024). doi:10.1039/d3se01550e
  198. Juillard, S. *et al.* Mechanical Reliability of Flexible Encapsulated Organic Solar Cells: Characterization and Improvement. *ACS Appl. Mater. Interfaces* **10**, 29805–29813 (2018).
  199. Sendner, M., Trollmann, J. & Pucci, A. Dielectric function and degradation process of poly(triarylamine) (PTAA). *Org. Electron.* **15**, 2959–2963 (2014).
  200. Rombach, F. M., Haque, S. A. & Macdonald, T. J. Lessons learned from spiro-OMeTAD and PTAA in perovskite solar cells. *Energy Environ. Sci.* **14**, 5161–5190 (2021).
  201. Yaghoobi Nia, N. *et al.* Beyond 17% stable perovskite solar module via polaron arrangement of tuned polymeric hole transport layer. *Nano Energy* **82**, 105685 (2021).
  202. Döscher, H., Geisz, J. F., Deutsch, T. G. & Turner, J. A. Sunlight absorption in water-efficiency and design implications for photoelectrochemical devices. *Energy Environ. Sci.* **7**, 2951–2956 (2014).
  203. Holmes-Gentle, I., Tembhurne, S., Suter, C. & Haussener, S. Kilowatt-scale solar hydrogen production system using a concentrated integrated photoelectrochemical device. *Nat. Energy* **8**, 586–596 (2023).
  204. Yang, G. *et al.* Shunt mitigation toward efficient large-area perovskite-silicon tandem solar cells. *Cell Reports Phys. Sci.* **4**, 101628 (2023).
  205. Charton, S., Maragno, A. R. A., Matheron, M. & Artero, V. Convertisseur photoélectrochimique. FR2313467.
  206. Aydin, E. *et al.* Pathways toward commercial perovskite/silicon tandem photovoltaics. *Science (80-. )*. **383**, 1–13 (2024).
  207. Lubbe, F., Rongé, J., Bosserez, T. & Martens, J. A. Golden hydrogen. *Curr. Opin. Green Sustain. Chem.* **39**, 100732 (2023).
  208. Honsberg, C. & Bowden, S. www.pveducation.org. 2019 [cited 2024 Apr 22]. Solar radiation on a Tilted Surface. Available at: <https://www.pveducation.org/pvcdrom/properties-of-sunlight/solar-radiation-on-a-tilted-surface>.
  209. Jia, J. *et al.* Solar water splitting by photovoltaic-electrolysis with a solar-to-hydrogen efficiency over 30%. *Nat. Commun.* **7**, (2016).
  210. Kistler, T. A. *et al.* Emergent Degradation Phenomena Demonstrated on Resilient, Flexible, and Scalable Integrated Photoelectrochemical Cells. *Adv. Energy Mater.* **10**, (2020).
  211. Park, H. *et al.* Water Splitting Exceeding 17% Solar-To-Hydrogen Conversion Efficiency Using Solution-Processed Ni-Based Electrocatalysts and Perovskite/Si Tandem Solar Cell. *ACS Appl. Mater. Interfaces* **11**, 33835–33843 (2019).



212. Pan, S. *et al.* An over 20% solar-to-hydrogen efficiency system comprising a self-reconstructed NiCoFe-based hydroxide nanosheet electrocatalyst and monolithic perovskite/silicon tandem solar cell. *J. Mater. Chem. A* **9**, 14085–14092 (2021).
213. Wang, M. *et al.* Integrated and Unassisted Solar Water-Splitting System by Monolithic Perovskite/Silicon Tandem Solar Cell. *Sol. RRL* **6**, 1–7 (2022).
214. Sharma, A. *et al.* Direct solar to hydrogen conversion enabled by silicon photocathodes with carrier selective passivated contacts. *Sustain. Energy Fuels* **6**, 349–360 (2022).
215. Song, Z. *et al.* All-Perovskite Tandem Photoelectrodes for Unassisted Solar Hydrogen Production. *ACS Energy Lett.* **8**, 2611–2619 (2023).
216. Gao, J. *et al.* Solar Water Splitting with Perovskite/Silicon Tandem Cell and TiC-Supported Pt Nanocluster Electrocatalyst. *Joule* **3**, 2930–2941 (2019).
217. Pehlivan, İ. B. *et al.* NiMoV and NiO-based catalysts for efficient solar-driven water splitting using thermally integrated photovoltaics in a scalable approach. *iScience* **24**, 101910 (2021).
218. Calnan, S. *et al.* Development of Various Photovoltaic-Driven Water Electrolysis Technologies for Green Solar Hydrogen Generation. *Sol. RRL* **6**, (2022).
219. Lee, M., Haas, S., Smirnov, V., Merdzhanova, T. & Rau, U. Scalable Photovoltaic-Electrochemical Cells for Hydrogen Production from Water - Recent Advances. *ChemElectroChem* **9**, e202200838 (2022).
220. Pornrunroj, C. *et al.* Hybrid photothermal–photocatalyst sheets for solar-driven overall water splitting coupled to water purification. *Nat. Water* **1**, 952–960 (2023).
221. Segev, G. *et al.* The 2022 solar fuels roadmap. *J. Phys. D. Appl. Phys.* **55**, 323003 (2022).
222. Andrei, V. *et al.* Floating perovskite-BiVO<sub>4</sub> devices for scalable solar fuel production. *Nature* **608**, 518–522 (2022).
223. Larrazábal, G. O., Martín, A. J. & Pérez-Ramírez, J. Building Blocks for High Performance in Electrocatalytic CO<sub>2</sub> Reduction: Materials, Optimization Strategies, and Device Engineering. *J. Phys. Chem. Lett.* **8**, 3933–3944 (2017).
224. Rönsch, S. *et al.* Review on methanation - From fundamentals to current projects. *Fuel* **166**, 276–296 (2016).
225. Frontera, P. *et al.* Supported Catalysts for CO<sub>2</sub> Methanation: A Review. *Catalysts* **7**, (2017).
226. Hren, R. *et al.* Hydrogen production, storage and transport for renewable energy and chemicals: An environmental footprint assessment. *Renew. Sustain. Energy Rev.* **173**, (2023).
227. Maragno, A. R. A. *et al.* Thermally integrated photoelectrochemical devices with perovskite / silicon tandem solar cells : a modular approach for scalable direct water splitting. *ChemRxiv* 1–24 (2024). doi:<https://doi.org/10.26434/chemrxiv-2024-xc4rq>
228. Lourenço, A. C., Reis-Machado, A. S., Fortunato, E., Martins, R. & Mendes, M. J. Sunlight-driven CO<sub>2</sub>-to-fuel conversion: Exploring thermal and electrical coupling between photovoltaic and electrochemical systems for optimum solar-methane production. *Mater. Today Energy* **17**, 100425 (2020).
229. Yamaguchi, S., Watanabe, K., Minegishi, T. & Sugiyama, M. Solar to hydrogen

- efficiency of 28.2% under natural sunlight achieved by a combination of five-junction concentrator photovoltaic modules and electrolysis cells. *Sustain. Energy Fuels* **7**, 1377–1381 (2023).
230. Cwicklinski, G. *et al.* Development of a CO<sub>2</sub>-biomethanation reactor for producing methane from green H<sub>2</sub>. *Sustain. Energy Fuels* **8**, 1068–1076 (2024).
  231. Aydin, E. *et al.* Interplay between temperature and bandgap energies on the outdoor performance of perovskite/silicon tandem solar cells. *Nat. Energy* **5**, 851–859 (2020).
  232. Charton, S., Janvier, J., Rivalier, P., Chaînet, E. & Caire, J. P. Hybrid sulfur cycle for H<sub>2</sub> production: A sensitivity study of the electrolysis step in a filter-press cell. *Int. J. Hydrogen Energy* **35**, 1537–1547 (2010).
  233. Goyal, N., Zhou, Z. & Karimi, I. A. Metabolic processes of *Methanococcus maripaludis* and potential applications. *Microb. Cell Fact.* **15**, 107 (2016).
  234. Jud, G., Schneider, K. & Bachofen, R. The role of hydrogen mass transfer for the growth kinetics of *Methanobacterium thermoautotrophicum* in batch and chemostat cultures MgCl<sub>2</sub> · 6H<sub>2</sub>O (1.5 mM); NTA (nitrilo-triacetate, 1.2 mM). *J. Ind. Microbiol. Biotechnol.* **19**, 246–251 (1997).
  235. Thema, M. *et al.* Biological CO<sub>2</sub>-methanation: An approach to standardization. *Energies* **12**, (2019).
  236. Wang, Y. *et al.* Direct Solar Hydrogen Generation at 20% Efficiency Using Low-Cost Materials. *Adv. Energy Mater.* **11**, 1–11 (2021).
  237. Chen, Z. *et al.* Grain-Boundary-Rich Copper for Efficient Solar-Driven Electrochemical CO<sub>2</sub> Reduction to Ethylene and Ethanol. *J. Am. Chem. Soc.* **142**, 6878–6883 (2020).
  238. Gurudayal *et al.* Si photocathode with Ag-supported dendritic Cu catalyst for CO<sub>2</sub> reduction. *Energy Environ. Sci.* **12**, 1068–1077 (2019).
  239. Jia, Q., Tanabe, S. & Waki, I. Direct gas-phase CO<sub>2</sub> reduction for solar methane generation using a gas diffusion electrode with a BiVO<sub>4</sub>:Mo and a Cu-In-Se photoanode. *Chem. Lett.* **47**, 436–439 (2018).
  240. Sekimoto, T. *et al.* Wireless InGaN – Si / Pt device for photo- electrochemical water splitting. *Jpn. J. Appl. Phys.* **55**, 088004 (2016).
  241. Gurudayal *et al.* Efficient solar-driven electrochemical CO<sub>2</sub> reduction to hydrocarbons and oxygenates. *Energy Environ. Sci.* **10**, 2222–2230 (2017).
  242. Huan, T. N. *et al.* Low-cost high-efficiency system for solar-driven conversion of CO<sub>2</sub> to hydrocarbons. *Proc. Natl. Acad. Sci. U. S. A.* **116**, 9735–9740 (2019).
  243. Ren, D., Loo, N. W. X., Gong, L. & Yeo, B. S. Continuous Production of Ethylene from Carbon Dioxide and Water Using Intermittent Sunlight. *ACS Sustain. Chem. Eng.* **5**, 9191–9199 (2017).
  244. Creissen, C. E. & Fontecave, M. Solar-Driven Electrochemical CO<sub>2</sub> Reduction with Heterogeneous Catalysts. *Adv. Energy Mater.* **11**, 1–12 (2021).
  245. Rahaman, M. *et al.* Solar-driven liquid multi-carbon fuel production using a standalone perovskite–BiVO<sub>4</sub> artificial leaf. *Nat. Energy* **8**, 629–638 (2023).
  246. Zoller, S. *et al.* A solar tower fuel plant for the thermochemical production of kerosene from H<sub>2</sub>O and CO<sub>2</sub>. *Joule* **6**, 1606–1616 (2022).

247. Luo, G. & Angelidaki, I. Integrated biogas upgrading and hydrogen utilization in an anaerobic reactor containing enriched hydrogenotrophic methanogenic culture. *Biotechnol. Bioeng.* **109**, 2729–2736 (2012).
248. Murano, R., Maisano, N., Selvaggi, R., Pappalardo, G. & Pecorino, B. Critical issues and opportunities for producing biomethane in Italy. *Energies* **14**, 1–14 (2021).
249. Babics, M. *et al.* One-year outdoor operation of monolithic perovskite/silicon tandem solar cells. *Cell Reports Phys. Sci.* **4**, 101280 (2023).
250. Aydin, E. *et al.* Enhanced optoelectronic coupling for perovskite/silicon tandem solar cells. *Nature* **623**, 732 (2023).
251. James, B. D., Baum, G. N., Perez, J. & Baum, K. N. Technoeconomic Analysis of Photoelectrochemical (PEC) Hydrogen Production. *DOE Contract Number GS-10F-009J 22201*, 1–128 (2009).